

# The Influence of In-Cylinder Flows on Spark-Ignition Engine Combustion

Am Fachbereich Maschinenbau  
der Technischen Universität Darmstadt

zur Erlangung des Grades eines  
Doktors der Ingenieurwissenschaften (Dr.-Ing.)  
genehmigte

**Dissertation**

von

**Cooper Haddad Welch, M.Sc.**

aus McKinney, Vereinigte Staaten von Amerika

Berichterstatter:	Prof. Dr. habil. A. Dreizler
Mitberichterstatter:	Dr. B. Peterson
Tag der Einreichung:	15. August 2023
Tag der mündlichen Prüfung:	17. Oktober 2023

Darmstadt 2023

D17

**Welch, Cooper Haddad:**

“The Influence of In-Cylinder Flows on Spark-Ignition Engine Combustion”

Darmstadt, Technische Universität Darmstadt

Jahr der Veröffentlichung der Dissertation auf TUPrints: 2024

URN: urn:nbn:de:tuda-tuprints-263403

URI: <https://tuprints.ulb.tu-darmstadt.de/id/eprint/26340>

Tag der mündlichen Prüfung: 17.10.2023

Veröffentlicht unter CC BY-SA 4.0 International

<https://creativecommons.org/licenses/by-sa/4.0/>

*Short cuts make long delays.*  
J.R.R. Tolkien





## Erklärung

Hiermit erkläre ich an Eides statt, dass ich die vorliegende Dissertation selbstständig verfasst und keine anderen als die von mir angegebenen Hilfsmittel verwendet habe. Ich erkläre außerdem, dass ich bisher noch keinen Promotionsversuch unternommen habe.

A handwritten signature in black ink, appearing to read 'Cooper Haddad Welch'. The signature is written in a cursive, flowing style.

Cooper Haddad Welch

Darmstadt, den 15. August 2023



## Acknowledgments

I would like to express my sincere gratitude to all those who have been instrumental in making this dissertation a reality. The personal and professional growth I have experienced over these challenging yet rewarding years would not have been possible without the support and encouragement of numerous individuals.

First and foremost, I would like to express my deepest appreciation to my advisor, Prof. Dr. rer. nat. habil. Andreas Dreizler, not only for providing me with the resources and environment to conduct research, but also for his invaluable guidance, insightful feedback, and mentorship throughout the course of this work. I am equally indebted to my group leader and mentor, Dr.-Ing. Benjamin Böhm, for his unwavering support and constant availability for almost daily spontaneous discussions where he provided ideas, feedback, and reassurance during turbulent times. My gratitude also extends to Dr. Brian Peterson, who agreed to co-examine my dissertation. His collaboration and mentorship over the past five years has provided invaluable insight, and his feedback and critiques have led to great improvements in this work.

Next, I would like to thank my friends and colleagues who have directly and indirectly supported my research and whose camaraderie has made this journey unforgettable. First, I would like to extend my heartfelt gratitude to Dr.-Ing. Marius Schmidt, whose daily collaboration was an integral part of this dissertation. This work would not have been possible without the countless hours Marius has dedicated to supporting me through cooperative measurement campaigns, assistance with data processing and code troubleshooting, and invaluable feedback on my papers and thesis. Furthermore, I greatly appreciate the personal conversations we had during our time working together, which not only made my time more interesting, but also contributed to my personal growth. Similarly, I would like to thank Lars Illmann for his dedicated support in many aspects that led to the completion of this thesis. I am deeply grateful for the many hours we shared in the lab, the collaborative data processing efforts, and our many engaging conversations. In addition, Christopher Geschwindner has played an influential role in my doctoral work, and I sincerely thank him for his collaboration on experimental work and publications, and his never-ending willingness to offer help along the way. I am equally grateful for the personal role he played in my time in Germany through his early acceptance and continued friendship. I would also like to express my gratitude to the many colleagues at RSM who have supported my work in various ways over the years or who have contributed to a pleasant working environment: Dr.-Ing. Johannes Bode, Dr.-Ing. Carl-Philipp Ding, Jannick Erhard, Dr.-Ing. Christian Fach, Dr.-Ing. Max Greifenstein, Dr.-Ing. Tao Li, Dr.-Ing. Yongxiang Li, Dr.-Ing. Andreas Preusche, Dr.-Ing. Florian Ries, Sandra Schary, Henrik Schneider, and Dr.-Ing. Florian Zentgraf, just to name a few.

I am also very grateful to my collaborators and co-authors from different working groups and institutions. I would like to thank the colleagues at our sister institute, STFS, for their contribution to the great working culture at RSM. I am especially grateful to Dr.-Ing. Andrea Pati and Prof. Dr.-Ing. Christian Hasse for performing simulations and providing invaluable feedback on the design of the flow bench used in this thesis. In addition, I would like to thank the collaborators in my final funding project, FOR 2687, for fruitful discussions that led to successful cooperation and publications.

This dissertation would not have been possible without the continued support of the RSM operations staff, whose behind-the-scenes work keeps the institute running smoothly. In particular, I would like to thank the secretarial staff, Marion Müller, Angela Berger, and Patricia John, who have assisted me in every step of the doctoral process, from finding my first apartment

in Germany to completing the final paperwork for thesis submission. In addition, the tireless work of RSM's IT team, especially Dr. rer. nat. Steven Wagner, Hardy Hamel, Henrik Matero, Janik Hebel, and Robin Schultheis, is highly appreciated. Furthermore, I would like to extend my appreciation to Andreas Ludwig and Gabriele Goet for their dedicated support in running the laboratory operations and in supporting the ordering of equipment essential to my research. Lastly, I am grateful for the unparalleled craftsmanship and design advice of the workshop staff, especially Roland Berntheisel and Dirk Feldmann, who assisted in or personally performed the fabrication of countless components integral to this thesis.

I would like to acknowledge my close friends and family for their steadfast support and encouragement that helped me overcome the countless challenges along the way. I am forever indebted to my parents, Joani and Gary, for raising me to have a curious mind and always encouraging me to pursue my dreams, even if it meant moving 5000 miles away. In addition, I would like to express my deepest gratitude to the Abrolats for welcoming me into their family from the beginning and providing me with a home away from home. Finally, I am especially grateful to my partner, Carina, whose countless sacrifices and endless support have made this work possible and carried me to the finish line.

Darmstadt, the 15<sup>th</sup> of August, 2023

Cooper Haddad Welch

## Abstract

The urgent need for a global energy transition from traditional fossil fuels to renewable sources has been underscored by the alarming rise in global temperatures and growing concerns about air pollution. Light-duty internal combustion engines, despite years of technological advances, continue to contribute significantly to greenhouse gas emissions and harmful pollutants, necessitating further progress in engine technologies for a multi-faceted solution to combat climate change and improve air quality. This cumulative dissertation addresses the critical challenge of understanding and controlling the cycle-to-cycle variability in engine combustion that directly impacts emissions. It extensively investigates the influence of in-cylinder flows on combustion phenomena in an optically accessible spark-ignition engine with the overarching goal of reducing cycle-to-cycle variations. The study includes five peer-reviewed articles and unpublished work, providing a comprehensive analysis of the relationship between engine flows and combustion processes from simplified to realistic engine configurations.

High-speed diagnostics and robust analysis techniques are employed to advance the development of predictive combustion models that contribute to improved engine design. This work extends existing measurement techniques by combining cutting-edge equipment with novel analysis approaches, culminating in the development of phenomenological models. In addition, it provides a vast database of accurate boundary conditions and multi-parameter vector and scalar data to benefit the engine research community and improve numerical simulations and models.

The thesis is structured in two parts, with each publication building on the previous one and increasing in complexity. The first part focuses on the fundamental processes of intake flows and their interaction with direct injection sprays. A designed flow bench integrated into the engine test cell is used to study turbulent intake flows of the spray-guided cylinder geometry, providing valuable validation data and controlled flow conditions for spray analysis. Building on the flow bench study, the investigation of backflow-induced pressure oscillations in the intake manifold during part-load motored operation reveals their significant impact on intake flow and tumble development, emphasizing the need to consider acoustics and accompanying physics in engine simulations. Finally, the relationship between in-cylinder flows and direct injection sprays is investigated by analyzing the influence of flow on spray morphology under different conditions, providing essential boundary conditions and multi-parameter data for validation.

The second part builds on the knowledge and techniques developed in the first part to explore cyclic variations in engine performance under diluted fired conditions. The use of different levels of external exhaust gas recirculation to alter flame speed, enhances the effects of flow on the combustion process, particularly ignition and flame development. Analysis of the influence of flow on ignition using measured voltage and current of the ignition coil, combined with flow fields, spark plasma images, and flame visualizations, sheds light on the significance of horizontal flow across the spark plug in promoting more stable and faster combustion. Multivariate and conditioned statistical analysis techniques are used to develop flow-flame and flow-misfire combustion models that describe cycle-to-cycle variations under diluted conditions, offering further promise for optimized design and control.

This dissertation makes substantial contributions to the engine research community by emphasizing the pivotal role of in-cylinder flows in the combustion processes of spark-ignition engines. Furthermore, the availability of a comprehensive database of controlled boundary conditions and well-documented multi-parameter data facilitates the further development of phenomenological models and computational fluid dynamics simulations, thereby promoting continued advances in engine technology for a sustainable future.

## Kurzfassung

Die weltweite Dringlichkeit eines Übergangs von fossilen zu erneuerbaren Energiequellen wird durch den alarmierenden Anstieg der globalen Temperaturen und wachsende Luftverschmutzung betont. Trotz technologischer Fortschritte tragen Verbrennungsmotoren weiterhin signifikant zu Treibhausgas- und Schadstoffemissionen bei, weshalb Fortschritte in Motorentchnologien für eine ganzheitliche Lösung zur Bekämpfung des Klimawandels und zur Verbesserung der Luftqualität notwendig sind.

Diese kumulative Dissertation widmet sich der entscheidenden Herausforderung, die Zyklus-zu-Zyklus-Variabilität in der Motorenverbrennung zu verstehen und zu kontrollieren, da sie direkte Auswirkungen auf die Emissionen hat. Dabei wird umfassend die Wirkung der Zylinderströmungen auf die Verbrennungsphänomene in einem optisch zugänglichen Ottomotor untersucht, um die Schwankungen zu reduzieren. Die Arbeit umfasst fünf wissenschaftliche Artikel und unveröffentlichte Arbeiten, die eine umfassende Analyse der Beziehung zwischen Motorströmung und Verbrennungsprozessen in verschiedenen Motorkonfigurationen bieten.

Die Dissertation erweitert bestehende Messverfahren durch die Kombination von moderner Hochgeschwindigkeitsmesstechnik mit neuartigen Analyseansätzen und entwickelt phänomenologische Modelle zur Verbesserung des Prozessverständnisses und Motordesigns. Zudem stellt sie eine umfangreiche Datenbank mit präzisen Randbedingungen und vielfältigen Parametern bereit, die der motorischen Forschung zugutekommen und numerische Simulationen und Modelle verbessern.

Die Arbeit gliedert sich in zwei Teile, wobei jede Veröffentlichung auf der vorherigen aufbaut und an Komplexität zunimmt. Der erste Teil fokussiert sich auf die Einlassströmung und ihre Wechselwirkung mit der Direkteinspritzung. Ein eigens entwickelter Strömungsprüfstand wird genutzt, um die turbulente Einlassströmung in einer strahlgeführten Zylindergeometrie zu untersuchen und validierte Strömungsbedingungen für die Direkteinspritzung zu bieten. Die Untersuchung der Einlassströmung während des Betriebs bei Teillast zeigt den signifikanten Einfluss auf die Zylinderinnenströmung und betont die Bedeutung von Akustik und begleitender Physik in Motorsimulationen. Abschließend analysiert die Arbeit die Beziehung zwischen Zylinderströmungen und Direkteinspritzung und liefert Randbedingungen und Mehrfachparameterdaten für die Validierung.

Der zweite Teil baut auf den Erkenntnissen des ersten Teils auf, um zyklische Variationen in der Motorleistung bei Abgasrückführung zu untersuchen. Durch Variation der Abgasrückführung und Flammengeschwindigkeit werden die Auswirkungen der Strömung auf den Verbrennungsprozess, insbesondere die Zündung und Flammenausbreitung, verstärkt. Der Einfluss der Strömung auf die Zündung wird anhand von Strom- und Spannungsverläufen in Kombination mit Strömungsfeldern und Visualisierung von Zündfunken und Flammen analysiert. Mithilfe von multivariater und konditionierter Statistik werden Modelle entwickelt, die zyklische Schwankungen bei Betrieb mit Abgasrückführung beschreiben und Möglichkeiten für ein optimiertes Design eröffnen.

Diese Dissertation betont die entscheidende Rolle der Zylinderströmungen in Verbrennungsprozessen von Ottomotoren und fördert die Entwicklung nachhaltiger Motortechnologie durch die Bereitstellung einer umfassenden Datenbank mit kontrollierten Randbedingungen und dokumentierten Parametern für die Weiterentwicklung von Modellen und Simulationen.

# Contents

List of Figures . . . . .	III
List of Tables . . . . .	V
Nomenclature . . . . .	XI
List of Publications . . . . .	XI
<b>1 Introduction</b>	<b>1</b>
1.1 Motivation . . . . .	1
1.2 Current State of Research . . . . .	2
1.2.1 In-Cylinder Flows . . . . .	2
1.2.2 Spray-Guided Direct Injection . . . . .	4
1.2.3 Ignition and Flame Propagation . . . . .	5
1.2.4 Cycle-to-Cycle Variations . . . . .	6
1.3 Aim and Structure of the Work . . . . .	8
1.3.1 Aim . . . . .	8
1.3.2 Structure . . . . .	9
<b>2 Theoretical Background</b>	<b>13</b>
2.1 Spark-Ignition Engine Combustion . . . . .	13
2.1.1 In-Cylinder Flows . . . . .	13
2.1.2 Mixture Formation . . . . .	16
2.1.3 Sparking and Flame Development . . . . .	17
2.1.4 Sources of Cyclic Variability . . . . .	18
2.2 Optical Diagnostics . . . . .	19
2.2.1 Mie Scattering and Particle Image Velocimetry . . . . .	19
<b>3 Experimental Methodology</b>	<b>23</b>
3.1 Darmstadt Engine Test Bench . . . . .	23
3.2 Operating Conditions . . . . .	25
3.3 Optical Diagnostics and Processing . . . . .	26
3.3.1 High-speed PIV . . . . .	26
3.3.2 Spray Visualization . . . . .	28
3.3.3 Flame Visualization . . . . .	28
3.3.4 Spark Imaging . . . . .	28
3.4 Summary of Techniques Used . . . . .	29
<b>4 Experimental Characterization of the Intake Flow</b>	<b>31</b>
4.1 Dynamics Governing Intake Flows . . . . .	31
4.1.1 Investigation of Turbulent Intake Flows in a Flow Bench . . . . .	31
4.1.2 The Influence of Intake Manifold Pressure Oscillations on In-Cylinder Flows	35
4.2 Spray-Flow Interaction . . . . .	37

4.2.1	Survey of the Spray Morphology under Varying Flow Bench Mass Flow Rates . . . . .	38
4.2.2	Analysis of the Intake Flow's Effects on Early Direct Injection Sprays . .	39
4.3	Summary . . . . .	41
<b>5</b>	<b>In-Cylinder Flows and Cyclic Instability</b>	<b>43</b>
5.1	Definition and Characterization of Operating Conditions . . . . .	43
5.2	Evaluation of the Flow's Effects on Spark Behavior and Ignition . . . . .	45
5.3	The Impact of Flow on the Cause-and-Effect Chain . . . . .	47
5.4	Summary . . . . .	51
<b>6</b>	<b>Summary and Outlook</b>	<b>53</b>
6.1	Summary . . . . .	53
6.2	Outlook . . . . .	54
	<b>Bibliography</b>	<b>64</b>
<b>A</b>	<b>Journal Publications</b>	<b>65</b>
A.1	Paper I . . . . .	65
A.2	Paper II . . . . .	93
A.3	Paper III . . . . .	123
A.4	Paper IV . . . . .	153
A.5	Paper V . . . . .	185



# List of Figures

1.1	Structure of this dissertation and connection between the investigations. Figures adapted from [102–106]. . . . .	10
2.1	(a) Experimental arrangement and (b) digital processing scheme for planar PIV. Adapted from schematics in [127, 128]. . . . .	20
3.1	(a) Schematic of the engine test bench. The red dashed box indicates the cross-sectional plane for (b) and (c). (b) Cross-sectional view of the engine. (c) Cross-sectional view of the flow bench in the valve plane. . . . .	24
3.2	(a) Valve lift curves and piston velocity for 800 rpm and 1500 rpm. (b), (c), and (d) Phase-averaged intake pressure $p_{in}$ , in-cylinder pressure $p_{cyl}$ , and exhaust pressure $p_{ex,1}$ , respectively. . . . .	26
3.3	(a) Schematic of the PIV and volumetric Mie scattering setup for the flow bench. (b) Top-view schematic of the camera arrangement for the flow bench and motored engine experiments in Papers I, II, and III. (c) Side-view schematic of the PIV and volumetric Mie scattering setup for the motored engine. (d) Top-view schematic of the camera arrangement for the fired engine experiments in Papers IV and V. . . . .	27
3.4	Example binarization images from the same fired cycle. (a) Extracted flame boundaries superimposed on the dewarped PIV camera image. (b) Extracted skeletal spark plasma location superimposed on the dewarped spark camera image. . . . .	28
4.1	Comparison of the intake velocity of the motored engine OC A (0.95 bar and 800 rpm) at $-270^\circ\text{CA}$ and the flow bench at 100 % MFR in the symmetry and valve planes. Adapted from [102]. . . . .	32
4.2	Comparison of the turbulent kinetic energy $k$ fields. The average flow direction is represented by the streamlines. Adapted from [102]. . . . .	33
4.3	Comparison of the streamline $S$ velocity. (a) The definition of the streamwise $s$ and normal $n$ components. (b) and (c) Profiles of the mean streamwise and normal components, respectively, along $S$ . (d) Fast Fourier transform spectrum of $n$ at the first position along $S$ . Adapted from [102]. . . . .	34
4.4	Mean velocity field of the coherent flapping for the 100 % MFR case. The streamline of the center of the jet is compared for two opposite flapping modes. Modes are obtained by calculating the mean velocity of every 8.31 <sup>st</sup> flow field. Adapted from [102]. . . . .	35
4.5	(a) Phase-averaged intake pressure sweep. (b) Phase-averaged intake velocity in the symmetry plane. Intake velocity is spatially averaged in a $3 \times 3 \text{ mm}^2$ region near the valves. (c) Left: Difference of phase-averaged pressure from the cyclic and phase mean. Right: Piston velocity. The intake valve timing is indicated by the gray shaded curve. Adapted from [103]. . . . .	36

4.6	Average velocity magnitude in the valve plane at selected crank-angles. At $-60^{\circ}\text{CA}$ , the magnitude is multiplied by 8 to use the same color bar. Adapted from [103]. . . . .	37
4.7	Comparison of spray morphology at $t = 640\ \mu\text{s}$ aSOI. (a) Average extracted spray contours. (b) and (c) Box plots of computed axial penetration length $L$ and the radial penetration length of the left side of the injector axis $L_{\text{rad, left}}$ , respectively.	38
4.8	Turbulent kinetic energy $k$ during injection. (a) Region of interest (ROI) for calculating the spatial mean of $k$ . (b) Spatially-averaged turbulent kinetic energy $\langle k \rangle$ from the ROI in (a). Adapted from [104]. . . . .	39
4.9	Comparison of the spray morphology of different OCs. (a) Average binarized spray boundary for near-atmospheric bulk gas density OCs at $698.7\ \mu\text{s}$ aSOI. (b) and (c) average penetration length $L$ and spray angle $\alpha$ , respectively, for all OCs. Standard deviations $\sigma$ and the 95 % confidence interval $\text{CI}_{95}$ at $640\ \mu\text{s}$ aSOI are indicated. Adapted from [104]. . . . .	40
5.1	(a) In-cylinder pressure over crank-angle. Average and standard deviation $p_{\text{cyl}}$ indicated by solid lines and shaded areas, respectively. (b) Violin plot of $p_{\text{max}}$ . Adapted from [106]. . . . .	44
5.2	Phase-averaged velocity field at each OC's ignition timing. Adapted from [106]. . . . .	44
5.3	(a) Voltage trace from a 0 % EGR cycle exemplifying restrike. (b) Plasma images corresponding to the voltage trace. Adapted from [105]. . . . .	45
5.4	Conditional statistics comparison between all non-RS and all RS cycles of the 12.9 % EGR case. (a) Velocity field comparison at ignition timing. (b) Spark plasma center PDF at $t = 400\ \mu\text{s}$ after ignition. (c) Extracted evolution of the flame PDF. Adapted from [105]. . . . .	46
5.5	(a) Flame PDF at $-18^{\circ}\text{CA}$ and (b) average centroid trajectory for the 0 % and 12.9 % EGR cases conditioned to the 10 % lowest and highest pressure combustion cycles. Adapted from [106]. . . . .	47
5.6	Average spatial correlation between $u$ (left) and $v$ (right) and 10 flame features for the 12.9 % EGR case. Adapted from [106]. . . . .	48
5.7	Flow-Flame CCV model. (a) Conditionally averaged velocity fields for the 50 lowest and highest centroidX cycles. (b) Conditioned flame PDFs box plots of $p_{\text{max}}$ , and flow representation of the model. Adapted from [106]. . . . .	49
5.8	Misfire CCV model. (a) conditionally averaged velocity fields of the 90 misfire and 90 highest $p_{\text{max}}$ cycles of the 14.3 % EGR case. (b) Correlation field between $u$ and $v$ and $p_{\text{max}}$ . (c) Conditioned flame PDFs and flow representation of the model. Adapted from [106]. . . . .	50

# List of Tables

3.1	Optically accessible engine parameters. . . . .	23
3.2	Average parameters for motored operation of the standard operating conditions. . . . .	25
4.1	Relevant engine and flow bench boundary conditions. Standard uncertainties are shown in parentheses. . . . .	31



# Nomenclature

## Lowercase Latin Letters

		Unit
$b$	Bore diameter	m
$d_p$	Particle diameter	m
$dt$	Time delay	s
$dx, dy$	Spatial displacement	pixel
$f$	Focal length	m
$f$	Frequency	Hz
$f_w$	Vortex shedding frequency	Hz
$h$	Clearance height	m
$k$	Turbulent kinetic energy	$\text{m}^2/\text{s}^2$
$l$	Characteristic length	m
$\dot{m}$	Mass flow rate	kg/s
$n$	Cycle number	-
$n$	Engine speed	rpm
$n$	Normal component of velocity	m/s
$p$	Pressure	bar
$r$	Distance between points	m
$s$	Streamwise component of velocity	m/s
$t$	Time	s
$u$	Fluctuating component of velocity	m/s
$u, v$	$x$ -, $y$ -component of velocity	m/s
$\mathbf{x}$	Location	m
$x, y, z$	Spatial coordinates	m/s

## Uppercase Latin Letters

		Unit
$D$	Pipe diameter	m
$L$	Integral length scale	m
$L$	Penetration length	m
$R$	Correlation	-
Re	Reynolds number	-
$S$	Streamline	-
St	Strouhal number	-

## Nomenclature

---

$T$	Integral time scale	s
$T$	Temperature	K
$U$	Velocity or velocity magnitude	m/s
$U_p$	Piston velocity	m/s
$V$	Voltage	V

### Lowercase Greek Letters

---

Unit

$\alpha$	Spray angle	ř
$\eta$	Kolmogorov length scale	m
$\theta$	Crank-angle	ř
$\lambda$	Fuel-air equivalence ratio	-
$\lambda$	Wavelength	m
$\sigma$	Standard deviation	-

### Uppercase Greek Letters

---

Unit

$\Phi$	Relative humidity	%
--------	-------------------	---

### Indices

---

cyl	Cylinder
ex	Exhaust
g	Gross
$i$	Integer index
in	Intake
left	Left side
max	Maximum
rad	Radial

### Operators and Mathematical Symbols

---

$\langle \rangle$	Time- or phase-average
$\Delta$	Difference in quantity

---

**Abbreviations**

---

2D2C	Two-dimensional two-component
2D3C	Two-dimensional three-component
3D	Three-dimensional
CI <sub>95</sub>	95 % confidence interval
aSOI	After start of injection
CCV	Cycle-to-cycle variation
CFD	Computational fluid dynamics
CL	Chemiluminescence
CMOS	Complementary metal-oxide semiconductor
COV	Coefficient of variation
DBI	Diffuse back-illumination
DISI	Direct-injection spark-ignition
ECN	Engine Combustion Network
EEI	Earth energy imbalance
EGR	Exhaust gas recirculation
EOI	End of injection
eSOI	Electronic start of injection
EU	European Union
EV	Electric vehicles
FFT	Fast Fourier transform
FM	Flowmeter
GH	Gas heater
GHG	Greenhouse gas
GMS	Gas mixture system
HC	High-pressure cycle
HS	High-speed
ICE	Internal combustion engine
IMEP	Indicated mean effective pressure
IW	Interrogation window
LC	Low-pressure cycle
LDV	Laser Doppler velocimetry
LES	Large-eddy simulation
LIF	Laser-induced fluorescence
MFC	Mass flow controller
MFR	Mass flow rate
NF	No-flow
OC	Operating condition
PDF	Probability density function
PFI	Port fuel injection
PHEV	Plug-in hybrid electric vehicle

## *Nomenclature*

---

PIV	Particle image velocimetry
PM	Particulate matter
PTV	Particle tracking velocimetry
PV	Pneumatic control valve
ROI	Region of interest
RS	Restrike
SCR	Selective catalytic reduction
SG	Spray-guided
SI	Spark-ignition
SP	Symmetry plane
TCI	Transistorized coil ignition
TWC	Three-way catalyst
VP	Valve plane
WG	Wall-guided
YAG	Yttrium aluminum garnet



# List of Publications

## Publications Included in this Dissertation

This thesis is based on the following publications:

- I. **C. Welch**, L. Illmann, M. Schmidt, B. Böhm: Experimental Characterization of the Turbulent Intake Jet in an Engine Flow Bench. *Experiments in Fluids* 64, 91 (2023). <https://doi.org/10.1007/s00348-023-03640-9>
- II. **C. Welch**, M. Schmidt, K. Keskinen, G. Giannakopoulos, K. Boulouchos, A. Dreizler, B. Böhm: The Effects of Intake Pressure on In-Cylinder Gas Velocities in an Optically Accessible Single-Cylinder Research Engine. *SAE Technical Paper 2020-01-0792* (2020). <https://doi.org/10.4271/2020-01-0792>
- III. **C. Welch**, M. Schmidt, C. Geschwindner, S. Wu, M. S. Wooldridge, B. Böhm: The Influence of In-cylinder Flows and Bulk Gas Density on Early Spray G Injection in an Optical Research Engine. *International Journal of Engine Research* 24, 1 (2023). <https://doi.org/10.1177/14680874211042320>
- IV. **C. Welch**, L. Illmann, M. Schmidt, A. Dreizler, B. Böhm: Experimental Evaluation of Spark Behavior under Diluted Conditions in an Optically Accessible Engine. *International Journal of Engine Research* (2023). <https://doi.org/10.1177/14680874231197492>
- V. **C. Welch**, M. Schmidt, L. Illmann, A. Dreizler, B. Böhm: The Influence of Flow on Cycle-to-Cycle Variations in a Spark-Ignition Engine: A Parametric Investigation of Increasing Exhaust Gas Recirculation Levels. *Flow, Turbulence and Combustion* 110: 185-208 (2023). <https://doi.org/10.1007/s10494-022-00347-5>

## Publications not Included in this Dissertation

Peer-reviewed publications not included in this thesis in chronological order of publication:

- VI. C. Geschwindner, P. Kranz, **C. Welch**, M. Schmidt, B. Böhm, S. A. Kaiser, J. D. L. Morena: Analysis of the Interaction of Spray G and In-Cylinder Flow in Two Optical Engines for Late Gasoline Direct Injection. *International Journal of Engine Research* 21, 1 (2020). <https://doi.org/10.1177/1468087419881535>
- VII. M. Haussmann, F. Ries, J. B. Jeppener-Haltenhoff, Y. Li, M. Schmidt, **C. Welch**, L. Illmann, B. Böhm H. Nirschl, M. J. Krause, A. Sadiki: Evaluation of a Near-Wall-Modeled Large Eddy Lattice Boltzmann Method for the Analysis of Complex Flows Relevant to IC Engines. *Computation* 8(2), 43 (2020). <https://doi.org/10.3390/computation8020043>
- VIII. A. Hanuschkin, S. Zündorf, M. Schmidt, **C. Welch**, J. Schorr, S. Peters, A. Dreizler, B. Böhm: Investigation of Cycle-to-Cycle Variations in a Spark-Ignition Engine Based on

- a Machine Learning Analysis of the Early Flame Kernel. *Proceedings of the Combustion Institute* 38, 4: 5751-5759 (2021). <https://doi.org/10.1016/j.proci.2020.05.030>
- IX. D. Dreher, M. Schmidt, **C. Welch**, S. Ourza, S. Zündorf, J. Maucher, S. Peters, A. Dreizler, B. Böhm, A. Hanuschkin: Deep Feature Learning of In-Cylinder Flow Fields to Analyze Cycle-to-Cycle Variations in an SI Engine. *International Journal of Engine Research* 22, 11 (2021). <https://doi.org/10.1177/1468087420974148>
- X. A. Pati, D. Paredi, **C. Welch**, M. Schmidt, C. Geschwindner, B. Böhm, T. Lucchini, G. D'Erizzo, C. Hasse: Numerical and Experimental Investigations of the Early Injection Process of Spray G in a Constant Volume Chamber and an Optically Accessible DISI Engine. *International Journal of Engine Research* 23, 12 (2022). <https://doi.org/10.1177/14680874211039422>
- XI. H. Chu, **C. Welch**, H. Elmestikawy, S. Cao, M. Davidovic, B. Böhm, A. Dreizler, H. Pitsch: A Combined Numerical and Experimental Investigation of Cycle-to-Cycle Variations in an Optically Accessible Spark-Ignition Engine. *Flow, Turbulence and Combustion* 110: 3-29 (2023). <https://doi.org/10.1007/s10494-022-00353-7>
- XII. M. Schmidt, **C. Welch**, L. Illmann, A. Dreizler, B. Böhm: High-Speed Measurements and Conditional Analysis of Boundary-Layer Flows at Engine Speeds up to 2500 rpm in a Motored IC Engine. *Proceedings of the Combustion Institute* (2022). <https://doi.org/10.1016/j.proci.2022.07.199>
- XIII. L. Engelmann, **C. Welch**, M. Schmidt, D. Meller, P. Wollny, B. Böhm, A. Dreizler, A. Kempf: A Temporal Fluid-Parcel Backwards-Tracing Method for Direct-Numerical and Large-Eddy Simulation Employing Lagrangian Particles. *Applied Energy* 342 (2023). <https://doi.org/10.1016/j.apenergy.2023.121094>

## Conference Papers

Full-length conference papers not included in this thesis in chronological order of presentation:

- XIV. H. Chu, M. Davidovic, H. Elmestikawy, **C. Welch**, B. Böhm, A. Dreizler, H. Pitsch: Investigation of residual gas effects on early flame kernel development under engine conditions. *10th European Combustion Meeting*, Naples, Italy (2021).
- XV. **C. Welch**, L. Illmann, M. Schmidt, B. Böhm: The Impact of Flow and Turbulence on Spray G Direct Injection. *Large-Eddy Simulation for Energy Conversion in Electric and Combustion Engines*, Paris, France (2021).
- XVI. **C. Welch**, M. Schmidt, C. Geschwindner, A. Dreizler, B. Böhm: Experimentelle Untersuchung der Spray-G-Direkteinspritzung in einem optisch zugänglichen Motor. *30. Deutscher Flammentag*, Hannover-Garbsen, Germany (2021).
- XVII. M. Schmidt, L. Illmann, **C. Welch**, A. Dreizler, B. Böhm: Messung der wandnahen Gastemperatur in einem Otto-motor mit 2-Farben-LIF und simultaner PIV. *30. Deutscher Flammentag*, Hannover-Garbsen, Germany (2021).
- XVIII. L. Engelmann, **C. Welch**, B. Böhm, A. Kempf: Numerical review on the suitability of models for the prediction of cyclical flow field variations in IC-engines. *18th International Conference on Numerical Combustion*, San Diego, USA (2022).

- 
- XIX. **C. Welch**, M. Khawar, B. Böhm, A. Gryczke, F. Ries: Experimental Assessment of Breakup Regimes of a PVP-VA Solution Using a Two-fluid Swirl Injector. *32nd European Conference on Liquid Atomization and Spray Systems*, Naples, Italy (2023).
- XX. L. Illmann, **C. Welch**, M. Schmidt, A. Dreizler, B. Böhm: Untersuchung der frühen Flammenausbreitung bei direkteingespritzten ottomotorischen Betriebspunkten zum Katalysatorheizen. *31. Deutscher Flammentag*, Berlin, Germany (2023).



# 1 Introduction

## 1.1 Motivation

One of the greatest challenges facing the modern world is anthropogenic climate change, a problem caused primarily by the unbalanced release of greenhouse gases (GHG) into the Earth's atmosphere by humans. As a result of the Earth's energy imbalance,<sup>1</sup> global temperatures have risen steadily over the past four decades and more severe weather patterns, such as droughts and floods, have occurred, which may have irreversible effects on land and ocean ecosystems [2]. The global transportation sector is the second largest contributor to total GHG emissions as CO<sub>2</sub> from fuel combustion, after the power generation and heating industry (22.7% and 38.2% for transportation and power industries, respectively, in 2020) [3]. Within the transportation sector, light-duty vehicles accounted for the largest share of CO<sub>2</sub> emissions in 2020, equaling 45.6% (10.1% of total global CO<sub>2</sub> emissions), while heavy-duty vehicles contributed to 24.6% (5.4% of the total) [3, 4].

Since the 2015 Paris Agreement, an international treaty on climate change whose primary goal is to limit the global average temperature increase to 1.5 °C above pre-industrial levels, countries have been submitting concrete plans to achieve this goal, called nationally determined contributions, on a five-year cycle of increasingly ambitious climate action [5]. To this end, increasingly stringent legislation, such as the European Union's (EU's) agreement to produce only zero-emission passenger vehicles from 2035 [6] or the new Euro 7 emission standards proposal [7], has become popular among developed countries. However, despite significant efforts to electrify new production vehicles, the growing global population and economic power of developing countries is expected to result in the total global passenger vehicle fleet growing by approximately 70% from 2020 to 2050, with only 31% of the future fleet being either electric vehicles (EVs) or plug-in hybrid electric vehicles (PHEVs) [8]. While consumer caution or skepticism remains a challenge to the widespread adoption of EVs in developed countries due to concerns about their high cost, lack of charging infrastructure, battery charge range, relatively short battery life, and battery safety issues [9], these challenges are especially prevalent in developing countries. Therefore, it is clear that the internal combustion engine (ICE) will remain a critical component in the diversification of future mobility technologies in the rapidly evolving energy transition.

In addition to GHG emissions, conventional ICEs in passenger cars also emit harmful pollutants such as NO<sub>x</sub>, CO, unburned hydrocarbons, and particulates into the atmosphere. The European Commission reported that in 2018, ground transportation was responsible for 39% of NO<sub>x</sub> emissions in the EU and 47% of NO<sub>x</sub> emissions in urban areas [7]. In addition, the effects of NO<sub>x</sub> exposure are estimated to have caused 49 000 premature deaths, while exposure to fine particulate matter resulted in another 238 000 premature deaths in 2020 in the EU alone, which has some of the strictest emission standards in the world [10]. Although diesel engines are more efficient than spark-ignition (SI) engines, they produce a significant amount of NO<sub>x</sub> and

---

<sup>1</sup>The Earth energy imbalance (EEI) is a number commonly used in quantifying global warming and climate change [1].

particulate matter (PM) due to the complex reactions of the diffusion flame consumption of the fuel-air mixture, and the incomplete combustion at high loads [11]. Despite the availability of particulate filters, which do not separate the smallest particles, and selective catalytic reduction (SCR) for diesel engines, it is widely accepted that SI engines are a cleaner ICE technology for passenger cars. However, the current state of SI ICE technology is far from being fully optimized in terms of efficiency, fuel consumption, and emissions. Therefore, a better understanding of the underlying physics of modern SI ICE processes is required for their continued optimization to meet increasingly ambitious global climate neutrality goals.

## 1.2 Current State of Research

Since the advent of mass-produced road vehicles in the twentieth century, hundreds of millions of people have relied on SI ICEs for daily transportation. As a result, engine technology research has received a great deal of attention over the past century, resulting in the development of highly efficient powertrain systems. The purpose of this section is to summarize the current state of research, focusing mainly on the fundamental studies of the last few decades that led to the investigations of this dissertation.

### 1.2.1 In-Cylinder Flows

As one of the most important aspects governing SI engine processes, in-cylinder flows are critical in determining combustion and overall engine performance. Therefore, proper characterization of in-cylinder flows through robust measurement techniques must first be achieved before other combustion processes can be understood and predicted.

There are several options for optical access to engines that allow measurement of in-cylinder velocities, and the selection is mainly driven by the desired outcome of the measurements [12]. However, the more realistic the engine, the less optical access is typically available [13]. Early applications of laser diagnostics in optically accessible engines to measure the in-cylinder velocity include measurements through a quartz glass window [14] or quartz glass cylinder head [15] using laser Doppler velocimetry (LDV), a non-invasive technique that acquires time-resolved velocity data at a single point in the cylinder. These investigations demonstrated the feasibility of crank-angle-resolved in-cylinder flow measurements and their large potential for studying engine flow phenomena. Over the last few decades, however, LDV has been largely replaced by particle image velocimetry (PIV) or related techniques due to recent rapid advances in laser and camera technology that allow higher repetition rates in higher spatial dimensions, such as two-dimensional two-component (2D2C), two-dimensional three-component (2D3C, stereo), or three-dimensional (3D, tomographic) PIV. In-cylinder PIV is typically achieved by mixing a fluidized or nebulized tracer, such as silicone oil droplets, in the intake air and calculating the statistical displacement of the tracer using a cross-correlation algorithm after imaging the Mie scattering of the illuminated tracers. The work of Reuss et al. [16] and Reeves et al. [17] are early adaptations of PIV in research engines that laid the foundation for full-field engine flow measurements and analysis.

The development of high-speed (HS) PIV measurement systems has allowed the transition from cycle-resolved to crank-angle-resolved or burst measurements within a cycle, enabling full-cycle and cycle-to-cycle variation (CCV) analysis of in-cylinder flows. Early research on HS PIV in single-cylinder engines was conducted by Towers and Towers [18], who achieved an acquisition rate of 13.5 kHz, and were capable of showing a significant influence of different intake geometries

on the CCV, and by Ghandhi et al. [19], who acquired full-cycle PIV at 1 kHz, and compared the velocity data on a statistical and single cycle basis of different spatial and temporal filtering schemes. However, the subsequent wide commercial availability of frequency-doubled HS Nd:YAG (or similar) lasers and complementary metal-oxide-semiconductor (CMOS) cameras pushed the limits of HS PIV even further. Such an extension of the capabilities of HS PIV was demonstrated by Peterson and Sick [20], who performed crank-angle-resolved simultaneous PIV and planar laser-induced fluorescence (LIF) experiments at 800 rpm (4.8 kHz) for 150 consecutive cycles, allowing spatial and temporal analysis and correlation of fuel concentration with the in-cylinder flow. Further advances in in-cylinder flow diagnostics were made by Baum et al. [21], who acquired a large database of HS 2D2C, low-speed stereo (2D3C), and low-speed tomographic (3D) PIV, which provided comparison of the data from each experiment and then analysis and valuable insight into engine flows at high temporal resolution and spatial dimensions. More recently, HS tomographic PIV has also been demonstrated in a single-cylinder research engine at 1500 rpm and 10 $\mu$ s temporal resolution by Braun et al. [22], who used the data to study the CCV of flow structures in 3D. In addition to tomographic PIV, HS scanning PIV has been used to obtain quasi-simultaneous two-plane [23] and quasi-3D (three-plane) [24] velocity fields, which proved to be useful in providing a more complete representation of the flow over single-plane PIV for studying CCV.

In addition to improving temporal resolution to study engine flows on a crank-angle and sub-crank-angle basis at higher and more technically relevant engine speeds, researchers are also interested in increasing spatial resolution. Achieving high spatial resolution is a challenge inherent to PIV due to the spatial averaging involved in the vector calculation. Despite overlapping and sliding interrogation window schemes, vector resolution is still limited by the final interrogation window size. Jainski et al. successfully used HS micro-PIV to resolve the boundary layer above the piston at various engine speeds and found difficulty resolving the viscous sublayer at 1100 rpm due to insufficient seeding density [25]. Although Jainski et al. attempted to use a hybrid PIV/PTV (particle tracking velocimetry) algorithm, seeding density proved to be an issue in the initial PIV processing and there was insufficient statistics to generate an average vector grid. However, improvements in high-resolution in-cylinder flow measurements were then made by Renaud et al. [26] who successfully demonstrated hybrid PIV/PTV for hundreds of cycles at different crank-angles in compression and showed that the piston boundary layer, the result of the fundamentally non-stationary engine, behaves differently from boundary layers in canonical flows such as those developing on a flat plate, a finding consistent with the aforementioned work by Jainski et al. [25]. Recent improvements in boundary layer measurements have been made by Schmidt et al. using HS PIV/PTV to resolve high statistics at higher technically relevant engine speeds up to 2500 rpm [27, 28].

Other types of optically accessible engines or engine-like experimental test cells have also been developed over the past decades to study in-cylinder flows. Endoscopic optical access, originally motivated as a cost-effective alternative to expensive traditional optically accessible single-cylinder research engines [29], can provide more realistic boundary conditions due to a smaller piston crevice and lower heat losses at the smaller quartz windows [30, 31]. However, it may also be more cost effective to use simplified engine-like configurations such as flow benches with engine manifold and cylinder head geometries to simulate intake flows while allowing easier control of variables. While flow benches have historically been used in the automotive industry to characterize flow behavior with various parameters such as geometric variations, more recent flow bench research has focused on using PIV or other advanced diagnostics to provide boundary conditions and validation data for the development of computational fluid dynamics (CFD) models. One

such experimental investigation by Freudenhammer et al. used magnetic resonance velocimetry (MRV) to measure the 3D velocity field of water flow bench adaptations of the Darmstadt engine geometry [32, 33]. The MRV flow bench data have since served as valuable validation data for simulations due to the full cylinder and intake manifold resolution of the 3D velocity components provided by the technique [34]; however, MRV can only provide ensemble-averaged data of the intake flow. Therefore, other recent experimental studies have employed PIV or PTV in air flow benches to provide instantaneous snapshots and ensemble-averaged 3D [35], 2D3C [36, 37], and 2D2C [38–44] flow fields. Most of these recent experimental investigations are accompanied by CFD studies, which provide more information in hard-to-measure locations, such as the intake port geometry, and higher spatial dimension data. However, to date, none of these investigations have acquired 2D2C HS data, which is required to study the turbulent intake jet using time-correlation methods. Using state-of-the-art equipment and processing techniques, HS PIV of an air flow bench can complement existing crank-angle or sub-crank-angle engine velocity data to better understand the relationship between the intake jet and subsequent in-cylinder flows.

### 1.2.2 Spray-Guided Direct Injection

Over the past few decades, direct-injection spark-ignition (DISI) engines have become a popular alternative to port fuel injection engines due to their ability to precisely control the amount of fuel injected. In particular, spray-guided (SG) DISI research has recently gained popularity for two modes: stratified (globally lean) and homogeneous (globally stoichiometric) combustion. Stratified charge DISI has been studied extensively because of its advantage of globally lean combustion and the challenges associated with CCV of the flow and local mixture formation. Therefore, stratified charge research in optically accessible engines has largely been performed using simultaneous multi-parameter diagnostics to study combustion CCV resulting from local fuel inhomogeneities. An early example of multi-parameter measurements by Peterson and Sick [20], previously cited with reference to HS PIV, used simultaneous HS PIV and LIF to investigate the relationship between the spray and flow and the correlation between the flow and fuel concentration. A subsequent study by Peterson and Sick demonstrated simultaneous HS PIV, LIF, and spark measurements to study the influence of flows on mixture formation and ignition performance [45]. They found that mixture formation near the spark plug at ignition timing is not the only influencing variable causing partial burn or misfire cycles. Further work by Peterson et al. [46] extended previous experiments to include simultaneous HS PIV, LIF, flame imaging, and spark measurements to investigate in detail the development of the ignition and flame propagation and the mechanisms behind slower combustion, namely lean mixtures, external dilution, and impeding velocities. High-speed PIV and Mie scatter imaging of a triple injection strategy operating condition of an SG engine by Stiehl et al. revealed strong interactions between the sprays and the flow, where flow structures due to the sprays have a significant effect on the next spray [47]. Stiehl et al. used correlation analysis of the flow fields of HS PIV with the spray morphology and showed significant correlations between the second spray and the flow before the first injection. Peterson et al. extended previous measurements by combining HS planar PIV with phase-locked tomographic PIV and studied spray-induced turbulence with the 3D flow data, demonstrating an increase in turbulent kinetic energy, shear, and vorticity magnitudes by  $\approx 400\%$  compared to flows without sprays [48]. Hill et al. extended the analysis of the combined HS PIV and tomographic PIV and focused specifically on the turbulence associated with a spray-induced jet [49]. More recently, Laichter and Kaiser evaluated the effects of fuel concentration and flow on combustion CCV by comparing port fuel injection cycles with a dual injection strategy, and found that the flow and flame become less correlated when DI is used



and the mixture formation is more important [50].

While stratified combustion offers global lean operation, homogeneous DI has recently gained popularity due to its use in full load and speed ranges, charge cooling, and compatibility with efficient three-way catalysts (TWCs) [11, 51], the latter of which is critical as manufacturers need different, more expensive aftertreatment systems when the combustion mixture is not stoichiometric. Due to the predominantly homogeneous fuel-air mixtures provided by early injection, most research over the past decades with optically accessible engines has focused on stratified combustion due to the variability of spray, flow, and mixture near the spark plug at ignition. However, even early injection sprays can have different effects on the combustion, largely depending on the geometry or operating conditions. Therefore, in an effort to facilitate international and inter-institutional collaboration on DISI, the Engine Combustion Network (ECN) has established a set of standard operating conditions for a single injector geometry for isoocatane fuel, the so-called *Spray G* injector and conditions [52]. Several experimental [53–57] and numerical [58, 59] studies have provided detailed characterization of the injector and operating conditions. However, few have studied the injector in the dynamic environment of an engine [50, 60–63], and outside of work related to the experiments from this thesis, only one publication presented early Spray G injection within an engine [60]. Gutierrez et al. studied Spary G morphology using HS diffuse back-illumination (DBI) and Mie scattering to compare the results of quiescent conditions in a constant volume chamber with sprays in the dynamic environment of an engine operating at different speeds and intake pressures [60]. While a strong dependence of spray shape on operating conditions was observed, in-cylinder velocity was not measured due to limitations of optical access to the engine. Thus, while detailed flow and spray morphology data are scarce for any injector in a running engine, they are particularly rare for the Spray G injector under early injection conditions.

### 1.2.3 Ignition and Flame Propagation

The ignition process plays a critical role in the combustion of SI engines. Therefore, the spark behavior in flow channel or engine experiments has been extensively studied to understand the conditions affecting the sparking process and the effects of the spark behavior on the subsequent combustion. Simplified engine-like pressure chamber and flow channel experiments offer the advantages of better optical access and precise control of boundary conditions. In an early study by Maly and Vogel, the spark ignition, the size, the expansion velocity and the radial temperature of the flame front of various lean methane-air mixtures were measured by means of interferometry in an optical chamber [64]. More recent publications have investigated ignition and flame propagation at varying or very high channel velocities [65–69], chamber pressures [65, 70], discharge currents [65, 68], or spark gap settings [71]. By varying spark gap velocities, researchers have shown that the velocity at ignition has an effect on plasma channel elongation and spark restrike (RS), which can affect the stability of the ignition process [45, 65, 66, 69, 72, 73].

Furthermore, the relationship between ignition, flame propagation, and cyclic performance in optically accessible engines has been studied over the past several decades. Early studies by Fansler et al. [72], Smith and Sick [74], Peterson and Sick [45], Drake et al. [75], and Dahms et al. [73] used HS imaging of the spark and flame [72, 73, 75], PIV to measure the local flow field [45, 73, 75], LIF to quantify the local mixture fraction near the spark plug [45, 74], and spark waveform measurements [45, 72–74] to investigate the complex relationship between the ignition processes and CCV. To varying degrees, these studies have shown that the spark and

flame development are related to the in-cylinder flow. A summary of significant experimental investigations and subsequently developed CFD ignition models is provided by a review paper by Fansler et al., which focuses on cycle-to-cycle variations of ignition in stratified charge engines [76]. More recently, however, the multi-plane HS PIV investigation by Bode et al. also examined spark luminosity and found that there are significant correlations between the spark position and flow behavior at ignition [24], a finding consistent with the aforementioned work by Drake et al. [75].

Based on the above research on spark and flame evolution, it is clear that there is a relationship between the velocity across the spark gap at ignition and early flame growth. To better understand the relationship between these phenomena, simultaneous multi-parameter measurements of flow and flame propagation are required. Therefore, over the past few decades, much effort has been devoted to the development of accurate, minimally invasive flame measurement techniques to allow for multi-parameter measurements to correlate the influencing variables that affect combustion in SI engines. With the wide availability of high dynamic range and HS cameras, the simplest method for flame visualization is chemiluminescence (CL) of the flame, which is recorded as higher intensity where high luminosity occurs due to reactions. Chemiluminescence not only offers the advantages of experimental simplicity, requiring only one camera and no external light source, but also images the full extent of the flame in the line of sight of the camera. Early studies used intensified cameras and bandpass filters to improve detection of luminosity at selected wavelengths such as for the luminosity of OH radicals [77–79], while more recent studies have employed CMOS cameras that are sensitive enough to detect CL at kilohertz speeds [30, 31, 50, 80–82]. On the other hand, some details, such as flame curvature, are lost in line-of-sight measurements, whereas combined planar flame imaging techniques in combination with other planar measurements, such as PIV, can be used to directly correlate the flame position and local velocity field. Therefore, planar techniques have been developed to measure the flame in ICEs. As a widely accepted method in the combustion community for measuring the flame front position [83–85], the excitation of diatomic molecules such as OH radicals via planar LIF has been extended to the application of SI engine diagnostics [86–89]. However, due to the need for tunable lasers, usually dye lasers, to excite the OH radicals in their narrow-band UV excitation range, a method for high-resolution in-cylinder flame imaging was developed by excitation of tracer SO<sub>2</sub> gas using the frequency-quadrupled wavelength of an Nd:YAG laser [90]. This SO<sub>2</sub> LIF technique was then extended to HS flame imaging for detailed simultaneous flame propagation and flow analysis near the piston surface [27, 91]. Finally, as an alternative to simultaneous CL imaging or planar LIF with PIV, the evaporation of tracer particles can be used to detect the burned gas region in planar Mie scattering images obtained for PIV [46, 92–96]. This method offers a reasonable compromise between measurement simplicity and resolution of flame features, since the resolution of fine details such as flame wrinkling depends on the density of tracer particles and the robustness of the flame detection algorithm, while the seeding density for optimal PIV would likely not be sufficient to resolve the flame front as well as using LIF-related techniques.

### 1.2.4 Cycle-to-Cycle Variations

Much of the ICE research discussed in the previous sections has been motivated by the study of combustion CCV. Therefore, this section will mainly focus on investigations that presented novel methods to quantify or study CCV in optically accessible engines. Typically, a cyclic quantity is chosen to determine engine CCV; therefore, it is beneficial to acquire data from many cycles. Advances in laser and imaging technology have allowed the acquisition of not only HS multi-

parameter data, but also data from many cycles for statistical processing techniques. One such technique to analyze CCV of flows, sprays, or combustion features is conditional averaging, where data are separated based on threshold values, and the different sets are studied using statistics. Recent examples of conditional averaging include work by Stiehl et al. [97], who showed a difference in the average flow field structure for cycles with high and low spray penetrations, Schmidt et al. [28], who found that the boundary layer velocity profile varies significantly based on different conditionally averaged flow structures, and Chu et al. [96], who analyzed large-eddy simulation (LES) data validated by measurements from this thesis and compared the flame and flow behavior for cycles conditioned to low and high maximum in-cylinder pressure  $p_{\max}$ . Analyzing conditioned cycles can provide a more valid representation of phenomena than single-cycle analysis since the results are backed by statistics, providing a higher degree of significance.

Likewise, correlation analysis can be performed to study the relationship between different variables and provide significance over multiple cycles. Specifically, correlation between a cyclic variable and the instantaneous velocity at each vector position, named a correlation field, can be used to visualize the spatial relationship between the variable and flow. Work by Stiehl et al. is an early example of utilizing correlation fields, and they showed high correlations between the velocity near the injector tip and the resulting spray penetration [97]. More recently, Laichter and Kaiser used correlation fields to visualize the flow structures significant in generating faster combustion, and they found that overall correlations between the flow field and combustion speed decrease when a DI strategy is employed [50].

Although correlations between a few variables, such as the  $p_{\max}$  and the velocity field, can be valuable when analyzing CCV, they are limited to linear and pairwise relationships. Therefore, machine learning (ML) has recently become a popular alternative or supplement to statistical approaches for analysis owing to its ability to find patterns or categorize seemingly uncorrelated data or predict the outcome given complex input parameters. Research by Kodavasal et al. [98] successfully used a decision tree-based ML method on LES data to train a model to predict  $p_{\max}$  based on pre-ignition flow fields and the flame shape. Di Mauro et al. used a model based on neural networks trained with 109 experimental inputs for 18 operating conditions, each with 625 cycles, to predict the indicated mean effective pressure (IMEP) and coefficient of variation (COV) of IMEP [99]. The work by Di Mauro et al. demonstrated a promising technique to automatically analyze large datasets; however, COV was largely over-predicted for cycles with low COVs and under-predicted for cycles with large COVs. Hanuschkin et al. employed different ML methods to dual-plane in-cylinder flow data from HS scanning PIV to predict cycles of high IMEP and found that flow features as early as 180 degrees before top dead center ( $-180^{\circ}\text{CA}$ ) can effectively be used to predict fast combustion [100]. Successive work by Hanuschkin et al. employed several ML methods to binarized planar flame data for one crank-angle per cycle for the Darmstadt engine to predict cycles of high  $p_{\max}$  [94]. Extending this work to include flow data, Dreher et al. used deep feature learning and baseline ML methods to predict  $p_{\max}$  [95]. Both works by Hanuschkin et al. and Dreher et al. found that the horizontal velocity near the spark plug is important in predicting  $p_{\max}$ , while Dreher et al. also showed prediction accuracy above chance level based on the velocity field as early as  $-290^{\circ}\text{CA}$  [94, 95]. While ML has proven to be a promising technique to analyze or predict CCV, the development of accurately trained ML models requires expert knowledge in the fields of engine data interpretation and ML as well as excessively large, and therefore, expensive datasets for the best results. Thus, a robust and cost-effective strategy for the selection of relevant variables for further analysis would be beneficial for the efficient investigation of engine CCV.

## 1.3 Aim and Structure of the Work

### 1.3.1 Aim

The interrelated processes of SI engines are strongly driven by in-cylinder velocities: from mixture formation to combustion initiation and evolution. To analyze the complex interactions of these processes and the causal chain of combustion development, experimental studies are essential to provide cost-effective, highly accurate, multi-scale data. Engine experiments range from laboratory-scale test cells to full-scale chassis dynamometers and are used by automotive engineers worldwide to study ICE processes and performance. This work focuses on laboratory-scale engine experiments to improve the understanding of the fundamental processes that link engine flows and combustion development.

Accordingly, the single-cylinder, optically accessible research engine test cell at the Technical University of Darmstadt was used in this work to gain new insights into the governing mechanisms behind CCV and other phenomena related to engine performance. Several aspects and considerations of experimental design are critical for laboratory-scale experimental investigations aimed at improving ICE design. Due to the multi-scale complexity of engine processes, a strategy to isolate variables and parametric variations in the measurements is required to better delineate the influences of phenomena on the process as a whole. For this purpose, the simultaneous use of HS diagnostic approaches from state-of-the-art equipment and novel processing techniques allows the analysis of multi-parameter data. Combining the in-depth study of increasingly complex configurations with multi-parameter data from the experiments in this thesis, as well as 3D simulations derived from the obtained well-controlled boundary conditions, such an investigation provides a holistic approach to the study of engine combustion. This thesis carefully considers these aspects with the overall goal of improving the understanding of engine flow and process dynamics. The following sections outline the considerations of this thesis in more detail to better describe the overall objectives and novelty of the work.

### Extension of Engine Diagnostics and Data Analysis

In order to investigate the complex relationship between engine parameters, the velocity field, and the resulting mixture formation or combustion development, simultaneous non- or minimally-invasive HS measurement techniques are required. In each experimental configuration of this thesis, HS PIV was used as the primary measurement technique to investigate the relationship between in-cylinder flows and combustion-related phenomena. In addition to the flow data, as a cost-effective alternative to simultaneous planar flame imaging, such as LIF of toxic SO<sub>2</sub> tracer gas, an approach was developed to extract the burned gas regions from the planar Mie scattering images acquired for PIV. By combining these methods with further simultaneous HS diagnostics on large data sets made possible by state-of-the-art equipment, conditional statistics, correlation analysis, and multivariate statistical approaches were developed to summarize the phenomenological influence of the flow on the engine combustion processes.

### Phenomenological Concentration

The principle focus of this thesis is to learn from phenomenological processes and apply the knowledge to different configurations of increasing complexity. Thus, the analysis relies on HS diagnostics and large statistics to provide scalar and vector quantities relevant to the description of the governing engine phenomena. Through controlled boundary conditions and detailed anal-

ysis of processed data, phenomenological models are generated by combining conventional and novel multivariate statistical approaches to characterize the effects of engine flows on combustion processes and evolution.

### Boundary Conditions for Model Development

The complexity of engine processes should be reduced by controlled parametric variations, where fundamental phenomena are studied in detail and tested in increasingly complex configurations or with different boundary conditions to increase the relevance of the parameters. Therefore, a methodological approach of controlled variation of boundary conditions was applied in this dissertation, starting from a simplified flow bench test configuration, to motored engine operation, and finally to direct injection tests and fired engine experiments, all using varying boundary conditions for further parametric investigation. In addition, a critical aspect of this thesis is the control and documentation of the boundary conditions so that experiments can be repeated, parameters changed, or simulations run and validated. Thus, the boundary conditions of the Darmstadt engine are well-controlled, measured, and experiments are documented, and all data are available to researchers performing CFD simulations. In this context, data are shared not only privately for institutional collaborations, but also within international workshops and communities such as the Darmstadt Engine Workshop [101] or the ECN [52] for the overall advancement of engine research.

#### 1.3.2 Structure

This cumulative dissertation presents a comprehensive, methodical approach to the study of the influence of in-cylinder flows on relevant combustion processes from direct injection sprays to spark plasma behavior and finally to flame propagation and growth, all of which are deterministic in the causal chain of SI engine performance. After an introduction to the theoretical background of the processes studied and methodology used in this work, the thesis consists of two main chapters, the first of which lays the foundation for the analysis in the latter. Chapter 4 first characterizes the turbulent intake flow of the spray-guided cylinder head of the optically accessible research engine, then applies this understanding to more complex motored engine parameters, and the characterization of the spray-flow interaction of a DISI configuration. The techniques and analyses performed in the papers in this chapter are then directly applied in Chapter 5 of the dissertation to study in depth the influence of in-cylinder flows on the combustion process of the engine under diluted conditions. An overview of the structure of this dissertation and the connection between the investigations is shown in Figure 1.1, and a more detailed overview is provided in the following paragraphs.

The first paper of interest for Chapter 4 proposes the extension of a previous methodology, namely the MRV water flow bench [33], for the study of the intake jet of the spray-guided cylinder head of the Darmstadt engine (**Paper I**) [102]. **Paper I** presents the development of an air flow bench for the application of HS PIV, which allows for the characterization and analysis of turbulent phenomena in the intake jet. The simplified engine configuration of the flow bench allows the reduction of the influencing variables inherent in engine flows, while maintaining the relevance to the actual intake jet of the motored engine through careful validation of the test case and operating conditions. Detailed analysis of intake turbulence, an approach not possible with the previous MRV flow bench because the velocity is averaged over time, is invaluable in gaining insight into intake flows and providing validation data for the development of advanced

simulation models. Furthermore, the flow bench study provides the framework for the delineating the influence of intake flows on engine phenomena.

The second work included in Chapter 4 concerns the characterization of the effects of intake pressure oscillations on the resulting in-cylinder flows at an engine speed of 1500 rpm and decreasing intake pressure in 6 steps from 0.95 bar to 0.4 bar (**Paper II**) [103]. **Paper II** bridges the complexity gap between the simplified ambient pressure flow bench configuration of **Paper I** [102] and the dynamic effects of pressure oscillations in the intake manifold on the intake velocity and the resulting bulk motion of the flow. A combined approach of experimental velocity measurements by HS PIV in the valve and symmetry planes and a 1D simulation model developed in the commercial software GT-POWER showed that the backflow from the cylinder to the intake pipe, which becomes more pronounced at lower intake pressures, induces high-frequency pressure oscillations in the intake manifold. The high-frequency pressure oscillations associated

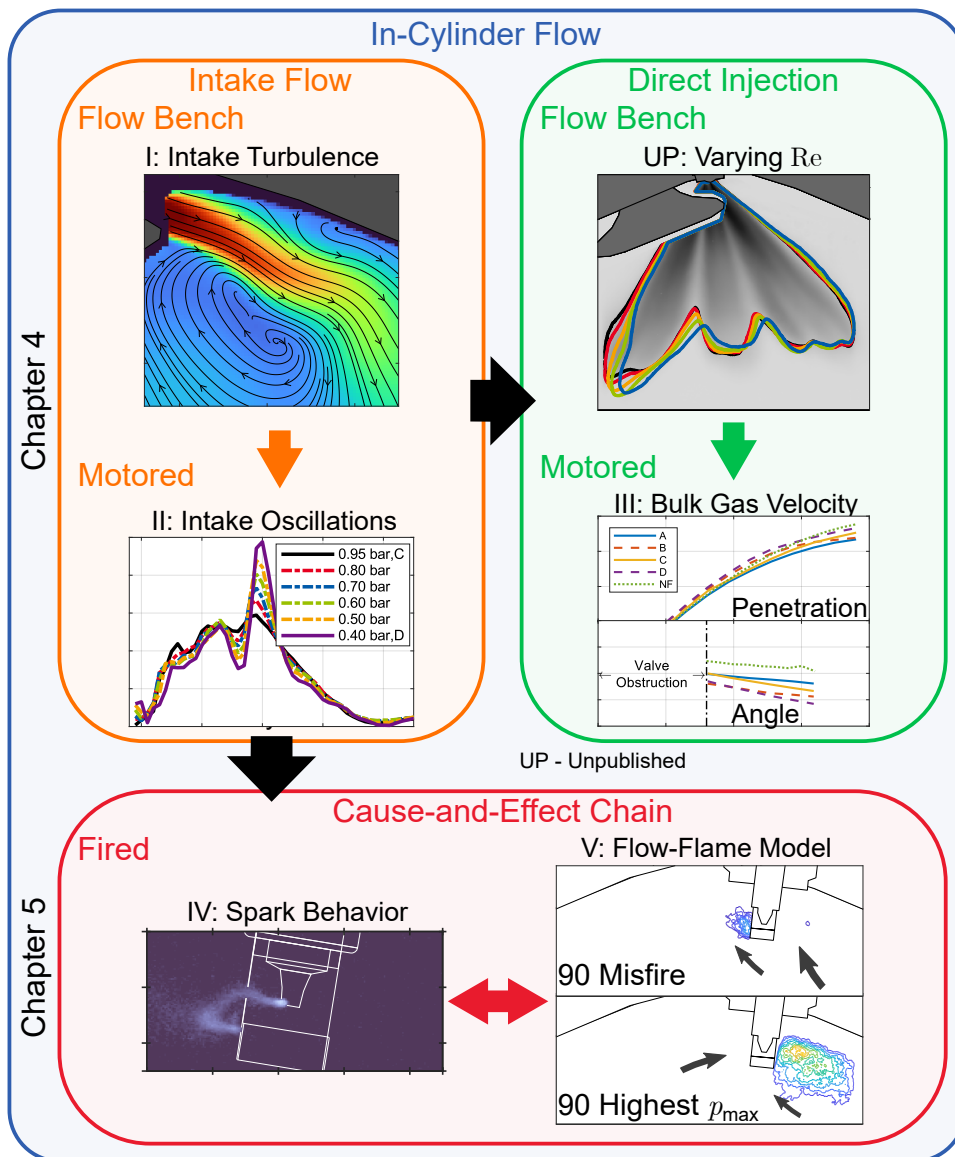


**Figure 1.1:** Structure of this dissertation and connection between the investigations. Figures adapted from [102–106].

with the part-load condition (0.4 bar intake pressure) have a consequential effect on the behavior of the intake flow, which is evident by rapid phase-locked flapping of the mean intake jet trajectory and by variations in the tumble trajectory. Thus, the backflow-induced oscillations have a critical impact on the average in-cylinder flow, a phenomenon that requires further study on a cyclic basis.

Following the first and second papers of Chapter 4, the next investigation examines spray morphology at different intake Reynolds numbers to more closely investigate the influence of flow on spray development. This unpublished study combines the flow bench experiment (**Paper I**) with the Spray G injector (**Paper III**) and provides insight into the statistical behavior of multi-hole sprays influenced by varying levels of turbulence.

The final study in Chapter 4, **Paper III**, investigates the effects of intake flow and bulk gas density on the early direct injection of the well-characterized *Spray G* injector [52] under four motored engine operating conditions ranging from 800 rpm to 1500 rpm with 0.4 bar and 0.95 bar intake pressures [104]. Using HS PIV of the bulk gas flow and Mie scatter imaging of the liquid sprays, the spray-flow interaction was studied in detail. A comparison of the four conditions with and without injection revealed that the average bulk velocity has the greatest influence on spray morphology, while the CCVs of the spray are less prevalent.

Chapter 5 contains two papers that aim to delineate the causes of CCV in fired engine operation under exhaust gas recirculation (EGR) conditions. Both papers use the same high engine speed (1500 rpm) and low intake pressure (0.4 bar) operating condition studied in Chapter 4 of this thesis; however, four different levels of homogeneously mixed intake gas with artificial EGR (by mixing air with controlled flow rates of  $N_2$  and  $CO_2$ ) were selected to parametrically study the effects of dilution on engine performance. Specifically, the interaction between the in-cylinder flow (characterized in Chapter 4) and the complex combustion physics on a small scale, namely ignition to early flame kernel growth, and on a larger scale, such as the cyclic maximum in-cylinder pressure. By using homogeneous mixtures of increasing EGR rates, the flame speed is reduced, while the importance of the effects of in-cylinder flows on subsequent phenomena and CCV is increased. In both works, simultaneous HS PIV and burned gas area extraction via evaporation of PIV tracer droplets visible by planar illumination were employed over hundreds of cycles to develop statistical techniques for identifying the cause-and-effect chain of CCV.

To this end, the operating conditions are first defined and characterized to provide context for the combustion speed and average in-cylinder velocity at the ignition time of each condition. Next, the main results of the first publication of Chapter 5 are presented. The first paper of Chapter 5 (**Paper IV**) [105] investigates the ignition behavior through spark circuit measurements of secondary voltage and current as well as simultaneous HS spark plasma imaging in combination with the flow and flame data presented in the second publication of this chapter, **Paper V** [106]. By first examining characteristic restrike cycles of the zero EGR and unstable EGR conditions and comparing them with non-restrike cycles, it is shown that the in-cylinder flow has a strong influence on the spark channel convection, voltage, and ultimately early flame growth. Using conditioned statistics of restrike and non-restrike cycles, as well as correlation fields with the in-cylinder flow, the horizontal velocity across the spark gap was identified as a critical quantity in determining more stable and faster combustion under diluted conditions.

The second publication of Chapter 5 (**Paper V**) [106] proposes several flame correlation techniques, most importantly a multivariate approach for the unstable EGR case that combines the correlations between a set of 10 flame features and the  $x$ - and  $y$ -components of the velocity over all cycles and all crank-angle phases at all vector positions along the flow field. The multivariate

correlation analysis is useful in revealing the most important flame features in their relation to the flow field, and it extends the basic correlation field technique used in recent research [23, 24, 31], while avoiding the constraining data size requirements associated with ML methods, such as those applied in the Darmstadt engine [94, 95]. The multivariate correlations of this paper, as well as the conditioned statistics of datasets with high and low values of the  $x$ -position of the flame centroid revealed that the initial flame growth direction is highly influential in determining combustion speed and stability.

Finally, Chapter 6 summarizes the results of the thesis and proposes future work.



## 2 Theoretical Background

This chapter provides the foundation and theoretical background on which the rest of this dissertation is based. First, the fundamentals of SI engine combustion and the interplay between the processes responsible are presented. Then, a concise introduction to the optical diagnostic techniques used in this thesis is provided.

### 2.1 Spark-Ignition Engine Combustion

The performance of modern ICEs is often defined by their consistency of operation over time. Consequently, abnormal combustion or CCV, such as misfire or, in extreme cases, knock, can adversely affect the performance and emission characteristics of ICEs. The cyclic variability of the combustion development in SI engines is mainly driven by the in-cylinder velocity, which influences the mixture formation, sparking, flame initiation and development, and the turbulent flame propagation [107]. Thus, the mechanisms behind SI engine flows and how they affect combustion-related phenomena are described in the following sections.

#### 2.1.1 In-Cylinder Flows

Spark-ignition engine in-cylinder flows are critical in forming an optimal fuel-air mixture; however, they also play an important role in the combustion process from the spark plasma and flame initiation to the turbulent flame propagation. Additionally, engine flows are a critical driving force for CCV and irregular combustion, or misfire, and they play an important role in post-combustion mixing, heat transfer, and mixing of crevice gases with the hot flow during the expansion stroke [108].

The general processes that characterize the in-cylinder flows of SI engines have interrelated steps that are driven by the cyclic motion of the four strokes. In simple terms, the process of a cycle begins with the intake flow and the formation of rotating bulk motion (tumble and swirl). Then, as the intake valves close, the compression stroke begins and the bulk structures are compressed until they ultimately break down into small-scale turbulence. After ignition near top dead center, the expansion or power stroke occurs, during which the hot gasses drive the piston downward. Finally, the burned gases are expelled during the exhaust stroke as the high-pressure gases equalize with the lower-pressure manifold upon opening of the exhaust valve and the upward motion of the piston facilitates in the expulsion of residual gases. Each of these processes is affected by factors such as engine geometry, operating and boundary conditions, and other phenomena such as spray-induced turbulence. Since ICE performance is largely influenced by the first three strokes of the engine, the complex processes and interactions from intake to combustion are discussed in further detail in the following sections.

### Intake Flows

The in-cylinder velocity of a four-stroke engine begins during the intake phase, when gas is directed into the cylinder as the intake valves open and the piston accelerates downward, creating a vacuum at the valve openings. This high-speed incoming gas is commonly referred to as the *intake jet*, and its impingement on the cylinder walls and piston is the basis for the formation of the tumble vortex. Since the intake jet directly influences the formation of the tumble vortex, slight variations in the jet velocity and direction can cause CCV in the kinetic energy stored in the tumble and the position of the tumble vortex, affecting the outcome of the cycle's combustion [108]. Although the intake jet forms very early in the cycle, variations in velocity at this stage of the cycle can affect the resulting combustion speed [95]. Therefore, understanding the intake flow is critical for design optimization in any ICE application.

Intake jets in ICEs are caused by the acceleration of the gas past the valves, which throttle the flow due to the valve stem, seat, and curtain geometries, and from the flow separation that results at the valve seat and lip [109, 110]. The high velocity flow, especially in the valve plane, is characterized by large velocity gradients or shear, and this shear is formed by an underflow valve separation, which occurs on the valve side facing the intake manifold, and an overflow valve separation (facing the spark plug), forming two jets, both of which interact with the cylinder wall and usually the piston. The shape and angle of the jets are determined by several factors that affect the large-scale tumble flow, notably the valve size, lip geometry (for example, the lip angle [109]), intake port geometry [97], valve seat geometry [111], and the valve and piston positions (or lift) [112] and speeds. However, geometry and engine speed are not the only considerations that shape intake jets and velocities. Sources of instability in the intake jet can also come from instabilities in the intake manifold velocity caused by pressure oscillations [103].

In general, ICE intake flows are studied using steady or unsteady flow bench configurations, optically accessible research engines, or CFD. Each type of experimental configuration has inherent advantages and disadvantages; however, they can be broadly characterized by having increasing cost or difficulty of measurement or accessibility with increasing level of complexity (that is, closer representation of real engine flows). Similarly, CFD studies can provide details that are impossible or too costly to obtain in experiments; however, accuracy depends on validation by reliable experimental data, model development, and computational resources. Thus, as with all ICE studies, the design of intake flow investigations is chiefly application-driven.

### Rotating Bulk Flows

Rotating bulk flows are critical to engine combustion processes because they store large amounts of kinetic energy to either assist in mixture formation or to release upon breakdown to facilitate the turbulent flame propagation. The resulting small-scale turbulent structures are required to promote stable combustion in non-ideal situations such as lean-burn or EGR dilution. There are two types of rotating bulk in-cylinder flows in ICEs: rotation about the cylinder-perpendicular axis, referred to as tumble flow, and rotation about the cylinder axis, referred to as swirl flow. In the context of SI engines, tumble flows are the primary bulk rotating flows used to induce faster combustion [11]. The intake jet is the primary facilitator of the high angular momentum tumble formation. In the compression phase, the tumble is characterized by a large bulk vortex with a more compact, defined center. Although aspects such as intake port and valve geometry are important in the formation of a strong intake jet and subsequent tumble, other considerations such as piston shape [113] or fuel injection [108] can also influence the generation of tumble flow.

## Turbulence and its Production

Generation of highly turbulent flows is required in SI ICEs to ensure proper air-fuel mixing and produce stable combustion. In a broad sense, the intake jet introduces the high momentum turbulent flow into the cylinder, and the large-scale rotating flows store and transport the turbulence for use in mixture preparation or turbulent combustion. While small-scale random velocity fluctuations, especially near the spark plug at ignition, are desired to achieve fast combustion, larger-scale, coherent velocity fluctuations can be considered flow CCV rather than turbulence and will be discussed in more detail in Chapter 5.

In ICE flows, the turbulent kinetic energy  $k$  is commonly used to quantify the extent of turbulent fluctuations in a flow field.  $k$  is defined as the average kinetic energy per unit mass in the fluctuating flow field and is expressed as follows [114]:

$$k = \frac{1}{2} \langle u_i u_i \rangle \quad (2.1)$$

where  $u_i$  denotes the  $i^{\text{th}}$  component of the fluctuating portion of the velocity.<sup>2</sup>  $u_i$ , as a function of the location  $\mathbf{x}$ , crank-angle  $\theta$ , and the cycle number  $n$ , can be obtained by subtracting the mean velocity  $\langle U_i \rangle$  from the instantaneous velocity  $U_i$  and can be expressed from the Reynolds decomposition equation as follows [108]:

$$u_i(\mathbf{x}, \theta, n) = U_i(\mathbf{x}, \theta, n) - \langle U_i \rangle(\mathbf{x}, \theta). \quad (2.2)$$

Since 3D experimental flow data are difficult to obtain in ICEs, it is common practice to include only the summation of two components as the planar  $k$ , for example, for planar PIV, and this quantity can be compared directly with 3D data, for example, from LES in the same plane.

Turbulence is characterized by random 3D vortices, or eddies, in a flow that vary in size. According to Richardson [115] and later Kolmogorov [116], kinetic energy is transferred from larger (most energetic) to smaller but comparable size scales by a cascading process until the smallest scales are reached and the energy is dissipated by viscous action [108, 114]. This process is referred to as the *energy cascade*, and the smallest scale at which viscous dissipation occurs is now called the Kolmogorov length scale  $\eta$ . Most of the turbulence in ICE flows is generated at the high-shear intake jet and its interaction with the walls. Therefore, the characteristic length scale  $l$  of the largest, most energetic eddies scales with the confinement of the cylinder geometry [108]. Thus, an order of magnitude estimate for  $l$  can be made by multiplying a constant parameter  $\alpha$  (Lumley suggests  $\alpha \approx 1/6$  as a reasonable value [117]), by the confinement length, for example, at bottom dead center,  $l \approx 1/6b$ , or during compression,  $l \approx 1/6h$ , where  $b$  and  $h$  are the bore diameter and clearance height, respectively. However, when the intake jet is considered at the valve plane, the high shear flow structure has a streamwise and jet-normal component, which can be used to obtain a more accurate estimate of  $l$  by calculating the integral length scale  $L$ .  $L$  is obtained by taking the integral of the normalized autocorrelation function of the velocity component as follows [118]:

$$L = \int_0^\infty \frac{\langle u_i(\mathbf{x}, t) u_i(\mathbf{x} + r, t) \rangle}{\langle u_i^2 \rangle} dr \quad (2.3)$$

where  $i$  is the component (streamwise or stream-normal),  $r$  is the distance between two points, and  $u_i$  is the instantaneous fluctuation of component  $i$ . In practice, given discrete experimental data, it is common to select the first zero crossing of the autocorrelation function as the integration limit to avoid including largely negative or oscillating correlation values. Since  $L$  is on

<sup>2</sup>The fluctuation of each component is summed

the order of millimeters or hundreds of microns in ICE flows, it is possible for conventional flow measurement techniques such as PIV to resolve the characteristic length scale, while the resolution of typical PIV setups in engines is insufficient to measure the smallest scales (especially  $\eta$ ) due to the very high Reynolds numbers.

Time scales are also a critical consideration in the study of engine flows. Similar to the estimating the characteristic length scale  $l$  by computing the integral length scale  $L$ , a characteristic time scale  $\tau$  can be estimated by the autocorrelation function of the velocity at a given position over time. Thus, the computation of the integral time scale  $T$  with experimental data, like  $L$ , requires a sufficiently high sampling resolution to obtain more accurate results. In practice, due to the unsteady nature of engine flows, or more precisely, the continuously changing geometry in the engine, it is not possible to achieve sufficiently high sampling rates for the calculation of  $T$  because the flow data must be statistically correlated and engine motion essentially prevents that from occurring. However, in a steady flow bench configuration, the intake flow can be simulated, and due to the steady valve position, a sampling rate on the order of kilohertz may be feasible for estimating  $T$ .

### 2.1.2 Mixture Formation

The mixture formation in SI ICEs refers to DI since it is assumed that the fuel mixes sufficiently well in port fuel injection before entering the cylinder. Fuel injection and mixing are critical to engine combustion and therefore overall performance. Depending on the configuration, DI offers many advantages: greater fuel efficiency, improved power output, and the use of a TWC (homogeneous), among others [11]. However, these benefits can be diminished by counterbalancing phenomena when injection conditions are not ideal. Therefore, careful consideration must be given to the proper implementation of DI systems in SI engines.

### Spray-Guided Direct Injection

In the last decade, research efforts have primarily concentrated on stratified (global lean) or homogeneous (global stoichiometric) combustion configurations, each offering unique advantages. In both configurations, SG designs have gained prominence as the preferred DI technology to mitigate wall wetting issues associated with the previously prevalent wall-guided (WG) systems. In SG designs, the spray itself aids in evaporation and mixing, typically employing multi-hole injectors to avoid spark plug wetting and fouling. This contrasts with WG systems, where fuel injection occurs towards a strong flow along the piston that is often bowl-shaped [119].

Spray-guided stratified combustion involves a precisely controlled high-pressure spray that rapidly evaporates and remains close to the spark plug during ignition timing, resulting in a locally ignitable mixture with globally lean combustion [119]. However, achieving such precise location and timing requirements for fuel vapor mixing makes SG stratified combustion susceptible to CCV, necessitating a robust fuel injection system. Furthermore, the late injection timing inherent in stratified combustion is often associated with piston wall wetting, leading to increased PM emissions. Additionally, globally lean mixtures, while advantageous in terms of fuel efficiency, can reduce the effectiveness of conventional TWCs in aftertreatment systems, which are optimized for  $\lambda = 1$  [11]. Therefore, the high cost of implementing stratified SG injection systems has become a concern for automotive engineers. In contrast, early injection homogeneous SG DI configurations have recently gained popularity. Despite offering reduced fuel economy compared to stratified combustion, early injection still benefits from charge cool-

ing due to fuel evaporation in the cylinder and can be employed over a wide range of engine loads, largely avoids piston wall wetting, and permits the efficient use of TWCs [11].

### 2.1.3 Sparking and Flame Development

Automotive engines typically employ transistorized coil ignition (TCI) systems to provide the energy required to generate a plasma and ignite the fuel-air mixture. Transistorized coil ignition systems store electrical energy in the inductance of a coil and release it over a period of  $\approx 2$  ms [11]. When the stored charge is released, a high voltage, on the order of kilovolts, and a high current, on the order of hundreds of amperes, are applied between the spark electrodes, resulting in the acceleration of electrons through the gap and the rapid dissociation and ionization of the gas molecules [64]. This release is referred to as the *breakdown* phase and occurs over a period of less than  $\approx 10$  ns [64]. During the breakdown, a plasma channel is formed along with a rapid rise in temperature to 60 000 K, where the supplied energy is transferred almost without loss [64]. The subsequent phase, which always follows the breakdown, is referred to as the *arc* phase, in which the plasma expands due to shock wave-induced heat conduction and mass diffusion [64]. The arc consists of voltages on the order of hundreds of volts, while the current can be as high as the impedance of the circuit allows; however, temperatures cannot exceed a few thousand Kelvin due to the constant energy losses [64]. Since the arc requires a hot cathode (ground electrode) spot, there is considerable erosion due to metal evaporation [64], which means that excessive energies can lead to faster deterioration of the spark plug. The arc is a critical stage for initiating a flame kernel because of the exothermic reactions leading to inflammation [11]. The arc typically occurs over a period of a few hundred microseconds [64]. The arc may be followed by a *glow discharge* in which the remaining stored energy is released into the discharge circuit [11, 64]. Glow is characterized by lower currents, higher voltage (hundreds of volts) due to the energy dumping, and lower ionization, dissociation, and gas temperatures than arc [64]. However, in typical TCI systems, glow occurs over the longest period of time, on the order of a few milliseconds, and supplies by far the most energy, while the energy transfer efficiency is the lowest [11, 64].

Depending on the conditions, a stoichiometric air-isooctane mixture may only require  $\approx 0.2$  mJ of energy to initiate a flame [120]. However, energies up to an order of magnitude greater may be required under dynamic conditions with leaner, richer, or diluted mixtures moving past the spark electrodes [11]. In addition, several other variables associated with engine operation such as fuel type, pressure, temperature, spark gap, mixture velocity, local fuel or EGR distribution, and fuel droplet diameter all affect the minimum ignition energy [120]. Although reactions occur a few nanoseconds after breakdown, the temperatures of the inner plasma are too high for combustion reactions to occur, so they begin at the outer plasma surface, where temperatures are only a few thousand Kelvin [11, 64]. Even though breakdown is by far the shortest phase, its characteristics have the largest impact on inflammation: increasing the breakdown energy affects the activated volume, the temperature difference across the spark kernel boundary, and the velocity of the boundary [11]. Nevertheless, for lean or diluted mixtures, the inflammation process, thickness, and flame propagation rate are significantly affected [11, 64]. Therefore, in order to ignite and sustain a flame at the lean or EGR limits, the ignition process and early flame growth must be augmented by increasing the supplied energy [64] or by increasing the flow velocity to enhance flame convection [68, 121]. Because of the limits of the spark energy deposition due to spark plug deterioration as mentioned previously, in-cylinder flows are a good candidate for counteracting slower flame speeds. As a result of increased flows across the spark gap, plasma channel stretching and elongation occurs in the direction of the flow, and re-ignition

or RS can occur at velocities exceeding  $\approx 15$  m/s, distributing energy into different channels [11]. Thus, increasing the spark gap velocities to the point where RS occurs can extend the lean or EGR limit [11, 73, 75]; however, due to the distribution of the energy over a larger volume, excessive velocities can slow combustion or blow-off can occur [69].

### 2.1.4 Sources of Cyclic Variability

Cycle-to-cycle variations in engine combustion cause losses in power and thermodynamic efficiency, as well as variations in the amount of work done [107]. Because CCV is more prevalent in lean and diluted conditions where the flame speed is slower, it limits the operating range of SI engines. Therefore, it has been the goal of automotive engineers for decades to understand the causes of CCV in order to optimize engine design and develop control strategies [76, 107, 122–125]. Ozdor et al. presented a comprehensive review of papers that have investigated the factors that influence CCV [107]; a brief summary of the most critical factors is provided in the following paragraph.

There are four main sources of CCV: (1) mixture composition, (2) cyclic cylinder charging, (3) spark and spark plug, and (4) in-cylinder mixture motion. (1): Mixture composition-related factors include the fuel type, total equivalence ratio, and amount of EGR, all of which affect the laminar flame speed and can seemingly be predetermined by the operating conditions. However, spatial inhomogeneities of the mixture equivalence ratio due to direct injection and EGR due to unavoidable residual gases are the major challenges in controlling mixture-related CCV. A robust injector design and injection strategy must be selected to promote efficient spray atomization and rapid mixing near the spark plug. However, when using a stratified injection strategy, homogeneity is not the goal, but rather consistency of mixture formation. Residual exhaust inhomogeneities can largely only be mitigated by generating higher turbulence to ensure complete mixing before the next ignition, while internal EGR can be controlled by adjusting the valve timing. In either case, in-cylinder flows have a large influence on the CCV of the spatial distribution of mixture inhomogeneities. (2): Cyclic cylinder charge-related factors of CCV include variations of mass trapped in the cylinder and affect pressure-related parameters, not combustion-related ones. These occur, for example, when cycles have the same crank-angle at which  $p_{\max}$  occurs but different  $p_{\max}$ . It is suggested that this is caused either by a combination of a slow initial flame speed followed by fast flame propagation and vice versa [126], or by variability in charging efficiency. (3): Spark and spark plug-related aspects include ignition system factors, which involves spark timing and discharge characteristics, as well as spark plug design influences, which include spark gap and electrode shape. With respect to ignition system influences, spark timing is typically predetermined by the operating conditions to have an optimized combustion phase at, for example,  $8^\circ\text{CA}$ . However, in the presence of lean or diluted mixtures, the optimum spark timing must be shifted earlier due to slower flame speeds. In addition, CCV of local mixture inhomogeneities adds to the complexity of spark timing optimization due to local variations of the flame speed. Spark discharge characteristics described in detail in the previous section; nevertheless, potential sources of combustion CCV must be addressed. The main characteristics that affect spark CCV are spark duration, spark energy, and energy release, all of which can influence each other. In-cylinder flows can affect these factors due to elongation and RS, as well as the transport of mixture inhomogeneities. For example, greater plasma elongation and more RS events shorten the spark duration and promote rapid energy deposition. Furthermore, spark plug design is another predetermined factor for engine operation and includes influences such as spark gap and electrode shape, which affect the total amount of energy deposited, as well as the volume and location where it is deposited. Thus, depending on these two factors, the

velocity through the gap may have a greater or lesser effect on the discharge characteristics. (4): In-cylinder mixture motion has the greatest influence on CCV in engine performance because of its relationship to the three factors previously explained. The turbulent nature of engine flows inevitably causes random velocity fluctuations in both small-scale and large-scale motion, both of which affect combustion; however, other factors such as the mean flow near the spark gap, spark plug orientation, and overall in-cylinder flow pattern also significantly affect CCV [107].

## 2.2 Optical Diagnostics

The theory behind the optical diagnostics used in this thesis is briefly introduced in this section. In addition, as the main measurement technique employed in this thesis, further information on PIV optimization and sources of error is provided.

### 2.2.1 Mie Scattering and Particle Image Velocimetry

The descriptions of Mie scattering and PIV in the context of the measurements of this dissertation are given briefly in this section. A comprehensive overview of the theory and practical guidelines for performing PIV can be found in the books by Tropea et al. [129], Adrian and Westerweel [130], and Raffel et al. [127]. Mie scattering refers to light scattered by particles whose diameter  $d_p$  is greater than the wavelength  $\lambda$  of the incident light ( $d_p/\lambda > 1$ ) [127, 129, 130]. Particle scattering is a function of particle size, shape, orientation, the ratio of the particle refractive index to the surrounding medium, polarization, and the angle of observation with respect to the incident light [127, 129, 130]. Particle image velocimetry is a widely used measurement technique in which particle-laden flows are illuminated with a light source and the displacement of particles over time is recorded. Velocity vectors are then calculated based on the statistical distribution of particle displacements within discretized regions called interrogation windows (IWs). Therefore, a fundamental requirement for PIV is Mie scattering, which enables the imaging of particle-laden flows and their displacement. To record particle shifts, small particles are introduced into the flow and two short pulses of light, typically from two laser cavities and formed into sheets, illuminate them with a time delay  $dt$  between them. Since engine flows exhibit constantly changing velocity scales,  $dt$  must be adjusted at different crank-angles and engine speeds to optimize particle displacement (see below for more details on PIV optimization). In the context of ICE flows, 2D2C PIV typically involves the acquisition of particle displacement images using two distinct frames. After applying perspective correction and spatial calibration, vector calculations are performed by cross-correlating the IWs in both frames. The ensemble of correlation peaks corresponds to the ensemble particle displacement ( $dx, dy$ ), providing a velocity vector for each IW and a vector field over the fixed grid of IWs [127–130]. Figure 2.1 depicts a schematic of planar 2D2C PIV in a generic channel flow, along with a corresponding representation of the processing scheme used to generate vector fields.

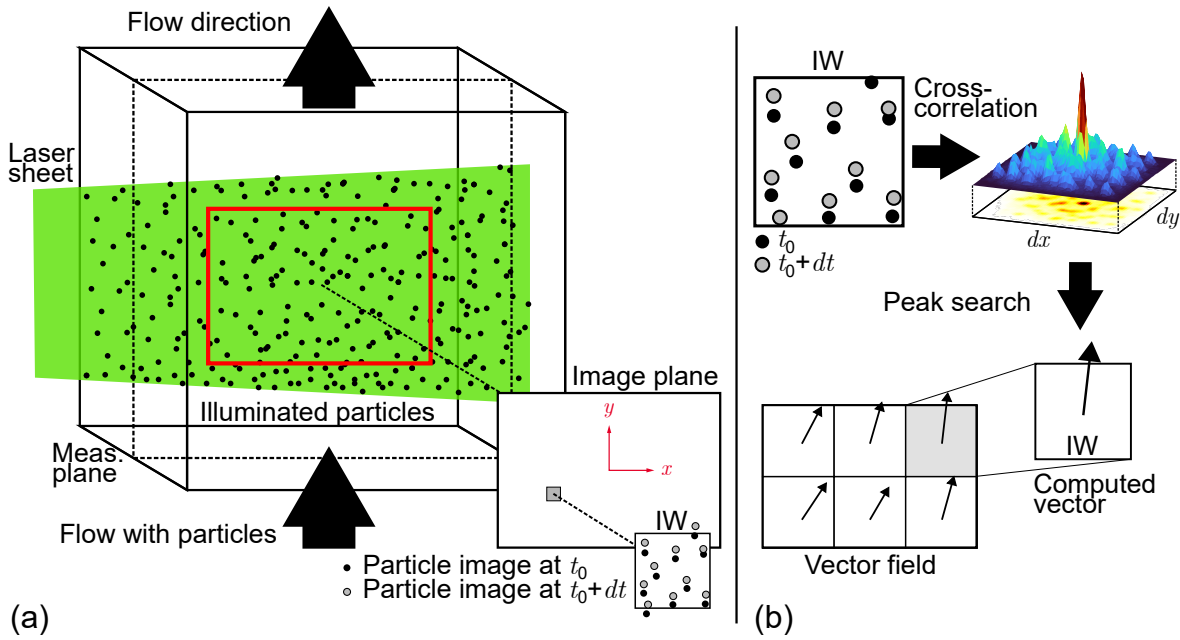


**Figure 2.1:** (a) Experimental arrangement and (b) digital processing scheme for planar PIV. Adapted from schematics in [127, 128].

## PIV Optimization and Sources of Uncertainty

**Optimization** Successful PIV is achieved by optimizing several parameters of the experimental setup, illumination and acquisition scheme, and data processing. The first consideration when setting up a PIV experiment is the selection of appropriate light sources and light sheet formation. For HS PIV, dual-cavity lasers are typically used to form light sheets; therefore, the characteristics of the two light sheets must be similar. In particular, a critical aspect when dealing with two laser sheets is beam overlap, as particle shifts from non-overlapping beams introduce avoidable systematic errors. The next consideration is particle selection, which includes size, density (number within a volume), and material. Engine experiments typically use nebulized silicone oil rather than solid particles, which cause rapid window fowling. Another advantage of silicone oil is its low vapor pressure, which largely resists evaporation at higher pressures. However, the upper limit of evaporation resistance balances the particle number density during compression, resulting in acceptable seed densities throughout a cycle and over a full range of engine operating conditions.

Another important consideration in optimizing PIV is the time separation  $dt$  between laser pulses. In the context of this work, which typically deals with transient engine flows,  $dt$  was optimized for each operating condition and at each crank-angle of a measurement to yield an average particle displacement between 4 and 5 pixels, depending on the IW size. Although a generally accepted rule of thumb is to keep particle displacements within a quarter of the IW size [127], the particle displacement optimization in this work is slightly more conservative to reduce measurement uncertainty due to flow acceleration or curved streamlines [131]. Another critical aspect of PIV optimization is the spatial resolution, which consists of the size of an IW before overlap. Interrogation windows should be small enough to resolve relevant engine fluid structures, yet large enough to contain approximately 10 particles [129]. Spatial resolution is a function of particle density (number of particles in a sheet), particle size, fluid velocity, camera pixel spacing, magnification, and desired particle displacement [131]. Magnification is



also limited by peak locking, which occurs when calculated pixel displacements preferentially lock onto full pixel values [127]. To avoid peak locking, particle image sizes should be at least 2 pixels [127]. Many of these properties interact, for example, varying magnification changes the particle density and pixel displacement; thus, there is a theoretical limit to the resolutions that can be achieved with PIV, and particle tracking methods such as PTV should be used instead.

Finally, the vector calculation algorithm and settings can affect the results of PIV data. Modern software such as DaVis version 10.2 (LaVision GmbH) employs state-of-the-art processing algorithms. Nevertheless, settings such as scheme (for example, cross-correlation), image pre-processing, masking, IW size, number of calculation iterations (passes), decreasing IW size, multi-pass overlap, and IW weight can affect the uncertainty. Apart from the importance of IW size, the multi-pass scheme and IW weight are of utmost importance. A good rule of thumb is to always use a multi-pass scheme with decreasing window size to increase the spatial resolution and produce fewer erroneous vectors [127]. In addition, strict vector post-processing should be performed to remove erroneous vectors and yield the most accurate results.

**Sources of Uncertainty** All calculated vectors are subject to random and systematic errors [131]; therefore, it is important to quantify an accurate representation of the measurement uncertainties. In addition to the sources of uncertainty already mentioned, such as excessive particle displacement, other sources can arise from the optical setup, including perspective errors, for example, due to the curved cylinder glass of the engine, and particle out-of-plane motion, due to the thickness of the laser sheet and the nature of the flow itself. Out-of-plane motion includes particle dropout as well as vectors calculated due to camera perspective and the non-zero laser sheet thickness. However, for engine flows, such as those in the center of the tumble and valve planes, the flows are likely to be symmetric about the laser plane and, on average, erroneous vectors due to out-of-plane particles are canceled out. Sources of flow-induced error also include sharp velocity gradients within IWs, which can cause particle slip, where particles no longer follow the flow; density gradients, such as when particles are forced to cluster; or bias due to positional disparity of particles within an IW [131].

Overall, by following the optimization rules outlined above, systematic error can be largely avoided. However, quantification of PIV uncertainty can be performed using a number of methods, such as those outlined by Sciacchitano [132]. For example, if all known sources of error are quantified, a task that requires all known parameters and their sensitivities, their effect on the overall uncertainty can be determined [131]. On the other hand, a method developed by Wieneke can be used to calculate the uncertainty based only on the correlation functions, which show asymmetric peaks due to the uncertainty-causing parameters [133]. While correlations from ideal noise-free particle images result in symmetric peaks when corresponding particle images are perfectly matched onto each other, correlation peaks from real measurement data appear asymmetric due to the positional disparity of mismatched particle images. Using the statistics of each pixel's contribution to the correlation peak shape, Wieneke's method derives the uncertainties of each displacement vector [133]. This method provides an alternative approach to the complex multi-parameter studies or Monte Carlo simulations that may be required to determine PIV uncertainty [127], and has been validated by benchmark experiments [134].



# 3 Experimental Methodology

## 3.1 Darmstadt Engine Test Bench

The single-cylinder, optically accessible research engine at the Technical University of Darmstadt (*Darmstadt Engine*) was designed to provide precisely controlled boundary conditions for the investigation of engine phenomena and for validation data. The engine, designed by AVL List GmbH, is controlled by an electric motor to allow operation in a *motored* or *fired* state while maintaining the same average engine speeds. Figure 3.1(a) shows a schematic of the complete engine test bench, and a brief explanation of the relevant components is given below. A gas mixing system (GMS) equipped with a plenum to mix the controlled gases from air, N<sub>2</sub>, and CO<sub>2</sub> mass flow controllers supplies the intake gases. A pneumatic control valve (PV) regulates the amount of gas supplied to the engine to maintain set intake pressures, then the gases are supplied to a storage plenum at the set pressure. Next, the intake gases pass through a rotary piston flowmeter (FM1) to measure mass flow rates before passing through a gas heater (GH), which was not used in the experiments of this thesis. Finally, the gases pass through a noise-reduction plenum into the intake manifold, which contains inlets for tracers and port fuel injection. The exhaust gases exit the engine into the exhaust manifold and pass through another noise reduction plenum and a rotary piston flowmeter before exiting the test stand through an exhaust ventilation system. Various pressure and temperature sensors, as well as a lambda sensor, are located throughout the test stand to provide indicating data for boundary conditions.

In this dissertation, a four-valve spray-guided cylinder head configuration with a pent roof was used, resulting in a compression ratio of 8.7 : 1. Optical access is provided through a fused silica glass flat piston window (75 mm diameter) using a Bowditch piston extension and piston mirror. In addition, a fused silica cylinder liner is used to provide access to the top 55 mm of the cylinder and an additional 8 mm in the pent roof. For fired operation, port fuel injection (PFI) can be introduced well upstream of the engine in the intake manifold, where the liquid or gaseous fuel can be sufficiently mixed before entering the cylinder. On the other hand, direct injection is

**Table 3.1:** Optically accessible engine parameters.

General parameters		Geometry	
Coolant temperature [K]	333	Bore / Stroke [mm]	86 / 86
Relative humidity $\Phi$ [%]	1.8 at 4̄C	Compression ratio [–]	8.7 : 1
Intake valve open / close [°CA]	325 / –125	Displacement vol. [cm <sup>3</sup> ]	499
Exhaust valve open / close [°CA]	105 / –345	Valve diameter [mm]	29
Maximum valve lift [mm]	9.5	Pipe Diameter $D$ [mm]	56.3
Optical access			
Piston / Cylinder / Pent-roof [mm]	75 / 55 / 8		

achieved using a spray-guided injector, the so-called *Spray G* injector from the ECN [52], which is centrally mounted at an angle of  $8^\circ$  with respect to the  $y$ -axis. Although the *Spray G* injector is used in this thesis to study the interaction between flow and sprays, only PFI with iso-octane fuel was used for the fired experiments. Table 3.1 shows the relevant parameters for the engine and test bench. Furthermore, Figure 3.1(b) shows a cross-sectional view of the engine in both the  $x - y$  and  $z - y$  planes with important geometric features highlighted.

In addition to conventional engine operation, an experimental flow bench setup was designed and implemented in this thesis for the detailed study of engine intake flows. By removing the piston and replacing the piston liner housing with a newly designed piston mirror housing with

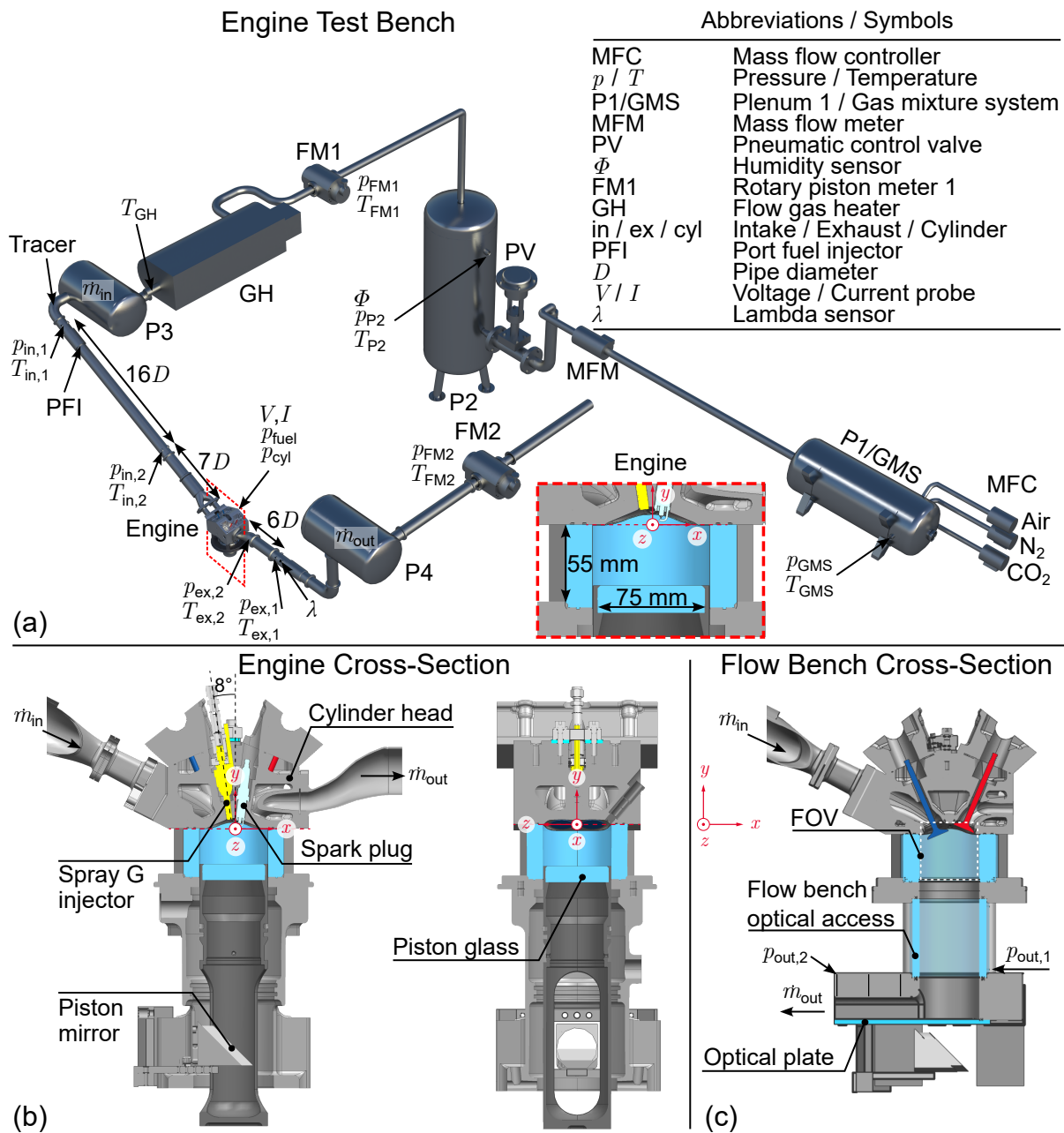


**Figure 3.1:** (a) Schematic of the engine test bench. The red dashed box indicates the cross-sectional plane for (b) and (c). (b) Cross-sectional view of the engine. (c) Cross-sectional view of the flow bench in the valve plane.

optical bottom plate and outlet channel, the intake flows are simulated in a simplified setup. For the flow bench experiments, FM1 (see Figure 3.1(a)) was removed and the air mass flow rates (MFRs) were controlled with the newly calibrated air mass flow controller (MFC) (Bronkhorst High-Tech B.V.) in the GMS. In addition, except for the moving valves case, the flow bench was operated without engine cooling and a valve bridge was used to hold the intake valves at a constant lift of 9.21 mm (equivalent to the valve lift at  $-270^\circ\text{CA}$ ). The Spray G injector was used for comparison with the motored engine and a flat spark plug dummy was inserted into the cylinder to simplify the geometry for simulations. Figure 3.1(c) shows a cross-sectional view of the spray-guided cylinder head and the flow bench piston mirror housing in the valve plane. Additional pressure sensors (indicated in Figure 3.1(c)) were used to provide more boundary conditions within the flow bench channel for validation. Finally, unsteady Reynolds-averaged Navier-Stokes simulations performed by Andrea Pati (Technical University of Darmstadt - Simulation of reactive Thermo-Fluid Systems) in combination with experimental flow measurements downstream of the outlet channel were used to ensure that no backflow occurs in the flow bench channel.

## 3.2 Operating Conditions

Four standard operating conditions (OCs), *A* through *D*, that cover a range of engine speeds and loads were used in this thesis. Table 3.2 shows the OCs and the average measured parameters from selected validation experiments under motored operation. In addition, Figure 3.2 shows the phase-averaged engine parameters from the same validation cycles. The valve motion (shown in Figure 3.2(a)) induces regular pressure oscillations that dissipate in amplitude with distance from the engine in both the intake and exhaust manifolds (see Figure 3.2(b) and (d)). Likewise, the valve timing overlap induces additional high-frequency pressure oscillations. An effect of the valve timing overlap can be observed in the in-cylinder pressure  $\langle p_{\text{cyl}} \rangle$  trace of OCs B and D (Figure 3.2(c)) by the transition from the ambient 1 bar exhaust pressure to the low, 0.4 bar intake pressure when the valves have equal lifts ( $-360^\circ\text{CA}/360^\circ\text{CA}$ ). The effects of this are discussed in detail in the chapters to follow and **Paper II**.

**Table 3.2:** Average parameters for motored operation of the standard operating conditions.

Parameter	A	B	C	D
Intake pressure $p_{\text{in},2}$ [bar]	0.95	0.40	0.95	0.40
Engine speed $n$ [rpm]	800	800	1500	1500
Piston speed $U_p$ [m/s]	2.93	2.93	4.30	4.30
Mass flow rate $\dot{m}_{\text{in}}$ [kg/h]	11.36	3.58	22.02	7.60
Intake temperature $T_{\text{in},2}$ [K]	307.7	315.3	307.5	310.6
Exhaust temperature $T_{\text{ex},2}$ [K]	311.1	364.5	313.8	375.3
Maximum in-cylinder pressure $p_{\text{max}}$ [bar]	13.27	5.37	14.61	6.14
Crank-angle at $p_{\text{max}}$ [ $^\circ\text{CA}$ ]	-2.03	-2.65	-1.83	-2.43

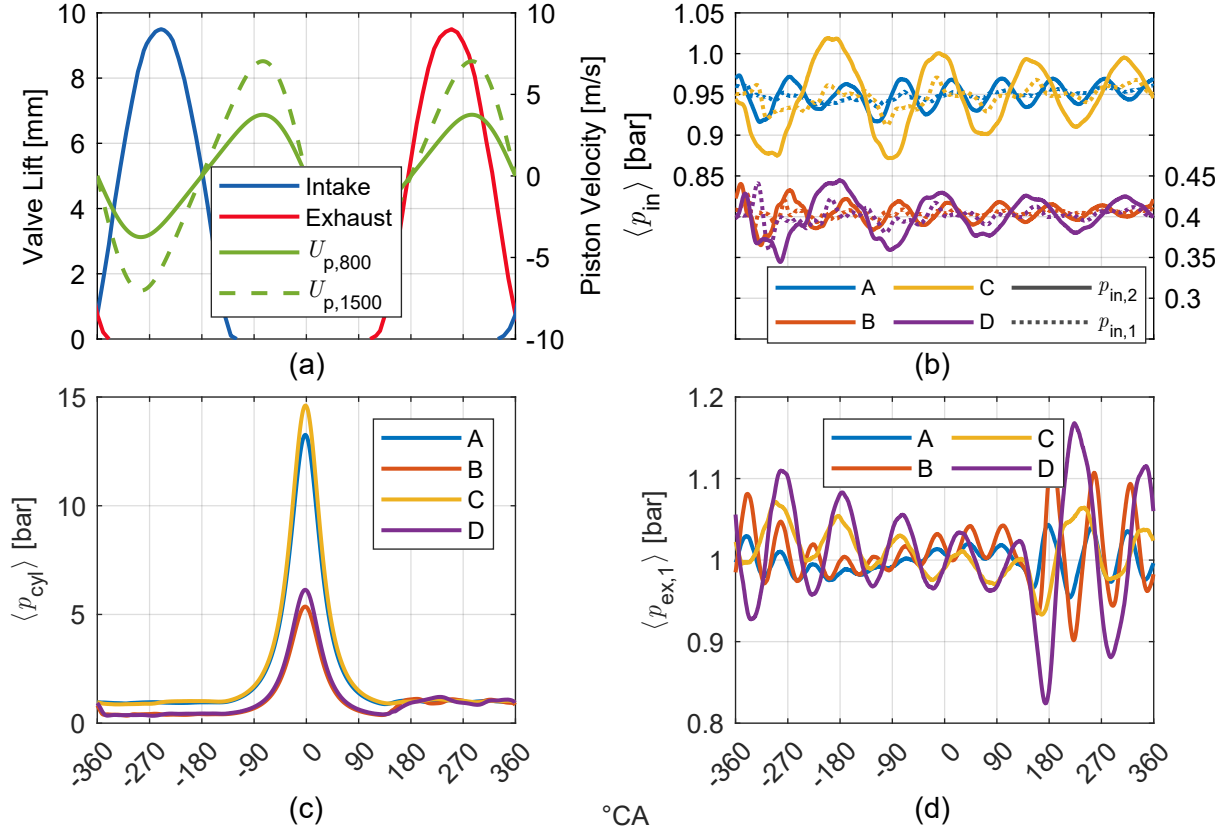


**Figure 3.2:** (a) Valve lift curves and piston velocity for 800 rpm and 1500 rpm. (b), (c), and (d) Phase-averaged intake pressure  $p_{in}$ , in-cylinder pressure  $p_{cyl}$ , and exhaust pressure  $p_{ex,1}$ , respectively.

### 3.3 Optical Diagnostics and Processing

Four different experiments were performed for this cumulative dissertation using the common diagnostic technique of HS PIV as a basis for investigating the influence of flow on other processes. Each publication contains specific details for its respective experiment and analysis techniques; however, this section aims to provide an overview of the experimental methodologies employed in this thesis.

#### 3.3.1 High-speed PIV

High-speed PIV was achieved by introducing a pair of laser sheets into the cylinder volume in either the symmetry plane (SP) or the valve plane (VP) through the bottom of the glass piston (or flow bench plate) via the piston mirror. The laser sheets were formed and directed to the engine by a series of sheet optics consisting of mirrors and cylindrical lenses to illuminate and image tracer particles from the side with a HS CMOS camera. In this work, various camera lenses with different distance rings and aperture settings were used to meet the different optical resolution and focusing requirements. The tracer particles were generated by a Palas AGF 10.0 seeder, which atomizes silicone oil (DOWSIL 510, DOW Inc.) with air to an average droplet diameter of  $\approx 500$  nm and is introduced just after the intake pressure oscillation plenum (labeled *Tracer* in Figure 3.1(a)) for sufficient mixing. Depending on the experiment, crank-angle resolutions of  $1^\circ\text{CA}$  (**Paper III**),  $2^\circ\text{CA}$  (**Papers IV and V**), and  $5^\circ\text{CA}$  (**Paper II**) were employed over a wide range of crank-angles from intake to top dead center, with varying optimized time separa-

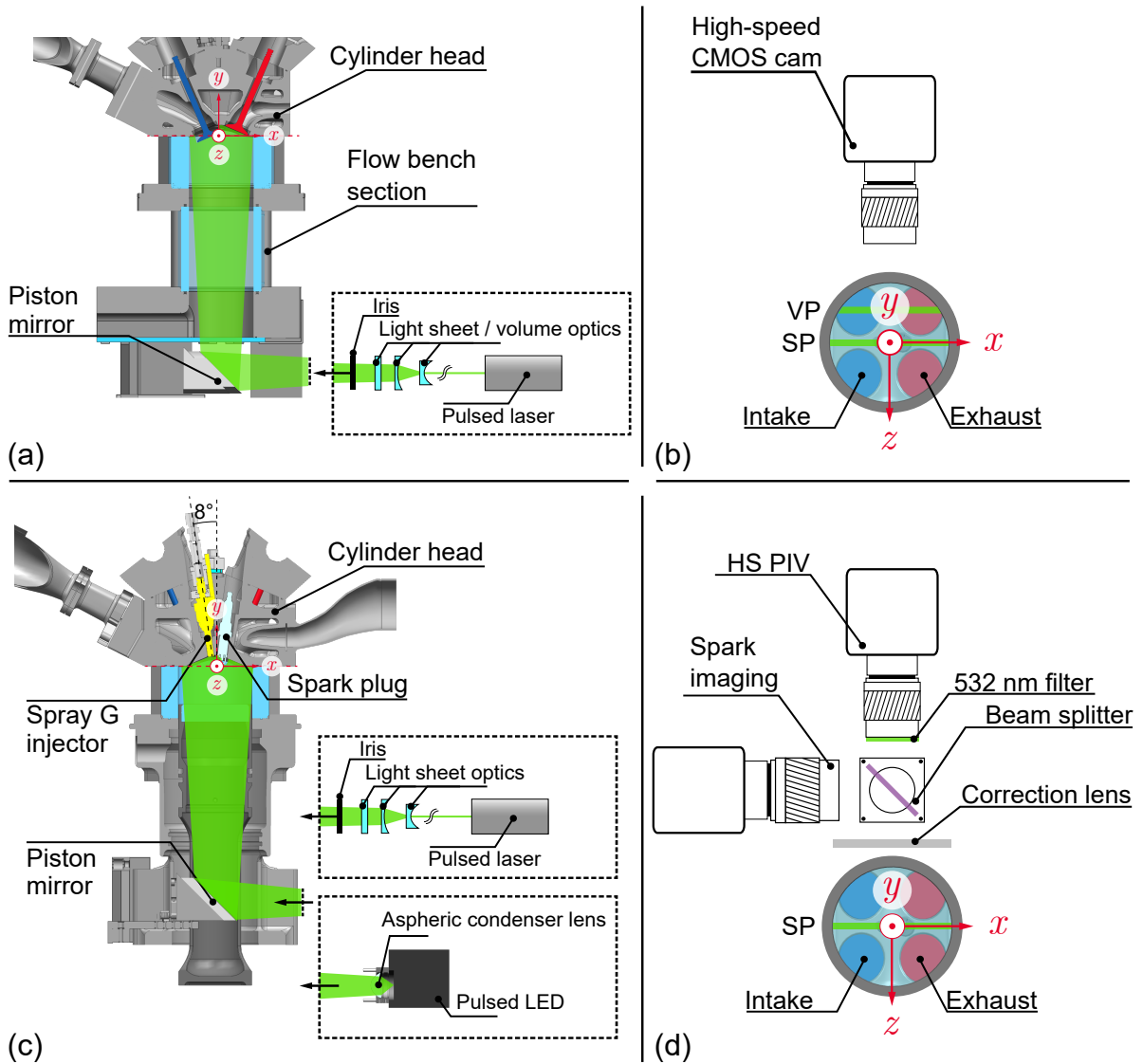


**Figure 3.3:** (a) Schematic of the PIV and volumetric Mie scattering setup for the flow bench. (b) Top-view schematic of the camera arrangement for the flow bench and motored engine experiments in Papers I, II, and III. (c) Side-view schematic of the PIV and volumetric Mie scattering setup for the motored engine. (d) Top-view schematic of the camera arrangement for the fired engine experiments in Papers IV and V.

tion  $dt$  between laser pulses. In the case of the flow bench, stationary valve experiments were conducted at 12.5 kHz and moving valve experiments had a crank-angle resolution of  $0.4^\circ\text{CA}$  (12 kHz, see **Paper I** for details). Side and top view schematics of the optical arrangements for the flow bench and engine are shown in Figure 3.3.

Images of a patterned two-plane target (058 – 5, LaVision GmbH) were recorded after each measurement session for dewarping and conversion of raw coordinates into real coordinates using a 3<sup>rd</sup> order polynomial (performed in DaVis software, LaVision GmbH). Vector calculation and processing was then performed using the commercial software DaVis, LaVision GmbH. A multi-step cross-correlation algorithm with decreasing interrogation window sizes was used for vector calculation and post-processing was done to remove spurious vectors. Further flow field processing, such as phase averaging or turbulent kinetic energy calculation was performed in MATLAB (The MathWorks, Inc.). Specific processing details are provided in each paper (see

Papers I, II, III, IV, and V).

### 3.3.2 Spray Visualization

The direct injection sprays were visualized using volumetric Mie scattering of iso-octane droplets captured by a HS CMOS camera with a large depth of field. As shown in Figure 3.3(a), the light volume for the flow bench experiment was created using volume optics and one HS laser cavity, while for the motored engine setup, the light volume was created using a HS LED (LPS II, ILA 5150 GmbH) equipped with an aspheric condenser lens. As with the laser sheets, volumetric light was directed into the engine through the piston mirror and Mie scattering was imaged from the side. In addition to dewarping, real-world scaling, and masking of reflective objects, several processing steps were performed in MATLAB to calculate the spray boundary (spray binarization). Briefly, the background was subtracted, a median filter ( $3 \text{ pixel} \times 3 \text{ pixel}$ ) was applied, spray images were normalized, and a single threshold was determined for each cycle or spray event (for more details, see **Paper III**).

### 3.3.3 Flame Visualization

Flame visualization was performed using the planar Mie scattering images acquired for PIV by calculating the separation of particle-laden and particle-void regions, where the latter is assumed to indicate the burned gas region due to the evaporated oil droplets. Similar to the spray binarization algorithm, burned gas regions, referred to as flame regions for simplicity, were calculated in several steps using MATLAB. After dewarping, scaling, and masking out reflective objects, images were normalized by maximum cyclic intensity, an entropy filter ( $5 \text{ pixel} \times 5 \text{ pixel}$ ) was applied, a division of each image by the background was conducted, and all pixels with values less than 1 were set to zero (for more details, see **Paper V**). Figure 3.4(a) shows an example of the resulting extracted flame boundaries from the algorithm. Although this method cannot resolve fine details around the flame front, it does resolve the bulk structure of the flame position and provides an economical alternative to other methods such as  $\text{SO}_2$  tracer or OH LIF.

### 3.3.4 Spark Imaging

High-speed spark imaging was performed from the same side as the PIV camera using a beam splitter arrangement consisting of a Chroma Technology Corporation T470lpxr-UF3 beam splitter (transmitting a range of 470 nm to 700 nm for the PIV images) inside a Thorlabs, Inc.

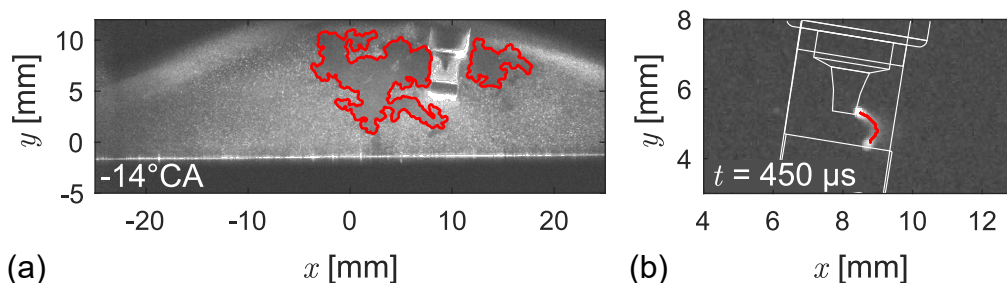


**Figure 3.4:** Example binarization images from the same fired cycle. (a) Extracted flame boundaries superimposed on the dewarped PIV camera image. (b) Extracted skeletal spark plasma location superimposed on the dewarped spark camera image.



compact cage cube. The beam splitter arrangement was used to allow the back of the cylinder to be painted black to reduce the effect of reflections on PIV and spark imaging. In addition, a cylindrical lens with  $f = +2000$  was used to correct for astigmatism due to the curvature of the cylinder glass. The camera and beam splitter setup for simultaneous PIV and spark imaging is shown in Figure 3.3(d). The binarization of the spark plasma images was the same as for the flame visualization, except that instead of an entropy filter and division, a binarization threshold of 3% of the maximum normalized intensity was set (for more details, see **Paper IV**). Additionally, a skeletal representation of the binarized plasma was used to illustrate the centerline plasma position for easier interpretation, for example, when plotting the probability density function (PDF) of the plasma. Figure 3.4(b) shows an example image of the skeletal plasma position superimposed on a dewarped plasma camera image.

### 3.4 Summary of Techniques Used

All papers in this thesis employed HS PIV and pressure and temperature sensor measurements. Although the details of each experimental setup are omitted due to their inclusion in each paper, this section provides a brief summary of the techniques used in each paper. Specifically, **Paper II** used HS PIV in the SP and VP and GT-POWER 1D simulations. Along with HS PIV, **Paper III** used HS Mie scatter imaging of the direct injection sprays of the motored engine (using the LED for volumetric light as in Figure 3.3(c)) and volumetric Mie scattering of the no-flow condition of the flow bench (using a laser cavity for volumetric light as in Figure 3.3(a)). **Paper V** used simultaneous HS PIV and flame visualizations with EGR conditions, while **Paper IV** used the same flow and flame data with the addition of simultaneous HS spark plasma imaging and spark probe measurements. Spark voltage and energy were measured using a Tektronix DPO7104 digital phosphor oscilloscope at a sampling rate of 5 MHz with a Tektronix P6015A high-voltage probe and a Tektronix TCP303 current probe and TCPA300 amplifier for voltage and current measurements, respectively. **Paper I** used HS PIV in the SP and VP of the newly designed air flow bench (Figure 3.3(a)) and compared the velocity fields with those obtained in the motored engine. Finally, an unpublished study of direct injection sprays in the flow bench is presented in this thesis, which combines the velocity data measured in **Paper I** with spray data obtained using the flow bench Mie scattering images as described in **Paper III**.



# 4 Experimental Characterization of the Intake Flows under Varying Engine Parameters

In this chapter, the main results of three papers are presented to provide a characterization of the intake flows under varying configurations and parameters of the Darmstadt engine. First, the turbulent intake flow is investigated through a simplified engine configuration: High-speed PIV of an air flow bench (**Paper I**). Next, the influence of intake pressure oscillations on the flow of motored engine operation are studied by varying the intake pressure and, in effect, the amount of backflow into the intake manifold (**Paper II**). Then, unpublished results of the flow bench test stand combined with direct injection sprays are presented to demonstrate the behavior of parametrically increasing steady flows on the sprays. Last, the role of intake flow and bulk gas density on the spray of a multi-hole injector under motored engine conditions is analyzed as an increase in the progression from simplified to complex engine configurations (**Paper III**). The final section then summarizes the main findings and provides an outlook for future research and the next chapter of this thesis.

## 4.1 Dynamics Governing Intake Flows

### 4.1.1 Investigation of Turbulent Intake Flows in a Flow Bench

The majority of the content from this section was first published in **Paper I** [102].

In-cylinder flows of ICEs are instrumental in the combustion process and play a significant role in provoking CCV. Engine flows have been observed to influence combustion speed as early as the intake phase [95, 106]. Therefore, a detailed study of the turbulent intake flows of the optically accessible research engine was performed by replacing the piston assembly with an open-ended outlet channel and measuring HS PIV at 12.5 kHz over 25 000 consecutive velocity fields. Thus, the engine test stand was converted into an air flow bench with steady (stationary valve lift) or unsteady (moving valves) MFR OCs based on the standard *A* OC of the Darmstadt engine

**Table 4.1:** Relevant engine and flow bench boundary conditions. Standard uncertainties are shown in parentheses.

Condition	$\dot{m}$ [kg/h]	Re [-]
Motored ( $-270^\circ\text{CA}$ )	11.35 (1.00)	37 200 (est.)
Mov. val. ( $-270^\circ\text{CA}$ )	19.90 (1.00)	–
100 % MFR	94.10 (1.00)	32 400 (400)
75 % MFR	70.63 (1.00)	24 300 (400)
50 % MFR	47.09 (1.00)	16 200 (400)

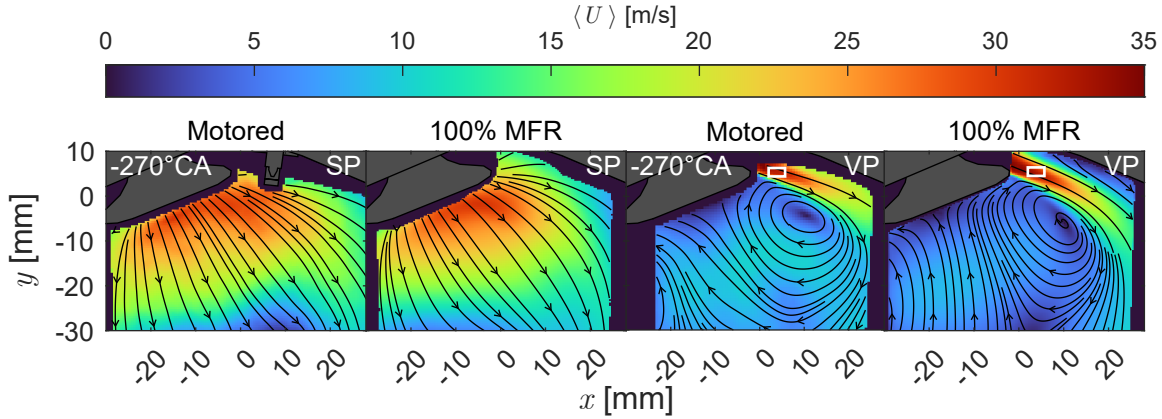


**Figure 4.1:** Comparison of the intake velocity of the motored engine OC A (0.95 bar and 800 rpm) at  $-270^\circ\text{CA}$  and the flow bench at 100% MFR in the symmetry and valve planes. Adapted from [102].

(0.95 bar and 800 rpm). To properly simulate the engine’s intake, the MFRs were chosen so that the average intake flow in a region downstream of the intake jet matched the velocity in the same region of the motored engine’s OC A at  $-270^\circ\text{CA}$ . This procedure was performed with the fixed valve lift of 9.21 mm and for the moving valves at the corresponding valve lift. Figure 4.1 shows a comparison between the motored engine and flow bench velocities for the 100% MFR case in the symmetry and valve planes (SP and VP, respectively). The white boxes in the VP flow fields represent the region where the mean velocity magnitude  $\langle U \rangle$  was compared to select the MFR. To further investigate the intake flows at different Reynolds numbers  $\text{Re}$ , a 75% and 50% MFR case were also selected. Table 4.1 shows a summary of the resulting boundary conditions of the investigation.

Due to the MFR selection procedure, velocities of the flow bench conditions match well with those of the engine in the regions near the intake valves. However, further downstream, the absence of engine dynamics, such as piston motion or volume confinement, has a noticeable effect on the flow. Such effects are visible in Figure 4.1 by the differences in velocity magnitude at  $y \approx -30$  mm and the vortex formed by the jet in the SP and VP cases, respectively.

Another method to compare the OCs is to calculate the turbulent kinetic energy  $k$ -fields. Figure 4.2 shows a comparison of the  $k$ -fields where each OC has a multiplication factor of the  $k$  so that a common color bar can be used. The  $k$ -fields have the same general structure of the turbulent fluctuations over all OCs, except for the 100% MFR case in the SP, which has a gap separating two large pockets of high turbulence. In addition, the amount of turbulence in the 100% MFR case is disproportionately high compared to the other steady flow bench cases (see Figures 10 and 11 of **Paper I** for the 75% MFR case). Instead of scaling quadratically, the spatially averaged  $k$  sampled in regions of high fluctuations ( $x \approx 10$  mm and  $y \approx 0$  mm and  $-10$  mm for VP and SP, respectively) have a scaling factor of 3.3 and 7.2 compared to the expected 1.78 and 4 for the 75% and 50% MFR cases, respectively.

Since the magnitude of  $k$  is nearly twice the expected value for the 100% MFR OC, additional detailed analysis of the intake jet is warranted. To focus on the jet behavior, velocity components relative to the computed mean jet streamline (based on the center of the jet taken from  $\langle U \rangle$ ) are defined, where  $s_S$  and  $n_S$  represent the streamwise and normal components along the streamline  $S$ , respectively. Figure 4.3(a) shows an example of the definition of the streamwise and normal components computed from the streamline of the 100% MFR case. The streamline components

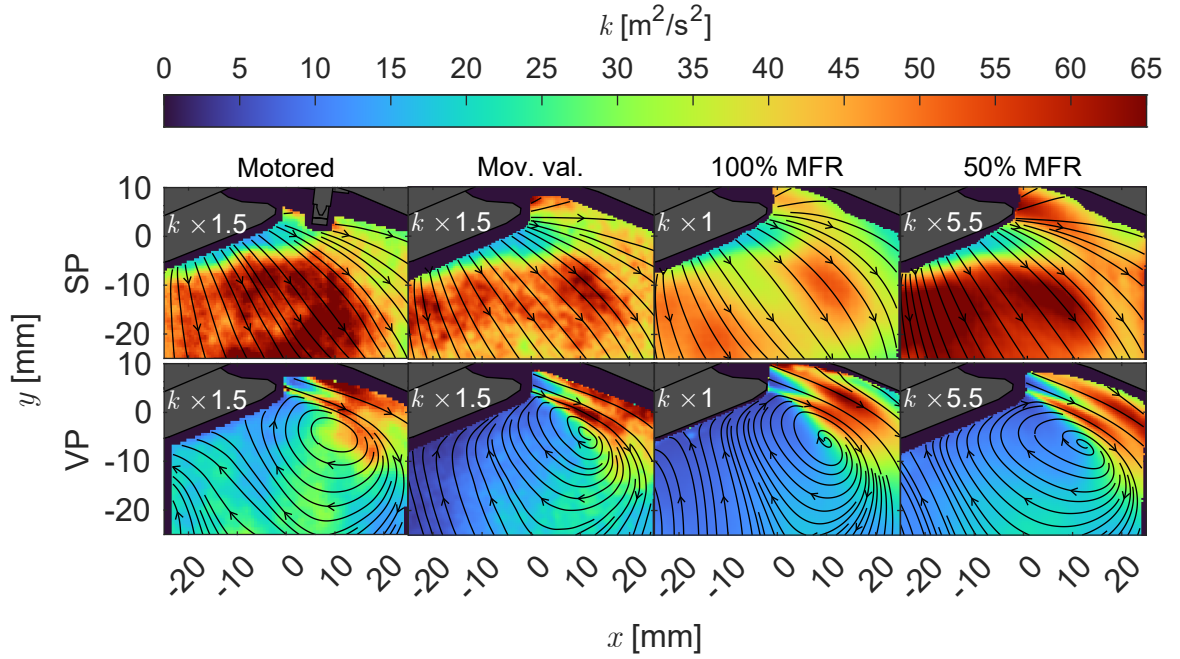


**Figure 4.2:** Comparison of the turbulent kinetic energy  $k$  fields. The average flow direction is represented by the streamlines. Adapted from [102].

of the velocity provide insight by directly comparing the magnitude and fluctuations of velocity along the individual streamlines of the OCs', which vary slightly in trajectory. Figure 4.3(b) shows a comparison of the mean streamwise velocity profiles along  $S$ . In particular, at the beginning of the jet, or within the first 10 mm along  $S$ , the 100% MFR case agrees almost perfectly with the motored and moving valve cases. Figure 4.3(c) displays the mean normal component along  $S$ , which is centered around zero and represents the average of the fluctuations along  $S$ . Although the average velocity fluctuations along  $S$  are close to zero, it was clear by the analysis of  $k$  that the 100% MFR case has a disproportionate amount of fluctuations compared to the other steady flow bench OCs. Consequently, the correlation  $R$  of the instantaneous velocity along  $S$  was computed for the steady flow bench OCs (see Figure 12 of **Paper I** for  $R$ ). The behavior of the average spatial correlation along  $S$  for the 100% MFR case is in stark contrast to the lower MFR cases, as  $\langle R_n \rangle$  crosses and appears to oscillate around zero, while the lower MFR cases have one zero crossing. Similarly, the autocorrelation of  $n$  over all cycles at the first position along  $S$  ( $n_1$ ) shows a clear oscillation around zero for the 100% MFR case, while the other cases do not cross zero at all. Further analysis of this oscillation phenomenon is performed by a fast Fourier transform (FFT) of  $n_1$  for each steady flow bench condition (Figure 4.3(d)). In the FFT of  $n_1$  for only the 100% MFR case, a dominant amplitude appears at  $f = 752.5$  Hz, meaning that the jet is flapping at a constant frequency of 752.5 Hz.

The frequency found in the 100% MFR case is so coherent that it can be used to reconstruct jet flapping modes from the mean velocity magnitude. Figure 4.4 shows the computed jet flapping of opposite modes calculated by phase averaging  $U$  over every 8.31<sup>st</sup> flow field (by interpolation), with a full flapping cycle occurring every 16.6<sup>th</sup> flow field (see Figure 13 of **Paper I** for all modes from  $0^\circ$  to  $270^\circ$ ). The coherent flapping modes exhibit a wave-like progression from each  $90^\circ$  mode until the modes shown in Figure 4.4, which show symmetric behavior with respect to each other. Despite phase averaging over hundreds of images of interpolated modes, sharp gradients or shear regions, are preserved, indicating that the 752.5 Hz frequency accurately captures the

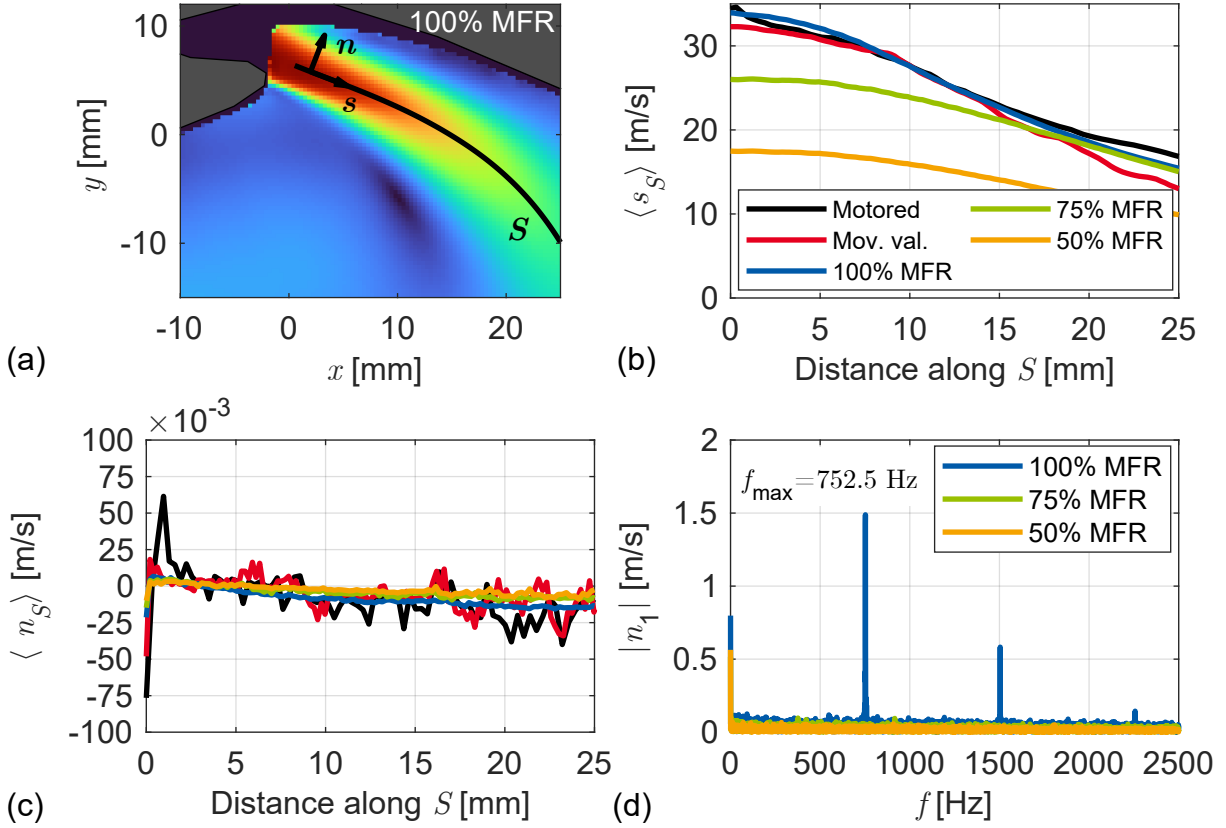


**Figure 4.3:** Comparison of the streamline  $S$  velocity. (a) The definition of the streamwise  $s$  and normal  $n$  components. (b) and (c) Profiles of the mean streamwise and normal components, respectively, along  $S$ . (d) Fast Fourier transform spectrum of  $n$  at the first position along  $S$ . Adapted from [102].

flapping.

The origin of the coherent jet flapping observed at a MFR of 100% is unknown despite the use of several analysis techniques. A possible cause of the jet flapping at a frequency of 752.5 Hz is the vortex shedding at the valve stem, which survives the acceleration through the valve gap. The vortex shedding frequency  $f_w$  is related to the dimensionless frequency, the Strouhal number  $St$ , and the characteristic velocity and length  $U$  and  $D$ , respectively, as  $f_w = StU/D$ . By using a velocity range of between 28 m/s and 34 m/s, which is obtained by the velocity near the stem from MRV flow bench measurements [111], a  $St$  in the range of 0.188 and 0.195, and a  $D$  of 8.3 mm, the shedding frequency falls in the range of 634 Hz and 799 Hz. Since the dominant frequency is well within the estimated  $f_w$  range, it is reasonable to assume that the vortices survive the acceleration through the valve gap. In addition, a slight vibration of the inlet valves at 752.5 Hz was also detected by an FFT of the intensity of a pixel at a position where the PIV laser sheet reflected with the valve. Effects such as laser intensity fluctuations are ruled out as a source of this observed frequency by further FFTs of particle-laden regions. While it is clear that the flapping frequency and the valve vibrations are related due to the same observed 752.5 Hz, a causal trend for one or the other phenomenon remains unclear. Furthermore, the evidence is not sufficient to conclude that the 752.5 Hz is due to vortex shedding, as optical access in the intake port was not available. Therefore, future experiments with optical access to the valve stem region or 3D CFD simulations may shed more light on the cause of this coherent flapping frequency and valve vibration. Nevertheless, the flow bench test stand and the resulting data provide invaluable

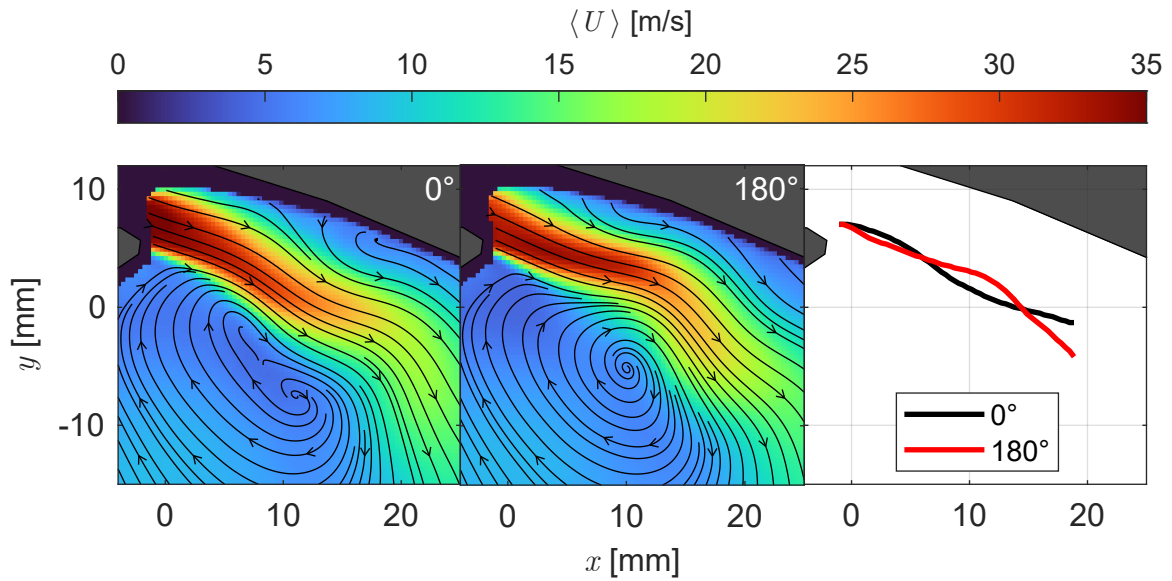


**Figure 4.4:** Mean velocity field of the coherent flapping for the 100% MFR case. The streamline of the center of the jet is compared for two opposite flapping modes. Modes are obtained by calculating the mean velocity of every 8.31<sup>st</sup> flow field. Adapted from [102].

insight into engine intake flows through geometric and process simplification. In the following sections, the interaction between the intake flows of the motored engine and the flow bench with increasingly complex processes, namely direct injection, will be further investigated.

#### 4.1.2 The Influence of Intake Manifold Pressure Oscillations on In-Cylinder Flows

The majority of the content from this section was first published in **Paper II** [103].

Analysis of the intake flows of the four standard operating conditions of the engine (A to D, ranging from 800 rpm to 1500 rpm and 0.95 bar 0.4 bar intake pressure) yielded an unexpected result: despite the same engine speed (1500 rpm), the tumble center of OC D (0.4 bar) at  $-90^\circ\text{CA}$  has a different shape and position than that of OC C (0.95 bar). As a standard test case of the engine, both experimentally and for numerical simulations, the delineation of the cause of this phenomenon is critical. Therefore, a parametric sweep of intake pressures was performed where the manifold pressure was varied from 0.95 bar to 0.4 bar in 0.1 bar increments. In addition to engine indicating data, HS PIV was measured at both the SP and VP to compare the effects of the manifold pressure on intake flow.

Figure 4.5(a) shows the transition of the phase-averaged intake manifold pressure  $p_{\text{in},2}$  from OC C to D. The intake and exhaust valve timings are indicated by the blue and red shaded curves, respectively. Two types of pressure oscillations occur in the intake manifold: low-frequency oscillations, which are characterized by large waveforms with amplitudes between  $\approx 0.6$  bar and 0.7 bar and are caused by the periodic motion of the valves; and high-frequency oscillations, which appear as disturbances in the large waveform oscillations with amplitudes less than  $\approx 0.3$  bar and are caused by backflow. As the average intake pressure decreases, the amplitude of the high-frequency oscillations increases, a phenomenon which is linked to the intake valve timing. Normally, when the intake valves close, a pressure wave of low-frequency, high-amplitude oscilla-



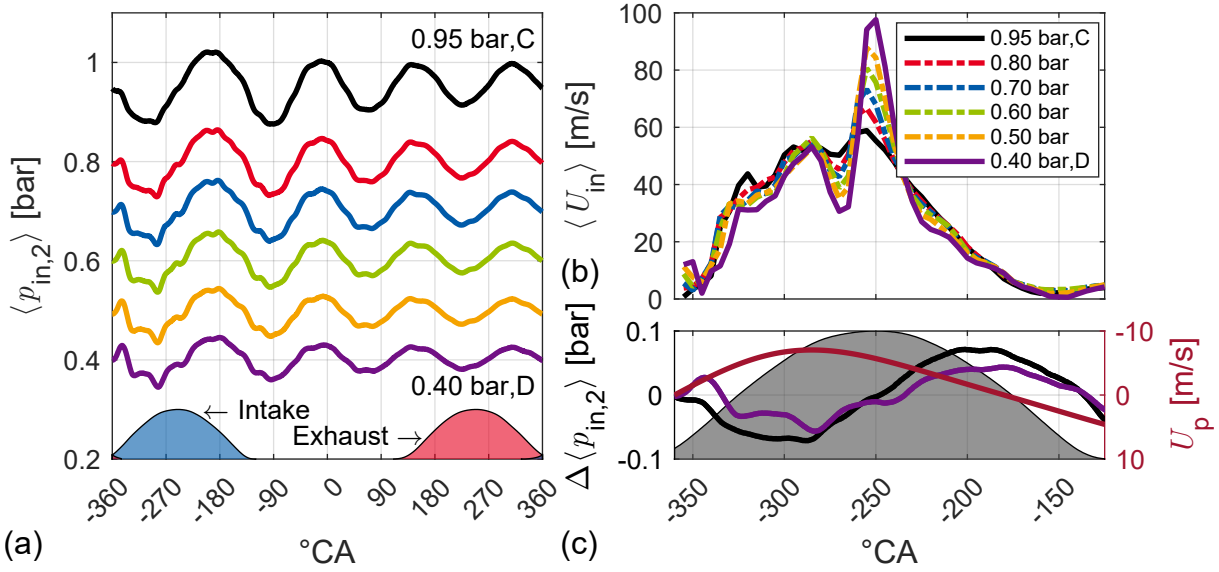


**Figure 4.5:** (a) Phase-averaged intake pressure sweep. (b) Phase-averaged intake velocity in the symmetry plane. Intake velocity is spatially averaged in a  $3 \times 3 \text{ mm}^2$  region near the valves. (c) Left: Difference of phase-averaged pressure from the cyclic and phase mean. Right: Piston velocity. The intake valve timing is indicated by the gray shaded curve. Adapted from [103].

tions forms, visible as the main sinusoidal waveform for each condition in Figure 4.5(a). However, at low intake pressures, most extreme in the 0.4 bar case, a backflow occurs when the exhaust and intake valve timings overlap, inducing an additional pressure wave of higher frequency and lower amplitude due to the equalization of the relatively high exhaust pressure with the low intake manifold pressure.

The induced high-frequency oscillations in the manifold have a significant effect on the velocity during intake. Figure 4.5(b) shows the phase-averaged intake velocity  $\langle U_{in} \rangle$  (the spatial average of a region of interest in the SP from  $x = -3$  to  $x = 0$  mm and  $y = -3$  to  $y = 0$  mm is considered  $\langle U_{in} \rangle$ ) for each corresponding average intake pressure. While the intake velocity remains similar for all cases up to  $-280^{\circ}\text{CA}$ , the low pressure conditions have a greater decrease in velocity, which reaches a minimum near  $-270^{\circ}\text{CA}$ , and rapidly increases with maximum velocities almost double those of the 0.95 bar case. In addition, the phase-averaged pressure fluctuations (phase-averaged pressure subtracted from the overall mean pressure) of C and D as well as the intake valve timing (gray shaded area) and the piston velocity  $U_p$  (blue curve) are plotted in Figure 4.5(c) on the same  $x$ -axis as 4.5(b) for comparison. The magnitude of the flow is determined by a combination of factors, including valve timing, piston velocity and position, gas properties, and manifold oscillations; however, since all other factors remain relatively constant from case to case, the phase-locked, backflow-induced, high-frequency oscillations interact with the other factors to produce the unbalanced inflow. The backflow was not only observed using HS PIV, but its effect on the intake flow dynamics was confirmed using GT-POWER 1D simulations of the 0.4 bar case, where the outlet pressure was set to 0.4 bar, effectively eliminating the backflow (see Figures 6 and 8 of **Paper II**). While the backflow-free case exhibits a nearly symmetric quadratic intake velocity profile, the dynamics associated with the backflow were also reproduced in GT-POWER, resulting in a similar increase in intake velocity as measured in the experiments. Interestingly, despite the seemingly small amplitudes of the high-frequency pressure oscillations of the 0.95 bar case, which has the least amount of backflow, the dynamics of the oscillations result in significant effects on the intake velocity.



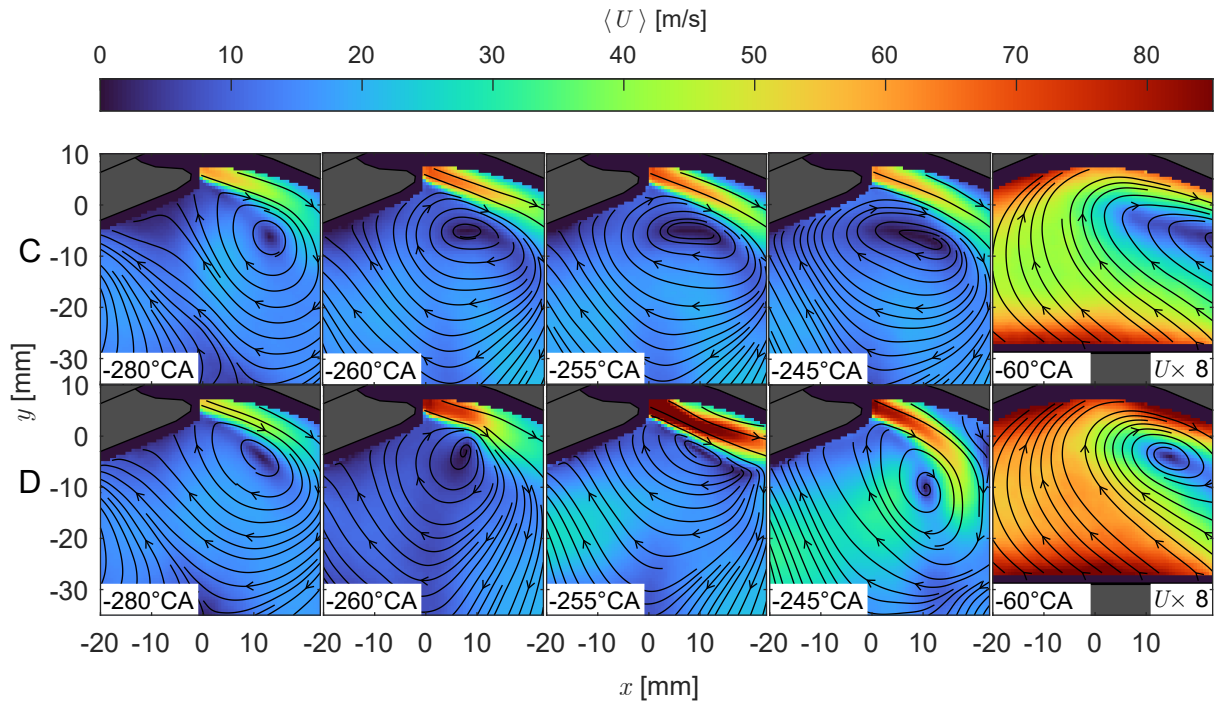


**Figure 4.6:** Average velocity magnitude in the valve plane at selected crank-angles. At  $-60^\circ\text{CA}$ , the magnitude is multiplied by 8 to use the same color bar. Adapted from [103].

The effects of high-frequency pressure oscillations are most apparent when comparing the intake jets of OC C and D, shown in Figure 4.6. As with the velocity profiles, the phase-averaged intake jets show similar behavior at  $-280^\circ\text{CA}$ . However, the velocity magnitude and curl of the partial load OC D jet changes rapidly during the period of the extreme intake velocity spike. It is important to note that the seemingly unstable jet flapping is actually the average over 250 consecutive cycles, meaning that the flapping behavior is phase-locked. Furthermore, the difference in intake velocities has a clear effect on the tumble formation, inducing a higher angular momentum. A comparison of the velocity fields during the compression phase and the tumble positions from the SP (see Figures 11 and 12 of **Paper II**) shows that the tumble vortex shape is more vertically elongated for OC D than C due to the higher vertical velocities and the tumble center develops closer to the spark plug.

This study demonstrates the importance of considering the entire intake manifold when performing full-scale engine simulations such as LES. Since manifold acoustics are unavoidable during part-load engine operation, they must be modeled to achieve the highest possible accuracy. Recognition of this phenomenon is especially critical since the investigations in Chapter 5 use only the part-load OC D to study cyclic variability under diluted fired conditions.

## 4.2 Spray-Flow Interaction

So far, this chapter has focused on the dynamics affecting the intake flows in the spray-guided cylinder head configuration of the Darmstadt engine. In this section, the influence of the flow on the development of early injection sprays from a multi-hole injector is examined. Not only are the sprays characterized under varying engine operating conditions, but they are also analyzed using fixed mass flow rates of the flow bench to simplify the processes and provide insight as

well as valuable validation data for the growing database of Sandia National Laboratories' ECN [52]. The well-characterized *Spray G* injector and its standardized OCs set by the ECN have been extensively studied by cooperating international institutions to better understand spray-guided direct injection. However, few of these works have studied Spray G injection in optically accessible engines, usually opting for constant volume chambers that neglect the effects of a flow environment on the spray. Therefore, in the following investigations, Spray G injector sprays are studied at varying flow bench flowrates, engine speeds, and intake pressures in the Darmstadt engine to investigate the dynamic interactions between the in-cylinder flows, engine motion, and spray during early injection.

#### 4.2.1 Survey of the Spray Morphology under Varying Flow Bench Mass Flow Rates

In this section, the methods of **Paper I** and **Paper III** (following section) are combined to study the effects of intake flow on spray morphology under parametrically varied MFRs of the air flow bench. The use of the flow bench reduces the influencing variables that affect spray morphology, such as unsteady volume confinement due to piston motion. As in **Paper I**, the varied flow bench MFRs are proportions of the 100% MFR case, which was selected after matching the intake velocity in the symmetry plane to that of the motored engine of OC A (0.95 bar intake pressure and 800 rpm engine speed) at  $-270^{\circ}\text{CA}$ . In addition to the 75% and 50% MFR cases analyzed in **Paper I**, sprays with a 20% MFR and a no-flow (NF) condition were investigated. 100 sprays from the Spray G injector for each condition with an electronic injection duration of  $680\ \mu\text{s}$  were recorded using volumetric Mie scattering imaging at a frame rate of 25 kHz.

Figure 4.7(a) shows the average binarized spray boundaries superimposed on the spray image of the NF case at  $t = 640\ \mu\text{s}$  after start of injection (aSOI), averaged over all cycles. In the first half of the spray (from the injector tip to  $\approx 50\%$  of penetration), the extracted shape rotates toward the exhaust with increasing Re. Beyond the first half of the spray, increasing MFR has an amplified effect on the penetration length of the plumes on the intake side. Interestingly, however, the 100% MFR spray appears to have a shorter penetration length than the 75% MFR case, which may be a result of the oscillatory dynamics of the flow bench present only in the 100% MFR case (see **Paper I**). A byproduct of the coherent flapping of the 100% MFR case is a more vertically oriented recirculation compared to the lower MFR cases (see, for example, Figure 10 of **Paper I**, visible in the average flow streamlines), which may result in

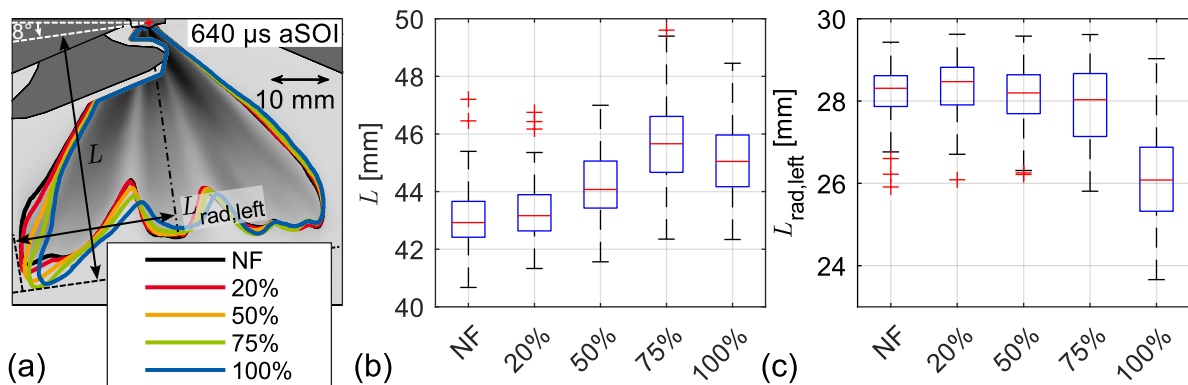


**Figure 4.7:** Comparison of spray morphology at  $t = 640\ \mu\text{s}$  aSOI. (a) Average extracted spray contours. (b) and (c) Box plots of computed axial penetration length  $L$  and the radial penetration length of the left side of the injector axis  $L_{\text{rad, left}}$ , respectively.

inhibition of spray penetration. To further examine the statistical differences over all 100 cycles in each OC, Figure 4.7(b) and (c) show box plot comparisons for the axial penetration length  $L$  and the left-side radial penetration  $L_{\text{rad, left}}$ , respectively, at  $t = 640 \mu\text{s}$  aSOI. As observed in the spray boundary comparison, the median  $L$  increases steadily until it peaks in the 75% MFR case. Similarly, the 100% MFR case displays contrasting behavior for the  $L_{\text{rad, left}}$  than the others. While from 20% to 75%, higher MFRs are associated with slight decreases in the median  $L_{\text{rad, left}}$ , the 100% MFR shows a much lower radial penetration, indicating that the stronger recirculation in this case may convect the left spray plumes further toward the center of the cylinder than in the other cases.

Aside from abnormalities originating from the coherent jet flapping of the 100% MFR case, the phenomena of the flows leading to different spray morphologies are expected and can be studied in detail through parametric variation. This test case is just one example of the potential of the flow bench to investigate phenomena with a simplified and well controlled, yet realistic engine flow configuration. Investigation of spray from other injectors and phenomena such as the flow induced by geometric variations of the intake port can be valuable in future studies. In addition, the simplified geometry and boundary conditions of the flow bench provide high-fidelity, well-documented data for the development of numerical models.

#### 4.2.2 Analysis of the Intake Flow's Effects on Early Direct Injection Sprays

The majority of the content from this section was first published in **Paper III** [104].

In addition to fixed parameters such as geometry and injection pressure, the morphology of spray-guided multi-hole injectors is mainly determined by the in-cylinder conditions during injection. As shown in the previous section, one of the most important of these is the in-cylinder velocity,

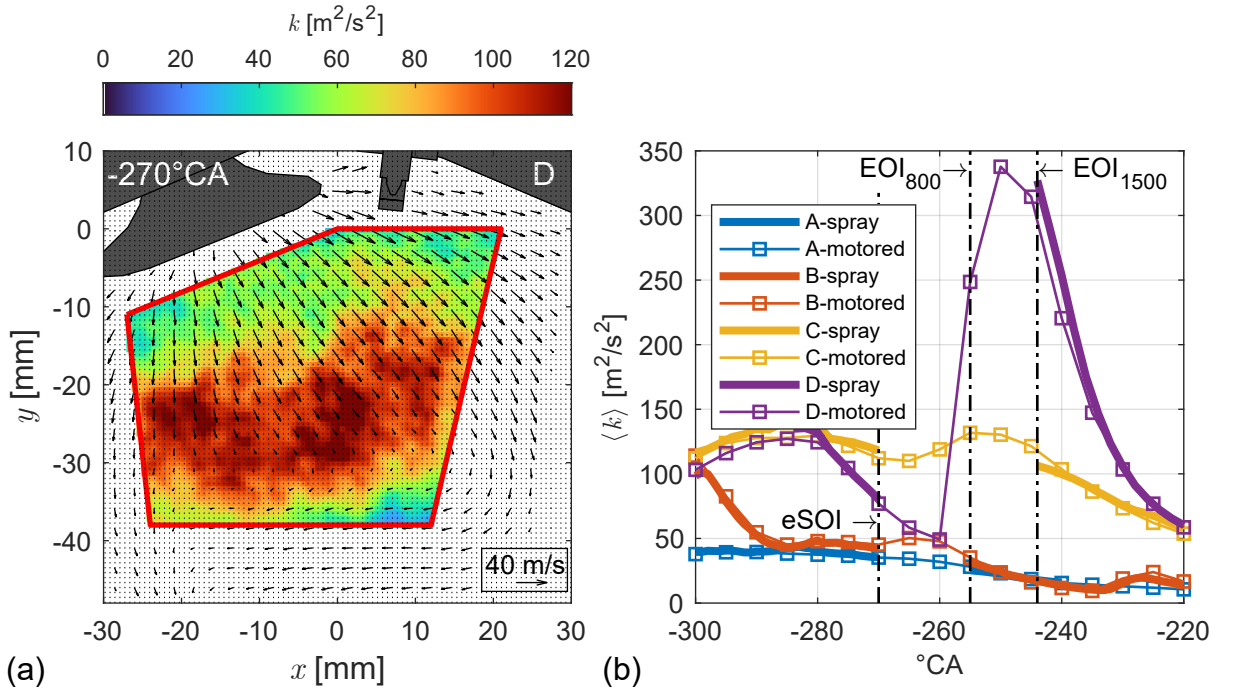


**Figure 4.8:** Turbulent kinetic energy  $k$  during injection. (a) Region of interest (ROI) for calculating the spatial mean of  $k$ . (b) Spatially-averaged turbulent kinetic energy  $\langle k \rangle$  from the ROI in (a). Adapted from [104].

which enhances evaporation and facilitates the critical process of fuel-air mixing. To investigate these phenomena in the dynamic environment of the motored engine, this paper presents a study of homogeneous Spray G direct injection, that is, fuel was injected during the intake phase at  $-270^\circ\text{CA}$ . To match the Spray G OCs, an electronic injection duration of  $680\ \mu\text{s}$  was used, which results in approximately  $1/3^{\text{rd}}$  of the fuel mass required to achieve a stoichiometric mixture in engine operation [52]. High-speed PIV and non-simultaneous volumetric Mie scattering imaging are used to analyze the pre- and post-injection flow and the resulting spray morphology.

The four OCs of the Darmstadt engine were employed to vary the flow field and bulk gas density at the time of injection. Due to the intake manifold pressure oscillations discussed in the previous section, the velocities at the time of injection vary relative to the piston speed from OC to OC and also during the injection event of OC D. To investigate the influence of the varying velocity profiles during injection, the velocity and its turbulence near  $-270^\circ\text{CA}$  must first be characterized. Figure 4.8(a) shows the turbulent kinetic energy  $k$  of OC D at  $-270^\circ\text{CA}$  in a region of interest (ROI) within the engine's optical access where the spray mainly develops. The average velocity is represented by the arrows in both direction and length. Before the spray appears in the cylinder, the  $k$ -field of D at  $-270^\circ\text{CA}$  shows fluctuations of up to  $\approx 120\ \text{m}^2/\text{s}^2$ . However, as shown by the profiles of the spatial mean of the ROI over crank-angles (Figure 4.8(b)),  $\langle k \rangle$  increases fourfold during the injection for D, which resembles the profile of the mean intake velocity shown in Figure 4.5. The mean  $k$  is displayed in Figure 4.8 for cycles without spray (designated as motored) and with spray, which have data removed from the beginning of electronic start of injection (eSOI) until the end of the effect of the spray on the flow field (end of injection, EOI). The  $k$  for all OCs is independent of the spray, which is evident by the nearly matching profiles between motored and spray cycles after EOI. This result is somewhat unexpected, but not unfathomable since the injection duration is short and it is possible that much of the turbulence has spread towards the piston which is out of the camera's field of view during intake.

Although the flow fields and turbulence are relatively independent of the spray activity, the flow and bulk gas density during injection have a large influence on the spray morphology.

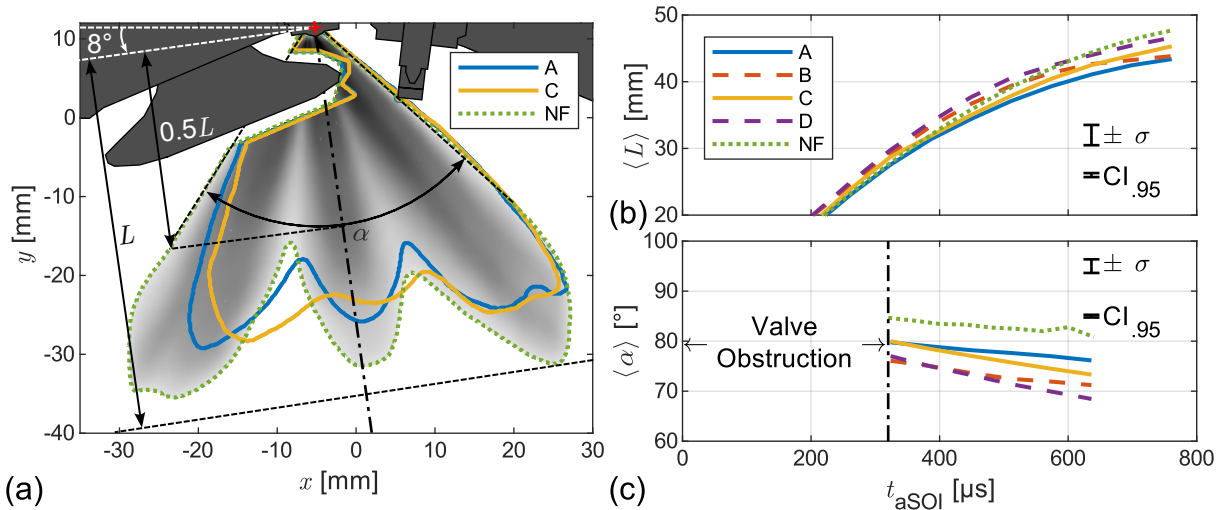


**Figure 4.9:** Comparison of the spray morphology of different OCs. (a) Average binarized spray boundary for near-atmospheric bulk gas density OCs at  $698.7\ \mu\text{s}$  aSOI. (b) and (c) average penetration length  $L$  and spray angle  $\alpha$ , respectively, for all OCs. Standard deviations  $\sigma$  and the 95% confidence interval  $\text{CI}_{.95}$  at  $640\ \mu\text{s}$  aSOI are indicated. Adapted from [104].

Figure 4.9(a) shows the average Mie scattering spray of a no-flow (NF) case, measured from the flow bench setup described in **Paper I**, and its binarized boundary. In addition, the average spray boundaries of the near-atmospheric cases A and C are shown to compare the spray shape at the end of the injection ( $t = 698.7 \mu\text{s}$  after start of injection, aSOI). The most obvious observation to be made from this comparison is that stronger flows influence the spray towards the positive  $x$ -direction, and the NF case has an almost symmetrical shape about the spray axis (dashed line). In addition, the NF case has a much larger penetration length  $L$  and spray angle  $\alpha$  due to the limited resistance provided by the surrounding gas, which induces evaporation in the engine cases. Another observation is that the sprays in the motored engine are affected by the spark plug (there is no spark plug present in the NF case), visible by a slight perturbation of the spray boundary, indicating that the injector orientation may need to be adjusted to avoid wall wetting and soot generation. Figure 4.9(b) and (c) show quantitative comparisons of the average  $L$  and  $\alpha$ , respectively, over all OCs. As observed in Figure 4.9(a), the NF case has the largest  $\langle L \rangle$ , followed by OC D, which has a high velocity directed downward toward the piston (also due to the intake pressure oscillations discussed earlier) and a low amount of resistance due to the low gas density at 0.4 bar. Likewise, the NF case has the largest  $\langle \alpha \rangle$ , followed by the near-atmospheric OCs. The low density cases (B and D) have the lowest  $\langle \alpha \rangle$  due to the tendency of sprays to collapse at low bulk gas densities. However, in these cases where total collapse does not occur, there is more plume-to-plume interaction at lower gas densities. These results show that flow field and bulk gas density conditions have a significant effect on the spray morphology during early injection, despite the use of a spray-guided injector whose operating principle is to form a stable spray over a wide range of operating conditions. In addition, the flow bench has proven to be a useful configuration for the simplification and control of variables.

### 4.3 Summary

This chapter presented several investigations of the in-cylinder flow with two overarching aims: first, to characterize and study the intake flows of the Darmstadt engine under various conditions; and second, to study the influence of the flow characteristics on the crucial process of direct injection. The flow bench design and implementation from **Paper I** was used to analyze turbulence phenomena from data that are difficult or impossible to measure in the unsteady environment of a dynamic engine. Close examination of the velocity fields in the symmetry and valve planes verified the fidelity of the flow bench operating conditions in comparison to the motored engine. Next, turbulence analysis revealed a coherent flapping with a frequency of 752.5 Hz in the 100% MFR case consistent with the estimated vortex shedding frequency of between 634 Hz and 799 Hz, suggesting that the vortex shedding at the intake valve stems may survive the acceleration through the valve gap in only this case. The flow bench was then proven useful as a test case for analyzing sprays, first with varying MFRs, then for a no-flow condition published in **Paper III**.

In-cylinder flows were also studied in detail under motored conditions in **Paper II**, since different flow magnitudes relative to the piston speed were observed for OC D (0.4 bar intake pressure and 1500 rpm engine speed) compared to the other OCs. The effects of backflow-induced high-frequency intake pressure oscillations were analyzed and it was found that at low intake pressures, where backflow is increased due to pressure equalization, the oscillations disrupt the pressure ratio between the valve gap and the cylinder, causing periods of low and subsequently high intake velocity. Analysis of the OC D intake jet revealed phase-locked flapping observed through the average velocity field over hundreds of cycles, indicating a stable and repeatable effect due

to the high-frequency pressure oscillations. The presence of coherent jet flapping in both the flow bench and motored operation suggests the need to capture full-scale acoustic dynamics as well as small-scale turbulence to accurately model engine flows. In **Paper III**, the in-cylinder flows of the motored conditions of the engine were also studied in relation to their influence on Spray G direct injection. The turbulent kinetic energy did not increase due to the spray, at least within the region of interest captured by PIV. However, the velocity before and during injection has a measurable effect on spray morphology and evolution, a phenomenon that is particularly evident when comparing the no-flow case with the other near-atmospheric OCs A and C.

The flow bench and motored conditions studied in this chapter provide new analysis and insight into turbulent in-cylinder flows and their relationship to combustion-related processes. In addition, these cases provide invaluable validation data and have been used in the development and testing of simulation models [43, 63, 135, 136]. Future experiments or LES of the flow bench may be performed to reproduce the coherent jet flapping and better delineate its causes. Perhaps more importantly, future experiments and simulations should build on the data and analysis provided in this chapter to study fired engine operation and the causes of combustion instability for the development of viable next-generation engine technologies. In the next chapter, one such technology for OC D, exhaust gas recirculation, is investigated through simultaneous multi-parameter measurements to provide a more complete model of the causal chain for spark-ignition combustion instability.

# 5 The Role of In-Cylinder Flows on Cyclic Instability under EGR Dilution

This chapter presents the main results of **Papers IV** and **V**, which investigated CCV of the fired engine under varying EGR levels. In the first section, the operating conditions used in both papers are defined and characterized to provide context for the in-cylinder conditions at the time of ignition. In the next section, the dynamics relating in-cylinder flows and the ignition process, specifically the spark behavior and the resulting flame propagation, are analyzed (**Paper IV**). In the following section, extensive statistical analyses are presented to further investigate the cause-and-effect relationship between flow and combustion performance, and flow-flame and misfire models are proposed (**Paper V**). Finally, the results are summarized and future work is recommended.

## 5.1 Definition and Characterization of Operating Conditions

This section introduces the operating conditions used in **Papers IV** and **V** to study combustion CCV. The majority of the content and figures from this section were first published in **Paper V** [106].

In contrast to the benefits of using EGR with stoichiometric mixtures in SI engines (see Chapter 2), the reduced flame speeds associated with mixture dilution are an obstacle to combustion stability. Therefore, the experimental investigation in this chapter utilized controlled amounts of externally mixed EGR to study the effects of reduced flame speed on CCV. To achieve this aim, the gas mixture system of the engine test stand introduced nitrogen and carbon-dioxide to the intake air to simulate exhaust gases. The use of a skip-fire strategy of igniting every seventh cycle ensured that residual combustion products from internal EGR were purged. In addition, fuel was injected within the intake port, providing completely homogeneous mixtures, reducing the influencing variables of the engine boundary conditions on the combustion process. Thus, the in-cylinder velocity was measured using HS PIV in the symmetry plane every second crank-angle-degree (4.5 kHz) and the spark plasma was recorded with a separate camera at a rate of 20 kHz. In addition to PIV and spark imaging, the burned gas regions (considered here as the flame) were extracted from the planar Mie scattering images and the ignition coil's voltage and current were recorded.

The standard OC D (0.4 bar intake pressure and 1500 rpm engine speed) was chosen due to its relatively higher  $p_{\max}$  COV compared with the other OCs. Furthermore, OC D was identified as the most prominent backflow case and was extensively studied in **Paper II**. Four EGR OCs were considered for a parametric variation of external EGR and CCV: 0 %, 10.5 %, 12.9 %, and 14.3 % EGR. Due to the decreasing flame speeds with increasing EGR, the ignition timing for each OC was adjusted to keep the combustion phase the same (50 % mass fraction burned at 8°CA). Figure 5.1(a) shows the average (solid line) and standard deviation (shaded area) of the in-cylinder pressure  $p_{cyl}$  for each OC over hundreds of cycles. The different ignition timings can



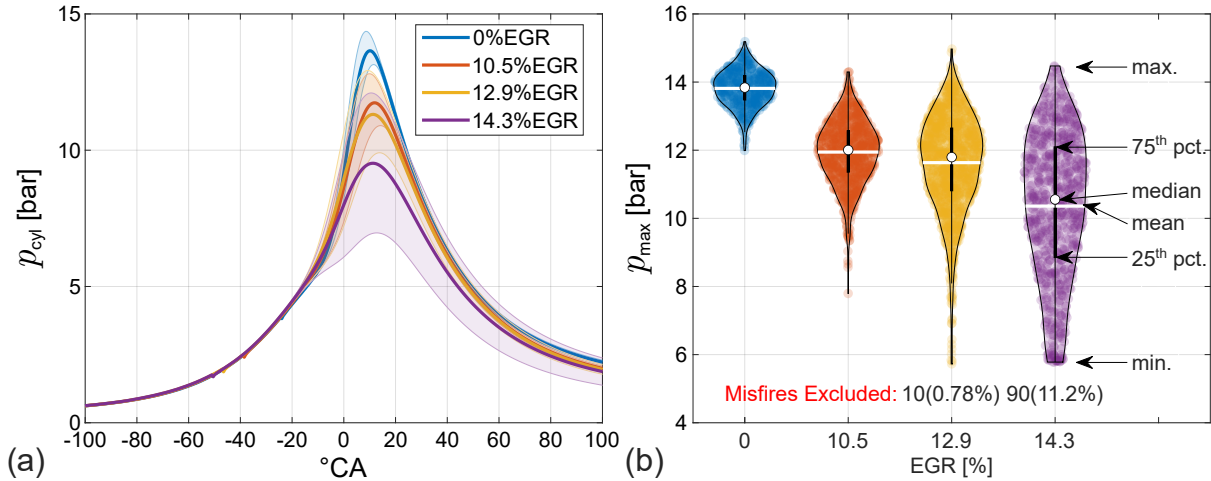


**Figure 5.1:** (a) In-cylinder pressure over crank-angle. Average and standard deviation  $p_{cyl}$  indicated by solid lines and shaded areas, respectively. (b) Violin plot of  $p_{max}$ . Adapted from [106].

be seen in the pressure curve by the slight dips due to electronic interference. More importantly, the pressure traces show that higher EGR and earlier spark timings result in lower  $p_{cyl}$  and higher standard deviation. To quantify the distribution of the cyclic maximum in-cylinder pressure  $p_{max}$ , Figure 5.1(b) displays violin plots showing the distribution and statistical parameters such as the mean (white line) and median (white circle) for each OC. As observed in the pressure traces, increasing EGR is associated with decreasing  $p_{max}$  and increasing cyclic instability. While the 0% EGR case has a tight, almost normal distribution, the 12.9% and 14.3% EGR cases have wide distributions with extremes exceeding the moderate 10.5% EGR case. Although misfire cycles, or cycles with a negative gross indicated mean effective pressure ( $IMEP_g$ ), were excluded from the violin plots, many extremely slow combustion cycles are observed in the highest EGR cases. In addition, the highest EGR cases indicate that some cycles combust extremely fast, a phenomenon that, although less common than extremely slow cycles, can occur when optimal conditions combine with early spark timing to produce a larger flame earlier in the compression phase.

Before further discussion of CCV, the velocity field at the ignition time of each OC must be characterized. Figure 5.2 shows the phase-averaged velocity fields over all cycles of each EGR condition (indicated in the upper right corner of each panel). It is important to characterize the flow fields at ignition because, on average, they are quite different and have distinct flow situations. The largest contrast is due to the late ignition timing of the 0% EGR case compared to the 14.3% EGR case. While the average flow field near the spark plug has a higher magnitude

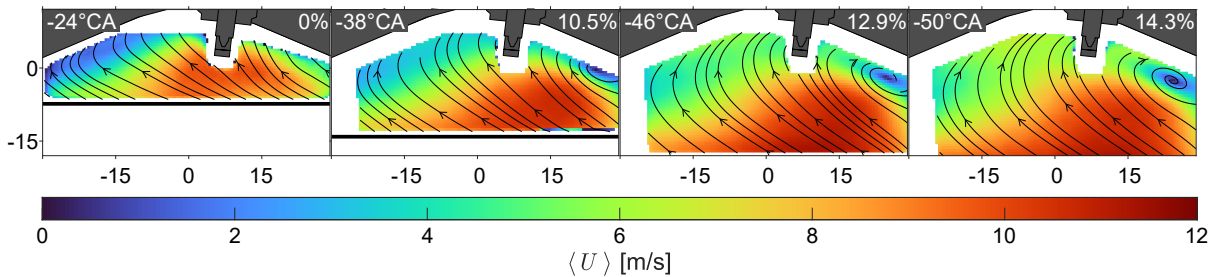


**Figure 5.2:** Phase-averaged velocity field at each OC's ignition timing. Adapted from [106].



and is directed toward the intake valves in the 0% EGR case, the high magnitude region near the piston surface is lower with respect to the spark plug in the 14.3% EGR case and there is a horizontal flow toward the exhaust valves. The influence of the different flow situations of the OCs and the cyclic variations of the velocity field near the spark plug on the combustion stability will be investigated in the next sections.

## 5.2 Evaluation of the Flow's Effects on Spark Behavior and Ignition

The majority of the content from this section was first published in **Paper IV** [105].

The first principle investigation of the EGR experiments focuses on the ignition process and its relationship to in-cylinder flows and the combustion development. A particularly interesting ignition phenomenon is spark re-ignition or RS, which occurs mainly when the plasma elongates due to the flow, effectively increasing the resistance between the electrodes, causing the discharge to reset to a path with less resistance. Thus, discharge RS is an event in which the velocity across the spark plug is high, a condition typically desired to accelerate combustion. However, while higher velocities can create more turbulence, which accelerates the flame propagation, they can also cause ignition difficulties due to blow-off or propagation to colder surfaces [69, 73]. Due to the strong cyclic variability and varying flow situations at ignition for the different EGR cases, RS is a parameter that can be easily identified within a cycle (by a sudden drop in the voltage trace) and studied on a statistical basis over all cycles.

Analysis of singular characteristic cycles with and without RS (referred to as non-RS) reveals different behavior for the two types of discharges: despite many peaks and sudden drops, RS has higher voltages on average over a shorter period of time, resulting in a faster and higher energy deposition (see Figure 3 of **Paper IV**). Figure 5.3(a) and (b) shows a portion of the voltage trace and corresponding plasma images illustrating RS events in the characteristic RS cycle of the 0% EGR case, where  $t$  represents the time after the start of the breakdown phase. Two events are highlighted in yellow and green in both the voltage trace and the instantaneous images. The first event, characterized by a drop of  $\approx 1$  kV, is visible in the image at  $t = 650 \mu\text{s}$ , where the relatively long camera exposure ( $\approx 50 \mu\text{s}$ ) captures the old (from  $t = 600 \mu\text{s}$ ) and the new length of the plasma channel. In contrast, the next RS event has a much larger voltage

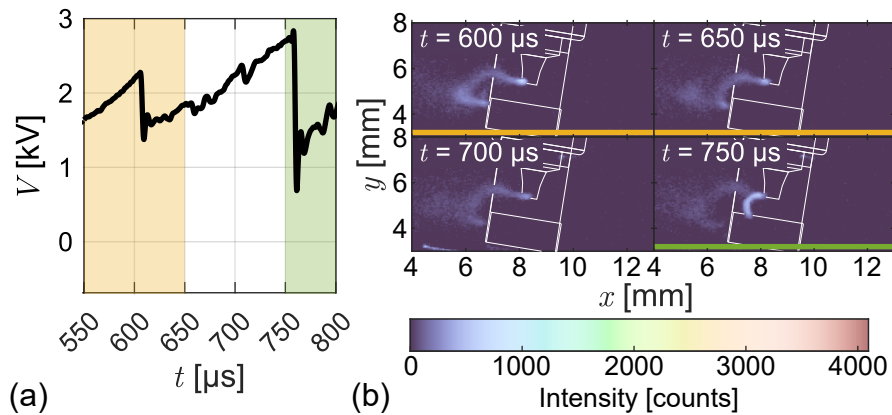


**Figure 5.3:** (a) Voltage trace from a 0% EGR cycle exemplifying restrike. (b) Plasma images corresponding to the voltage trace. Adapted from [105].

drop ( $\approx 2$  kV) and shows an almost complete reset of the plasma channel position at  $t = 750 \mu\text{s}$ . Examination of the entire voltage trace and corresponding plasma images for the RS cycles of both OCs (Figures 4 and 5 of **Paper IV**) shows that small voltage drops or seemingly noisy periods may actually correspond to physical events of RS or plasma displacement along the electrodes. Comparing the characteristic RS cycles of the 0% and 12.9% EGR cases, it is clear that the 0% case has more RS events and faster energy deposition, likely due to the higher velocity magnitudes at its ignition time (compare average flow fields in Figure 5.2). To confirm this hypothesis, the instantaneous velocity fields were compared (Figures 6 and 7 of **Paper IV**) and show a high velocity pocket toward the intake valves in the 0% case (more than twice the magnitude of that in the 12.9% case) and a rightward flow across the spark gap in the 12.9% case. Furthermore, along with plasma channel elongation in the direction of the flow near the spark plug, the flames propagate in the direction of the velocity field, with RS cycles showing larger flames. Although these results show correlations between the in-cylinder velocity near the spark plug and the subsequent ignition and flame growth, they only represent characteristic cycles. Therefore, statistics must be evaluated to confirm the phenomena for the whole.

To examine the spark behavior on a statistical level, all cycles were labeled as either non-RS or RS, with at least one clear RS event required for an RS designation. As shown in the characteristic cycle comparison, RS cycles have a higher average voltage with higher standard deviations over a shorter period of time, meaning they reach higher energy depositions faster. In addition, with the exception of the 0% EGR case, the flow fields at the time of ignition show different behavior between non-RS and RS cycles. Figure 5.4(a) shows an example of the different conditionally averaged velocity fields for the high 12.9% EGR case at its ignition time. Coincidentally, the averaged velocity fields match the general characteristics of the selected individual cycles for RS: for high EGR cases, RS cycles have a positive velocity magnitude across the spark gap and non-RS cycles have a more vertically oriented flow structure near the spark plug. Moreover, the average of the RS cycles shows a larger and wider tumble center just to the right of the spark plug, while the non-RS cycles have a more compact and rightward vortex centered almost outside of the field of view. Figure 5.4(b) shows a comparison of the PDF of the center positions of binarized plasma channels for non-RS and RS cycles of the 12.9% EGR case. The horizontal flow across the spark channel has a direct influence on the plasma elongation, as the RS spark cycles almost all have a right-skewed plasma distribution, while the non-RS cycles

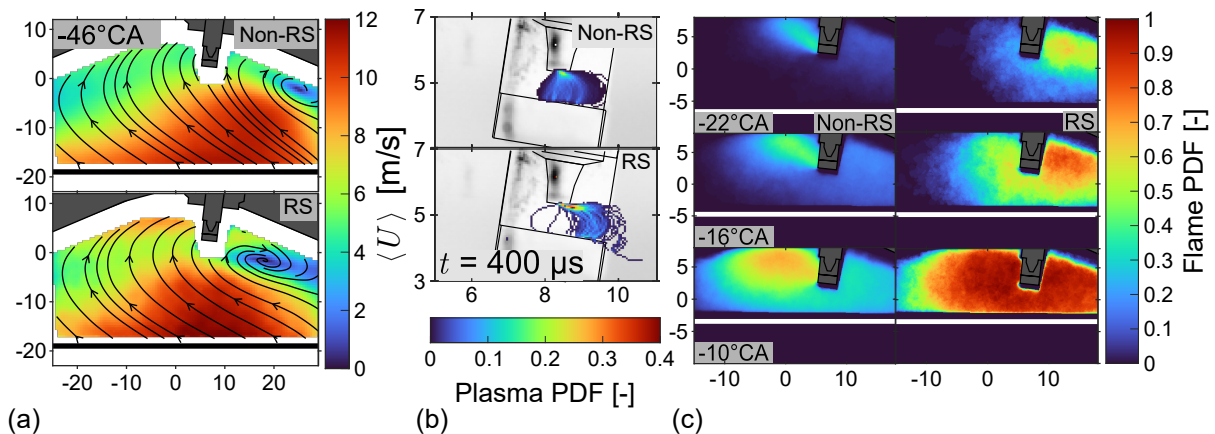


**Figure 5.4:** Conditional statistics comparison between all non-RS and all RS cycles of the 12.9% EGR case. (a) Velocity field comparison at ignition timing. (b) Spark plasma center PDF at  $t = 400 \mu\text{s}$  after ignition. (c) Extracted evolution of the flame PDF. Adapted from [105].

have a more uniform distribution, with a slight right-skewness. Similarly, the binarized flame PDFs (Figure 5.4(c)) of the RS cycles show a higher probability of flames initially propagating to the right. In addition, the planar flames are generally larger in RS, with most reaching nearly the full extent of the field of view by  $-10^\circ\text{CA}$ . A comparison of the conditional average early flame area and the spark energy (see Figure 13 of **Paper IV**) shows that the mean flame area of the RS cycles begins to exceed that of the non-RS cycles as soon as the mean energy traces also separate. This indicates that the greater and faster energy deposition associated with RS is related to larger early flame kernels, due in part to the larger volume in contact with fresh gases (longer plasma channel) and the greater flow magnitude supplying unburned gas to the spark gap where the RS ignites a new volume to join the existing flame. Instead of higher velocities causing ignition problems due to blow-off, the larger flow magnitudes across the spark gap induce RS events that are likely to produce larger, more corrugated flames. Finally, a comparison of the conditioned statistics of  $p_{\max}$  shows that in the higher EGR cases, RS is associated with greater stability (due to narrower distributions and fewer misfire cycles), while also leading to faster combustion (up to 25.6% greater median  $p_{\max}$  in the 14.3% EGR case). Therefore, in the presence of higher dilution, faster and more stable combustion can be achieved when there are larger horizontal velocity magnitudes across the spark gap, inducing faster energy deposition and flame growth.

### 5.3 The Impact of Flow on the Cause-and-Effect Chain

The majority of the content from this section was first published in **Paper V** [106].

Given the operating condition and ignition characterization provided in the previous sections, the final investigation of this thesis aims to use conditional and multivariate statistical techniques to analyze the influence of velocity on cyclic variations under the diluted conditions of EGR. When the cycles are separated in groups of the 10% lowest and highest  $p_{\max}$ , or low and high pressure combustion cycles (LC and HC, respectively), the conditioned flame PDFs (Figure 5.5(a)) show larger flames in the symmetry plane for HC, which is expected, but also more flame area to the right of the spark plug, especially in the high EGR cases, where more flames appear to the right than to the left at  $-18^\circ\text{CA}$  (see Figure 5 of **Paper V** for all OCs). Tracking the average centroid of the flame over crank-angles for the conditioned datasets Figure 5.5(b) shows that in the presence of EGR, the flame centroid either propagates first to the right or its centroid is further to the right for HC compared to LC (see Figure 6 of **Paper V** for all OCs). In addition, the mean velocity near the spark plug is typically greater for LC, and it points more toward the

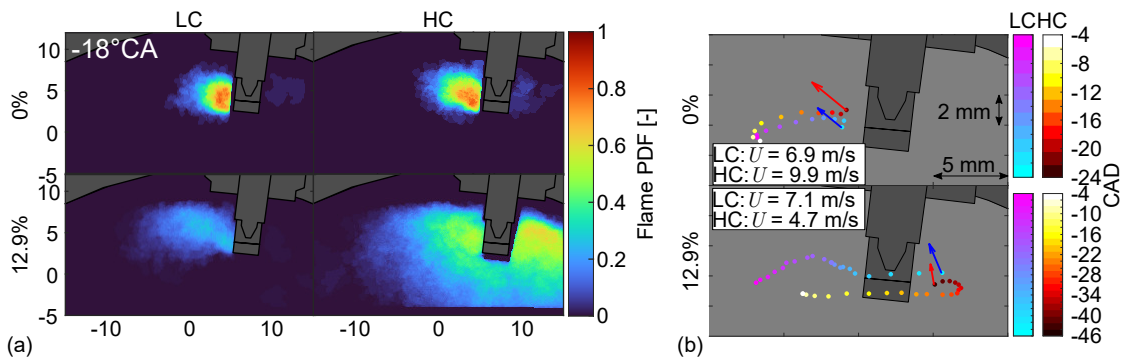


**Figure 5.5:** (a) Flame PDF at  $-18^\circ\text{CA}$  and (b) average centroid trajectory for the 0% and 12.9% EGR cases conditioned to the 10% lowest and highest pressure combustion cycles. Adapted from [106].

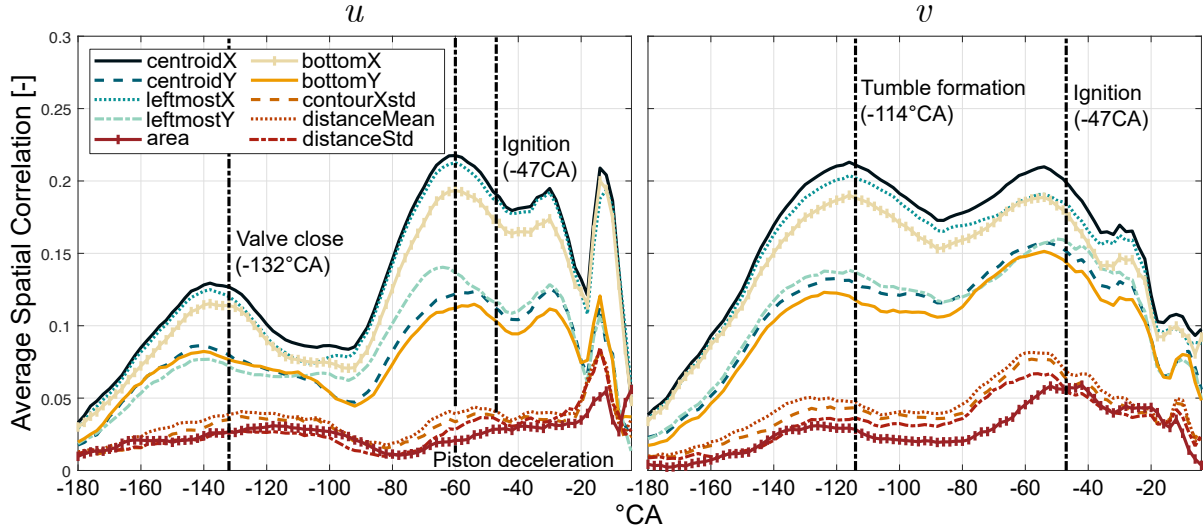


**Figure 5.6:** Average spatial correlation between  $u$  (left) and  $v$  (right) and 10 flame features for the 12.9% EGR case. Adapted from [106].

roof and the left than HC. These conditional statistics are consistent with those of the non-RS and RS sets presented in **Paper IV**, because for EGR, RS cycles were associated with higher  $p_{\max}$ .

The conditional statistics of HC agree well with those of RS; however, to develop a cause-and-effect chain model between flow and combustion, correlation analysis can be used to quantitatively examine the relationships between different variables. First, 10 flame features that were found to be important in predicting CCV in a previous work not included in this thesis were selected [94]. Next, each feature, which represents a cyclic quantity of the flame at each crank-angle, was used to calculate the Pearson correlation coefficient  $R$  with  $p_{\max}$ . The correlations showed that position-related features typically had the highest  $R$  near  $-30^\circ\text{CA}$ ,  $\approx 40$  to  $50^\circ\text{CA}$  before maximum pressure is reached, highlighting the importance of the direction of initiation of the early flame kernel on the overall combustion speed (see Figure 7 of **Paper V**). Then, using  $-30^\circ\text{CA}$  for the flame features, the correlation between the flame and velocity components  $u$  and  $v$  at each vector position was computed. Figure 5.6 shows the spatial average of  $R$  for each feature over all crank-angles for the 12.9% EGR case, which had the highest observed correlation values. By including the temporal dimension, this figure allows a broad comparison of the relationship between the velocity components, the flame features, and the repetitive events of the engine such as intake valve closing time, tumble center entering the field of view (tumble formation), start of the piston deceleration, and start of ignition. In both plots, the highest correlations occur with  $x$ -position-related flame features, with the highest occurring for the  $x$ -coordinate of the centroid (centroidX), indicating that both velocity components have a similar relationship with the horizontal position of the early flame. Such a spatial and spatio-temporal averaging of correlations is an alternative to expensive machine learning-based feature importance analysis, which requires even larger data sets for successful model training.

Due to its high correlations at  $-30^\circ\text{CA}$ , centroidX was selected for the conditional statistics, with the 50 lowest (left) and highest (right) centroidX cycles selected for variable separation. Figure 5.7(a) shows the conditionally averaged velocity fields at ignition for 12.9% EGR for low (blue outline) and high (red outline) centroidX cycles. The inclusion of flow fields highlighting the specific velocity components, especially  $u$ , accentuates the differences in velocities at ignition

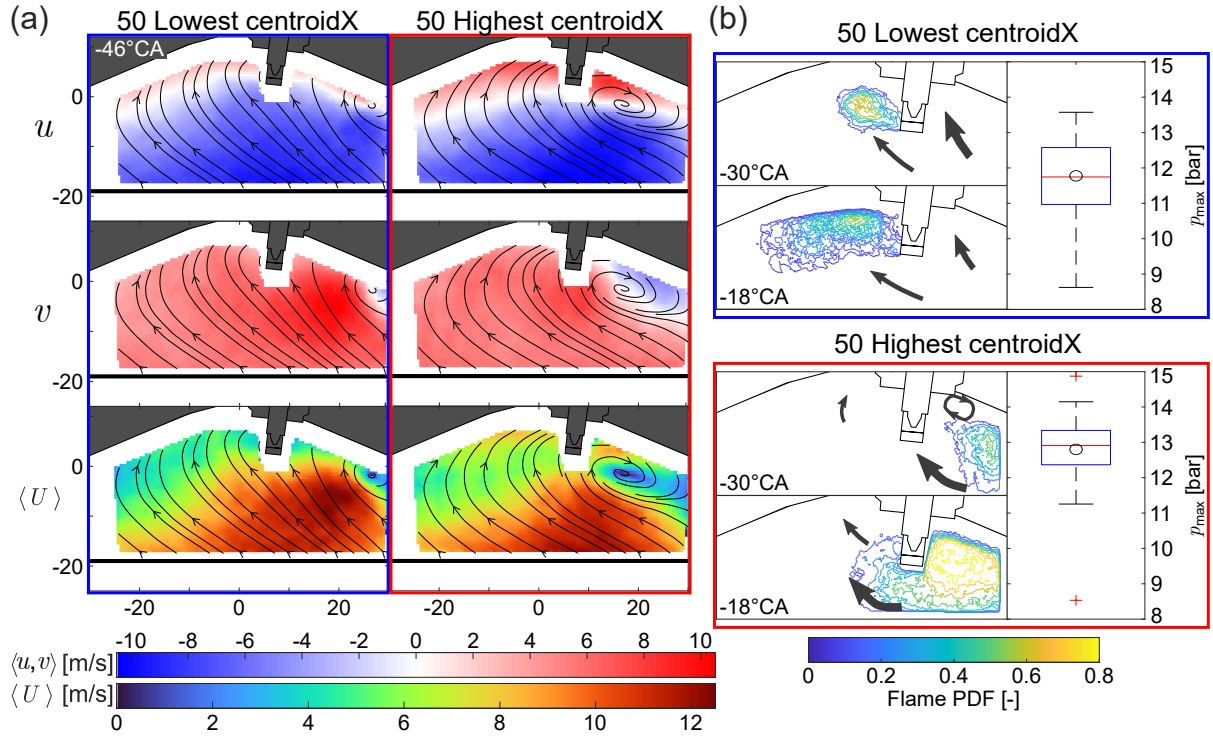


**Figure 5.7:** Flow-Flame CCV model. (a) Conditionally averaged velocity fields for the 50 lowest and highest centroidX cycles. (b) Conditioned flame PDFs box plots of  $p_{max}$ , and flow representation of the model. Adapted from [106].

that result in leftward or rightward early flames. As with the RS cycles examined in **Paper IV**, a strong horizontal velocity across the spark gap correlates with a rightward initial flame and is an expected result. Less anticipated, is the difference in  $p_{max}$  between the leftward and rightward flame sets. Figure 5.7(b) shows the conditioned flame PDFs and box plots of  $p_{max}$ . The low centroidX cycles have a broader distribution of  $p_{max}$ , with a median and mean  $\approx 1$  bar lower than that of the high centroidX set. Because of this difference in  $p_{max}$  for the conditioned sets, there is a correlation between rightward flames and faster combustion. Based on this finding and the velocity fields at  $-30$  and  $-18^\circ\text{CA}$  (not shown), a flow-flame CCV model is proposed and aided by the gray arrows in Figure 5.7(b): positive horizontal velocities and a large lingering tumble center promote rightward flame propagation and growth away from the cylinder roof, where flames can grow large before then spreading to the left side of the cylinder. This model can be linked to the behavior of spark RS cycles, as RS is more likely to occur with higher horizontal velocities across the spark gap. Conversely, strong leftward flows directed toward the bottom of the spark plug influence the flame to initiate and grow toward the roof in the center of the cylinder where wall temperatures are comparatively low, inhibiting flame growth and eventually spreading from the intake valve area to the rest of the cylinder.

While the centroidX flow-flame CCV model provides insight into the causes of CCV when the flame propagates in either direction, it is limited because the conditioned statistics are not based on a CCV quantity such as  $p_{max}$ . Therefore, Figure 5.8 provides a model based on the conditioned statistics of the 90 misfire and 90 highest  $p_{max}$  cycles for the 14.3% EGR case for a true measure of CCV. Figure 5.8(a) shows the conditionally averaged velocity fields from the end of intake to ignition. At  $-180^\circ\text{CA}$ , differences between the conditioned sets are already visible in the higher magnitude recirculation for the misfire cycles in the lower left corner of the field of view. This



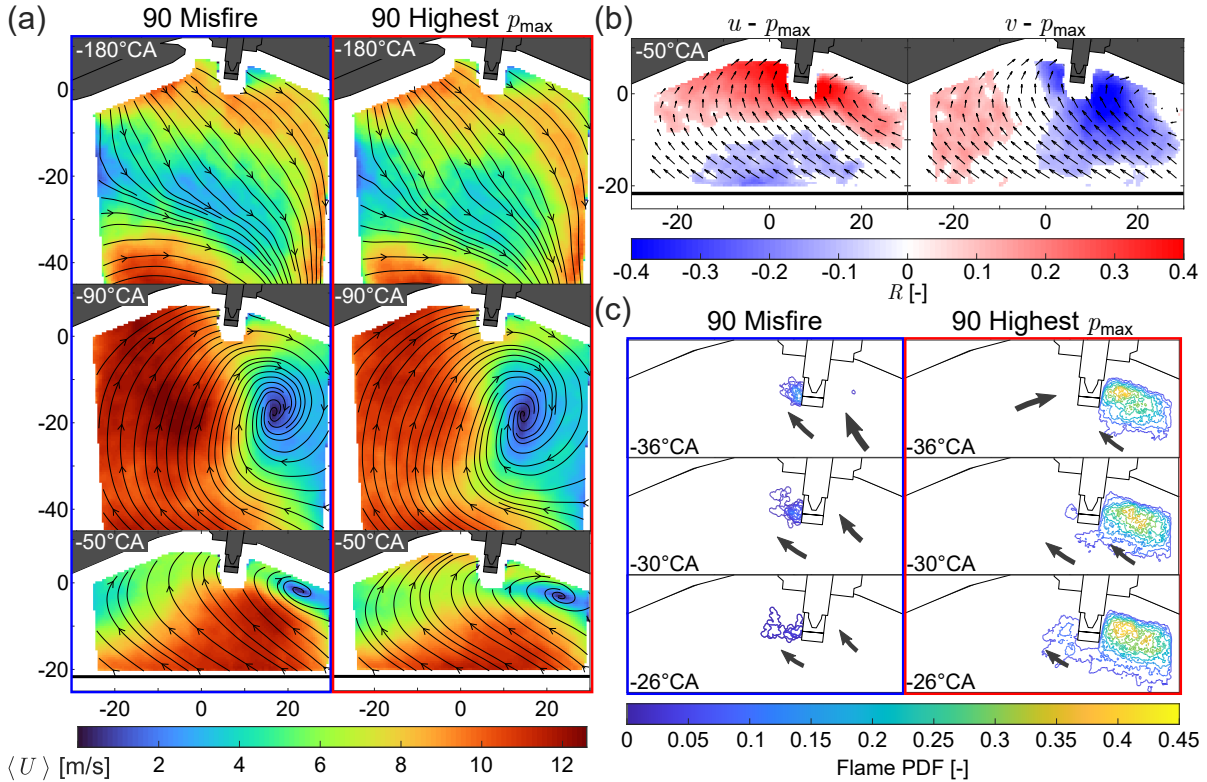


**Figure 5.8:** Misfire CCV model. (a) conditionally averaged velocity fields of the 90 misfire and 90 highest  $p_{max}$  cycles of the 14.3% EGR case. (b) Correlation field between  $u$  and  $v$  and  $p_{max}$ . (c) Conditioned flame PDFs and flow representation of the model. Adapted from [106].

indicates that already during the intake phase, the structure of the intake flow, in this case higher velocities inducing higher magnitude tumble recirculation, can be traced back to the combustion performance. During compression, the misfire cycles continue to show larger magnitudes in the tumble development, forming a more compact tumble center. As a result, at ignition, the misfire cycles have a larger magnitude flow structure impinging on the bottom of the spark plug, while the high  $p_{max}$  cycles have a larger horizontal velocity across the spark gap, similar to the high centroidX cycles. While the conditioned flow fields are useful for studying the flow fields that lead to CCV, the relationship between the flow structures and CCV can be quantified using direct linear correlations. Figure 5.8(b) shows the correlation between the  $u$  and  $v$  velocity components and  $p_{max}$  at each vector position. The correlation map provides a visualization of the mean flow direction (arrows) and its relationship with  $p_{max}$  or CCV: the sign of the correlation and the direction of the corresponding vector indicate the physical meaning of the relationship. The left panel of Figure 5.8(b) shows a positive correlation along the cylinder roof and the tumble center, with the highest correlations directly near the spark plug, indicating that higher horizontal flows near the spark plug are correlated with higher  $p_{max}$  (the reverse is also true). In addition, there is a negative relationship along the piston surface where flows are predominantly directed toward the intake valves, indicating that larger flows to the left (negative  $u$ ) are correlated with higher  $p_{max}$ . On the right panel, the correlations of  $v$  and  $p_{max}$  are mostly negative, while the mean  $v$  is typically positive (pointing toward the roof), indicating that higher vertical velocities near the spark plug correlate with slower combustion. The behavior of the correlation fields is consistent with the conditioned velocity fields of Figure 5.8(a); therefore, the final step in generating a CCV model for this condition is to examine the conditioned flame PDFs for the same misfire

and high  $p_{\max}$  sets and summarize the flow behavior causing the phenomena. Figure 5.8(c) shows the conditioned PDFs and representations of the bulk flow structure (gray arrows). Due to the large upward velocity directed toward the bottom of the spark plug, the early flame of misfire cycles cannot grow away from the colder surfaces of the spark plug and the cylinder roof, and they either quench or blow off. However, high  $p_{\max}$  cycles have a similar mechanism to high centroidX cycles: horizontal flow across the spark plug promotes rightward early flame propagation and growth away from the walls within the tumble vortex. In both CCV models, higher velocities near the spark plug are not always ideal: only the horizontal velocity across the spark plug induces faster combustion in the presence of high dilution, while strong vertical velocities can cause difficulties in the early stages of flame growth.

## 5.4 Summary

In this chapter, a comprehensive investigation of the influence of in-cylinder flows on ICE combustion and CCV was presented. By operating the engine with externally controlled EGR dilution, the flame speed was reduced and the effect of the flow on the combustion process was enhanced. In addition, further control of the gas composition through homogeneous port fuel injection and skip-fire ignition provided a reduction in complexity by eliminating the influence of the local mixture fraction on the flame speed. With a reduced number of variables, the first paper highlighted in this chapter, **Paper IV**, investigated the effects of flow on the ignition process. In particular, RS events, including their causes and effects, were extensively studied. The second study, **Paper V**, used advanced multivariate and conditioned statistics to develop flow-flame and CCV models for the high EGR cases.

Based on the analysis in the two papers in this chapter, generalizations can be made about the role of flow on CCV. At higher dilution conditions, larger velocity magnitudes are required to ignite, sustain, and accelerate flame growth. In particular, at the time of ignition of the high EGR cases, where the tumble center position and the overall velocity field are more variable, positive horizontal velocities across the spark plug are associated with faster and more stable combustion. The flow across the spark plug gap enhances plasma elongation, inducing more RS events that deposit energy faster and in more locations than normal, non-RS cycles. Due to the RS and flow direction, flames grow faster to the right of the spark plug within a lingering tumble center before spreading to the left and the rest of the cylinder. Conversely, if there is not a strong rightward velocity near the spark plug, the bulk velocity will continue to develop vertically against the bottom of the spark plug, causing the spark and early flame to favor the left side. When this happens, the flame grows slower, even though it initiates in the center of the cylinder, due to the influence of the flow on the flame toward the cylinder roof, which has comparatively colder temperatures. In addition, if the upward velocity near the spark plug is too great, the flame may be blown out or extinguished at the cylinder roof, causing misfire.

The general mechanisms linking flow to spark and flame initiation, such as the direction and magnitude of the velocity near the spark plug at ignition, can be applied to other engine OCs and configurations. However, it is unclear whether the specific direction of the flow, that is, positive velocity across the spark gap, has the same effect on different engines and OCs. For example, under OC C (0.95 bar intake pressure and 1500 rpm engine speed), the horizontal position of the early flame [94] and the horizontal velocity near the spark plug at ignition [95] are critical in determining CCV. Nevertheless, the methodology of simultaneous flow, flame, and spark measurements should be applied to other OCs, such as hydrogen-fueled operation, or to other engine configurations to confirm the universality of the mechanisms causing CCV.





# 6 Summary and Outlook

## 6.1 Summary

This cumulative dissertation studies the influence of in-cylinder flows on internal combustion engine processes by considering separate, fundamental experimental investigations before a comprehensive examination of fired operation and cyclic variability. Each successive investigation builds upon the previous in complexity to analyze first the fundamental process of intake flows, then the interaction between the flow and direct injection sprays, and finally the influence of in-cylinder flows on combustion stability. High-speed particle image velocimetry was used in each study to provide high spatial and temporal resolution velocity fields over a large number of cycles, allowing the use of existing and new statistical analysis techniques. In addition to PIV, other measurement methods such as engine indication data acquisition, volumetric or planar Mie scattering, spark energy, or spark plasma imaging were used to link the deterministic nature of in-cylinder flows to each engine phenomenon. Finally, the acquisition of large, high-quality data sets accompanying this thesis provides data for model and simulation validation.

The first investigation of this thesis focused on the turbulent intake flows of the engine using a flow bench test stand. The flow bench was designed to simulate the intake velocity of the standard OC A of the Darmstadt engine and was used to study the intake jet and turbulent phenomena such as jet flapping. The fidelity of the operating conditions of the flow bench compared to the engine was verified by analyzing the velocity fields in the symmetry and valve planes. Subsequent evaluation of the jet turbulence revealed coherent flapping at 752.5 Hz, which is within the estimated range of the valve stem vortex shedding frequency, indicating a possible link between jet flapping and vortex shedding that survives the valve gap acceleration. In addition, the flow bench provided a useful test case for studying direct injection, both for characterizing the spray morphology with parametric variations of the flow bench mass flow rate, and as a comparison with sprays in the motored engine. The next complete study was on the intake flow of the motored engine, due to the observation of an instability in the velocity profiles. Symmetry and valve plane PIV was used to evaluate the effects of backflow-induced high-frequency intake pressure oscillations on the resulting in-cylinder flow. Similar to the flow bench, the phase-averaged intake jet velocity fields exhibit coherent flapping, which occurs in the part-load condition. The results of both studies demonstrate the need for consideration of full-scale geometry modeling and the effects of acoustics since in-cylinder flows are sensitive to seemingly minor oscillations. Following the characterization of the flow bench and motored engine intake flows, the next comprehensive study focused on the application of direct injection and the spray-flow interaction. Using a short-duration, high-pressure, multi-hole spray-guided injector, an increase of turbulence due to spray was not observed, possibly due to the duration and limited field of view. However, the influence of flow on spray morphology was significant, with the highest prominence observed when comparing the no-flow (flow bench) case to the high engine speed case.

The principle flow characterization of the first part of the thesis was then applied to a comprehensive experimental investigation to study the influence of in-cylinder flows of a part-load condition with strong EGR dilution on combustion CCV. The significance of the effect of in-cylinder ve-

locity variations on combustion CCV increases with increasing EGR due to decreasing flame speed. Therefore, simultaneous flow, flame, and spark data were collected over a large number of cycles to investigate the interplay between velocity near the spark plug, ignition, and the flame growth. In general, higher EGR dilution requires higher velocities to ignite, sustain, and accelerate flame growth. Specifically, high horizontal velocities across the spark gap promote faster, more stable combustion. The resulting analysis of high EGR conditions points to a number of reasons for this: Strong flows across the spark enhance plasma channel elongation causing more RS events, accelerating energy deposition, and distributing it over a larger volume. Furthermore, cross-flows to the exhaust side are typically associated with a larger lingering tumble center just to the right of the spark plug, where the newly initiated flame can grow and accelerate away from the relatively cold cylinder roof due to the vortex motion, before rapidly spreading to the rest of the cylinder. On the other hand, the absence of strong horizontal flows across the spark gap is typically associated with stronger vertical flows toward the bottom of the ground electrode and the cylinder roof. Such vertical flows are associated with fewer RS events and consequently slower energy deposition. In addition, this flow mode exhibits flame convection and propagation that either remains close to the spark plug or moves toward the cylinder roof, ultimately inhibiting growth or causing misfire. Therefore, given the dilute operating conditions of this engine setup, high velocities across the spark gap to the exhaust side are required to ensure a higher probability of faster, more stable combustion.

## 6.2 Outlook

The analysis in Chapter 4 can be transferred to different engine configurations and liquid fuels to some degree. In addition, many of the mechanisms causing CCV discussed in Chapter 5, such as the influence of flow on the direction of the initial flame propagation, may also be applied in other engines. However, further research is needed to confirm the universality of these phenomena. Similar experiments could be performed in different engines to compare the mechanisms for CCV and misfire. Although other engines have been used to study similar phenomena, critical aspects, such as the use of a stratified injection strategy, usually make the process too different for comparison. Therefore, research on engine CCV would benefit not only from a larger database of similar experiments in other engines, but also from the use of similar analysis techniques. In addition, the large data sets developed in this thesis can be used as validation data for further CFD simulations that can investigate 3D or other difficult-to-measure quantities and phenomena. Finally, the tools gained from the experiments and simulations can be used to strategically design, for example, the intake port geometry, to enhance horizontal flows across the spark gap, allowing for greater stability with diluted mixtures.

Probably more important for future research would be to use the measurement, processing, and analysis techniques used in this thesis to investigate CCV with hydrogen fuel as a clean alternative to conventional carbon-based fuels. One of the major technical challenges of using lean hydrogen mixtures in ICEs is combustion stability. Therefore, several experimental investigations may be conducted to fill the large knowledge gap on this topic. Simultaneous flame, flow, and spark measurements can be used to study the CCV of lean homogeneous hydrogen-air mixtures with different equivalence ratios and EGR levels due to the added complexity and relative unknown nature of the influence of thermodynamic and hydrodynamic instabilities on the CCV of hydrogen-fueled engines. In addition to the conventional spark plug and coil used in this work, different ignition strategies, such as laser ignition to reduce obstruction and reflection where the early flame kernel develops, or different spark plug designs, should be employed.

Further studies can add the complexity of direct hydrogen injection and investigate the effects of mixture fraction on combustion development. Finally, the newly acquired data on hydrogen-fueled combustion can be used to develop future numerical models and to optimize the design of new engines. Despite the use of new technologies and different fuels, as long as combustion is used for propulsion in future engines, in-cylinder flow will remain a critical aspect of engine efficiency and durability.



# Bibliography

- [1] Karina von Schuckmann, Lijing Cheng, Matthew D. Palmer, James Hansen, Caterina Tassone, Valentin Aich, Susheel Adusumilli, Hugo Beltrami, Tim Boyer, Francisco José Cuesta-Valero, Damien Desbruyères, Catia Domingues, Almudena García-García, Pierre Gentine, John Gilson, Maximilian Gorfer, Leopold Haimberger, Masayoshi Ishii, Gregory C. Johnson, Rachel Killick, Brian A. King, Gottfried Kirchengast, Nicolas Kolodziejczyk, John Lyman, Ben Marzeion, Michael Mayer, Maeva Monier, Didier Paolo Monselesan, Sarah Purkey, Dean Roemmich, Axel Schweiger, Sonia I. Seneviratne, Andrew Shepherd, Donald A. Slater, Andrea K. Steiner, Fiammetta Straneo, Mary-Louise Timmermans, and Susan E. Wijffels. Heat stored in the earth system: where does the energy go? *Earth System Science Data*, 12(3):2013–2041, 2020.
- [2] NOAA National Centers for Environmental Information. State of the climate: Global climate report for annual 2021, 2022.
- [3] European Commission, Joint Research Centre. Global energy and climate outlook 2022: Energy trade in a decarbonised world: Dataset, 2022.
- [4] IEA. Global co2 emissions from transport by subsector, 2000-2030.
- [5] United Nations Framework Convention on Climate Change. What is the paris agreement?, 2023.
- [6] Gregor Erbach. Co2 emission standards for new cars and vans: 'fit for 55' package, 2022.
- [7] European Union. Euro 7 standards: new rules for vehicle emissions, 2022.
- [8] U.S. Energy Information Administration. Annual energy outlook 2021, 2021.
- [9] Jie Deng, Chulheung Bae, Adam Denlinger, and Theodore Miller. Electric vehicles batteries: Requirements and challenges. *Joule*, 4(3):511–515, 2020.
- [10] European Environment Agency. *Europe's air quality status 2021*. Publications Office, 2022.
- [11] John B. Heywood. *Internal combustion engine fundamentals*. McGraw-Hill Education, New York, second edition, 2018.
- [12] P. V. Farrell. Examples of in-cylinder velocity measurements for internal combustion engines. *Proceedings of the Institution of Mechanical Engineers, Part D: Journal of Automobile Engineering*, 221(6):675–697, 2007.
- [13] Paul C. Miles. The history and evolution of optically accessible research engines and their impact on our understanding of engine combustion. In *Proceedings of the ASME Internal Combustion Engine Division Fall Technical Conference 2014*, New York, 2014. ASME.
- [14] Rodney B. Rask. Laser doppler anemometer measurements in an internal combustion engine. *SAE Technical Paper 790094*, 1979.
- [15] T. Asanuma and T. Obokata. Gas velocity measurements of a motored and firing engine by laser anemometry. *SAE Technical Paper 790096*, 1979.
- [16] David L. Reuss, Ronald J. Adrian, Christopher C. Landreth, Donald T. French, and Todd D. Fansler. Instantaneous planar measurements of velocity and large-scale vorticity and strain rate in an engine using particle-image velocimetry. *SAE Technical Paper 890616*, 1989.
- [17] Mark Reeves. Full-field ic engine flow measurement using particle image velocimetry. *Optical Engineering*, 35(2):579, 1996.

- [18] D. P. Towers and C. E. Towers. Cyclic variability measurements of in-cylinder engine flows using high-speed particle image velocimetry. *Measurement Science and Technology*, 15(9):1917–1925, 2004.
- [19] J. B. Ghandhi, R. E. Herold, J. S. Shakal, and T. E. Strand. Time resolved particle image velocimetry measurements in an internal combustion engine. *SAE Technical Paper 2005-01-3868*, 2005.
- [20] B. Peterson and V. Sick. Simultaneous flow field and fuel concentration imaging at 4.8 khz in an operating engine. *Applied Physics B*, 97(4):887–895, 2009.
- [21] E. Baum, B. Peterson, B. Böhm, and A. Dreizler. On the validation of les applied to internal combustion engine flows: Part 1: Comprehensive experimental database. *Flow, Turbulence and Combustion*, 92(1-2):269–297, 2014.
- [22] Marco Braun, Wolfgang Schröder, and Michael Klaas. High-speed tomographic piv measurements in a disi engine. *Experiments in Fluids*, 60(9), 2019.
- [23] J. Bode, J. Schorr, C. Krüger, A. Dreizler, and B. Böhm. Influence of three-dimensional in-cylinder flows on cycle-to-cycle variations in a fired stratified disi engine measured by time-resolved dual-plane piv. *Proceedings of the Combustion Institute*, 36(3):3477–3485, 2017.
- [24] J. Bode, J. Schorr, C. Krüger, A. Dreizler, and B. Böhm. Influence of the in-cylinder flow on cycle-to-cycle variations in lean combustion disi engines measured by high-speed scanning-piv. *Proceedings of the Combustion Institute*, 37(4):4929–4936, 2019.
- [25] Christopher Jainski, Louise Lu, Andreas Dreizler, and Volker Sick. High-speed micro particle image velocimetry studies of boundary-layer flows in a direct-injection engine. *International Journal of Engine Research*, 14(3):247–259, 2013.
- [26] A. Renaud, C.-P. Ding, S. Jakirlic, A. Dreizler, and B. Böhm. Experimental characterization of the velocity boundary layer in a motored ic engine. *International Journal of Heat and Fluid Flow*, 71:366–377, 2018.
- [27] Marius Schmidt, Carl-Philipp Ding, Brian Peterson, Andreas Dreizler, and Benjamin Böhm. Near-wall flame and flow measurements in an optically accessible si engine. *Flow, Turbulence and Combustion*, 106(2):597–611, 2021.
- [28] M. Schmidt, C. Welch, L. Illmann, A. Dreizler, and B. Böhm. High-speed measurements and conditional analysis of boundary-layer flows at engine speeds up to 2500 rpm in a motored ic engine. *Proceedings of the Combustion Institute*, 39(4):4841–4850, 2023.
- [29] U. Dierksheide, P. Meyer, T. Hovestadt, and W. Hentschel. Endoscopic 2d particle image velocimetry (piv) flow field measurements in ic engines. *Experiments in Fluids*, 33(6):794–800, 2002.
- [30] Christian Fach, Nico Rödel, Jürgen Schorr, Christian Krüger, Andreas Dreizler, and Benjamin Böhm. Multi-parameter imaging of in-cylinder processes during transient engine operation for the investigation of soot formation. *International Journal of Engine Research*, 23(9):1573–1585, 2022.
- [31] Christian Fach, Nico Rödel, Jürgen Schorr, Christian Krüger, Andreas Dreizler, and Benjamin Böhm. Investigation of in-cylinder soot formation in a disi engine during transient operation by simultaneous endoscopic piv and flame imaging. *International Journal of Engine Research*, 24(3):1175–1189, 2023.
- [32] Daniel Freudenhammer, Elias Baum, Brian Peterson, Benjamin Böhm, Bernd Jung, and Sven Grundmann. Volumetric intake flow measurements of an ic engine using magnetic resonance velocimetry. *Experiments in Fluids*, 55(5):269, 2014.
- [33] Daniel Freudenhammer, Brian Peterson, Carl-Philipp Ding, Benjamin Boehm, and Sven Grundmann. The influence of cylinder head geometry variations on the volumetric intake flow captured by magnetic resonance velocimetry. *SAE International Journal of Engines*, 8(4):1826–1836, 2015.
- [34] Kaushal Nishad, Florian Ries, Yongxiang Li, and Amsini Sadiki. Numerical investigation of flow through a valve during charge intake in a disi -engine using large eddy simulation. *Energies*, 12(13):2620, 2019.
- [35] Hao Chen and Volker Sick. Three-dimensional three-component air flow visualization in a steady-state engine flow bench using a plenoptic camera. *SAE International Journal of Engines*, 10(2):625–635, 2017.

- 
- [36] Tobias Falkenstein, Mathis Bode, Seongwon Kang, Heinz Pitsch, Toshiyuki Arima, and Hiroyoshi Taniguchi. Large-eddy simulation study on unsteady effects in a statistically stationary si engine port flow. *SAE Technical Paper 2015-01-0373*, 2015.
- [37] Tobias Falkenstein, Seongwon Kang, Marco Davidovic, Mathis Bode, Heinz Pitsch, Toshihiro Kamatsuchi, Junji Nagao, and Toshiyuki Arima. Les of internal combustion engine flows using cartesian overset grids. *Oil & Gas Sciences and Technology – Revue d’IFP Energies nouvelles*, 72(6):36, 2017.
- [38] Frank Hartmann, Stefan Buhl, Florian Gleiss, Philipp Barth, Martin Schild, Sebastian A. Kaiser, and Christian Hasse. Spatially resolved experimental and numerical investigation of the flow through the intake port of an internal combustion engine. *Oil & Gas Science and Technology – Revue d’IFP Energies nouvelles*, 71(1):2, 2016.
- [39] Stefan Buhl, Frank Hartmann, Sebastian A. Kaiser, and Christian Hasse. Investigation of an ic engine intake flow based on highly resolved les and piv. *Oil & Gas Science and Technology – Revue d’IFP Energies nouvelles*, 72(3):15, 2017.
- [40] M. El-Adawy, M. R. Heikal, A. Rashid A. Aziz, M. I. Siddiqui, and Hasanain A. Abdul Wahhab. Experimental study on an ic engine in-cylinder flow using different steady-state flow benches. *Alexandria Engineering Journal*, 56(4):727–736, 2017.
- [41] Daming Liu, Tianyou Wang, Ming Jia, Wei Li, Zhen Lu, and Xudong Zhen. Investigation of the boundary layer flow under engine-like conditions using particle image velocimetry. *Journal of Engineering for Gas Turbines and Power*, 141(8), 2019.
- [42] Tobias Falkenstein, Marco Davidovic, Hongchao Chu, Mathis Bode, Seongwon Kang, Heinz Pitsch, Kei Murayama, and Hiroyoshi Taniguchi. Experiments and large-eddy simulation for a flowbench configuration of the darmstadt optical engine geometry. *SAE International Journal of Engines*, 13(4), 2020.
- [43] Marc Haussmann, Florian Ries, Jonathan B. Jeppener-Haltenhoff, Yongxiang Li, Marius Schmidt, Cooper Welch, Lars Illmann, Benjamin Böhm, Hermann Nirschl, Mathias J. Krause, and Amsini Sadiki. Evaluation of a near-wall-modeled large eddy lattice boltzmann method for the analysis of complex flows relevant to ic engines. *Computation*, 8(2):43, 2020.
- [44] Ji Hye Hyun and In Yong Ohm. The distribution according to the intake valve angle in steady flow of the pent-roof si engine. *International Journal of Automotive Technology*, 22(4):1003–1010, 2021.
- [45] B. Peterson and V. Sick. High-speed flow and fuel imaging study of available spark energy in a spray-guided direct-injection engine and implications on misfires. *International Journal of Engine Research*, 11(5):313–329, 2010.
- [46] Brian Peterson, David L. Reuss, and Volker Sick. On the ignition and flame development in a spray-guided direct-injection spark-ignition engine. *Combustion and Flame*, 161(1):240–255, 2014.
- [47] R. Stiehl, J. Schorr, C. Krüger, A. Dreizler, and B. Böhm. In-cylinder flow and fuel spray interactions in a stratified spray-guided gasoline engine investigated by high-speed laser imaging techniques. *Flow, Turbulence and Combustion*, 91(3):431–450, 2013.
- [48] B. Peterson, E. Baum, C.-P. Ding, D. Michaelis, A. Dreizler, and B. Böhm. Assessment and application of tomographic piv for the spray-induced flow in an ic engine. *Proceedings of the Combustion Institute*, 36(3):3467–3475, 2017.
- [49] H. Hill, C.-P. Ding, E. Baum, B. Böhm, A. Dreizler, and B. Peterson. An application of tomographic piv to investigate the spray-induced turbulence in a direct-injection engine. *International Journal of Multiphase Flow*, 121:103116, 2019.
- [50] Judith Laichter and Sebastian A. Kaiser. Optical investigation of the influence of in-cylinder flow and mixture inhomogeneity on cyclic variability in a direct-injection spark ignition engine. *Flow, Turbulence and Combustion*, 110(1):171–183, 2023.
- [51] John B. Heywood. *Internal Combustion Engine Fundamentals*. McGraw-Hill, New York, 1988.
- [52] Engine Combustion Network. Gasoline spray combustion, 2015.

- [53] Julien Manin, Yongjin Jung, Scott A. Skeen, Lyle M. Pickett, Scott E. Parrish, and Lee Markle. Experimental characterization of di gasoline injection processes. *SAE Technical Paper 2015-01-1894*, 2015.
- [54] Raul Payri, Francisco Javier Salvador, Pedro Martí-Aldaraví, and Daniel Vaquerizo. Ecn spray g external spray visualization and spray collapse description through penetration and morphology analysis. *Applied Thermal Engineering*, 112:304–316, 2017.
- [55] J. Lacey, F. Poursadegh, M. J. Brear, R. Gordon, P. Petersen, C. Lakey, B. Butcher, and S. Ryan. Generalizing the behavior of flash-boiling, plume interaction and spray collapse for multi-hole, direct injection. *Fuel*, 200:345–356, 2017.
- [56] Alessandro Montanaro, Luigi Allocca, and Maurizio Lazzaro. Iso-octane spray from a gdi multi-hole injector under non- and flash boiling conditions. *SAE Technical Paper 2017-01-2319*, 2017.
- [57] Panos Sphicas, Lyle M. Pickett, Scott A. Skeen, and Jonathan H. Frank. Inter-plume aerodynamics for gasoline spray collapse. *International Journal of Engine Research*, 19(10):1048–1067, 2018.
- [58] Davide Paredi, Tommaso Lucchini, Gianluca D’Errico, Angelo Onorati, Alessandro Montanaro, Luigi Allocca, and Roberto Ianniello. Combined experimental and numerical investigation of the ecn spray g under different engine-like conditions. *SAE Technical Paper 2018-01-0281*, 2018.
- [59] Davide Paredi, Tommaso Lucchini, Gianluca D’Errico, Angelo Onorati, Lyle Pickett, and Joshua Lacey. Validation of a comprehensive computational fluid dynamics methodology to predict the direct injection process of gasoline sprays using spray g experimental data. *International Journal of Engine Research*, 21(1):199–216, 2020.
- [60] Luis Gutierrez, Andrew B. Mansfield, Mohammad Fatouraie, Dimitris Assanis, Ripudaman Singh, Joshua Lacey, Michael Brear, and Margaret Wooldridge. Effects of engine speed on spray behaviors of the engine combustion network “spray g” gasoline injector. *SAE Technical Paper 2018-01-0305*, 2018.
- [61] Andrea Pati, Davide Paredi, Tommaso Lucchini, and Christian Hasse. Cfd modeling of gas-fuel interaction and mixture formation in a gasoline direct-injection engine coupled with the ecn spray g injector. *SAE Technical Paper 2020-01-0327*, 2020.
- [62] Christopher Geschwindner, Patrick Kranz, Cooper Welch, Marius Schmidt, Benjamin Böhm, Sebastian A. Kaiser, and Joaquin de La Morena. Analysis of the interaction of spray g and in-cylinder flow in two optical engines for late gasoline direct injection. *International Journal of Engine Research*, 21(1):169–184, 2020.
- [63] Andrea Pati, Davide Paredi, Cooper Welch, Marius Schmidt, Christopher Geschwindner, Benjamin Böhm, Tommaso Lucchini, Gianluca D’Errico, and Christian Hasse. Numerical and experimental investigations of the early injection process of spray g in a constant volume chamber and an optically accessible disi engine. *International Journal of Engine Research*, 23(12):2073–2093, 2022.
- [64] Rudolf Maly and Manfred Vogel. Initiation and propagation of flame fronts in lean ch4-air mixtures by the three modes of the ignition spark. *Symposium (International) on Combustion*, 17(1):821–831, 1979.
- [65] Taisuke Shiraishi, Atsushi Teraji, and Yasuo Moriyoshi. The effects of ignition environment and discharge waveform characteristics on spark channel formation and relationship between the discharge parameters and the egr combustion limit. *SAE International Journal of Engines*, 9(1):171–178, 2016.
- [66] Xiao Yu, Zhenyi Yang, Shui Yu, Mark Ives, and Ming Zheng. Discharge characteristics of current boosted spark events under flow conditions. In *Proceedings of the ASME Internal Combustion Engine Division Fall Technical Conference 2017*, New York, N.Y., 2017. American Society of Mechanical Engineering.
- [67] Xiaofeng Yang, Tang-Wei Kuo, Orgun Guralp, Ronald O. Grover, and Paul Najt. In-cylinder flow correlations between steady flow bench and motored engine using computational fluid dynamics. *Journal of Engineering for Gas Turbines and Power*, 139(7), 2017.
- [68] Zhenyi Yang, Xiao Yu, Shui Yu, Jianming Chen, Guangyun Chen, Ming Zheng, Graham Reader, and David S.-K. Ting. Impacts of spark discharge current and duration on flame development of lean mixtures under flow conditions. In *Proceedings of the ASME Internal Combustion Engine Fall Technical Conference -2018-*, New York, N.Y., 2018. American Society of Mechanical Engineering.



- [69] Shogo Sayama, Masao Kinoshita, Yoshiyuki Mandokoro, and Takayuki Fuyuto. Spark ignition and early flame development of lean mixtures under high-velocity flow conditions: An experimental study. *International Journal of Engine Research*, 20(2):236–246, 2019.
- [70] Myung Jun Lee, Matt Hall, Ofodike A. Ezekoye, and Ronald D. Matthews. Voltage, and energy deposition characteristics of spark ignition systems. *SAE Technical Paper 2005-01-0231*, 2005.
- [71] Shuai Huang, Tie Li, Pengfei Ma, Siyu Xie, Zhifei Zhang, and Run Chen. Quantitative evaluation of the breakdown process of spark discharge for spark-ignition engines. *Journal of Physics D: Applied Physics*, 53(4):045501, 2020.
- [72] T. D. Fansler, M. C. Drake, I. Düwel, and F. P. Zimmermann. Fuel-spray and spark plug interactions in a spray-guided direct-injection gasoline engine. In *Proceedings of the Seventh International Symposium on Internal Combustion Diagnostics*, pages 81–97, Mainz-Kastel, 2006. AVL Deutschland.
- [73] Rainer N. Dahms, Michael C. Drake, Todd D. Fansler, T.-W. Kuo, and N. Peters. Understanding ignition processes in spray-guided gasoline engines using high-speed imaging and the extended spark-ignition model sparkcimm. part a: Spark channel processes and the turbulent flame front propagation. *Combustion and Flame*, 158(11):2229–2244, 2011.
- [74] James D. Smith and Volker Sick. A multi-variable high-speed imaging study of ignition instabilities in a spray-guided direct-injected spark-ignition engine. *SAE Technical Paper 2006-01-1264*, 2006.
- [75] M. C. Drake, T. D. Fansler, and K. H. Peterson. Stratified ignition processes in spray-guided sidi engines. In *Proceedings of the Ninth International Symposium on Internal Combustion Diagnostics*, pages 87–98, Mainz-Kastel, 2010. AVL Deutschland.
- [76] Todd D. Fansler, David L. Reuss, Volker Sick, and Rainer N. Dahms. Invited review: Combustion instability in spray-guided stratified-charge engines: A review. *International Journal of Engine Research*, 16(3):260–305, 2015.
- [77] F. Bozza, A. Gimelli, S. S. Merola, and B. M. Vaglieco. Validation of a fractal combustion model through flame imaging. *SAE Technical Paper 2005-01-1120*, 2005.
- [78] Simona S. Merola and Bianca M. Vaglieco. Knock investigation by flame and radical species detection in spark ignition engine for different fuels. *Energy Conversion and Management*, 48(11):2897–2910, 2007.
- [79] K. Bizon, G. Continillo, E. Mancaruso, S. S. Merola, and B. M. Vaglieco. Pod-based analysis of combustion images in optically accessible engines. *Combustion and Flame*, 157(4):632–640, 2010.
- [80] M. Buschbeck, N. Bittner, T. Halfmann, and S. Arndt. Dependence of combustion dynamics in a gasoline engine upon the in-cylinder flow field, determined by high-speed piv. *Experiments in Fluids*, 53(6):1701–1712, 2012.
- [81] Linus Engelmann, Judith Laichter, Patrick Wollny, Markus Klein, Sebastian A. Kaiser, and Andreas M. Kempf. Cyclic variations in the flame propagation in an spark-ignited engine: Multi cycle large eddy simulation supported by imaging diagnostics. *Flow, Turbulence and Combustion*, 110(1):91–104, 2023.
- [82] Qiang Cheng, Shervin Karimkashi, Zeeshan Ahmad, Ossi Kaario, Ville Vuorinen, and Martti Larmi. Hyperspectral image reconstruction from colored natural flame luminosity imaging in a tri-fuel optical engine. *Scientific reports*, 13(1):2445, 2023.
- [83] John W. Daily. Laser induced fluorescence spectroscopy in flames. *Progress in Energy and Combustion Science*, 23(2):133–199, 1997.
- [84] R. Abu-Gharbieh, G. Hamarneh, T. Gustavsson, and C. Kaminski. Flame front tracking by laser induced fluorescence spectroscopy and advanced image analysis. *Optics express*, 8(5):278–287, 2001.
- [85] B. O. Ayoola, R. Balachandran, J. H. Frank, E. Mastorakos, and C. F. Kaminski. Spatially resolved heat release rate measurements in turbulent premixed flames. *Combustion and Flame*, 144(1-2):1–16, 2006.
- [86] S. H. R. Müller, B. Böhm, M. Gleißner, S. Arndt, and A. Dreizler. Analysis of the temporal flame kernel development in an optically accessible ic engine using high-speed oh-plif. *Applied Physics B*, 100(3):447–452, 2010.

- [87] B. Peterson, E. Baum, B. Böhm, and A. Dreizler. Early flame propagation in a spark-ignition engine measured with quasi 4d-diagnostics. *Proceedings of the Combustion Institute*, 35(3):3829–3837, 2015.
- [88] Carl-Philipp Ding, Rene Honza, Benjamin Böhm, and Andreas Dreizler. “simultaneous measurement of flame impingement and piston surface temperatures in an optically accessible spark ignition engine”. *Applied Physics B*, 123(4):2615, 2017.
- [89] Brian Peterson, Elias Baum, Andreas Dreizler, and Benjamin Böhm. An experimental study of the detailed flame transport in a si engine using simultaneous dual-plane oh-lif and stereoscopic piv. *Combustion and Flame*, 202:16–32, 2019.
- [90] Rene Honza, Carl-Philipp Ding, Andreas Dreizler, and Benjamin Böhm. Flame imaging using planar laser induced fluorescence of sulfur dioxide. *Applied Physics B*, 123(9), 2017.
- [91] C.-P. Ding, B. Peterson, M. Schmidt, A. Dreizler, and B. Böhm. Flame/flow dynamics at the piston surface of an ic engine measured by high-speed plif and ptv. *Proceedings of the Combustion Institute*, 37(4):4973–4981, 2019.
- [92] Chao He, Guido Kuenne, Esra Yildar, Jeroen van Oijen, Francesca Di Mare, Amsini Sadiki, Carl-Philipp Ding, Elias Baum, Brian Peterson, Benjamin Böhm, and Johannes Janicka. Evaluation of the flame propagation within an si engine using flame imaging and les. *Combustion Theory and Modelling*, 21(6):1080–1113, 2017.
- [93] Wei Zeng, Seunghwan Keum, Tang-Wei Kuo, and Volker Sick. Role of large scale flow features on cycle-to-cycle variations of spark-ignited flame-initiation and its transition to turbulent combustion. *Proceedings of the Combustion Institute*, 37(4):4945–4953, 2019.
- [94] A. Hanuschkin, S. Zündorf, M. Schmidt, C. Welch, J. Schorr, S. Peters, A. Dreizler, and B. Böhm. Investigation of cycle-to-cycle variations in a spark-ignition engine based on a machine learning analysis of the early flame kernel. *Proceedings of the Combustion Institute*, 38(4):5751–5759, 2021.
- [95] Daniel Dreher, Marius Schmidt, Cooper Welch, Sara Ourza, Samuel Zündorf, Johannes Maucher, Steven Peters, Andreas Dreizler, Benjamin Böhm, and Alexander Hanuschkin. Deep feature learning of in-cylinder flow fields to analyze cycle-to-cycle variations in an si engine. *International Journal of Engine Research*, 22(11):3263–3285, 2021.
- [96] Hongchao Chu, Cooper Welch, Hani Elmeistikawy, Shangyi Cao, Marco Davidovic, Benjamin Böhm, Andreas Dreizler, and Heinz Pitsch. A combined numerical and experimental investigation of cycle-to-cycle variations in an optically accessible spark-ignition engine. *Flow, Turbulence and Combustion*, 110(1):3–29, 2023.
- [97] Roman Stiehl, Johannes Bode, Jürgen Schorr, Christian Krüger, Andreas Dreizler, and Benjamin Böhm. Influence of intake geometry variations on in-cylinder flow and flow–spray interactions in a stratified direct-injection spark-ignition engine captured by time-resolved particle image velocimetry. *International Journal of Engine Research*, 17(9):983–997, 2016.
- [98] Janardhan Kodavasal, Ahmed Abdul Moiz, Muhsin Ameen, and Sibendu Som. Using machine learning to analyze factors determining cycle-to-cycle variation in a spark-ignited gasoline engine. *Journal of Energy Resources Technology*, 140(10), 2018.
- [99] Andrew Di Mauro, Hao Chen, and Volker Sick. Neural network prediction of cycle-to-cycle power variability in a spark-ignited internal combustion engine. *Proceedings of the Combustion Institute*, 37(4):4937–4944, 2019.
- [100] Alexander Hanuschkin, Steffen Schober, Johannes Bode, Jürgen Schorr, Benjamin Böhm, Christian Krüger, and Steven Peters. Machine learning–based analysis of in-cylinder flow fields to predict combustion engine performance. *International Journal of Engine Research*, 22(1):257–272, 2021.
- [101] Benjamin Böhm and Brian Peterson. Darmstadt engine workshop (dew), 2023.
- [102] Cooper Welch, Lars Illmann, Marius Schmidt, and Benjamin Böhm. Experimental characterization of the turbulent intake jet in an engine flow bench. *Experiments in Fluids*, 64(5), 2023.

- 
- [103] Cooper Welch, Marius Schmidt, Karri Keskinen, George Giannakopoulos, Konstantinos Boulouchos, Andreas Dreizler, and Benjamin Boehm. The effects of intake pressure on in-cylinder gas velocities in an optically accessible single-cylinder research engine. *SAE Technical Paper 2020-01-0792*, 2020.
- [104] Cooper Welch, Marius Schmidt, Christopher Geschwindner, Shengqi Wu, Margaret S. Wooldridge, and Benjamin Böhm. The influence of in-cylinder flows and bulk gas density on early spray g injection in an optical research engine. *International Journal of Engine Research*, 24(1):82–98, 2023.
- [105] Cooper Welch, Lars Illmann, Marius Schmidt, Andreas Dreizler, and Benjamin Böhm. Experimental evaluation of spark behavior under diluted conditions in an optically accessible engine. *International Journal of Engine Research*, 2023.
- [106] Cooper Welch, Marius Schmidt, Lars Illmann, Andreas Dreizler, and Benjamin Böhm. The influence of flow on cycle-to-cycle variations in a spark-ignition engine: A parametric investigation of increasing exhaust gas recirculation levels. *Flow, Turbulence and Combustion*, 110(1):185–208, 2023.
- [107] Nir Ozdor, Mark Dulger, and Eran Sher. Cyclic variability in spark ignition engines a literature survey. *SAE Technical Paper 940987*, 1994.
- [108] Jacques Borée and Paul C. Miles. In-cylinder flow. In David Crolla, David E. Foster, Toshio Kobayashi, and N. D. Vaughan, editors, *Encyclopedia of automotive engineering*, pages 1–31. Wiley, Chichester, West Sussex, United Kingdom, 2015.
- [109] A. F. Bicen, C. Vafidis, and J. H. Whitelaw. Steady and unsteady airflow through the intake valve of a reciprocating engine. *Journal of Fluids Engineering*, 107(3):413–420, 1985.
- [110] Frank Hartmann, Stefan Buhl, Florian Gleiss, Philipp Barth, Martin Schild, Sebastian A. Kaiser, and Christian Hasse. Spatially resolved experimental and numerical investigation of the flow through the intake port of an internal combustion engine. *Oil & Gas Science and Technology – Revue d’IFP Energies nouvelles*, 71(1):2, 2016.
- [111] Daniel Freudenhammer, Brian Peterson, Carl-Philipp Ding, Benjamin Boehm, and Sven Grundmann. The influence of cylinder head geometry variations on the volumetric intake flow captured by magnetic resonance velocimetry. *SAE International Journal of Engines*, 8(4):1826–1836, 2015.
- [112] Tianyou Wang, Daming Liu, Bingqian Tan, Gangde Wang, and Zhijun Peng. An investigation into in-cylinder tumble flow characteristics with variable valve lift in a gasoline engine. *Flow, Turbulence and Combustion*, 94(2):285–304, 2015.
- [113] Stefania Falfari, Federico Brusiani, and Piero Pelloni. 3d cfd analysis of the influence of some geometrical engine parameters on small pfi engine performances – the effects on the tumble motion and the mean turbulent intensity distribution. *Energy Procedia*, 45:701–710, 2014.
- [114] S. B. Pope. *Turbulent flows*. Cambridge University Press, Cambridge, 2000.
- [115] Lewis Fry Richardson. *Weather Prediction by Numerical Process*. Cambridge mathematical library. Cambridge University Press, Cambridge, second edition edition, 2007.
- [116] A. N. Kolmogorov. Local structure of turbulence in an incompressible viscous fluid at very high reynolds numbers. *Soviet Physics Uspekhi*, 10(6):734–746, 1968.
- [117] John L. Lumley. *Engines: An introduction / John L. Lumley*. Cambridge University Press, Cambridge, 1999.
- [118] H. Tennekes and John L. Lumley. *A first course in turbulence*. MIT Press, Cambridge, Mass., 1972.
- [119] Hiromitsu Ando and Constantine Arcoumanis. Flow, mixture preparation and combustion in four-stroke direct-injection gasoline engines. In Constantine Arcoumanis, editor, *Flow and combustion in automotive engines*, Experimental fluid mechanics, pages 137–171. Springer, Berlin and London, 2009.
- [120] D. R. Ballal and A. H. Lefebvre. Ignition and flame quenching of quiescent fuel mists. *Proceedings of the Royal Society of London. A. Mathematical and Physical Sciences*, 364(1717):277–294, 1978.

- [121] Dongwon Jung, Kosaku Sasaki, Kenji Sugata, Masayoshi Matsuda, Takeshi Yokomori, and Norimasa Iida. Combined effects of spark discharge pattern and tumble level on cycle-to-cycle variations of combustion at lean limits of si engine operation. *SAE Technical Paper 2017-01-0677*, 2017.
- [122] Michael B. Young. Cyclic dispersion in the homogeneous-charge spark-ignition engine—a literature survey. *SAE Technical Paper 810020*, 1981.
- [123] Charles E. A. Finney, Brian C. Kaul, C. Stuart Daw, Robert M. Wagner, K. Dean Edwards, and Johney B. Green. Invited review: A review of deterministic effects in cyclic variability of internal combustion engines. *International Journal of Engine Research*, 16(3):366–378, 2015.
- [124] Stéphane Richard, Alessio Dulbecco, Christian Angelberger, and Karine Truffin. Invited review: Development of a one-dimensional computational fluid dynamics modeling approach to predict cycle-to-cycle variability in spark-ignition engines based on physical understanding acquired from large-eddy simulation. *International Journal of Engine Research*, 16(3):379–402, 2015.
- [125] Benjamin Böhm and Andreas Kempf. Cyclic variations in internal combustion engines. *Flow, Turbulence and Combustion*, 110(1):1–2, 2023.
- [126] Frederic A. Matekunas. Modes and measures of cyclic combustion variability. *SAE Technical Paper 830337*, 1983.
- [127] Markus Raffel, Christian E. Willert, Fulvio Scarano, Christian J. Kähler, Steve T. Wereley, and Jürgen Kompenhans. *Particle image velocimetry: A practical guide*. Springer, Cham, 2018.
- [128] LaVision GmbH. *FlowMaster: Product Manual for DaVis 10.2*. LaVision GmbH, Göttingen, 2021.
- [129] Cameron Tropea, Alexander L. Yarin, and John F. Foss. *Springer Handbook of Experimental Fluid Mechanics*. Springer Berlin Heidelberg, Berlin, Heidelberg, 2007.
- [130] R. J. Adrian and J. Westerweel. *Particle Image Velocimetry*, volume 30 of *Cambridge Aerospace Series*. Cambridge University Press, Cambridge and New York, 2011, 2011.
- [131] Sven Scharnowski and Christian J. Kähler. Particle image velocimetry - classical operating rules from today's perspective. *Optics and Lasers in Engineering*, 135:106185, 2020.
- [132] A. Sciacchitano. Uncertainty quantification in particle image velocimetry. *Measurement Science and Technology*, 30(9):092001, 2019.
- [133] Bernhard Wieneke. Piv uncertainty quantification from correlation statistics. *Measurement Science and Technology*, 26(7):074002, 2015.
- [134] Andrea Sciacchitano, Douglas R. Neal, Barton L. Smith, Scott O. Warner, Pavlos P. Vlachos, Bernhard Wieneke, and Fulvio Scarano. Collaborative framework for piv uncertainty quantification: comparative assessment of methods. *Measurement Science and Technology*, 26(7):074004, 2015.
- [135] Zhihao Ding, Karine Truffin, Stéphane Jay, Marius Schmidt, Fabrice Foucher, and Jacques Borée. On the use of les and 3d empirical mode decomposition for analyzing cycle-to-cycle variations of in-cylinder tumbling flow. *Flow, Turbulence and Combustion*, 2023.
- [136] L. Engelmann, C. Welch, M. Schmidt, D. Meller, P. Wollny, B. Böhm, A. Dreizler, and A. Kempf. A temporal fluid-parcel backwards-tracing method for direct-numerical and large-eddy simulation employing lagrangian particles. *Applied Energy*, 342:121094, 2023.

# A Journal Publications

## A.1 Paper I

### **Experimental Characterization of the Turbulent Intake Jet in an Engine Flow Bench**

C. Welch, L. Illmann, M. Schmidt, B. Böhm: Experimental Characterization of the Turbulent Intake Jet in an Engine Flow Bench. *Experiments in Fluids* 64, 91 (2023) Springer Nature. <https://doi.org/10.1007/s00348-023-03640-9>

### **Paper I Permissions**

Paper I is reproduced with permission from Springer Nature. Permission to include Paper I in this cumulative dissertation is also granted by the authors who hold the copyright under a Creative Commons Attribution 4.0 International License. To view a copy of this license, visit <https://creativecommons.org/licenses/by/4.0/>.

---

# DECLARATION ON THE CONTRIBUTION TO THE SCIENTIFIC PUBLICATION

## Erklärung zum Eigenanteil der wissenschaftlichen Veröffentlichung

Cooper Welch, M.Sc.

### PAPER

C. Welch, L. Illmann, M. Schmidt, B. Böhm: Experimental Characterization of the Turbulent Intake Jet in an Engine Flow Bench. *Experiments in Fluids* (2023).

### CO-AUTHORS

Lars Illmann, M.Sc.

Marius Schmidt, M.Sc.  
Benjamin Böhm, Dr.-Ing.

### INDIVIDUAL CONTRIBUTIONS

- **Cooper Welch**
  - Jointly conducted experiments and processing of data with Lars Illmann.
  - Conducted post-processing and analysis of all data.
  - Main and corresponding author of the paper: performed literature research, generated all figures, and wrote the manuscript.
- **Lars Illmann**  
jointly conducted experiments and processing of data with Cooper Welch. Supported in the interpretation of the results and the proofreading of the manuscript.
- **Marius Schmidt**  
Assisted in conduction of experiments through advice from experience. Supported in the analysis and interpretation of results and the proofreading of the manuscript.
- **Benjamin Böhm**  
Provided resources for the conduction of the experiments. Supported in the interpretation and discussion of the results and the proofreading of the manuscript.

### OVERALL CONTRIBUTION OF COOPER WELCH


A leading role in the conduction of the experiments, data analysis and interpretation, and main author of the manuscript.

### USE OF PAPER CONTENTS IN OTHER DISSERTATIONS

This publication is not the subject of another ongoing or completed dissertation.

### SIGNATURES OF ALL AUTHORS

  
\_\_\_\_\_  
Cooper Welch

  
\_\_\_\_\_  
Marius Schmidt

  
\_\_\_\_\_  
Lars Illmann

  
\_\_\_\_\_  
Benjamin Böhm

# Experimental characterization of the turbulent intake jet in an engine flow bench

Cooper Welch\*, Lars Illmann, Marius Schmidt, Benjamin Böhm

Technical University of Darmstadt, Department of Mechanical Engineering, Reactive Flows and Diagnostics, Otto-Berndt-Str. 3, 64287 Darmstadt, Germany

\*Corresponding author: Cooper Welch, email: [welch@rsm.tu-darmstadt.de](mailto:welch@rsm.tu-darmstadt.de)

## ORCID ID:

Cooper Welch: 0000-0001-9067-9405

Lars Illmann: 0000-0001-6907-0064

Marius Schmidt: 0000-0002-5424-1251

Benjamin Böhm: 0000-0003-2654-6266

## ABSTRACT

The turbulent intake flow of an optically accessible internal combustion engine is modelled using an air flow bench to reduce the complexity in the number of variables inherent within engine flows. By removing the piston and introducing a new optically accessible housing and outlet channel, the flow bench design simulates engine flows in the region just downstream of the intake valves and offers the possibility to measure and calculate quantities that would be difficult or impossible to obtain in the unsteady environment of a dynamic engine. Velocity data obtained via high-speed particle image velocimetry of the flow bench in the symmetry and valve planes are compared with data from a base operating condition of the motored engine at an intake pressure of 0.95 bar and a speed of 800 rpm at  $-270^\circ\text{CA}$  (270 crank-angle-degrees before compression top dead center), beginning with stationary valves at the corresponding valve lift of  $-270^\circ\text{CA}$ , then with moving valves. Analysis of the intake jet turbulence for increasing mass flow rates reveals a coherent flapping of the jet at a frequency of 752.5 Hz for only the 100% mass flow rate case. The vortex shedding frequency of the valve stem is estimated to being in the range of 634 Hz and 799 Hz, indicating a possible link between the coherent jet flapping and the vortex shedding surviving the acceleration through the valve gap. Through comprehensive analysis, this study provides valuable validation data and insight into the intake flows of internal combustion engines.

## KEYWORDS

Internal Combustion Engine, Flow Bench, Turbulence, Intake Jet, Jet flapping

## 1 INTRODUCTION

The internal combustion engine (ICE) is likely to remain an important player in future global transport systems due to the unparalleled energy storage of combustible fuels. Therefore, the increase of efficiency and decrease of emissions continues to be a critical topic in the development of future highly optimized ICEs. One influential aspect of the cyclical performance of ICEs is the intake flow, which is linked in the deterministic causal chain of the combustion process (Dreher et al. 2021; Welch et al. 2023a). In particular, the high velocity flow issuing from the valve gap into the cylinder, referred to as the intake jet, has been a focus of research as it is integral in engine phenomena such as the formation of the tumble (Borée and Miles 2015) or the rapid evaporation of fuel injections in spray-guided

configurations. The intake jet of ICEs presents a challenging case for study due to the complex interaction of the flows with dynamic engine geometries, namely the valves and the piston. To reduce the complexity for the development of high-fidelity engine simulation models, engine-relevant flows have been studied using flow bench configurations, in which the engine geometry is altered to allow a steady flow through the intake valve gaps to an open-ended cylinder. Using such configurations, the intake flow at certain steady valve lift positions can be considered as a temporal snapshot of the intake flow of the real engine at the corresponding valve lifts. Furthermore, time-averaged velocity data can be directly compared with the phase-averaged data of engine flows to validate the test case.

Over the last decade, improvements in the fields of diagnostics and computational engineering have allowed for the accurate study of flow bench configurations in high time and spatial resolution as well as in the 2- and 3-dimensional (2- and 3-D) space. Freudenhammer et al. conducted magnetic resonance velocimetry (MRV) experiments with the Darmstadt engine geometry under steady conditions using water as the fluid at matching Reynolds numbers ( $Re$ ) to the motored engine at 800 rpm with intake pressure of 0.95 bar and a valve lift of 9.21 mm (corresponding to  $-270^\circ CA$ , that is 270 crank-angle-degrees before compression top dead center) (Freudenhammer et al. 2014; Freudenhammer et al. 2015). The MRV measurements established a database of high-fidelity 3-D velocity data of the intake flow for simulation model validation. Subsequent research employed air flow bench configurations to measure the velocity with 3-D, three-component (3D3C) (Chen and Sick 2017), 2-D, three-component (2D3C) (Falkenstein et al.; Falkenstein et al. 2017), and 2-D, two-component (2D2C) (Buhl et al. 2017; El-Adawy et al. 2017; Falkenstein et al. 2020; Hartmann et al. 2016; Haussmann et al. 2020; Hyun and Ohm 2021; Liu et al. 2019) particle tracking velocimetry or particle image velocimetry (PIV). The majority of the aforementioned investigations are accompanied by computational fluid dynamics (CFD) studies, which complement the low-speed and 2-D experimental data by providing insight into the 3-D space as well as in the intake port where experiments with realistic engine geometries are difficult to conduct.

While a number of simulation studies in the literature have examined the turbulence of the intake flows in engine-relevant configurations, as of yet, no high-speed 2-D experimental data are available to validate spatial flow for the analysis of turbulence in an ICE flow configuration. This work aims to fill this gap by employing high-speed PIV in an air flow bench to characterize the intake flow of the optically accessible research engine of TU Darmstadt under various operating conditions. The use of high-speed PIV over tens of thousands of consecutive flow fields allows not only the computation of phase-locked quantities such as the turbulent kinetic energy, but also time-resolved statistics relevant for the characterization of the turbulence of the intake flow. This work is presented as follows: first, the experimental methods are introduced to describe the engine test bench and the flow bench adaptation, as well as the PIV setup and data processing techniques. Then, the results are presented and discussed beginning with the validation of the flow bench operating conditions in the symmetry and valve planes, then with the results of the turbulent analyses including an investigation of coherent jet flapping and its plausible sources. Finally, conclusions are drawn and recommendations for future work are given.

## 2 METHODS

### 2.1 Engine Test Bench

The engine test bench used in this study is a single-cylinder optically accessible research engine which has been designed to offer consistent boundary conditions over a wide range of operating parameters (Baum et al. 2014). The quartz glass liner of the spray-guided cylinder head and quartz glass flat piston (with Bowditch extension) grant optical access (Freudenhammer et al. 2015; Geschwindner et al. 2020; Welch et al. 2020). The cylinder head configuration used has a compression ratio of 8.7:1 and allows a maximum planar field of view (FOV) of 75 mm  $\times$  55 mm (width  $\times$  height) plus an extra 8 mm due to



the pent roof. Although the engine can be fired with port fuel injection or direct injection (DI) of fuel, the operating condition (OC) used in this study is representative of motored (unfired) engine operation at 800 rpm and an intake pressure of 0.95 bar. This OC “A” was selected since it is one of the most studied OCs of the Darmstadt engine and it matches the condition used in the MRV experiments. As the focus of this study is to examine the intake flow of this engine in a simplified flow bench configuration, the reader is directed to (Baum et al. 2014; Schmidt et al. 2021; Welch et al. 2020; Welch et al. 2023b) for more information on the motored engine test bench.

## 2.2 Flow Bench

An air flow bench has been designed to simulate the intake flow in the region near the intake valves of the engine in a simplified configuration by removing complexities derived from the moving piston. To that end, the piston was removed and a separate optical housing with an outlet channel replaced the original mirror housing of the engine to allow constant, uninterrupted flow from the intake valves to the outlet. Figure 1 shows the unchanged intake manifold of the engine test bench coupled with the spray-guided cylinder head and the flow bench housing section. The new optical section and outlet channel were designed such that no backflow was measured (verified via outlet channel PIV). The channel has a flat quartz glass bottom (optical plate) allowing the same bottom illumination for optical measurements as the motored engine configuration. The in-cylinder geometry was also simplified by removing the spark plug and inserting a smooth plug as well as by replacing the DI injector with a smooth-surfaced dummy. The air flow bench of this study with a stationary valve lift of 9.21 mm has already been used for validation and comparison of highly-resolved wall-modeled LES techniques and has been demonstrated as a useful test case (Hausmann et al. 2020).

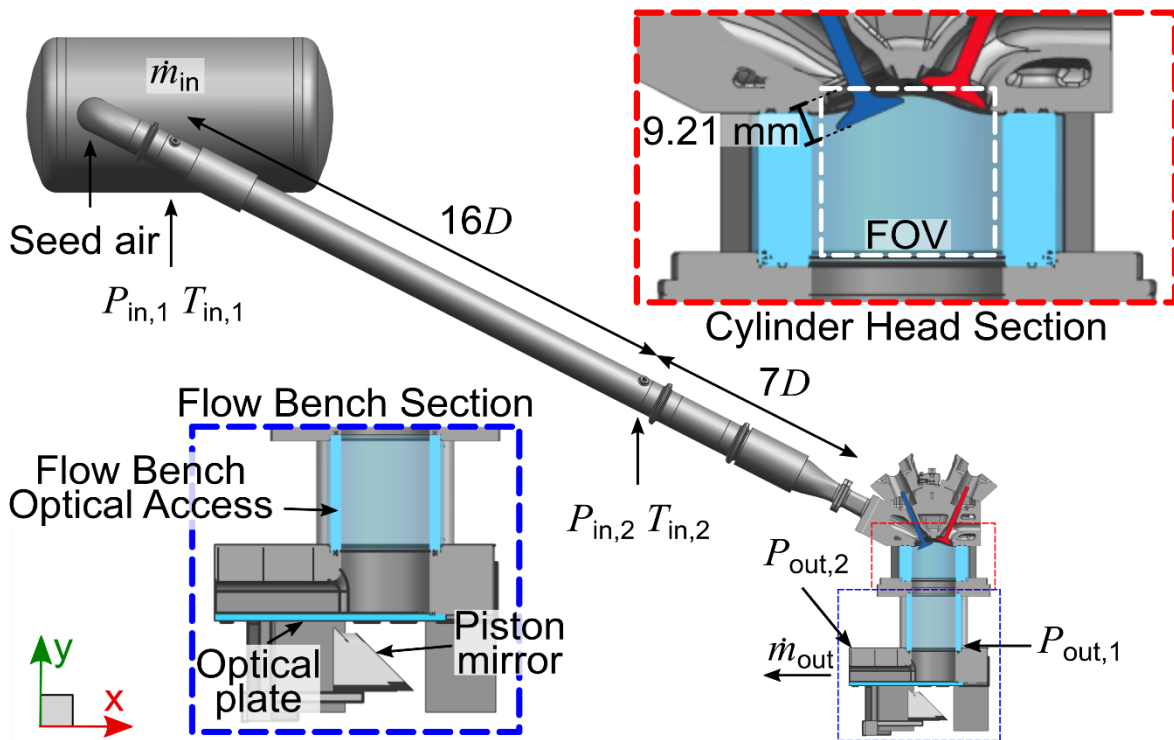


Figure 1. Flow bench experimental setup. Boundary conditions obtained from valve plane measurements are provided in Table 1.

While the air flow bench offers a simplified geometry and test case, it closely simulates the real intake flow of the motored engine and offers direct comparison of dry air velocities. Since high-speed PIV can be applied, an improvement is made over the MRV measurements of the water flow bench conducted in the past (Freudenhammer et al. 2014; Freudenhammer et al. 2015). Furthermore,

the complexity of the test case can be increased from stationary valves with steady-state turbulent flows to moving valves with dynamic flows closer resembling the intake velocity of the motored engine. In this study, the intake flow of the flow bench with stationary valves at 9.21 mm valve lift as well as moving valves are investigated, whereby the mass flow rates (MFRs) of the respective operating conditions (OCs) were set to match the intake velocity of the motored engine at  $-270^{\circ}\text{CA}$  (see Section 3.1.1 for details on MFR selection). In addition, two more OCs at 75% and 50% MFR of the stationary (fixed) valve MFR were studied to include variations in  $Re$ . Table 1 shows the OCs of this paper with boundary conditions and estimated  $Re$ . The  $Re$  in Table 1 are calculated using the corresponding MFRs, the intake pipe diameter  $D$  of 56.3 mm as the characteristic length, and a dynamic viscosity  $\mu$  of  $1.83 \times 10^{-5}$  kg/ms. The dynamic viscosity was obtained using Sutherland's law (White 2006). As displayed in Figure 1, several pressure and temperature ports are located from the intake manifold to the outlet channel to provide comparison for simulations; the most relevant variables are provided in Table 1.

**Table 1. Experimental boundary conditions. Standard uncertainties are indicated in parentheses.**

Condition	$\dot{m}_{in}$ [kg/h]	$T_{in,2}$ [ $^{\circ}\text{C}$ ]	$P_{in,2}$ [bar]	$\rho$ [kg/m <sup>3</sup> ]	$Re$ [-]
Motored ( $-270^{\circ}\text{CA}$ )	11.35(1.00)	35.7(0.5)	0.951(0.001)	1.07(0.001)	37200(est.)
Mov. val. ( $-270^{\circ}\text{CA}$ )	19.90(1.00)	25.5(0.5)	1.011(0.001)	1.18(0.001)	-
100% MFR	94.10(1.00)	22.7(0.5)	1.000(0.001)	1.18(0.001)	32400(400)
75% MFR	70.63(1.00)	23.2(0.5)	1.006(0.001)	1.18(0.001)	24300(400)
50% MFR	47.09(1.00)	23.2(0.5)	1.004(0.001)	1.18(0.001)	16200(400)

Figure 2 displays the phase-averaged pressure at various locations labeled in Figure 1. Figure 2(a) shows the phase-averaged intake pressure measured just downstream of the noise reduction plenum and just upstream of the intake valves of a single motored engine run encompassing 400 consecutive cycles at 800 rpm and 0.95 bar average intake pressure. Despite the presence of plenums meant to reduce pressure oscillations, the regular movement of the valves in combination with the long intake pipe characteristic of the research engine setup induces a coherent resonance in the pressure curves which must be considered when modelling the engine (Baum et al. 2014; Welch et al. 2020). Vertical dashed lines indicate the timing for the intake valve opening (IVO) and closing (IVC). Figure 2(b) displays the average intake pressure and the pressure at the end of the outlet channel for a flow bench experimental run with moving valves. Similar to the motored engine OC, the moving valves OC exhibits a coherent resonance due to the periodic intake flow. As soon as the intake valves close, the pressure in the intake manifold oscillates predictably; however, while the intake valves are open from  $325^{\circ}\text{CA}$  until  $-125^{\circ}\text{CA}$ , the amplitudes of the oscillations and the mean pressure decrease as the air flows into the open-ended cylinder. As shown in previous work by the authors, in the case of the motored engine, pressure oscillations during intake can have an effect on the velocity field; however, the influence on the velocity was larger when high-frequency oscillations induced by a backflow occurred (Welch et al. 2020). These backflows occur mainly in the part-load conditions when the higher in-cylinder pressure equalizes with the lower intake manifold pressure. Due to a lack of backflow in the flow bench (backflow also largely does not occur in the full-load motored case of this study), these influential high-frequency pressure oscillations do not occur and there is no observable effect on the flow, namely a spike in the intake flow (compare Figure 5 of this work to Figure 9 of (Welch et al. 2020)). Figure 2(c) displays the mean intake and outflow pressure of the steady flow bench at 100% MFR. Since this OC is a steady flow, the pressures are only phase-averaged and

displayed on a CA-basis on the same horizontal axis as the top 2 panels of the figure for visualization purposes. From further upstream to the outlet, the pressure drops on average by less than 0.4%, yet it is a measurable difference just within the measurement uncertainties based on the sensor accuracy. One final consideration with the open configuration of the flow bench test stand is the state of the weather at the time of the measurement because the atmospheric conditions determine the pressure and the temperature of the system (relative humidity is held constant at approximately 1.8% by a condenser upstream of the air compressors), namely the ambient pressure can have a measurable effect on the outlet pressure. Due to this reason, a pressure drop from  $P_{in,1}$  to  $P_{out,2}$  is not always observed, for example, when the ambient pressure is too high. Therefore, it is recommended that the MFR be used as a boundary condition for simulations of this flow bench configuration, rather than the pressure drop.

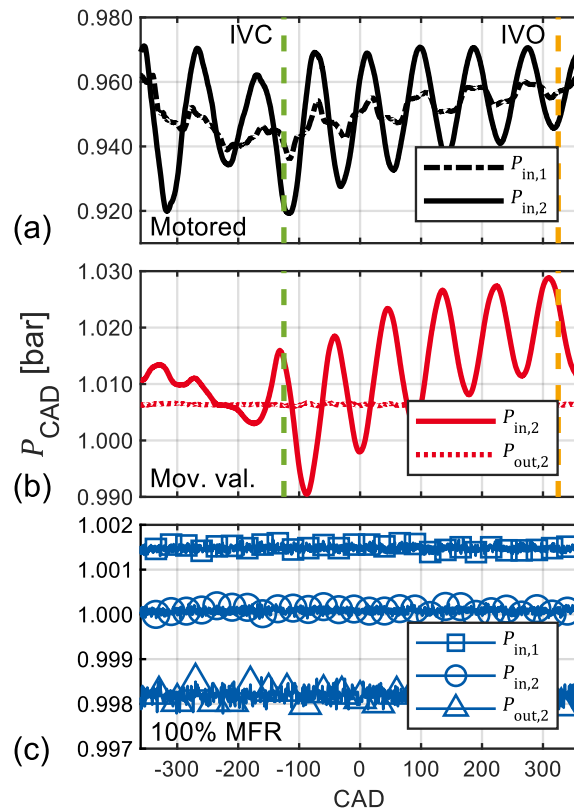


Figure 2. Phase-averaged pressure for motored engine (a), moving valve flow bench (b), and steady flow bench (c) operation. Intake valve opening (IVO) and closing (IVC) are indicated by the vertical dashed lines.

### 2.3 Velocity Measurements

Velocity measurements were performed in separate experimental campaigns: first with the motored engine configuration at 0.95 bar intake pressure and 800 rpm (Exp. I) as a benchmark for comparison with the flow bench; and the flow bench experiment (Exp. II). Both campaigns included the symmetry and valve-center planes (SP and VP) in non-simultaneous measurements of planar high-speed PIV. The experimental setup of both PIV planes in Exp. I is outlined in (Welch et al. 2020) and the PIV setup of Exp. II is provided in (Hausmann et al. 2020); however, Table 2 provides a summary of the optical setup, vector calculation, and processing of both campaigns. Figure 3 likewise shows a diagram of the PIV system for the flow bench. In short summary, high-speed PIV was conducted using pulsed laser sheets of two cavities with various time separation  $dt$  between pulses. Nebulized silicone oil (Dow Corning, DOWSIL 510) droplets were introduced to the intake pipe just upstream of probe locations of  $P_{in,1}$  and  $T_{in,1}$  indicated in Figure 1 and allowed to mix well with the rest of the bulk mass flow of air. Image pairs were captured by high-speed CMOS cameras (see Table 2) in double-frame mode.

Finally, after each measurement day or movement of the laser sheet, a series of target images from a 058-5 dual-plane calibration target from LaVision was captured to allow for scaling and dewarping of images before processing (based on 3rd order polynomial).

**Table 2. Summary of optical setups and vector processing for Exp. I and Exp. II.**

Experiment	I		II	
	SP	VP	SP	VP
Laser	EdgeWave Nd:YAG		EdgeWave Nd:YVO <sub>4</sub>	
Sheet thickness [mm]	0.620	0.540	0.850	
$dt$ at $-270^{\circ}\text{CA}$ [ $\mu\text{s}$ ]	9.0	9.3	10, 12, 18 (100%, 75%, 50%)	8.0, 11, 17 (100%, 75%, 50%)
Camera	Photron SA-X2	Phantom v1610	Phantom v2640	
Lens	Sigma $f = 105\text{ mm } f/11 + 20\text{ mm extension rings}$		Nikon $f = 85\text{ mm } f/1.4 + 35\text{ mm extension rings}$	
Acquisition [Hz]	960	960	12500(12000 for MV)	
Processing	SP	VP	SP	VP
Software	DaVis 8.4.0		DaVis 10.0.5	
Pre-processing	Spatial sliding background subtraction-8 pixel		Time filter subtraction	
Multi-pass iteration	Passes 1&2: $64 \times 64$ , 50% overlap; passes 3&4: $32 \times 32$ , 75% overlap		Passes 1&2: $48 \times 48$ , 50% overlap; passes 3&4: $24 \times 24$ , 75% overlap	
Post-processing	Peak ratio criterion $< 1.3$ ; universal outlier detection $7 \times 7$			
Interrogation window size [mm]	2.02	2.41	1.54	1.45

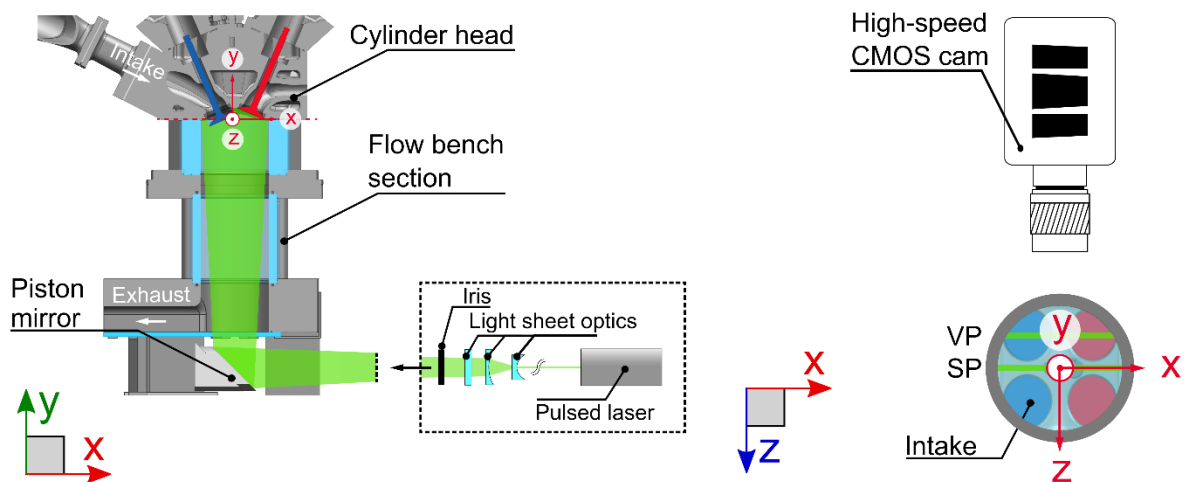


**Figure 3. Particle image velocimetry setup for the flow bench.**

## 2.4 Data Processing

Processing and calculation of vectors were carried out using the commercial software DaVis (LaVision). Table 2 provides the detailed settings of the processing for each experimental setup. The methodology for the PIV processing follows the same formula: first, masking of raw images was done to remove reflective components such as the intake valves. Next, image pre-processing was conducted to prepare raw image pairs for vector calculation. Then, a multi-pass cross-correlation algorithm of decreasing interrogation window size was employed to calculate vector fields. Finally, vector post-processing was used to remove spurious vectors.

Velocity measurement uncertainties for the 100% MFR flow bench case were quantified by a correlation statistics approach described by Wieneke (Wieneke 2015) and applied using DaVis. The time-averaged uncertainty of the velocity magnitude of instantaneous flow fields varies locally. In the jet center of the VP near the valve and close to the cylinder wall, the uncertainty normalized to the maximum jet velocity is calculated to be approximately 4% and 10%, respectively. In the region below the center line of the intake jet where the highest velocity gradients occur, the normalized uncertainty is between approximately 6% and 9%. Further uncertainties that may not be accounted for in the approach from Wieneke, such as perspective errors, are discussed for the 100% MFR case by Haussmann et al. (Haussmann et al. 2020).

Measured pressure and temperature data were processed in MATLAB 2021b for further analysis and visualization. Similarly, all further velocity data post-processing not shown in Table 2 and generation of figures were completed using MATLAB and some image post-processing (and creation of schematic figures) was conducted using Inkscape 1.2.

## 3 RESULTS AND DISCUSSION

### 3.1 Flow Bench Operating Condition Validation

In the following sections, the procedure for selecting the MFRs to properly simulate the intake flow of the motored engine at 800 rpm and 0.95 bar is outlined and a validation of the flow fields of the OCs is presented.

#### 3.1.1 Selection of Mass Flow Rates

The selection of the MFRs of the flow bench OCs was conducted by iteratively measuring the flow field in the SP and comparing the velocity field near the intake valves to that of the motored engine at  $-270^{\circ}\text{CA}$ . The upper section of Figure 4 displays the mean flow field of the motored engine at  $-270^{\circ}\text{CA}$  (left) and the fixed valve flow bench at 100% MFR (right) in the SP. White dot-dashed lines represent the  $y$ -axis locations for the velocity profiles of Figure 6. Furthermore, the mean velocity magnitude and direction is shown by the color map and the streamline arrows, respectively. It can be observed that the number of resolved vectors in each FOV is different. This is due to changes in the experimental setup, for example, switching from VP to SP several times over the course of the experimental campaigns. Nevertheless, although the physical processes involved in motored engine intake are different than those of the stationary valve flow bench, namely the dynamic valve and piston motion facilitating the flow, the open-ended flow bench configuration still has the same mean intake flow structure in the SP directly downstream of the valves.

Using the stationary valve flow bench MFR obtained by examining the flow fields in the SP, the velocity fields in the VP are compared in the lower panel of Figure 4. The white dot-dashed lines represent the profile locations of Figure 7. Also, in the VP, the mean intake velocity of the flow bench matches very well with the motored engine. Despite the smaller FOV of the motored case, the characteristic high-velocity intake jet with clearly defined shear and the formation of a tumble vortex

appears in both configurations. In addition to the jets having similar trajectories, the velocity magnitudes along the jet match very well (compare Figure 7 and Figure 9).

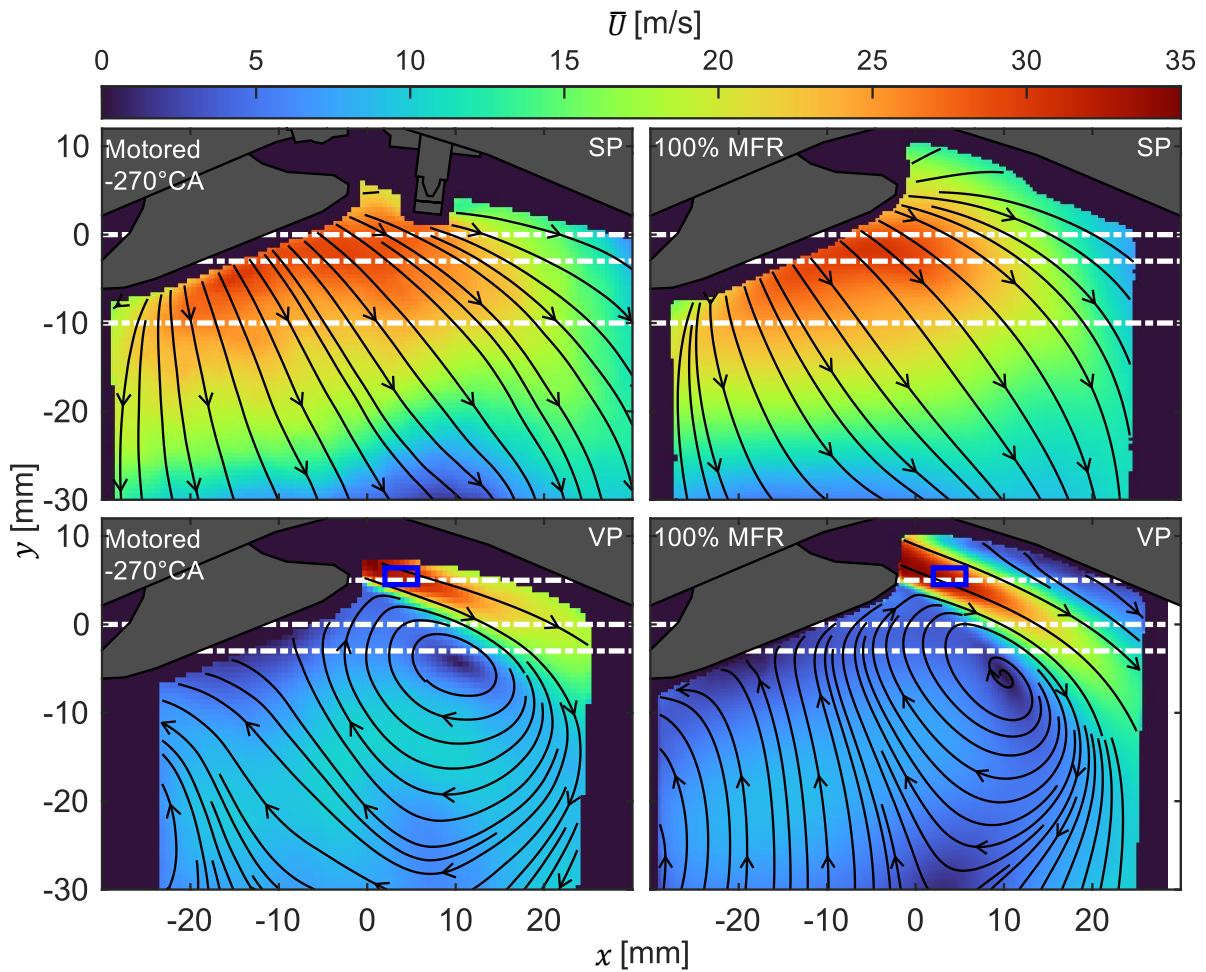


**Figure 4. Comparison of average velocity magnitude between the motored engine at  $-270^{\circ}\text{C}$  and the flow bench with 100% MFR. The mean velocity profile region of interest of Figure 5 is represented by the blue box. Velocity profile lines for Figure 6 and Figure 7 are shown in white.**

The determination of the MFR for the dynamic valve flow bench configuration involved a similar iterative procedure as with the stationary valve case. However, with the moving valves OC, the mean intake jet in a region of interest (ROI) downstream of the intake valves (indicated by the blue boxes in Figure 4) was used for the comparison of the velocity to the motored case, whereby the MFR was adjusted until the peak of the mean velocity profiles over time matched. Figure 5 shows the mean velocity profile comparison over CAD for the VP jet near the valve for the motored and moving valves flow bench cases at the selected MFR (Figure 5(a)) and the valve lift and piston velocity over CAD (Figure 5(b)). Although the flow bench OC was designed to match the peak velocity of this profile to the motored engine, there is a slower, more symmetric decline of peak velocities. This is due to the fundamentally different flow process involved in the open-ended flow bench configuration. From the beginning of the IVO, a low velocity flow is present in the ROI for both cases; however, once the jet begins to form, the velocities of both OCs rapidly increase until they reach their maximum. In the case of the motored engine, as air enters the cylinder and the piston starts to decelerate, the intake velocity begins to decrease as the piston loses its sucking power and the flow meets resistance of the confined volume. This is not the case with the flow bench, however, as the in-cylinder air is allowed to pass through the outlet channel. Therefore, the resulting intake flow profile for the flow bench is symmetric and closely follows the intake valve lift curve. Despite contrasting intake velocity profiles over the

whole intake phase, the velocity profiles of the intake jets are nearly identical before the piston reaches its peak downward velocity, resulting in similar velocities at the valve lift of interest, 9.21 mm.

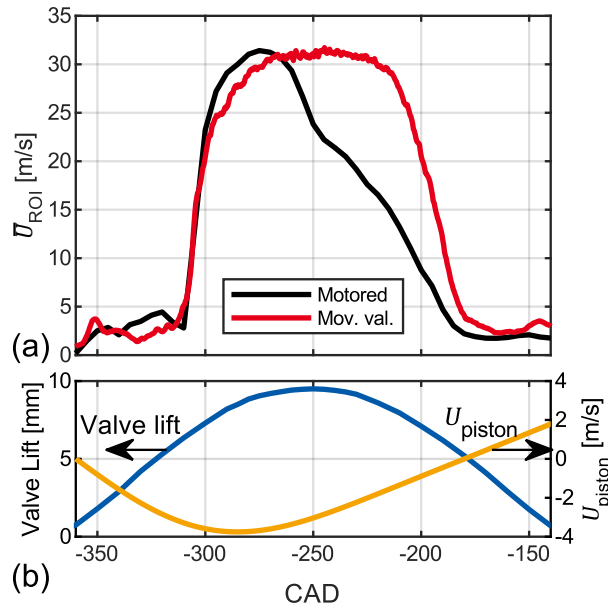


**Figure 5 (a) Mean intake velocity of the region of interest within the intake jet (blue boxes in Figure 4) for motored and moving valves flow bench operation. (b) The intake valve lift curve (blue line, left axis) and the piston velocity (yellow line, right axis).**

### 3.1.2 Symmetry Plane

As discussed in the previous section, MFRs were selected for the stationary valve flow bench case by comparing the velocity magnitudes in the SP to those of the motored engine operation. Figure 6 displays a profile comparison of the mean velocity  $x$ - and  $y$ -components  $\bar{u}$  and  $\bar{v}$ , respectively, as well as the mean velocity magnitude  $\bar{U}$  at the three horizontal locations indicated in the upper section of Figure 4. Since the MFRs of the flow bench were based especially on matching the velocity field of the motored engine in a region between  $y = 0$  mm and  $y = -3$  mm and  $x = -10$  mm and  $x = 10$  mm, all velocity components of the 100% MFR case compare well with the motored engine case. Additionally, the velocities of the lower MFR cases scale nearly perfectly with the reduction in MFR. However, there are characteristic differences between the flow bench and motored cases which merit closer inspection. First, although the sample size has no effect on the interpretation of the mean flow field (see Figure 4), the smaller sample size is visible in increased fluctuations in the profiles, especially closer to the intake valves. While it is interesting to also examine the standard deviation of the profiles, especially when considering possible velocity fluctuations, standard deviation is discussed in detail in Section 3.2 Turbulence Analysis. A further difference between the velocity profiles of the 100% MFR case and the non-stationary valve cases is the slope and offset of the  $\bar{u}$  profile starting at approximately  $x > 0$  mm. This difference in velocity must be attributed to the motion of the valves since the moving valve flow bench case and motored case have nearly the same horizontal profile. The lack of the spark plug in all flow bench cases also rules out the influence of the spark plug on this increase in horizontal velocity present in both dynamic valve cases. Furthermore, due to the difference in horizontal velocity, the magnitude  $\bar{U}$  is affected accordingly, despite very close profiles for the vertical component  $\bar{v}$ .



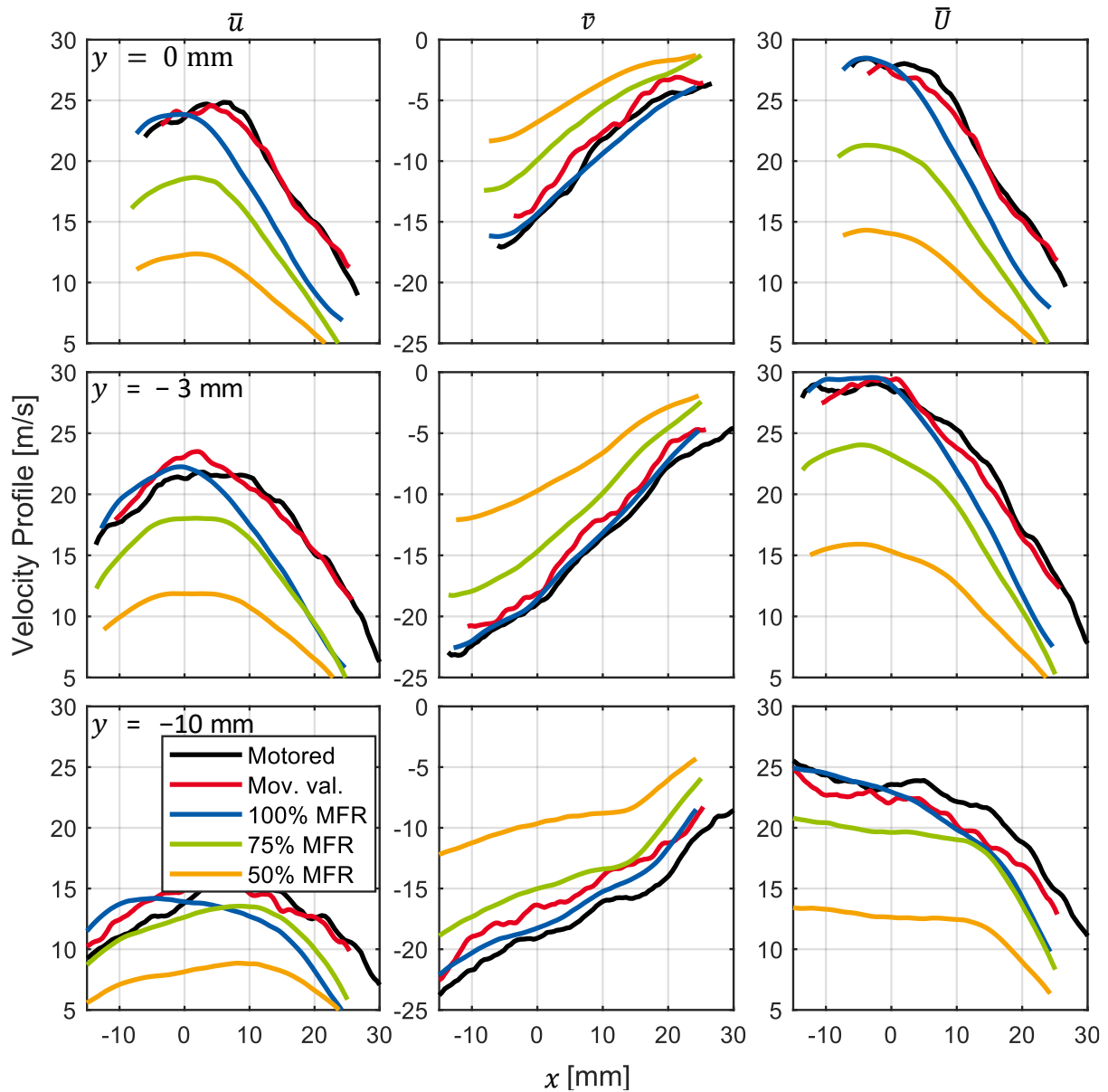


Figure 6. Mean velocity profiles taken from the symmetry plane.

### 3.1.3 Valve Plane

The valve plane velocity profiles, originating from the horizontal lines at the bottom of Figure 4, are displayed in Figure 7. As observed with the symmetry plane profiles in Figure 6, the 100% MFR flow bench velocity profiles match well with the dynamic valve cases, especially closer to the valves; yet further away from the intake valves, the slopes for the dynamic cases change with the motored case displaying the least steep velocity slope. This indicates that the motored case has the intake jet with the furthest horizontal extension, an observation which may have been made by examining the flow field in Figure 4. However, it may also be inferred from the profiles that the motored case has a slight shift in the jet's curl. This is not surprising since the intake velocity is constantly changing as the valves and the piston moves, resulting in a dynamic jet angle. Furthermore, the motored case generally has a weaker downward velocity component  $\bar{v}$ , despite having comparable  $\bar{u}$  profiles to the other cases. This probably relates to the constantly changing jet curvature associated with the combination of the moving valves and piston as well as the decreasing suction of the piston and more resistance due to the confined volume (compare Figure 5).



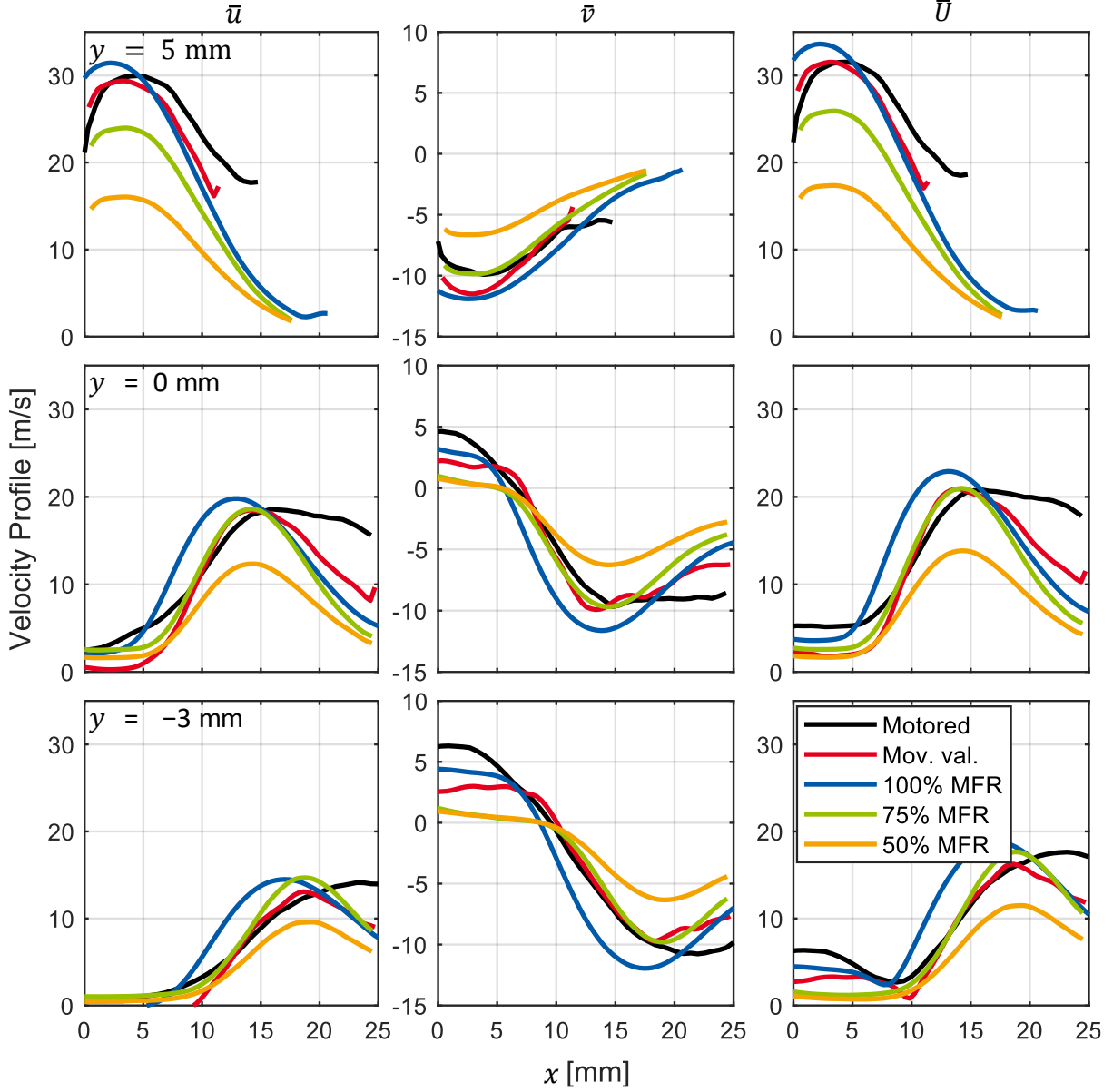


Figure 7. Mean velocity profiles taken from the valve plane.

To improve the comparability of the jets, a streamline of the mean intake jet is defined. Thereby, the centerline is defined by the 2-D streamline computed from a uniform starting position for all cases using the built-in MATLAB function *stream2* (The MathWorks, Inc. 2021). Figure 8(a) displays the defined jet profile and the newly defined streamwise component  $s$  and normal component  $n$  for the flow bench case of 100% MFR. First, the cartesian velocity components were interpolated along the streamline  $S$ . Then,  $s$  and  $n$  were obtained by rotating the components by the local streamline angle  $\theta_S$ :

$$\begin{bmatrix} \bar{s} \\ \bar{n} \end{bmatrix}_S = \begin{bmatrix} \cos\theta & -\sin\theta \\ \sin\theta & \cos\theta \end{bmatrix}_S \begin{bmatrix} \bar{u} \\ \bar{v} \end{bmatrix}_S \quad (1)$$

where the subscript  $S$  represents the position along the streamline. The origin point for the computation of the streamline was selected uniformly for all OCs such that the streamline intersects each jet through the center, beginning from the first position where a sufficient number of vectors are resolved to represent the center of the jet of the smallest FOV case; consequently, in the case of 100% MFR as shown in Figure 8(a), the origin is slightly downstream of the intake jet since Experiment II

resolves a larger jet region than Experiment I. Figure 8(b) shows the different computed intake jet streamline trajectories. All cases have nearly identical trajectories in the first 15 mm along the streamline, with the exception of the motored case, which likely stems from differences caused by the presence of the piston and therefore the overall 3-D structure of the flow field. However, 15 mm downstream of the origin point, the trajectory of the 100% MFR case also begins to curl more heavily away from the cylinder wall and differs greatly from the other cases. Although it may be expected for such velocity profiles to differ further away from the origin, such a large discrepancy in the macroscopic flow structure of the main flow bench case merits further study (see Section 3.2 Turbulence Analysis).

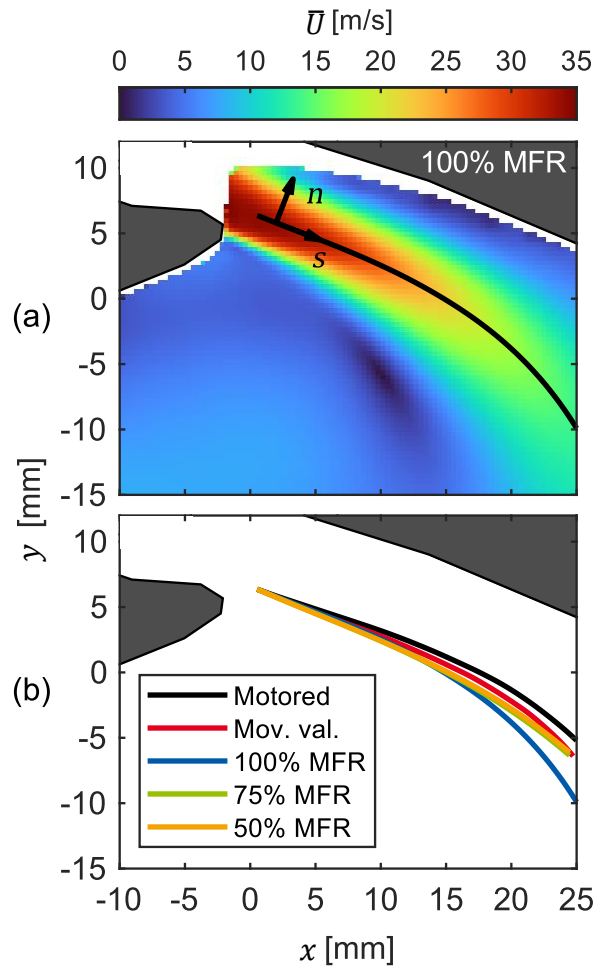


**Figure 8. (a) Example velocity magnitude in the valve plane and the streamline velocity components defined from a single origin in the middle of the intake jet for all cases. (b) Streamline trajectory for all cases.**

The mean velocity profiles of components  $s$  and  $n$  along the streamline  $S$  are shown in Figure 9. In Figure 9(a), the streamwise velocity along  $S$  for each case shows comparable values for the first 15 mm along  $S$ . It is interesting, however, that after a distance of 15 mm, the streamwise velocity of the 100% MFR case begins to sharply taper off and converge with the 75% MFR case, while that of the moving valves case decreases below the 75% MFR case. The decline of the slope of the mean streamwise velocity further from the valve exit corresponds well with a similar taper in the curl of the jet trajectory shown in Figure 8(b). As previously discussed, it is not surprising that after the initial strong shear region of the jet where the velocity gradient rapidly drops, which lasts until approximately 15 mm along  $S$  for the 100% MFR case (or 22 m/s for  $\bar{U}$  from Figure 8(a)), the mean streamwise velocities differ. However, it is noteworthy that the velocity profiles of the motored engine and moving valves cases exemplify stark contrasts from one another, demonstrating the impact of the moving

piston and confined volume on the observed velocities. Additionally, Figure 9(b) displays the mean normal component of velocity along the streamline. Per definition of a streamline, the mean normal component of velocity  $\bar{n}_s$  is centered at a velocity of zero and consists only of the mean of the velocity fluctuations about the streamline. Therefore, the stationary valve flow bench cases, which each have a sample of 25000 consecutive flow fields, have the smoothest  $\bar{n}_s$  curves. A further observation of Figure 9(b) is the slightly decreasing mean velocity along the streamline. Seeing as Figure 9 only represents the mean streamline velocity components, the instantaneous fluctuations will be explored in the next section.

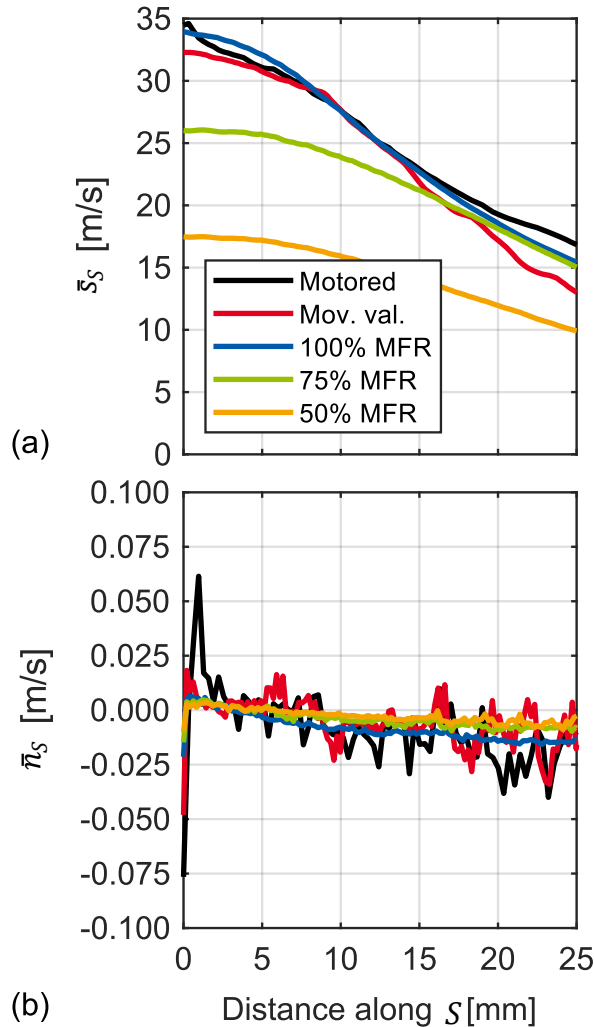


Figure 9. (a) Mean velocity profile of the streamwise component  $s$  along the streamline. (b) Mean velocity profile of the streamwise-normal component  $n$  along the streamline.

## 3.2 Turbulence Analysis

Due to several dissimilar phenomena between the intake velocities in the SP and VP between each OC, such as the difference in slope of the velocity profiles for cases with similar  $Re$  at the exit of the valve, a detailed analysis of the turbulence is required to elucidate the causes for such contrasting results.

### 3.2.1 Turbulent Kinetic Energy

The turbulent kinetic energy  $k$  quantifies the amount of turbulence in a flow field through the difference in rms velocity fluctuations. For the purposes of this work which deals with 2-D planar velocity components, only the 2-D  $k$  is considered and can be defined as:

$$k = \frac{1}{2} \left( \overline{(u')^2} + \overline{(v')^2} \right) \quad (2)$$

where the over-line bar represents the mean and the “prime” denotes the fluctuations from the mean. Turbulent kinetic energy therefore encompasses the standard deviation of the velocity over both components. Figure 10 displays the  $k$ -field over all conditions and both measurement planes. For simpler visualization, each field shares the same color bar and contains a multiplication factor shown in the upper left corner of each panel. Additionally, mean flow directions are represented by the black streamline arrows and the white boxes shown in the motored panels represent the location for the ROIs of  $\bar{k}$  displayed in Figure 11. Despite the motored, moving valves, and 100% MFR cases each having similar mean velocities, the 100% MFR case clearly has the greatest number of fluctuations in the VP downstream of the jet’s shear layer (region of the jet where the greatest velocity gradients occur, compare Figure 4), indicated by the multiplication factor of only 1. Nevertheless, apart from the differences in required multiplication factor of  $k$  to share the color map, the shape of the fluctuations for each case is generally comparable. In each case, greater velocity fluctuations appear around the shear layer of the intake jet in the VP, meaning the highest velocity jet region is relatively stable and further away more variation occurs. Yet, the extent of this high  $k$  region in the 100% MFR case is slightly wider than the other stationary valve conditions, suggesting a wider flapping motion. Likewise, in the SP, the greatest  $k$  occurs downstream of the high velocity region. However, the 100% MFR case in the SP exhibits a diagonal streak of comparatively lower  $k$ , while each other flow bench OC has a largely singular high fluctuation region similar to the motored case. This observation indicates another characteristic of the 100% MFR case that differs from the others, meriting closer inspection of the OC (see subsequent section). Furthermore, a distinctive characteristic of the dynamic cases emerges: the fluctuations of the dynamic cases attenuate and disperse more quickly, while for the stationary valve cases the region of high fluctuations continues further towards the cylinder wall at +38 mm (VP case). This likely indicates further effects due to the dynamic movement of the valves, such as the presence of different vortices lingering from earlier CADs. In other words, the smooth  $k$ -field and jet velocity towards the wall of the stationary valve flow bench appears due to the lack of dynamic effects since the jet continuously issues from the valve to the cylinder wall uninterrupted.

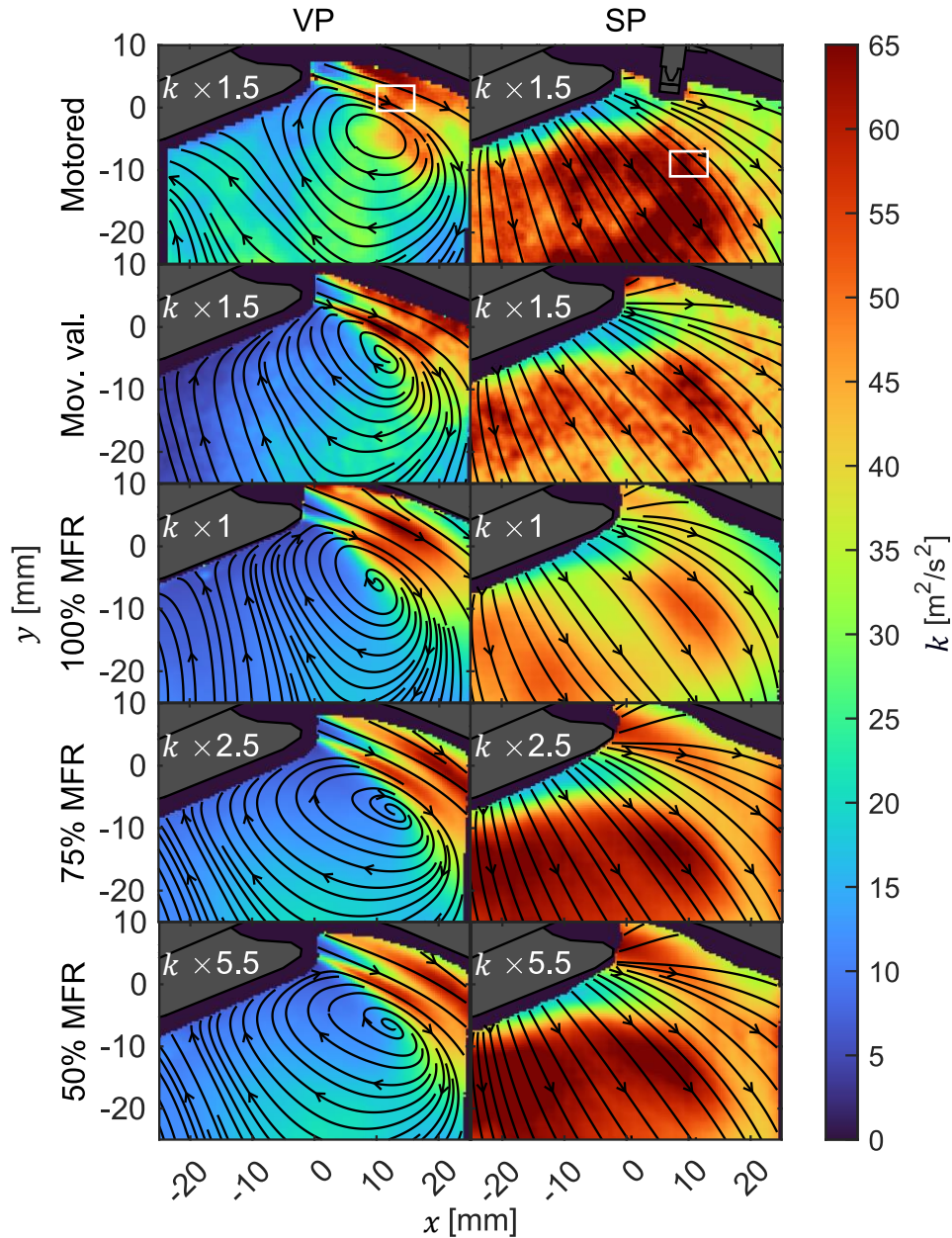


Figure 10. Turbulent kinetic energy  $k$  for each operating condition. A multiplication factor is used to plot each condition with the same colorbar. White boxes in the top panels represent the region of interest for the calculation of  $\bar{k}$  shown in Figure 11.

Rather than relying on the multiplication factors shown in Figure 10, a bar graph comparison between the mean  $k$  within the white ROIs shown in Figure 10 is displayed in Figure 11. Assuming a constant turbulence intensity,  $k$  should scale quadratically with changes in mean velocity, for example, going from 50% MFR to 100% MFR, the velocity doubles; therefore,  $k$  should increase by a factor of four in the 100% MFR case. While this trend holds true for the dynamic valve conditions in comparison with the lower MFR cases, the 100% MFR case has more than 50% greater  $\bar{k}$  in the VP than its dynamic counterparts. Subsequently, its ratios of 3.3 and 7.2 compared to the expected 1.78 and 4 of the 75% MFR and 50% MFR cases, respectively, are disproportionately high. This incongruity, especially in the VP, indicates there is likely more systematic flapping near the end of the jet than is present in the other conditions. Furthermore, since an abnormally great  $\bar{k}$  appears for the 100% MFR case in both planes, which were measured on different days, it is not simply due to measurement error; rather, the OC itself possesses an abnormality which needs further investigation.

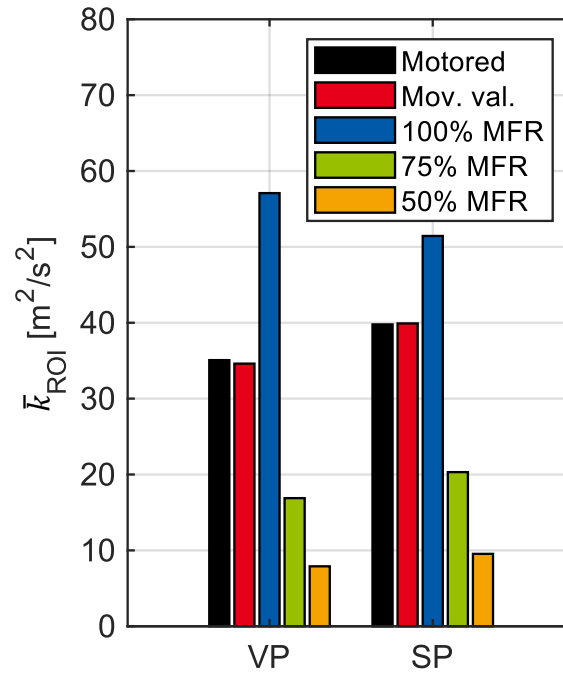


Figure 11. Mean turbulent kinetic energy  $\bar{k}$  in the white region of interest shown in Figure 10.

### 3.2.2 Coherent Jet Flapping

Further examination of the turbulence of the stationary valve flow bench operating conditions is required to interpret the contrasting observed  $k$ . Accordingly, the correlation  $R$  of the instantaneous streamline velocity components computed over all velocity fields at the fixed positions along  $S$  is calculated only in the fixed valve flow bench cases since they contain continuous data over the sample, in other words, successive velocity fields are correlated to one other. Figure 12(a) shows the mean autocorrelation of  $n$  at each position along  $S$  over all velocity fields, that is, the autocorrelation along the jet is calculated for each flow field sample, then the mean result over all fields is plotted. As observed with the analysis of  $k$ , the mean autocorrelation curve of the 100% MFR case has altogether different characteristics than the curves of the other two cases. While  $\bar{R}_n$  of the 75% MFR and 50% MFR cases only crosses zero once and then continues to approach zero after a short peak, for the 100% MFR case, it crosses zero three times as the correlation peaks at least two more times after the first zero crossing. Seeing that the autocorrelation is calculated along the streamline, the presence of more than one peak after the first zero crossing indicates that there is potentially repeating structures in the jet due to the relatively high correlation value after the first zero crossing.

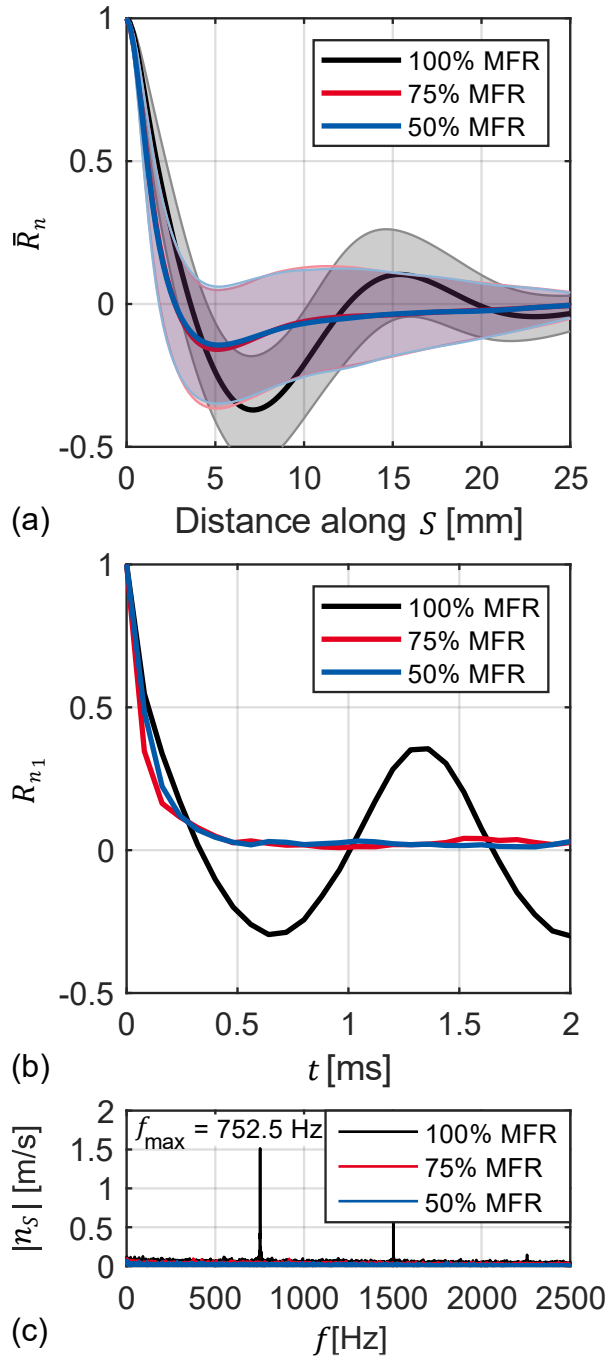


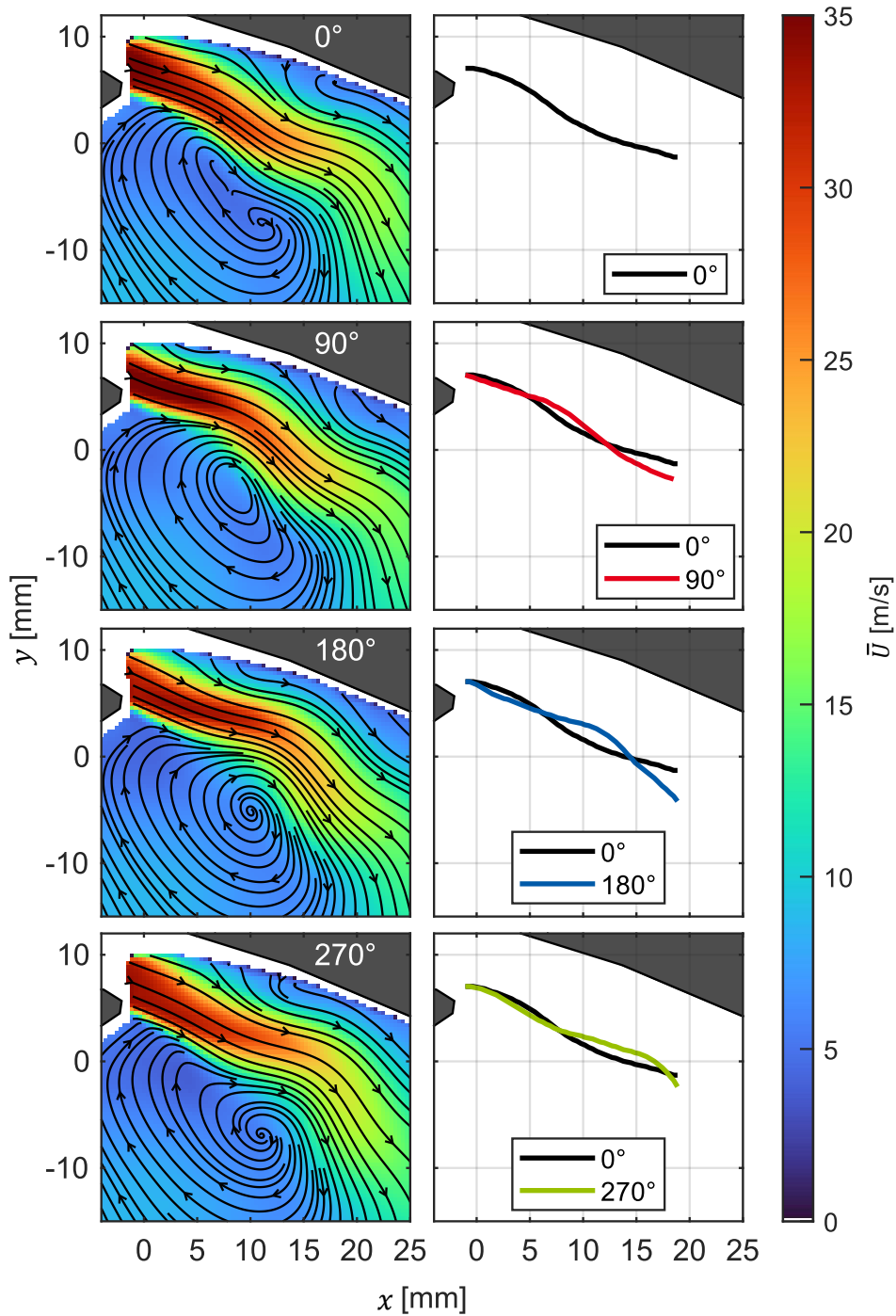
Figure 12. (a) Mean (solid line) and standard deviation (shaded area) autocorrelation of  $n_s$  over all points in time. (b) Autocorrelation of  $n_s$  over the first position along the streamline. (c) Fast Fourier transform spectrum of  $n_s$  for the stationary valve flow bench.

Figure 12(b) displays the autocorrelation curve of each stationary valve flow bench condition at the first position along  $S$  over all data points in the time series. Comparable to the mean autocorrelation curves of the normal component along  $S$ , the curves of the 75% MFR and 50% MFR cases of Figure 12(b) are different than that of the 100% MFR case. While the correlations of the lower MFR cases show exponential decay, the correlation of the 100% MFR case decays then crosses zero before following a continuous sinusoidal pattern of peaks and valleys symmetric about zero. This process of repeating increasing and decreasing correlations over the time series indicates a repeating pattern in the flow. To further examine this observed pattern, Figure 12(c) shows a fast Fourier transform (FFT) of the  $n$  component of velocity over the entire time series at the first position along  $S$ . The FFT reveals a dominant amplitude at a frequency of 752.5 Hz for the 100% MFR case with the

second and third harmonic frequencies appearing with greater amplitudes than the surrounding frequencies. Since 752.5 Hz and its harmonic frequencies are the only positions on the FFT with high amplitudes and since the frequency range of dominant amplitudes is narrow, this indicates a highly repeatable flow pattern or flapping in the intake jet. Furthermore, Figure 12(c) shows that the 75% MFR and 50% MFR cases do not have any dominant frequencies in the intake velocity at the first position along  $S$  and although it is not shown in this work, the FFT at all points along  $S$  yield the same result, pointing to purely stochastic jet flapping in these cases.

Due to the presence of a coherent jet flapping in the 100% MFR case, the structure of the jet and its flapping modes will be examined in the following. With a flapping frequency of 752.5 Hz and an imaging rate of 12.5 kHz, the flapping cycle repeats itself every 16.6 images. Over the entire sample of 25 000 flow fields, the cycle is repeated 1506 times. In order to display the periodic flapping at four successive, evenly spaced phase angles of  $0^\circ$ ,  $90^\circ$ ,  $180^\circ$ , and  $270^\circ$ , mean interpolated flow fields have to be determined. Therefore, each  $16.6^{\text{th}}$  flow field was computed by linear interpolation in time, for example, the  $16.6^{\text{th}}$  image was computed from the  $16^{\text{th}}$  and the  $17^{\text{th}}$  instantaneous flow fields, and then the mean was computed at each phase. Here, phase refers to the cycle's relative position in time from index 1 to 16.6, for example, the first phase, phase 0, contains cycles 1, 17.6, 34.2, etc. Given the desired evenly spaced phase angles of  $0^\circ$ ,  $90^\circ$ ,  $180^\circ$ , and  $270^\circ$ , the corresponding instantaneous flow fields were again determined by an interpolation, and the averaged phases for the desired phase angles or index positions were determined (that is, index position 0, 4.15, 8.3, and 12.45, respectively). Then a phase average was calculated. The resulting interpolated phases are displayed in Figure 13. The right plot of each mode displays the computed centerline of the mean jet flow compared with that of the first mode at  $0^\circ$ . The mean flow fields in Figure 13 show a progression of wave-like intake jets. Since the calculated phase averages show distinctly different flow fields with steep gradients close to the intake valves, the previously determined frequency of 752.5 Hz captures the behavior of the flapping well, indicative of a high stability of the amplitude and frequency. Furthermore, the overlapping centerline plots of the modes support this coherence through their corresponding links with the  $0^\circ$  mode, for example, the  $180^\circ$  mode has an inverted jet trajectory to that of  $0^\circ$ .





**Figure 13.** Mean velocity field of the coherent jet flapping for the 100% MFR OP. The center line of flapping modes is compared with the phase at  $0^\circ$  (right side). Modes are obtained by calculating the mean of every 4. 155<sup>th</sup> field through interpolation.

Although the flapping modes are well-predicted, the origin of the coherent flapping with only the 100% MFR stationary valve case at 9.21 mm valve lift is less clear. A turbulent two-dimensional backward-facing step (BFS) flow offers a simplified problem in comparison to intake flows of IC engines, yet has complex fluid dynamic phenomena, such as the interaction between the reattaching shear layer and the recirculation zone, that precipitate unsteady flapping motion (Ma and Schröder 2017). The flow bench configuration is analogous to BFS flows in that a stream passes over a plane with a turbulent boundary layer (valve), then a separated shear layer develops beyond the step (valve tip), and a recirculation zone forms below the shear layer. However, the flow bench intake flow must

contend with more parameters, namely, the valve seat geometry which controls the acceleration of the flow through the valve gap and affects the direction and shape of the intake jet (Freudenhammer et al. 2015), the cylinder roof which bounds the flow above the shear layer rather than below, the cylinder walls, which also direct the flow downwards and augment the recirculation zone after impingement below the curved jet, and chiefly the vortex shedding at the valve stem of the highly turbulent flow. Cross-flow-induced vortex shedding has an immense impact on the stability of many engineering applications (Kaneko et al. 2008) and has been studied in the context of intake flows passing the valve stem of engines with steady flow bench configurations (Hartmann et al. 2016; Kapitza et al. 2010). A Karman vortex street forms in the wake of a cross-flow over a bluff body, in this case, the valve stem, when periodic vortex shedding occurs. The vortex shedding frequency  $f_w$  is expressed by the dimensionless frequency, the Strouhal number  $St$ , as:

$$f_w = \frac{StU}{D} \quad (3)$$

where  $St$  is a function of the Reynolds number  $Re$ ,  $U$  is the stream velocity, and  $D$  is the characteristic length. The stream velocity was not obtained in the PIV experiments of this work since optical access in the intake ports is not possible in this configuration. However, the flow bench magnetic resonance velocimetry (MRV) measurements of Freudenhammer et al. (Freudenhammer et al. 2015) and the LES results of Haussmann et al. (Haussmann et al. 2020) under the same engine cylinder geometry, valve lift, and  $Re$  provide an estimate of the intake port velocity for the present operating condition of between 28 and 34 m/s. As in Hartmann et al. (Hartmann et al. 2016), the characteristic length  $D$  is taken as the hydraulic diameter, or 4 times the area divided by the wetted perimeter. As the valves are angled with respect to the intake flow, the wetted section of the valve stem is treated as an ellipse and the dimensions are calculated based on the angle of attack of the flow relative to the valve stem. With the angle of the free stream flow inside the intake pipe of  $24^\circ$  relative to the  $x$ -axis and the angle of the valve stem of  $23^\circ$  relative to the  $y$ -axis, the resulting angle of attack is  $43^\circ$ . The axes of the ellipse are therefore taken as the valve stem diameter of 7 mm and  $10.3 \text{ mm} \left( \frac{7 \text{ mm}}{\sin(43^\circ)} \right)$ , and result in a hydraulic diameter of 8.3 mm. Based on the empirically obtained curve of Norberg (Norberg 2001) which plots  $St$  vs  $Re$  up to very high  $Re$ ,  $St$  is likely within a range of 0.188 and 0.195 at  $Re$  between 15000 and 18200 based on the valve stem ( $\rho$  of  $1.18 \text{ kg/m}^3$ ,  $U$  of 28 m/s to 34 m/s,  $D$  of 8.3 mm, and  $\mu$  of  $1.83 \times 10^{-5} \text{ kg/ms}$ ). Using the provided  $St$  and  $U$  ranges and the calculated  $D$ , the shedding frequency is estimated to be between 634 Hz and 799 Hz, which encompasses the observed frequency of 752.5 Hz. Although the exact values of  $St$  and  $U$  of this problem are not obtainable from the given data, it is plausible that the vortices shedding from the intake valve stems are sustained through the acceleration of the valve gap leading to regular fluctuations of the intake jet in the 100% MFR case and not the others. Hartmann et al. (Hartmann et al. 2016) also demonstrated through their LES study of a similar flow bench setup that the velocity fluctuation frequencies at different locations downstream of the valve stem correspond approximately to the calculated shedding frequency, and they implied that the vortex shedding “survives” the acceleration through the valve gap having an effect on the jet. One key difference in the setup of the current study is that the observed flapping occurs in the measured  $x - y$  plane, which is orthogonal to the vortex street ( $x - z$ ) plane; nevertheless, velocity fluctuations in the vortex street plane can still have an effect on the measurement plane.

Although vortex shedding is a plausible source of the coherent jet flapping in the 100% MFR case, the other flow bench cases do not show evidence that such vortices persist through the valve gap. One possible explanation for this persistence through the valve gap in only the 100% MFR case is forced valve stem vibration induced by Karman vortex shedding. When considering a cylinder subjected to a cross-flow, synchronous vibrations are likely to occur when the shedding frequency approaches the cylinder’s, or in this case, the valve stem’s natural frequency (Kaneko et al. 2008). The

valve stem alone likely has a natural frequency on the order of kHz since it is a rigid cylinder body; however, when in combination with the valve spring and the custom valve lift bridge, which is a pair of cylinders that compress and hold the valves and springs at 9.21 mm, a decrease in the system's natural frequency to the relevant shedding frequency range could be feasible. To assess this hypothesis, raw images of the intake valves were examined for signs of visible vibration. At a first glance, no movement of the valve in the measurement plane was visible in any of the stationary valve flow bench cases. However, the images were then examined at the laser reflection line where subtle movements were detected by changing image intensity  $I$  at pixels along the gradient of the peak  $I$  due to the laser reflection. Figure 14(a) shows a zoomed in example raw image of the valve and an exemplary point (in green, enlarged for visibility) along the laser reflection where  $I$  is sampled for an FFT. Figure 14(b) displays the resulting FFT of  $I$  at the extracted point from the second image of each PIV pair for the three stationary valve flow bench cases. The FFT reveals that once again in the case of only the 100% MFR case, there is a dominant frequency of 752.5 Hz. To rule out fluctuating laser intensity as a source of the dominant frequency of the FFT, the mean intensity of three distinct, equal-sized ROIs (indicated in Figure 14(a)) is extracted and the resulting FFTs are displayed in Figure 14(c). The three ROIs were selected to display three different situations: ROI1 is in the jet region where particle voids are visible due to less Mie scattering where particles are unhomogenized due to the rotation of vortices. Here, despite the FFT using the mean  $I$ , which may smooth out the motion of the particle voids, the particle void structures coming in and out of the ROI have a clear effect on the FFT, showing the same frequency as the jet flapping and valve vibrations. Region of interest 2 is directly below the point extraction on the laser line and the mean  $I$  of this region has no dominant frequencies. Since ROI1 and ROI2 have the same size window and similar mean  $I$  at a single snapshot, the laser itself does not have a significant fluctuation of intensity that creates artificial results in the FFTs. Finally, ROI3 was selected to display a region of low signal where laser reflections are minimal and the particles are not illuminated to further rule out laser illumination fluctuations as the source for the detected frequency. The resulting FFT shows low signal without a laser reflection line or illuminated particles for contrast and no dominant frequency emerges. Therefore, since the particle void FFT of ROI1 and the valve laser reflection point FFT show the same exact dominant frequency as the jet velocity, the observed jet flapping and the slight vibrations of the intake valves are related.

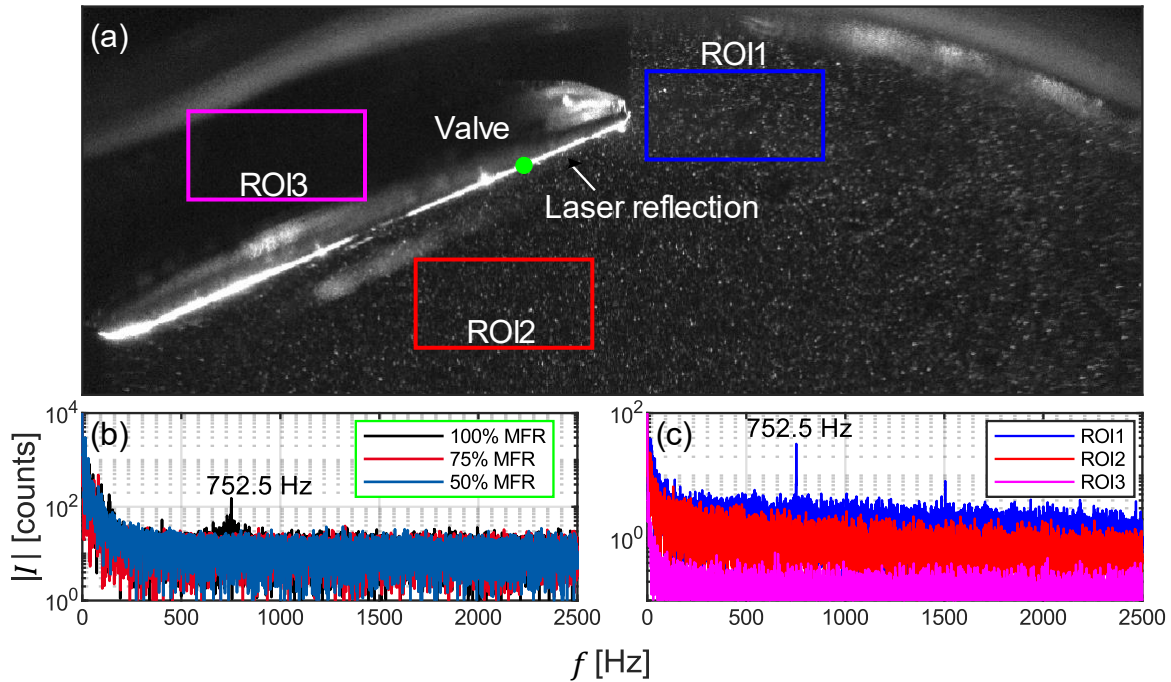


**Figure 14. (a) Zoomed in snapshot of a PIV image showing the laser reflection along the intake valve. The green dot represents the location along the laser reflection where image intensity data are extracted for the FFT Figure 14(b). The three ROI boxes represent ROIs where the mean intensity is taken for the FFT in Figure 14(c). (b) Fast Fourier transform of the intensity at a point along the laser reflection on the bottom of the intake valve. (c) Fast Fourier transform of the mean intensity of different ROIs for the 100% MFR case.**

In previous work by the authors, it was demonstrated that intake pressure oscillations can have a large influence on the intake jet of the motored engine, which can switch the direction of the curl of the intake jet from up towards the cylinder roof to down towards the piston over the course of 10 CADs (Welch et al. 2020). The prescribed changes in the OCs of the flow bench experiment demonstrate that varying the flow condition within the intake pipe can have a great effect on the resulting flow, such as the presence of coherent flapping. Consequently, it is plausible that vortex shedding of the valve stem can have an effect on dynamic valves which would affect the development of the intake jet, and later, the tumble formation in the motored engine. Since vortex shedding occurs in the highly turbulent flows of the intake and since the intake of moving valves at different engine operating conditions offers a constantly changing environment, the critical flapping regime would likely occur only for specific and short time windows during the cycle. Furthermore, investigation of these phenomena in the motored engine is warranted in which a high spatial and ultra-high temporal resolution imaging system of the valve in combination with high-speed valve plane PIV would be employed to evaluate whether vibrations occur and if coherent flapping is detected within a cycle and if these phenomena have an effect on the flow in motored engine operation.

The presence of an unexpected coherent jet flapping in the 100% MFR case illustrates the need for accurate, full-scale numerical simulations in delineating different causes of cyclical variability in engines. In the case of the flow bench under 100% MFR conditions, the exact sources for the highly predictable jet flapping remain unknown. If in future studies it is found that there is a significant effect on motored engine flows due to measured coherent jet flapping, then simulations must employ larger domains to include the intake manifold as well as more sophisticated meshing tools to realistically capture phenomena related to the valve stem. Nevertheless, in spite of the coherent jet flapping that occurs only at the mass flow rate and valve lift (9.21 mm) of the 100% MFR operating condition of this study, the mean intake jet resembles that of the motored and moving valve flow bench cases. Therefore, the air flow bench of this work presents a challenging and realistic, yet simplified test case

for numerical simulations. With the availability of data from configurations ranging from the simplified dynamics of stationary valve lifts of a single or different lifts (Hausmann et al. 2020) to more complex and realistic configurations such as the moving valves case presented in this work or the stationary valve flow bench with direct injection, the test cases offer a valuable opportunity to validate numerical models focusing on a wide range of engine applications from turbulence to wall models.

## 4 SUMMARY AND CONCLUSIONS

This paper presents a detailed investigation of the development of an engine air flow bench based on the standard operating condition A (800 rpm at 0.95 bar) of the optically accessible single cylinder research engine at TU Darmstadt. The design of the flow bench allows a continual steady or dynamic (due to moving valve geometry) flow of dry air through the normal optically accessible spray-guided cylinder head combined with a smooth outlet channel with optical access. The MFR selection of the stationary and dynamic valve operating conditions was conducted to match the mean velocity field near the intake valves of the motored engine condition at  $-270^{\circ}\text{CA}$  (9.21 mm valve lift). The resulting mean flow fields show congruous velocity characteristics near the intake valve in the upper section of the field of view of the measurements. Mean horizontal line profiles of the velocity reveal slight deviations in the slopes of the flow bench profiles compared with that of the motored engine further away from the intake valves due to the lack of in-cylinder dynamics such as the motion of the piston and increasing resistance due to the confined volume shaping the direction and formation of a tumble vortex. However, the streamwise and normal velocity components to the streamline of the center of the intake jet show even more agreement between the flow bench and motored conditions. Nevertheless, analysis of the turbulent kinetic energy revealed an unproportionate increase in velocity fluctuations present in the 100% MFR flow bench case. Through spatial and temporal autocorrelations of the flow fields along the streamline of the intake jet, it was also discovered that the 100% MFR flow bench case has a coherent flapping frequency of 752.5 Hz observable in the velocity fields. Using the observed dominant frequency, several velocity modes were reconstructed and resulting flow fields and jet trajectories show predictable flapping which is systematically repeated hundreds of times. An estimation of the vortex shedding frequency of the intake flow across the valve stem resulted in a possible range of between 634 Hz and 799 Hz, which indicates the vortices might survive the acceleration through the valve gap and they could have an effect on the flow. Furthermore, slight vibrations of the intake valve at the same flapping frequency were detected via changing intensity at pixels along the laser line reflection. The vibration was only detected in the flow bench case with the coherent flapping of the velocity field, which points towards a possible connection between the valve vibrations and the jet flapping. However, after extensive analysis, the causes of the coherent jet flapping in the 100% MFR remain unknown, which merits further investigation, especially with full-scale 3-D CFD simulations to delineate these sources.

The availability of flow bench data in various conditions with increasing complexity from stationary valves to moving valves or DI sprays with various MFRs provides the framework for the delineation of the intake flow's effects on engine phenomena and the development and validation of future CFD models. In future work, high resolution intake valve imaging and simultaneous high-speed PIV of the intake jet in different motored engine conditions would be invaluable in determining whether significant valve vibrations or coherent jet flapping during engine operation occur and whether there is a subsequent effect on the flow characteristics leading up to ignition. Due to the presence of coherent jet flapping in the flow bench, researchers conducting high-fidelity 3-D simulations can choose to select conditions affected by such phenomena to test larger-scale domains, or they can avoid such conditions to accurately validate other modeling strategies such as the employment of new wall or spray breakup models.

## DECLARATIONS

### Ethical Approval

This declaration is not applicable to this study.

### Competing Interests

The authors declare no competing interests.

### Authors' Contributions

All authors contributed to the study conception and design. BB acquired funding. Experimental preparation and data collection were performed by CW, LI, and MS. Data analysis, generation of figures, and the preparation of the first draft of the manuscript were performed by CW. All authors commented on previous versions of the manuscript. The final discussion and analysis of results were performed by CW and MS. All authors read and approved the final manuscript.

### Funding

Open Access funding was provided by Projekt DEAL. The author(s) disclosed receipt of the following financial support for the research, authorship, and/or publication of this article: Deutsche Forschungsgemeinschaft through SFB/Transregio 150 (project number 237267381-TRR150).

### Availability of Data and Materials

The computer-aided design models of the engine test bench, the boundary conditions, and mean and standard deviation of the flow fields are available online in the following links: CAD models – <https://doi.org/10.48328/tudatalib-1111>; boundary conditions – <https://doi.org/10.48328/tudatalib-1113>; velocity fields – <https://doi.org/10.48328/tudatalib-1114>. Further data are available upon request.

### Acknowledgements

CW and BB acknowledge support by the Fritz und Margot Faudi-Stiftung under project number 94. The authors kindly acknowledge Andreas Dreizler (Reactive Flows and Diagnostics, TU Darmstadt) for providing invaluable resources and advice in conducting the experiments. Additionally, the authors would like to acknowledge Andrea Pati, Hao-Pin Lien, and Christian Hasse (Simulation of reactive Thermo-Fluid Systems, TU Darmstadt) for fruitful discussion and for providing unsteady RANS data in optimizing the design of the flow bench.

### Open Access

This article is licensed under a Creative Commons Attribution 4.0 International License, which permits use, sharing, adaptation, distribution and reproduction in any medium or format, as long as you give appropriate credit to the original author(s) and the source, provide a link to the Creative Commons license, and indicate if changes were made. The images or other third-party material in this article are included in the article's Creative Commons license, unless indicated otherwise in a credit line to the material. If material is not included in the article's Creative Commons license and your intended use is not permitted by statutory regulation or exceeds the permitted use, you will need to obtain permission directly from the copyright holder. To view a copy of this license, visit <http://creativecommons.org/licenses/by/4.0/>.

## REFERENCES

Baum E, Peterson B, Böhm B, Dreizler A (2014) On The Validation of LES Applied to Internal Combustion Engine Flows: Part 1: Comprehensive Experimental Database. *Flow Turbulence Combust* 92:269–297. <https://doi.org/10.1007/s10494-013-9468-6>

- Borée J, Miles PC (2015) In-Cylinder Flow. In: Crolla D, Foster DE, Kobayashi T, Vaughan ND (eds) Encyclopedia of automotive engineering. Wiley, Chichester, West Sussex, United Kingdom, pp 1–31
- Buhl S, Hartmann F, Kaiser SA, Hasse C (2017) Investigation of an IC Engine Intake Flow Based on Highly Resolved LES and PIV. *Oil Gas Sci. Technol. – Rev. IFP Energies nouvelles* 72:15. <https://doi.org/10.2516/ogst/2017012>
- Chen H, Sick V (2017) Three-Dimensional Three-Component Air Flow Visualization in a Steady-State Engine Flow Bench Using a Plenoptic Camera. *SAE Int. J. Engines* 10:625–635. <https://doi.org/10.4271/2017-01-0614>
- Dreher D, Schmidt M, Welch C, Ourza S, Zündorf S, Maucher J, Peters S, Dreizler A, Böhm B, Hanuschkin A (2021) Deep feature learning of in-cylinder flow fields to analyze cycle-to-cycle variations in an SI engine. *International Journal of Engine Research* 22:3263–3285. <https://doi.org/10.1177/1468087420974148>
- El-Adawy M, Heikal MR, Aziz ARA, Siddiqui MI, Abdul Wahhab HA (2017) Experimental study on an IC engine in-cylinder flow using different steady-state flow benches. *Alexandria Engineering Journal* 56:727–736. <https://doi.org/10.1016/j.aej.2017.08.015>
- Falkenstein T, Bode M, Kang S, Pitsch H, Arima T, Taniguchi H Large-Eddy Simulation Study on Unsteady Effects in a Statistically Stationary SI Engine Port Flow. *SAE Technical Paper* 2015-01-0373. <https://doi.org/10.4271/2015-01-0373>
- Falkenstein T, Kang S, Davidovic M, Bode M, Pitsch H, Kamatsuchi T, Nagao J, Arima T (2017) LES of Internal Combustion Engine Flows Using Cartesian Overset Grids. *Oil & Gas Sciences and Technology – Revue d’IFP Energies nouvelles* 72:36. <https://doi.org/10.2516/ogst/2017026>
- Falkenstein T, Davidovic M, Chu H, Bode M, Kang S, Pitsch H, Murayama K, Taniguchi H (2020) Experiments and Large-Eddy Simulation for a Flowbench Configuration of the Darmstadt Optical Engine Geometry. *SAE Int. J. Engines* 13. <https://doi.org/10.4271/03-13-04-0032>
- Freudenhammer D, Baum E, Peterson B, Böhm B, Jung B, Grundmann S (2014) Volumetric intake flow measurements of an IC engine using magnetic resonance velocimetry. *Exp Fluids* 55:269. <https://doi.org/10.1007/s00348-014-1724-6>
- Freudenhammer D, Peterson B, Ding C-P, Boehm B, Grundmann S (2015) The Influence of Cylinder Head Geometry Variations on the Volumetric Intake Flow Captured by Magnetic Resonance Velocimetry. *SAE International Journal of Engines* 8:1826–1836. <https://doi.org/10.4271/2015-01-1697>
- Geschwindner C, Kranz P, Welch C, Schmidt M, Böhm B, Kaiser SA, La Morena J de (2020) Analysis of the interaction of Spray G and in-cylinder flow in two optical engines for late gasoline direct injection. *International Journal of Engine Research* 21:169–184. <https://doi.org/10.1177/1468087419881535>
- Hartmann F, Buhl S, Gleiss F, Barth P, Schild M, Kaiser SA, Hasse C (2016) Spatially Resolved Experimental and Numerical Investigation of the Flow through the Intake Port of an Internal Combustion Engine. *Oil Gas Sci. Technol. – Rev. IFP Energies nouvelles* 71:2. <https://doi.org/10.2516/ogst/2015022>
- Hausmann M, Ries F, Jeppener-Haltenhoff JB, Li Y, Schmidt M, Welch C, Illmann L, Böhm B, Nirschl H, Krause MJ, Sadiki A (2020) Evaluation of a Near-Wall-Modeled Large Eddy Lattice Boltzmann Method for the Analysis of Complex Flows Relevant to IC Engines. *Computation* 8:43. <https://doi.org/10.3390/computation8020043>
- Hyun JH, Ohm IY (2021) TKE Distribution According to the Intake Valve Angle in Steady Flow of the Pent-Roof SI Engine. *Int.J Automot. Technol.* 22:1003–1010. <https://doi.org/10.1007/s12239-021-0090-7>
- Kaneko S, Nakamura T, Inada F, Kato M (2008) Flow-induced vibrations: Classifications and lessons from practical experiences, 1st edn. Elsevier Science, Oxford

- Kapitza L, Imberdis O, Bensler HP, Willand J, Thévenin D (2010) An experimental analysis of the turbulent structures generated by the intake port of a DISI-engine. *Exp Fluids* 48:265–280. <https://doi.org/10.1007/s00348-009-0736-0>
- Liu D, Wang T, Jia M, Li W, Lu Z, Zhen X (2019) Investigation of the Boundary Layer Flow Under Engine-Like Conditions Using Particle Image Velocimetry. *Journal of Engineering for Gas Turbines and Power* 141. <https://doi.org/10.1115/1.4043444>
- Ma X, Schröder A (2017) Analysis of flapping motion of reattaching shear layer behind a two-dimensional backward-facing step. *Physics of Fluids* 29:115104. <https://doi.org/10.1063/1.4996622>
- Norberg C (2001) Flow Around a Circular Cylinder: Aspects of Fluctuating Lift. *Journal of Fluids and Structures* 15:459–469. <https://doi.org/10.1006/jfls.2000.0367>
- Schmidt M, Ding C-P, Peterson B, Dreizler A, Böhm B (2021) Near-Wall Flame and Flow Measurements in an Optically Accessible SI Engine. *Flow Turbulence Combust* 106:597–611. <https://doi.org/10.1007/s10494-020-00147-9>
- The MathWorks, Inc. (2021) MATLAB Function Reference: stream2, 2021st edn., Natick, MA
- Welch C, Schmidt M, Keskinen K, Giannakopoulos G, Boulouchos K, Dreizler A, Boehm B (2020) The Effects of Intake Pressure on In-Cylinder Gas Velocities in an Optically Accessible Single-Cylinder Research Engine. *SAE Technical Paper 2020-01-0792*. <https://doi.org/10.4271/2020-01-0792>
- Welch C, Schmidt M, Illmann L, Dreizler A, Böhm B (2023a) The Influence of Flow on Cycle-to-Cycle Variations in a Spark-Ignition Engine: A Parametric Investigation of Increasing Exhaust Gas Recirculation Levels. *Flow Turbulence Combust* 110:185–208. <https://doi.org/10.1007/s10494-022-00347-5>
- Welch C, Schmidt M, Geschwindner C, Wu S, Wooldridge MS, Böhm B (2023b) The influence of in-cylinder flows and bulk gas density on early Spray G injection in an optical research engine. *International Journal of Engine Research* 24:82–98. <https://doi.org/10.1177/14680874211042320>
- White FM (2006) *Viscous fluid flow*, 3rd edn. McGraw-Hill series in mechanical engineering. McGraw-Hill Higher Education, New York, NY, London
- Wieneke B (2015) PIV uncertainty quantification from correlation statistics. *Measurement Science and Technology* 26:74002. <https://doi.org/10.1088/0957-0233/26/7/074002>



## A.2 Paper II

### The Effects of Intake Pressure on In-Cylinder Gas Velocities in an Optically Accessible Single-Cylinder Research Engine

C. Welch, M. Schmidt, K. Keskinen, G. Giannakopoulos, K. Boulouchos, A. Dreizler, B. Böhm: The Effects of Intake Pressure on In-Cylinder Gas Velocities in an Optically Accessible Single-Cylinder Research Engine. *SAE Technical Paper 2020-01-0792* (2020) SAE International. <https://doi.org/10.4271/2020-01-0792>

#### Paper II Permissions

Used with permission of SAE International, from C. Welch, M. Schmidt, K. Keskinen, G. Giannakopoulos, K. Boulouchos, A. Dreizler, B. Böhm: The Effects of Intake Pressure on In-Cylinder Gas Velocities in an Optically Accessible Single-Cylinder Research Engine. *SAE Technical Paper 2020-01-0792* (2020) SAE International. <https://doi.org/10.4271/2020-01-0792>; permission conveyed through Copyright Clearance Center, Inc. Permission to include Paper II in this cumulative dissertation:

This is a License Agreement between Cooper Welch ("User") and Copyright Clearance Center, Inc. ("CCC") on behalf of the Rightsholder identified in the order details below. The license consists of the order details, the Marketplace Permissions General Terms and Conditions below, and any Rightsholder Terms and Conditions which are included below.

All payments must be made in full to CCC in accordance with the Marketplace Permissions General Terms and Conditions below.

<b>Order Date</b>	20-Jun-2023	<b>Type of Use</b>	Republish in a thesis/dissertation
<b>Order License ID</b>	1367238-1	<b>Publisher Portion</b>	SAE International Chapter/article
<b>System ID</b>	2020-01-0792		

## LICENSED CONTENT

<b>Publication Title</b>	The Effects of Intake Pressure on In-Cylinder Gas Velocities in an Optically Accessible Single-Cylinder Research Engine : 2020-01-0792	<b>Rightsholder</b>	SAE International
<b>Author/Editor</b>	Welch, Cooper, Schmidt, Marius	<b>Publication Type</b>	Report
<b>Date</b>	01/01/2020		

## REQUEST DETAILS

<b>Portion Type</b>	Chapter/article	<b>Rights Requested</b>	Main product
<b>Page Range(s)</b>	1-12	<b>Distribution</b>	Worldwide
<b>Total Number of Pages</b>	12	<b>Translation</b>	Original language of publication
<b>Format (select all that apply)</b>	Print, Electronic	<b>Copies for the Disabled?</b>	No
<b>Who Will Republish the Content?</b>	Author of requested content	<b>Minor Editing Privileges?</b>	No
<b>Duration of Use</b>	Life of current edition	<b>Incidental Promotional Use?</b>	No
<b>Lifetime Unit Quantity</b>	Up to 499	<b>Currency</b>	EUR

## NEW WORK DETAILS

<b>Title</b>	The Influence of In-Cylinder Flows on Spark-Ignition Engine Combustion	<b>Institution Name</b>	Technische Universität Darmstadt
<b>Instructor Name</b>	Cooper Welch	<b>Expected Presentation Date</b>	2023-10-17

## ADDITIONAL DETAILS

<b>Order Reference Number</b>	WELCH_2023	<b>The Requesting Person/Organization to Appear on the License</b>	Cooper Welch
-------------------------------	------------	--	--------------

## REQUESTED CONTENT DETAILS

<b>Title, Description or Numeric Reference of the Portion(s)</b>	Whole article	<b>Title of the Article/Chapter the Portion Is From</b>	The Effects of Intake Pressure on In-Cylinder Gas Velocities in an Optically Accessible Single-Cylinder Research Engine
<b>Editor of Portion(s)</b>	N/A	<b>Author of Portion(s)</b>	Welch, Cooper; Schmidt, Marius; Keskinen, Karri; Giannakopoulos, George; Boulouchos, Konstantinos; Dreizler, Andreas; Boehm, Benjamin
<b>Volume / Edition</b>	N/A	<b>Issue, if Republishing an Article From a Serial</b>	N/A
<b>Page or Page Range of Portion</b>	1-12	<b>Publication Date of Portion</b>	2020-04-14

## Marketplace Permissions General Terms and Conditions

The following terms and conditions (“General Terms”), together with any applicable Publisher Terms and Conditions, govern User’s use of Works pursuant to the Licenses granted by Copyright Clearance Center, Inc. (“CCC”) on behalf of the applicable Rightsholders of such Works through CCC’s applicable Marketplace transactional licensing services (each, a “Service”).

1) **Definitions.** For purposes of these General Terms, the following definitions apply:

“License” is the licensed use the User obtains via the Marketplace platform in a particular licensing transaction, as set forth in the Order Confirmation.

“Order Confirmation” is the confirmation CCC provides to the User at the conclusion of each Marketplace transaction. “Order Confirmation Terms” are additional terms set forth on specific Order Confirmations not set forth in the General Terms that can include terms applicable to a particular CCC transactional licensing service and/or any Rightsholder-specific terms.

“Rightsholder(s)” are the holders of copyright rights in the Works for which a User obtains licenses via the Marketplace platform, which are displayed on specific Order Confirmations.

“Terms” means the terms and conditions set forth in these General Terms and any additional Order Confirmation Terms collectively.

“User” or “you” is the person or entity making the use granted under the relevant License. Where the person accepting the Terms on behalf of a User is a freelancer or other third party who the User authorized to accept the General Terms on the User’s behalf, such person shall be deemed jointly a User for purposes of such Terms.

“Work(s)” are the copyright protected works described in relevant Order Confirmations.

2) **Description of Service.** CCC’s Marketplace enables Users to obtain Licenses to use one or more Works in accordance with all relevant Terms. CCC grants Licenses as an agent on behalf of the copyright rightsholder identified in the relevant Order Confirmation.

3) **Applicability of Terms.** The Terms govern User’s use of Works in connection with the relevant License. In the event of any conflict between General Terms and Order Confirmation Terms, the latter shall govern. User acknowledges that Rightsholders have complete discretion whether to grant any permission, and whether to place any limitations on any grant, and that CCC has no right to supersede or to modify any such discretionary act by a Rightsholder.

4) **Representations; Acceptance.** By using the Service, User represents and warrants that User has been duly authorized by the User to accept, and hereby does accept, all Terms.

5) **Scope of License; Limitations and Obligations.** All Works and all rights therein, including copyright rights, remain the sole and exclusive property of the Rightsholder. The License provides only those rights expressly set forth in the terms and conveys no other rights in any Works

6) **General Payment Terms.** User may pay at time of checkout by credit card or choose to be invoiced. If the User chooses to be invoiced, the User shall: (i) remit payments in the manner identified on specific invoices, (ii) unless otherwise specifically stated in an Order Confirmation or separate written agreement, Users shall remit payments upon receipt of the relevant invoice from CCC, either by delivery or notification of availability of the invoice via the Marketplace

platform, and (iii) if the User does not pay the invoice within 30 days of receipt, the User may incur a service charge of 1.5% per month or the maximum rate allowed by applicable law, whichever is less. While User may exercise the rights in the License immediately upon receiving the Order Confirmation, the License is automatically revoked and is null and void, as if it had never been issued, if CCC does not receive complete payment on a timely basis.

7) **General Limits on Use.** Unless otherwise provided in the Order Confirmation, any grant of rights to User (i) involves only the rights set forth in the Terms and does not include subsequent or additional uses, (ii) is non-exclusive and non-transferable, and (iii) is subject to any and all limitations and restrictions (such as, but not limited to, limitations on duration of use or circulation) included in the Terms. Upon completion of the licensed use as set forth in the Order Confirmation, User shall either secure a new permission for further use of the Work(s) or immediately cease any new use of the Work(s) and shall render inaccessible (such as by deleting or by removing or severing links or other locators) any further copies of the Work. User may only make alterations to the Work if and as expressly set forth in the Order Confirmation. No Work may be used in any way that is unlawful, including without limitation if such use would violate applicable sanctions laws or regulations, would be defamatory, violate the rights of third parties (including such third parties' rights of copyright, privacy, publicity, or other tangible or intangible property), or is otherwise illegal, sexually explicit, or obscene. In addition, User may not conjoin a Work with any other material that may result in damage to the reputation of the Rightsholder. Any unlawful use will render any licenses hereunder null and void. User agrees to inform CCC if it becomes aware of any infringement of any rights in a Work and to cooperate with any reasonable request of CCC or the Rightsholder in connection therewith.

8) **Third Party Materials.** In the event that the material for which a License is sought includes third party materials (such as photographs, illustrations, graphs, inserts and similar materials) that are identified in such material as having been used by permission (or a similar indicator), User is responsible for identifying, and seeking separate licenses (under this Service, if available, or otherwise) for any of such third party materials; without a separate license, User may not use such third party materials via the License.

9) **Copyright Notice.** Use of proper copyright notice for a Work is required as a condition of any License granted under the Service. Unless otherwise provided in the Order Confirmation, a proper copyright notice will read substantially as follows: "Used with permission of [Rightsholder's name], from [Work's title, author, volume, edition number and year of copyright]; permission conveyed through Copyright Clearance Center, Inc." Such notice must be provided in a reasonably legible font size and must be placed either on a cover page or in another location that any person, upon gaining access to the material which is the subject of a permission, shall see, or in the case of republication Licenses, immediately adjacent to the Work as used (for example, as part of a by-line or footnote) or in the place where substantially all other credits or notices for the new work containing the republished Work are located. Failure to include the required notice results in loss to the Rightsholder and CCC, and the User shall be liable to pay liquidated damages for each such failure equal to twice the use fee specified in the Order Confirmation, in addition to the use fee itself and any other fees and charges specified.

10) **Indemnity.** User hereby indemnifies and agrees to defend the Rightsholder and CCC, and their respective employees and directors, against all claims, liability, damages, costs, and expenses, including legal fees and expenses, arising out of any use of a Work beyond the scope of the rights granted herein and in the Order Confirmation, or any use of a Work which has been altered in any unauthorized way by User, including claims of defamation or infringement of rights of copyright, publicity, privacy, or other tangible or intangible property.

11) **Limitation of Liability.** UNDER NO CIRCUMSTANCES WILL CCC OR THE RIGHTSHOLDER BE LIABLE FOR ANY DIRECT, INDIRECT, CONSEQUENTIAL, OR INCIDENTAL DAMAGES (INCLUDING WITHOUT LIMITATION DAMAGES FOR LOSS OF BUSINESS PROFITS OR INFORMATION, OR FOR BUSINESS INTERRUPTION) ARISING OUT OF THE USE OR INABILITY TO USE A WORK, EVEN IF ONE OR BOTH OF THEM HAS BEEN ADVISED OF THE POSSIBILITY OF SUCH DAMAGES. In any event, the total liability of the Rightsholder and CCC (including their respective employees and directors) shall not exceed the total amount actually paid by User for the relevant License. User assumes full liability for the actions and omissions of its principals, employees, agents, affiliates, successors, and assigns.

12) **Limited Warranties.** THE WORK(S) AND RIGHT(S) ARE PROVIDED "AS IS." CCC HAS THE RIGHT TO GRANT TO USER THE RIGHTS GRANTED IN THE ORDER CONFIRMATION DOCUMENT. CCC AND THE RIGHTSHOLDER DISCLAIM ALL OTHER WARRANTIES RELATING TO THE WORK(S) AND RIGHT(S), EITHER EXPRESS OR IMPLIED, INCLUDING WITHOUT LIMITATION IMPLIED WARRANTIES OF MERCHANTABILITY OR FITNESS FOR A PARTICULAR PURPOSE. ADDITIONAL RIGHTS MAY BE REQUIRED TO USE ILLUSTRATIONS, GRAPHS, PHOTOGRAPHS, ABSTRACTS, INSERTS, OR OTHER PORTIONS OF THE WORK (AS OPPOSED TO THE ENTIRE WORK) IN A MANNER CONTEMPLATED BY USER; USER UNDERSTANDS AND AGREES THAT NEITHER CCC NOR THE RIGHTSHOLDER MAY HAVE SUCH ADDITIONAL RIGHTS TO GRANT.

13) **Effect of Breach.** Any failure by User to pay any amount when due, or any use by User of a Work beyond the scope of the License set forth in the Order Confirmation and/or the Terms, shall be a material breach of such License. Any breach not cured within 10 days of written notice thereof shall result in immediate termination of such License without further notice. Any unauthorized (but licensable) use of a Work that is terminated immediately upon notice thereof may be liquidated by payment of the Rightsholder's ordinary license price therefor; any unauthorized (and unlicensable) use that is not terminated immediately for any reason (including, for example, because materials containing the Work cannot

reasonably be recalled) will be subject to all remedies available at law or in equity, but in no event to a payment of less than three times the Rightsholder's ordinary license price for the most closely analogous licensable use plus Rightsholder's and/or CCC's costs and expenses incurred in collecting such payment.

14) **Additional Terms for Specific Products and Services.** If a User is making one of the uses described in this Section 14, the additional terms and conditions apply:

a) ***Print Uses of Academic Course Content and Materials (photocopies for academic coursepacks or classroom handouts).*** For photocopies for academic coursepacks or classroom handouts the following additional terms apply:

i) The copies and anthologies created under this License may be made and assembled by faculty members individually or at their request by on-campus bookstores or copy centers, or by off-campus copy shops and other similar entities.

ii) No License granted shall in any way: (i) include any right by User to create a substantively non-identical copy of the Work or to edit or in any other way modify the Work (except by means of deleting material immediately preceding or following the entire portion of the Work copied) (ii) permit "publishing ventures" where any particular anthology would be systematically marketed at multiple institutions.

iii) Subject to any Publisher Terms (and notwithstanding any apparent contradiction in the Order Confirmation arising from data provided by User), any use authorized under the academic pay-per-use service is limited as follows:

A) any License granted shall apply to only one class (bearing a unique identifier as assigned by the institution, and thereby including all sections or other subparts of the class) at one institution;

B) use is limited to not more than 25% of the text of a book or of the items in a published collection of essays, poems or articles;

C) use is limited to no more than the greater of (a) 25% of the text of an issue of a journal or other periodical or (b) two articles from such an issue;

D) no User may sell or distribute any particular anthology, whether photocopied or electronic, at more than one institution of learning;

E) in the case of a photocopy permission, no materials may be entered into electronic memory by User except in order to produce an identical copy of a Work before or during the academic term (or analogous period) as to which any particular permission is granted. In the event that User shall choose to retain materials that are the subject of a photocopy permission in electronic memory for purposes of producing identical copies more than one day after such retention (but still within the scope of any permission granted), User must notify CCC of such fact in the applicable permission request and such retention shall constitute one copy actually sold for purposes of calculating permission fees due; and

F) any permission granted shall expire at the end of the class. No permission granted shall in any way include any right by User to create a substantively non-identical copy of the Work or to edit or in any other way modify the Work (except by means of deleting material immediately preceding or following the entire portion of the Work copied).

iv) Books and Records; Right to Audit. As to each permission granted under the academic pay-per-use Service, User shall maintain for at least four full calendar years books and records sufficient for CCC to determine the numbers of copies made by User under such permission. CCC and any representatives it may designate shall have the right to audit such books and records at any time during User's ordinary business hours, upon two days' prior notice. If any such audit shall determine that User shall have underpaid for, or underreported, any photocopies sold or by three percent (3%) or more, then User shall bear all the costs of any such audit; otherwise, CCC shall bear the costs of any such audit. Any amount determined by such audit to have been underpaid by User shall immediately be paid to CCC by User, together with interest thereon at the rate of 10% per annum from the date such amount was originally due. The provisions of this paragraph shall survive the termination of this License for any reason.

b) ***Digital Pay-Per-Uses of Academic Course Content and Materials (e-coursepacks, electronic reserves, learning management systems, academic institution intranets).*** For uses in e-coursepacks, posts in electronic reserves, posts in learning management systems, or posts on academic institution intranets, the following additional terms apply:

i) The pay-per-uses subject to this Section 14(b) include:

A) **Posting e-reserves, course management systems, e-coursepacks for text-based content**, which grants authorizations to import requested material in electronic format, and allows electronic access to this material to members of a designated college or university class, under the direction of an instructor designated by the college or university, accessible only under appropriate electronic controls (e.g., password);



**B) Posting e-reserves, course management systems, e-coursepacks for material consisting of photographs or other still images not embedded in text**, which grants not only the authorizations described in Section 14(b)(i)(A) above, but also the following authorization: to include the requested material in course materials for use consistent with Section 14(b)(i)(A) above, including any necessary resizing, reformatting or modification of the resolution of such requested material (provided that such modification does not alter the underlying editorial content or meaning of the requested material, and provided that the resulting modified content is used solely within the scope of, and in a manner consistent with, the particular authorization described in the Order Confirmation and the Terms), but not including any other form of manipulation, alteration or editing of the requested material;

**C) Posting e-reserves, course management systems, e-coursepacks or other academic distribution for audiovisual content**, which grants not only the authorizations described in Section 14(b)(i)(A) above, but also the following authorizations: (i) to include the requested material in course materials for use consistent with Section 14(b)(i)(A) above; (ii) to display and perform the requested material to such members of such class in the physical classroom or remotely by means of streaming media or other video formats; and (iii) to "clip" or reformat the requested material for purposes of time or content management or ease of delivery, provided that such "clipping" or reformatting does not alter the underlying editorial content or meaning of the requested material and that the resulting material is used solely within the scope of, and in a manner consistent with, the particular authorization described in the Order Confirmation and the Terms. Unless expressly set forth in the relevant Order Confirmation, the License does not authorize any other form of manipulation, alteration or editing of the requested material.

ii) Unless expressly set forth in the relevant Order Confirmation, no License granted shall in any way: (i) include any right by User to create a substantively non-identical copy of the Work or to edit or in any other way modify the Work (except by means of deleting material immediately preceding or following the entire portion of the Work copied or, in the case of Works subject to Sections 14(b)(1)(B) or (C) above, as described in such Sections) (ii) permit "publishing ventures" where any particular course materials would be systematically marketed at multiple institutions.

iii) Subject to any further limitations determined in the Rightsholder Terms (and notwithstanding any apparent contradiction in the Order Confirmation arising from data provided by User), any use authorized under the electronic course content pay-per-use service is limited as follows:

A) any License granted shall apply to only one class (bearing a unique identifier as assigned by the institution, and thereby including all sections or other subparts of the class) at one institution;

B) use is limited to not more than 25% of the text of a book or of the items in a published collection of essays, poems or articles;

C) use is limited to not more than the greater of (a) 25% of the text of an issue of a journal or other periodical or (b) two articles from such an issue;

D) no User may sell or distribute any particular materials, whether photocopied or electronic, at more than one institution of learning;

E) electronic access to material which is the subject of an electronic-use permission must be limited by means of electronic password, student identification or other control permitting access solely to students and instructors in the class;

F) User must ensure (through use of an electronic cover page or other appropriate means) that any person, upon gaining electronic access to the material, which is the subject of a permission, shall see:

- a proper copyright notice, identifying the Rightsholder in whose name CCC has granted permission,
- a statement to the effect that such copy was made pursuant to permission,
- a statement identifying the class to which the material applies and notifying the reader that the material has been made available electronically solely for use in the class, and
- a statement to the effect that the material may not be further distributed to any person outside the class, whether by copying or by transmission and whether electronically or in paper form, and User must also ensure that such cover page or other means will print out in the event that the person accessing the material chooses to print out the material or any part thereof.

G) any permission granted shall expire at the end of the class and, absent some other form of authorization, User is thereupon required to delete the applicable material from any electronic storage or to block electronic access to the applicable material.

iv) Uses of separate portions of a Work, even if they are to be included in the same course material or the same university or college class, require separate permissions under the electronic course content pay-per-use Service. Unless otherwise provided in the Order Confirmation, any grant of rights to User is limited to use completed no later than the end of the academic term (or analogous period) as to which any particular permission is granted.

v) Books and Records; Right to Audit. As to each permission granted under the electronic course content Service, User shall maintain for at least four full calendar years books and records sufficient for CCC to determine the numbers of copies made by User under such permission. CCC and any representatives it may designate shall have the right to audit such books and records at any time during User's ordinary business hours, upon two days' prior notice. If any such audit shall determine that User shall have underpaid for, or underreported, any electronic copies used by three percent (3%) or more, then User shall bear all the costs of any such audit; otherwise, CCC shall bear the costs of any such audit. Any amount determined by such audit to have been underpaid by User shall immediately be paid to CCC by User, together with interest thereon at the rate of 10% per annum from the date such amount was originally due. The provisions of this paragraph shall survive the termination of this license for any reason.

c) ***Pay-Per-Use Permissions for Certain Reproductions (Academic photocopies for library reserves and interlibrary loan reporting) (Non-academic internal/external business uses and commercial document delivery).*** The License expressly excludes the uses listed in Section (c)(i)-(v) below (which must be subject to separate license from the applicable Rightsholder) for: academic photocopies for library reserves and interlibrary loan reporting; and non-academic internal/external business uses and commercial document delivery.

i) electronic storage of any reproduction (whether in plain-text, PDF, or any other format) other than on a transitory basis;

ii) the input of Works or reproductions thereof into any computerized database;

iii) reproduction of an entire Work (cover-to-cover copying) except where the Work is a single article;

iv) reproduction for resale to anyone other than a specific customer of User;

v) republication in any different form. Please obtain authorizations for these uses through other CCC services or directly from the rightsholder.

Any license granted is further limited as set forth in any restrictions included in the Order Confirmation and/or in these Terms.

d) ***Electronic Reproductions in Online Environments (Non-Academic-email, intranet, internet and extranet).*** For "electronic reproductions", which generally includes e-mail use (including instant messaging or other electronic transmission to a defined group of recipients) or posting on an intranet, extranet or Intranet site (including any display or performance incidental thereto), the following additional terms apply:

i) Unless otherwise set forth in the Order Confirmation, the License is limited to use completed within 30 days for any use on the Internet, 60 days for any use on an intranet or extranet and one year for any other use, all as measured from the "republication date" as identified in the Order Confirmation, if any, and otherwise from the date of the Order Confirmation.

ii) User may not make or permit any alterations to the Work, unless expressly set forth in the Order Confirmation (after request by User and approval by Rightsholder); provided, however, that a Work consisting of photographs or other still images not embedded in text may, if necessary, be resized, reformatted or have its resolution modified without additional express permission, and a Work consisting of audiovisual content may, if necessary, be "clipped" or reformatted for purposes of time or content management or ease of delivery (provided that any such resizing, reformatting, resolution modification or "clipping" does not alter the underlying editorial content or meaning of the Work used, and that the resulting material is used solely within the scope of, and in a manner consistent with, the particular License described in the Order Confirmation and the Terms.

## 15) Miscellaneous.

a) User acknowledges that CCC may, from time to time, make changes or additions to the Service or to the Terms, and that Rightsholder may make changes or additions to the Rightsholder Terms. Such updated Terms will replace the prior terms and conditions in the order workflow and shall be effective as to any subsequent Licenses but shall not apply to Licenses already granted and paid for under a prior set of terms.

b) Use of User-related information collected through the Service is governed by CCC's privacy policy, available online at [www.copyright.com/about/privacy-policy/](http://www.copyright.com/about/privacy-policy/).

c) The License is personal to User. Therefore, User may not assign or transfer to any other person (whether a natural person or an organization of any kind) the License or any rights granted thereunder; provided, however, that, where

applicable, User may assign such License in its entirety on written notice to CCC in the event of a transfer of all or substantially all of User's rights in any new material which includes the Work(s) licensed under this Service.

d) No amendment or waiver of any Terms is binding unless set forth in writing and signed by the appropriate parties, including, where applicable, the Rightsholder. The Rightsholder and CCC hereby object to any terms contained in any writing prepared by or on behalf of the User or its principals, employees, agents or affiliates and purporting to govern or otherwise relate to the License described in the Order Confirmation, which terms are in any way inconsistent with any Terms set forth in the Order Confirmation, and/or in CCC's standard operating procedures, whether such writing is prepared prior to, simultaneously with or subsequent to the Order Confirmation, and whether such writing appears on a copy of the Order Confirmation or in a separate instrument.

e) The License described in the Order Confirmation shall be governed by and construed under the law of the State of New York, USA, without regard to the principles thereof of conflicts of law. Any case, controversy, suit, action, or proceeding arising out of, in connection with, or related to such License shall be brought, at CCC's sole discretion, in any federal or state court located in the County of New York, State of New York, USA, or in any federal or state court whose geographical jurisdiction covers the location of the Rightsholder set forth in the Order Confirmation. The parties expressly submit to the personal jurisdiction and venue of each such federal or state court.

*Last updated October 2022*



---

# DECLARATION ON THE CONTRIBUTION TO THE SCIENTIFIC PUBLICATION

## Erklärung zum Eigenanteil der wissenschaftlichen Veröffentlichung

Cooper Welch, M.Sc.

### PAPER

C. Welch, M. Schmidt, K. Keskinen, G. Giannakopoulos, K. Boulouchos, A. Dreizler, B. Böhm: The Effects of Intake Pressure on In-Cylinder Gas Velocities in an Optically Accessible Single-Cylinder Research Engine. *SAE Technical Paper* 2020-01-0792 (2020). <https://doi.org/10.4271/2020-01-0792>

### CO-AUTHORS

Marius Schmidt, M.Sc.  
Karri Keskinen, D.Sc.  
George Giannakopoulos, Ph.D.

Konstantinos Boulouchos, Prof. em. Dr.  
Andreas Dreizler, Prof. Dr. habil.  
Benjamin Böhm, Dr.-Ing.

### INDIVIDUAL CONTRIBUTIONS

- **Cooper Welch**
  - Jointly conducted experiments with Marius Schmidt.
  - Jointly conducted processing and analysis of experimental data with Marius Schmidt.
  - Main author of the paper: performed literature research, generated schematic figures, wrote most of the manuscript, and wrote and managed the review process.
- **Marius Schmidt**
  - Conceived the hypothesis leading to the conduction of the experiments.
  - Jointly conducted experiments with Cooper Welch.
  - Jointly conducted processing and analysis of experimental data with Cooper Welch.
  - Leading author of the paper: generated most of figures, coordinated cooperation with simulation researchers, and wrote part of the manuscript.
- **Karri Keskinen and George Giannakopoulos**

Conducted or guided in the conduction of GT-POWER simulations. Wrote the Numerical Setup section of the manuscript. Supported in the interpretation and discussion of the results and the proofreading of the manuscript.
- **Konstantinos Boulouchos, Andreas Dreizler, and Benjamin Böhm**

Provided resources for the conduction of the experiments or simulations. Supported in the interpretation and discussion of the results and the proofreading of the manuscript.

### OVERALL CONTRIBUTION OF COOPER WELCH

A leading role in the conduction of the experiments, data analysis and interpretation, and writing of the manuscript.


### USE OF PAPER CONTENTS IN OTHER DISSERTATIONS

This publication is not the subject of another ongoing or completed dissertation.

---


SIGNATURES OF ALL AUTHORS

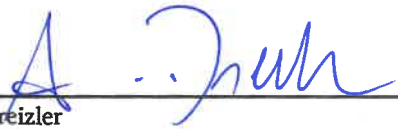
  
\_\_\_\_\_  
Cooper Welch

  
\_\_\_\_\_  
George Giannakopoulos

  
\_\_\_\_\_  
Marius Schmidt

  
\_\_\_\_\_  
Konstantinos Boulouchos

  
\_\_\_\_\_  
Karri Keskinen

  
\_\_\_\_\_  
Andreas Dreizler

  
\_\_\_\_\_  
Benjamin Böhm

# The Effects of Intake Pressure on In-Cylinder Gas Velocities in an Optically Accessible Single-Cylinder Research Engine

Cooper Welch<sup>1</sup>, Marius Schmidt<sup>1</sup>, Karri Keskinen<sup>2</sup>, George Giannakopoulos<sup>2</sup>, Konstantinos Boulouchos<sup>2</sup>, Andreas Dreizler<sup>1</sup>, Benjamin Böhm<sup>1</sup>

<sup>1</sup>Technical University of Darmstadt, Department of Mechanical Engineering, Reactive Flows and Diagnostics, Otto-Berndt-Str. 3, 64287 Darmstadt, Germany

<sup>2</sup>ETH Zürich, Department of Mechanical and Process, Leonhardstrasse 21, 8092 Zürich, Switzerland

## Abstract

Particle image velocimetry measurements of the in-cylinder flow in an optically accessible single-cylinder research engine were taken to better understand the effects of intake pressure variations on the flow field. At a speed of 1500 rpm, the engine was run at six different intake pressure loads from 0.4 to 0.95 bar under motored operation. The average velocity fields show that the tumble center position is located closer to the piston and velocity magnitudes decrease with increasing pressure load. A closer investigation of the intake flow near the valves reveals sharp temporal gradients and differences in maximum and minimum velocity with varying intake pressure load which are attributed to intake pressure oscillations. Despite measures to eliminate acoustic oscillations in the intake system, high-frequency pressure oscillations are shown to be caused by the backflow of air from the exhaust to the intake pipe when the valves open, exciting acoustic modes in the fluid volume. This phenomenon is much stronger in the throttled-load cases because of the high differential between exhaust and intake gases. In addition, 1-D simulations of the engine at varying intake pressures and pipe geometries provide insight into the interactions between the pressure variations, high-frequency oscillations, and intake flow.

## 1 Introduction

In-cylinder flows are responsible for determining key processes of engine combustion such as mixing, ignition, and flame propagation which all define engine performance and efficiency. In spark-ignited (SI) internal combustion engines, the in-cylinder flow is typically characterized by a large-scale vortex rotating perpendicular to the cylinder axis, the so-called tumble flow. The tumble structure is unstable near the end of compression, resulting in tumble breakdown where its kinetic energy is transferred to smaller scale turbulence [1]. This combination of large-scale flow and turbulence characterizes fuel-air preparation [2, 3, 4], ignition [5, 6], and early flame propagation [7, 8]. For example, from using simultaneous particle image velocimetry (PIV) and spray [3] or spark visualizations [9], it was shown that variations in the tumble vortex location from cycle-to-cycle can significantly alter the performance of individual cycles within steady-state engine operation. The creation of this organized large-scale tumble rotation strongly depends on the engine geometry, where small changes of the intake system and in-cylinder geometry can have a strong effect on tumble strength and the tumble vortex location [10, 11]. Further, the tumble is affected by more phenomena including varying initial conditions, periodically varying boundary conditions during the cycle, unsteady intake flow, and stochastic flow events.

The intake flow is determined by valve timing and piston motion and is therefore inherently unsteady. The coupling of the unsteady intake flow with the acoustics of the intake system has been recognized to impact volumetric efficiency. A properly designed intake system should take advantage of the inertia and elasticity of the gas flow. This so-called “tuning” of the intake system can lead to

significant gains in engine performance for a given engine speed and can increase engine torque by more than 10% [12]. The early stage of the intake process is determined by the instantaneous piston velocity and the open area under the valve. Later on, the action of resonant waves dominates the intake process. The flow over the intake valves is coupled with the wave dynamics in the intake system by a two-way coupling: the unsteady flow causes wave action, which in turn influences the unsteady flow if the waves are sufficiently intense. The waves can be reflected from many points in the intake system resulting in complex acoustic fields [13].

The induction related dynamic phenomena not only affects the intake flow but can influence the evolution of the in-cylinder flow over the entire cycle. Margary et al. have shown using in-cylinder flow measurements in a motored diesel engine using laser Doppler velocimetry (LDV) that the swirl flow magnitude significantly increased as resonance of the intake system was reached [14]. A variation of the intake duct length revealed that the intake duct acted as a quarter-wavelength pipe for tuned conditions when the system was in resonance. In the absence of such induction-related dynamic phenomena, the flow field scaled well with engine speed for the investigated speed range of 1000 to 3000 rpm. The interaction of the intake runner and in-cylinder flow was investigated by Justham et al. using two high-speed PIV systems simultaneously [15]. The flow measurements in the runner revealed oscillations and a backflow during the intake valves' closure period. The bulk flow motion was found to behave in a repeatable manner from cycle-to-cycle with only variations in flow structure details. The work by Lee et al. [16] confirms the repeatability of the bulk flow through the valves. They report a flapping of the intake jet, the flow entering the cylinder over the valves. Margary et al [14] summarized that nonlinearities introduced by the induction dynamics need to be considered when engine speed or intake pressure variations are investigated. This is especially important when such data is used for the validation of numerical simulations, which often do not include the entire intake system and oversimplify the induction process.

This work is motivated by a previous work from the authors [17] in the same optically accessible research engine, where high resolution flow field measurements were performed near the piston surface to resolve the boundary layer flow and parts of the bulk flow. The visible bulk flow scaled well with the piston speed for 800 and 1500 rpm at full-load (0.95 bar intake pressure), while the flow changed significantly for part-load conditions (0.4 bar), especially for 1500 rpm. The objective of this paper is to understand the effect of this intake pressure variation on the evolution of the in-cylinder flow in the same SI engine under motored conditions. High-speed PIV was utilized to capture the evolution of the in-cylinder flow in the valve-and symmetry-planes. The intake pressure was acquired simultaneously in order to investigate the coupling of the pressure wave with flow field fluctuations. The following sections present the experimental setup and operational conditions, an analysis of the pressure fluctuations accompanied by 1D simulations, and a detailed analysis of the in-cylinder flow.

## 2 Methods

### 2.1 Experimental Setup

#### 2.1.1 Engine Test Bench

Measurements were performed in the four-stroke single-cylinder SI optical research engine at Technische Universität Darmstadt. The Darmstadt engine (AVL) is equipped with a four-valve spray-guided pent-roof cylinder head configuration with a compression ratio of 8.7:1 and a bore and stroke of 86 mm each. Optical access is made possible by an optical-grade fused-silica cylinder liner and a flat fused-silica piston window, which is connected to a Bowditch piston extension for mirror access. In the spray-guided cylinder configuration, the top 55 mm of the stroke and an additional 8 mm in the pent-roof are visible. Additional detailed information about the engine and test bench can be found in [10, 18].

The engine runs under controlled boundary conditions for consistent operation. The intake system uses a large plenum to limit the effect of pressure perturbations from single-cylinder operation. Additionally, a sound reduction plenum is used far upstream of the intake valves while a similar plenum has the same effect downstream of the exhaust valves. Figure 1 shows a cross-sectional representation of the engine and the intake and exhaust pipes until the sound reduction plenums; a complete diagram of the engine test bench and flow systems is found in [18]. The long intake pipe allows fuel for port fuel injection and seed particles for PIV to homogeneously mix with the air before entering the combustion chamber. Within the intake pipe, two relative pressure sensors (GU21C, AVL, referenced to PMP4070, Kistler), labeled  $P_{in,1}$  and  $P_{in,2}$  in dark blue in Figure 1, measure the pressure just downstream of the noise reduction plenum and just before the intake valves.  $P_{in,2}$  allows the more accurate measurement of the intake pressure since it is closer to the intake valves and it is far downstream of the plenum. Despite measures to reduce pressure perturbations in the engine test bench,  $P_{in,1}$  and  $P_{in,2}$  have always measured large-frequency pressure oscillations characteristic of the valves opening and closing [18].

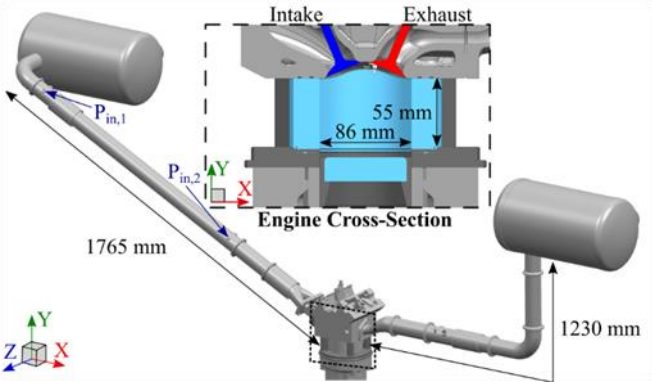


Figure 1. Cross-sectional representation of the engine and flow pipes.

The standard operating conditions of the engine test bench are shown in Table 1. To investigate the effect of intake pressure on the engine flow, four additional operating points were defined within this work for 1500 rpm with intermediate intake pressures of 0.5, 0.6, 0.7 and 0.8 bar.

Table 1. Standard operating conditions of the engine test bench.

	Intake Pressure	
Engine Speed	0.95 bar	0.4 bar
800 rpm	A	B
1500 rpm	C	D

2.1.2 High-Speed PIV

High-speed PIV was used in two separate experimental configurations in this study. These configurations involve flow measurements inside the engine cylinder in different vertical planes: symmetry-plane (SP) and valve-plane (VP). In these configurations, laser sheets (~0.8 mm thick at 13.5% of the max. intensity) from two frequency-doubled Nd:YAG cavities entered the cylinder via the piston mirror and a high-speed CMOS camera (Phantom v1610) equipped with a Sigma lens (105mm F2.8 Macro, f/11) measured image pairs of varying, optimized time separation between 51 and 3  $\mu$ s, depending on the intake pressure and measurement plane of interest. Data shown in this work are phase-averaged (average over cycles at fixed crank angles) and have a 5° crank angle resolution.

Nebulized DOWSIL 510 (Dow Corning) silicone oil was introduced to the intake flow near Pin,1 as tracer particles. Figure 2 a) and b) show a simplified schematic representation of the PIV measurements in the SP and VP of the engine. The commercial software DaVis 8.4 (LaVision) was used to calculate flow fields by means of cross-correlation with multi-pass iterations of decreasing window size (twice: 64 x 64 pixels, 50% overlap; twice: 32 x 32 pixels, 75% overlap), a peak ratio threshold of 1.3, and a universal outlier median filter to remove false vectors. More information on specific optics, vector calculations, and vector post- processing can be found in [2].

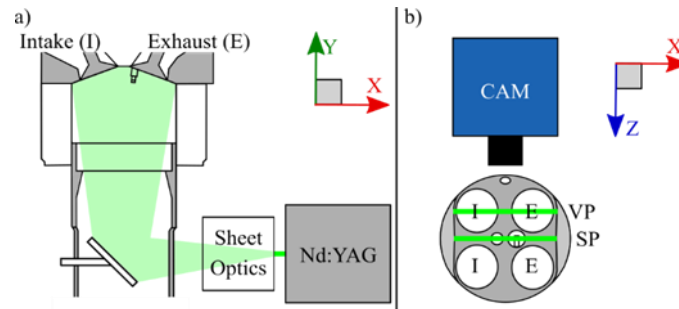


Figure 2. Arrangement of PIV measurement systems.

## 2.2 Numerical Setup

One-dimensional simulations of the spray-guided engine were carried out with the commercial software GT-POWER (Gamma Technologies). The model is based on a setup used for simulations of a wall-guided cylinder head on the same engine test bench conducted by Buhl et al. [19], which was then tuned to meet the current engine test bench's specific geometrical specifications such as the pipe diameter and lengths (intake noise reduction plenum until the exhaust noise reduction plenum), compression ratio, valve geometries, engine bore, and engine stroke. The boundary conditions were set to match the real engine conditions at 1500 rpm and the heat transfer coefficient was carefully tuned so the simulation in-cylinder pressure curve matched that of experiment. Table 2 shows the input parameters for the 1-D simulations.

Table 2. Input parameters derived from experiments for 1-D simulations<sup>a</sup>.

Engine Speed	1500 rpm
Intake Pressure	0.4, 0.5, 0.6, 0.7, 0.8, and 0.95 bar
Exhaust Pressure	1.0 bar
Intake Temperature	333 K
Exhaust Temperature	295 K
Pipe Diameter	56.3 mm
Intake/Exhaust Pipe Length	1765/1230 mm
Valve Diameter/Maximum Lift	29 mm/9.5 mm
Intake/Exhaust Valve Open <sup>b</sup>	325°CA/105°CA
Intake/Exhaust Valve Close	-125°CA/-345°CA

<sup>a</sup> Geometrical specifications previously mentioned in this work are excluded.

<sup>b</sup> Quantities labeled (number)°CA signify crank angle degrees after compression top dead center (TDC); negative quantities signify before compression TDC.

### 3 Results and Discussion

#### 3.1 Pressure Oscillations

Figure 3 shows the phase-averaged intake manifold pressure  $P_{in,2}$  over 220 cycles from 0.4 to 0.95 bar at 1500 rpm ( $0^\circ\text{CA}$  denotes compression TDC,  $P_{in,2}$  represents the measured quantities from sensor  $P_{in,2}$ ). At a first glance, each pressure trace is similar in that the low-frequency (long-wavelength) oscillations due to the cyclic intake process (valve opening) are phase-locked and all intake pressures show a damped oscillation with four periods per cycle. From the near-atmospheric intake-load (0.95 bar) to throttled-load (0.4 bar), high-frequency oscillations become more pronounced in the intake pipe. Shortly after the start of the cycle, each of the part-load cases shows a sudden increase in pressure, with a higher gradient as the load decreases, while the full-load case drops in pressure. Additionally, the part-load cases show a more pronounced local minimum near  $-285^\circ\text{CA}$  as well as damped high-frequency fluctuations throughout the rest of the cycle compared with the full-load case. Intuitively, the first peak in pressure followed by the local minimum, not observed in the full-load case, is caused by backflow from the exhaust air into the intake pipe. Since in the part-load cases the manifold pressure is below atmospheric pressure and there is a small overlap in intake and exhaust valve opening, it is no surprise that the exhaust gas at atmospheric pressure causes an increase in intake manifold pressure until the exhaust valves close ( $-345^\circ\text{CA}$ ). Furthermore, the exhaust gas leftover in the cylinder at TDC is expanded into the intake manifold. The resulting backflow seems to excite oscillations, which are already significantly reduced in amplitude as the intake valves close ( $-125^\circ\text{CA}$ ).

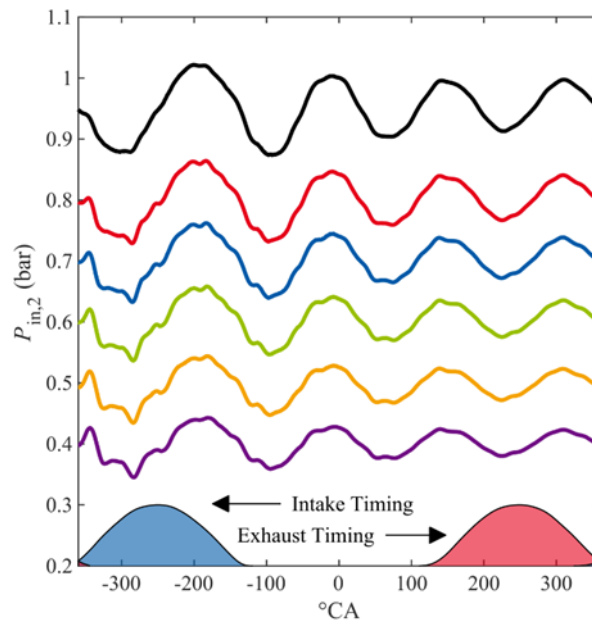


Figure 3. Phase-averaged  $P_{in,2}$  for 0.4, 0.5, 0.6, 0.7, 0.8, and 0.95 bar at 1500 rpm.

To further analyze the origin and characteristics of the different oscillations and their increase and decrease in prominence with changing intake pressure, the pressure traces were transformed into the frequency space. Figure 4 shows the fast Fourier transform (FFT) of  $P_{in,2}$  (continuous trace of 220 cycles, sampled every  $0.5^\circ\text{CA}/\sim 18\text{kHz}$ ) on a logarithmic scale for the 0.95 and 0.4 bar cases. While the low-frequency range is surrounded by very low amplitude noise, a distinctive peak in amplitude is observed at 12.5 Hz and its higher subsequent harmonics including 50 Hz, the peak amplitude for both cases. The sparseness in the frequency space is a result of the excitation of the system, the periodic intake flow. This excitation can be modeled as a smoothed rectangular wave (representing velocity or

pressure amplitudes). Figure 5 depicts the first period of an artificial sinusoidal wave with a duty cycle of 28%. Transformed into the frequency domain, it is evident that the highest amplitude peak appears at the fundamental frequency of 12.5 Hz. Higher harmonics of this frequency are also visible, but decay in an oscillatory manner, while other frequencies are vacant. The shape of the decay depends on the duty cycle and smoothness of the signal.

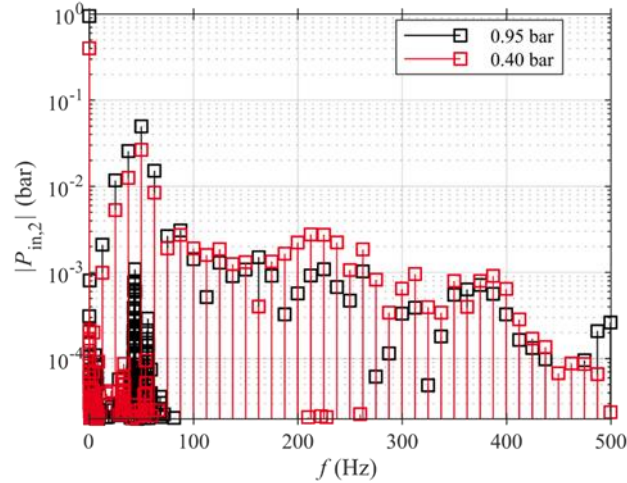


Figure 4. Fast Fourier transform of  $P_{in,2}$  for 0.95 and 0.4 bar.

To obtain the system response, the excitation is convoluted with the system's transfer function. This step is a multiplication in the frequency space. In a first approximation, the intake manifold can be viewed as a column of air in a pipe with one open end (the plenum) and one open or closed end (the intake valves). Such a system will have distinct resonance peaks at frequencies which permit standing waves of pressure (and gas velocity) to appear [20]. Amplitudes at resonance frequencies can become greater than the original excitation and will reside longer than others. Equation 1 defines the resonant (harmonic) frequencies for a simple open-closed pipe and the relationship for open-open pipes is shown in Equation 2:

$$f = \frac{nc}{4L} \quad n \in 1,3,5 \dots \quad (1)$$

$$f = \frac{nc}{2L} \quad n \in 1,2,3 \dots \quad (2)$$

With  $c$  being the speed of sound and  $L$  the pipe length. Alternatively, the engine during intake can be viewed as a Helmholtz resonator, with the cylinder volume acting as the cavity against which the column of air in the intake pipe moves:

$$f_H = \frac{c}{2\pi} \sqrt{\frac{A}{LV}} \quad (3)$$

Here  $A$  is the area of the cross-section of the intake pipe and  $V$  represents the volume of the resonator chamber. For applications in the context of an engine, several modifications of Equation 3 have been suggested [12, 21], e.g., replacing the volume term with an effective engine volume.



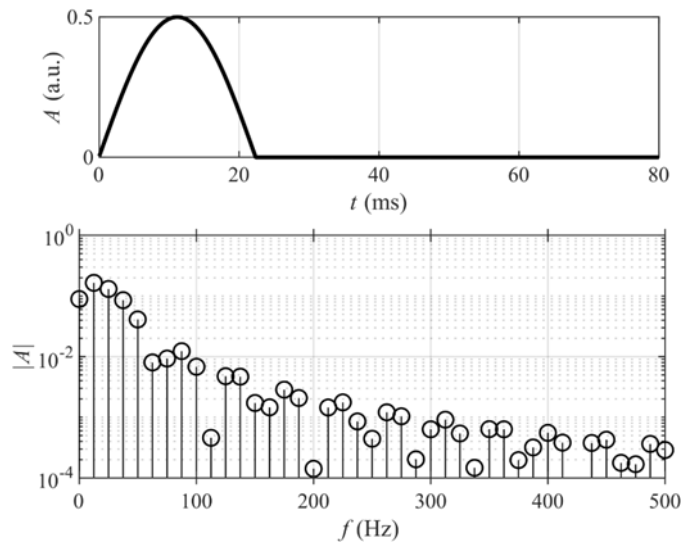


Figure 5. Artificial smoothed square wave excitation in the time domain and the resulting FFT.

Examining the FFT of the experimentally gained pressure traces (Figure 4) again, three observations can be made: first, the spectrum shows a dominant frequency mode around 50 Hz; this is the low-frequency oscillation visible in the pressure traces. Applying Equation 1 with an intake pipe length of 1765 mm and a speed of sound of 357 m/s (at  $T = 45^{\circ}\text{C}$ , an intermediate value to incorporate the temperature gradient along the intake system) results in a first resonant frequency of 51 Hz. Therefore, the low-frequency oscillation can be ascribed to the intake flow, and as a consequence thereof, the pressure and velocity perturbations induced in the intake manifold. This excites the first resonance of the open-closed system. Secondly, the amplitudes decrease with increasing frequency, which is also explained by the primarily low-frequency excitation of the intake process. Thirdly, while the amplitude spectrum of the part-load (0.4 bar, case D) matches quite well with that of the full-load (0.95 bar, case C), there is a distinct region around 220 Hz where case D shows higher amplitudes. These are the high-frequency components observed in Figure 2. Our hypothesis is that these high-frequency modes can be attributed to the backflow happening in low-load cases.

While this hypothesis is tested in the following chapter, the connection to a resonant frequency is less obvious. The second harmonic of the open-open pipe (Equation 2) at  $\sim 200$  Hz is close, but on the lower end of this frequency peak. The temperature sensitivity of this calculation is small, even though the temperature, and therefore the speed of sound profile along the pipe, is not exactly known. Moreover, additional end-of-pipe-corrections further decrease the resonant frequencies [12]. Reasons for this incongruity could be the greater complexity of the real system, which cannot be fully represented by an idealized straight air column. Furthermore, transient effects could play a role, shifting frequencies over time with higher frequencies, and therefore smaller wave-lengths, being more sensitive to changes in geometry like the valve closures.

Pressure oscillations in the intake are clearly mainly influenced by the intake geometry and engine speed, while additional factors such as the intake pressure can also play a crucial role. To investigate this further, numerical simulations of the engine processes were conducted.

### 3.1.1 Pressure Oscillations in 1-D Simulations

One-dimensional simulations calculated with GT-POWER exhibit similar high-frequency fluctuations when compared with the results from experiments. Figure 6 shows a comparison between GT-POWER results and measured  $P_{in,2}$  at 0.4 (bottom panel) and 0.95 bar (top panel) and 1500 rpm. In addition, the pressure trace of a simulation with the exhaust pressure set to the same level as the intake pressure (0.4 bar) is shown. This eliminates backflow since the intake, in-cylinder, and exhaust pressures are identical during the opening of the intake valve. Overall, the simulation results agree

reasonably well with the measured pressures. The general shapes of pressure oscillations, both low- and high-frequency, match those in the experiment. However, a few differences can be observed. First, the simulation results appear to be phase- shifted by approximately  $-3^\circ\text{CA}$  which also applies to the no-backflow case. This discrepancy could be a result of a number of factors including differences in the actual temperature profile along the intake system, due to intake pipe wall- heating and engine cooling set to 333 K, which would change the speed of sound inside the pipe, shifting the phase. Another reason for the difference is a possible discrepancy in the valve timing provided by the manufacturer, which has a resolution of  $10^\circ\text{CA}$  and had to be interpolated in simulations. Furthermore, inaccuracies in the valve discharge parameter can affect the exact timing of the intake flow. A second difference can be observed after the intake valves close: the pressure traces appear to be much smoother in the simulations, implying a stronger dampening, which reduces the effects of the backflow, possibly causing the shallower gradient in  $P_{in,2}$  at  $-360^\circ\text{CA}$ . Finally, the amplitudes of  $P_{in,2}$  in simulation overshoot those in the experiments after the valves close, which is probably another effect of the discrepancies of the real in-pipe geometry and temperature. All in all, a reasonably good agreement of the pressure trace is achieved, which is confirmed in a comparison of the frequency spectrum (not shown to reduce redundancy).

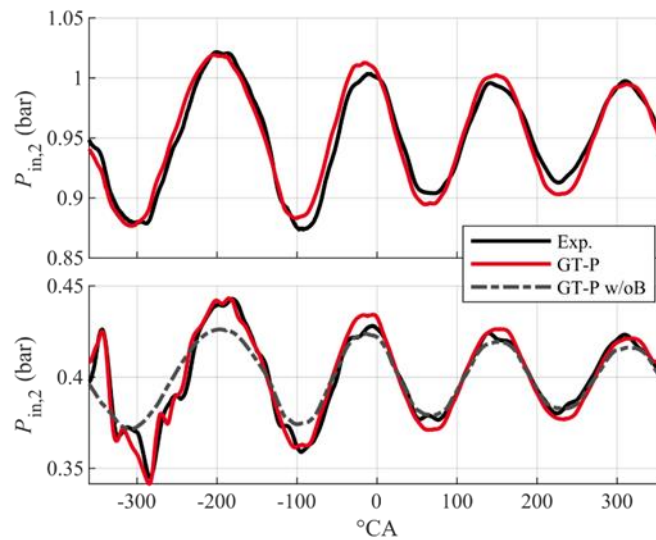


Figure 6. Comparison between simulation and measured  $P_{in,2}$  for 0.95 bar (top) and 0.4 bar (bottom) at 1500 rpm. A no-backflow case is displayed with a gray dashed line.

When comparing the simulated pressure trace with no backflow to the simulated standard case D, it is apparent, that no higher frequencies are excited in the former. At  $-360^\circ\text{CA}$ , instead of the sharp rise in pressure, the pressure drops due to the piston's downward movement being the driving force. Moreover, in the frequency spectrum (not shown), the 220 Hz peak is reduced by an order of magnitude in the no-backflow case. This confirms the hypothesis that the higher frequencies are a result of the backflow into the intake system after intake valve opening.

Apart from the possibility of investigating an ideal case in which no backflow is present, 1-D simulations are also useful in that they offer the chance to simulate alterations in other important parameters to explore the effects on engine operation. One such important parameter that can help to understand the high-frequency fluctuations in  $P_{in,2}$  is test bench geometry, namely the intake pipe length. As is previously shown with Equation 1 in a closed-end pipe, the harmonic frequency of a standing wave depends on the pipe length and the speed of sound. As the pipe length is changed, an inverse relationship to the harmonic frequency follows. The top panel of Figure 7 shows an FFT of the standard pipe configuration for the 1-D simulation calculated at 0.4 bar and 1500 rpm. As with the experimental data, several harmonic frequencies are visible with the first being at 50 Hz. As the harmonic frequency

peaks are less obvious in the sparse frequency spectrum, a Gaussian fit, shown by the thin red line, is used to determine the peak frequency for each harmonic. The bottom panel of Figure 7 shows the first and second observed harmonic frequencies obtained by the location of the maximum of each Gaussian fit with varying pipe length. The vertical dashed black line represents the standard pipe length and the blue line represents the ideal linear relationship for the first frequency mode found in Equation 1. The good agreement between theoretical and simulated frequencies as well as the apparent dependence of the high-frequency peak on the pipe length, points to their resonant mode nature.

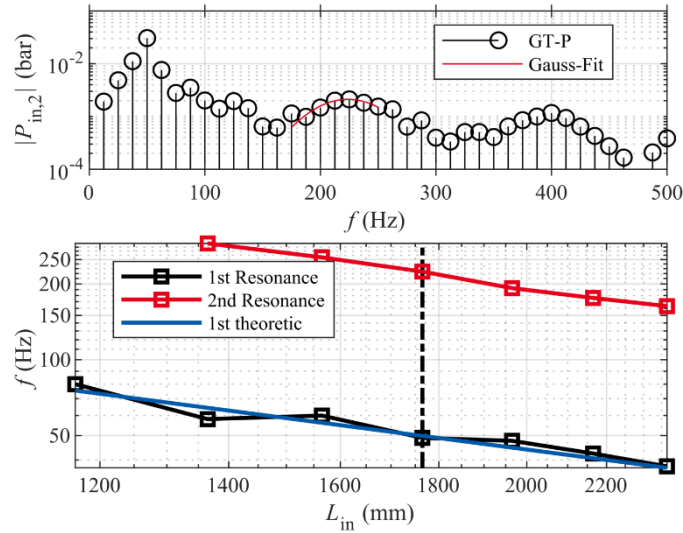


Figure 7. Fast Fourier transform of  $P_{in,2}$  with the standard pipe length and 0.4 bar at 1500 rpm (top). Shift of the high frequency mode with varying pipe lengths (bottom).

The intake flow is heavily affected by the oscillations in the intake pressure, which can be visualized by the simulated valve-gap velocities. Figure 8 shows the simulated valve-gap velocity for case D with and without backflow compared with the experiment. Experimental velocities were obtained by PIV in the VP and taking the average of a small region in the valve-plane jet. It is clear that the backflow-induced pressure oscillations bring about severe fluctuations of the intake velocity, with high flow gradients doubling the velocity magnitude within  $10^\circ\text{CA}$ . To further investigate the interaction between pressure oscillations and flow field, the following chapter analyzes the in-cylinder flow via PIV measurements.

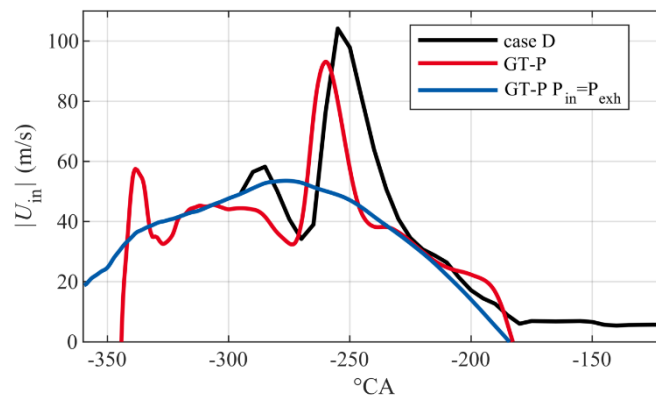


Figure 8. Comparison between simulation valve-gap velocity and measured valve-plane velocity for 0.4 bar and 1500 rpm.

## 3.2 Effects of Intake Pressure on Measured In-Cylinder Velocities

### 3.2.1 In-Cylinder Velocities during Intake

#### 3.2.1.1 Intake Velocities for the C to D Transition

The in-cylinder flow field can be used to understand the effects of a variation of intake pressure loads on the engine operating at 1500 rpm. Figure 9 displays the measured phase-averaged intake velocity magnitude  $U_{in}$  in the SP for varying intake pressures at 1500 rpm. Velocities are shown for steps of the intake manifold pressure from 0.4 to 0.95 bar. Additionally, the phase-averaged pressure oscillation  $\Delta P_{in,2}$  for the 0.4 and 0.95 bar cases as well as the intake valve timing (shaded gray curve) and piston speed (blue curve) are displayed in the bottom panel. The intake velocities negatively correlate with local extremes in  $P_{in,2}$ . For example, the local peaks in  $P_{in,2}$  for part-load cases correspond directly with a local minimum in  $U_{in}$  and the same phenomenon happens for the opposite, i.e. minimum  $P_{in,2}$  means maximum  $U_{in}$ . This is due to the interaction between piston movement and pressure oscillations. In general, the intake phase is dominated by the inter- play of valve opening and piston movement. Rapid displacement of the piston creates a favorable pressure ratio along the valve, sucking air into the cylinder [13]. The highest flow velocities are therefore reached near the crank angle of maximum piston speed (Figure 8 in blue, Figure 9 in black). In the absence of high-frequency oscillations (case C), the low-frequency oscillations are not intense enough to heavily disturb the pressure ratio so there is always enough time for intake pressure and cylinder pressure to be in phase. For decreasing load, it can be observed that there is a linear increase in flow fluctuations, signifying that this is not a semi- stable system that switches to another state, but an incrementally increasing dominance of pressure wave action.

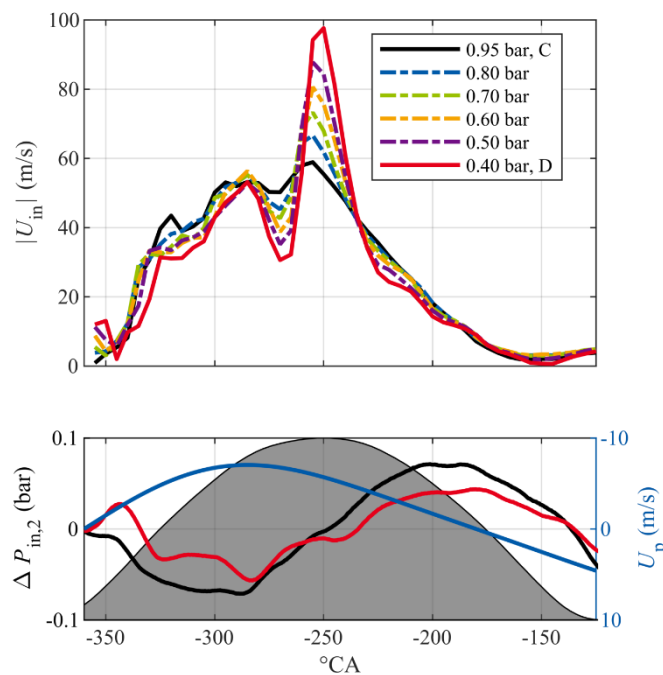


Figure 9. Average intake velocity magnitudes  $U_{in}$  for 0.4, 0.5, 0.6, 0.7, 0.8, and 0.95 bar  $P_{in,2}$  at 1500 rpm (top) and average pressure fluctuations for case C and D, the intake valve timing (shaded gray curve), and the piston speed in blue (bottom).

For the part-load case (0.4 bar, D), there is a local minimum in intake pressure around  $-280^{\circ}\text{CA}$ , induced by the high-frequency oscillations. This is followed by a significant reduction in intake velocities, which in turn reduces the in-cylinder pressure due to missing air mass. Shortly after, the high-frequency wave bounces back to local high intake pressures, leading to an extremely favorable pressure ratio along the valve and, in combination with the high piston speed at  $-260^{\circ}\text{CA}$ , to a severe

rise in intake velocities. At these high frequencies, the cylinder pressure and intake pressure are out of sync, causing the severe gradients. The peak velocity reaches nearly 100 m/s, which is nearly double the amount of the high-load case. After this adjustment of the mass and consequently the pressure ratio, all cases follow a similar trend with the piston speed, valve gap, and intake velocity decreasing. For the 0.95 bar case (C), the velocity curve is generally smoother than those of higher backflow. However, as shown with the 1-D simulations, any amount of backflow present in the intake pipe causes instabilities in the intake flow, preventing a smooth transfer of mass into the cylinder. Consequently, the following sections turn towards the impact of these fluctuations on the flow field development.

### 3.2.1.2 Valve-Plane Jet

In this section, the effect of increasing the load of  $P_{in,2}$  on the intake jet is visualized by means of PIV in the VP. Figure 10 shows the phase-averaged flow fields in the VP for cases C (left) and D (right) for selected crank angles. Streamlines display the flow direction and the blue-yellow colormap represents the velocity magnitude. Clearly visible in the top of the field of view is a flow with high velocity magnitudes over the valve: the intake jet. As engine flows are inherently turbulent by nature, it is important to note that the unsteady jet flapping due to turbulence in instantaneous cycles is smoothed out by the phase-averaging and the following analysis relates only to the shape and magnitudes of the phase-averaged flow fields over 250 consecutive cycles.

At  $-280^\circ\text{CA}$ , the average intake jets in both cases are relatively similar in shape with nearly the same maximum magnitudes near the valve ( $\sim 60$  m/s for C and  $\sim 53$  m/s for D). Each case shows a diverging jet that forces a small tumble vortex to form as the jet is slowed down and redirected by the cylinder wall. The vortex in case C is stronger since the jet velocities are higher at this instance in time. From the analysis in Figure 9, the intake velocities at this time are decreasing, which is much more extreme for case D, and is complemented with a drop in cylinder pressure.

The flow field at  $-260^\circ\text{CA}$  for case D shows the resurgence of the flow after the extreme dip in cylinder pressure and intake mass flow is counteracted by the increase in valve gap pressure gradient and the peak piston velocity. In the SP velocities shown in Figure 9, there is an intersection between intake velocities of both cases. However, this is not the case in the VP at this crank angle as the maximum average velocity for case D is over 82 m/s and for case C it is 13 m/s slower. A severe change from 42 m/s at  $-265^\circ\text{CA}$  to 82 m/s at  $-260^\circ\text{CA}$  causes the first visible jet flapping mode, or more accurately, a direction change of the instantaneous jets in case D as flow magnitudes increase. The average flow field indicates that most of the instantaneous jets are first directed along the angled cylinder roof. Then downstream of the high-speed jet, lies a wide distribution of instantaneous jets, many of which sharply curl down. In case C, the more gradual increase in velocity over the previous crank angles results in a jet that follows the shape of the cylinder head longer than at  $-280^\circ\text{CA}$ .

At  $-255^\circ\text{CA}$ , case C achieves its maximum velocity, which is a marginal change from  $-260^\circ\text{CA}$ , resulting in a similar average flow field. In contrast, case D increases by nearly 24 m/s to over 106 m/s near the valve. The resulting average flow structure is a jet that curls up along the cylinder roof towards the wall. There is a strong gradient between the jet structure and the rest of the average velocity field, which indicates that most of the instantaneous turbulent jets followed the same path as the intake jet reached its maximum magnitude.

At  $-245^\circ\text{CA}$ , both cases show a decrease in velocity, with the gradient in case D being stronger than in case C. This manifests itself in that the average jet in case C is angled slightly downward compared with the instance of its maximum velocity and the average jet in case D curls severely downward, a change of over  $70^\circ$  from  $-255^\circ\text{CA}$ . With such a strong curl, the jet in case D creates a well-defined vortex. Additionally, stronger velocity magnitudes throughout the field indicate that the intake jet in case D is influencing the rest of the flow field in view much more than in case C. After  $-245^\circ\text{CA}$ , the intake velocities in both cases continue to decrease and eventually the average jet shapes are

similar as they travel along the cylinder roof and curl down along the wall, each facilitating the formation of the tumble vortex.

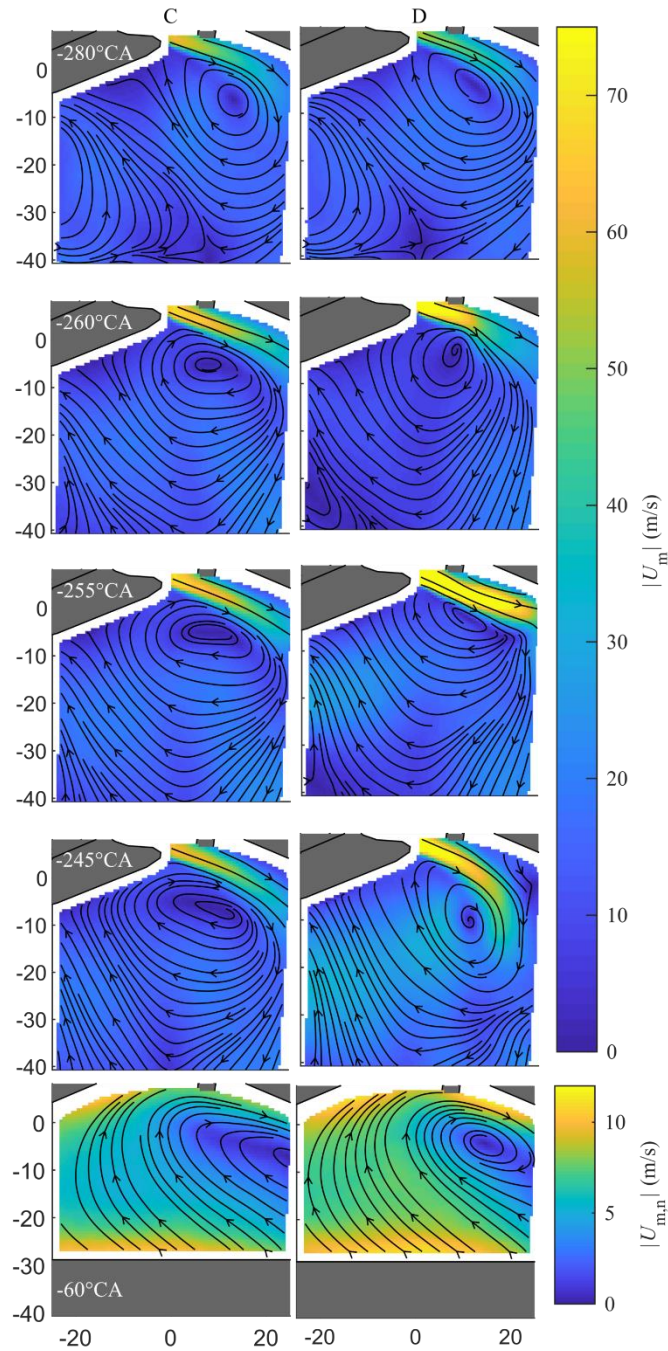


Figure 10. Phase-averaged flow fields in the valve-plane for 1500 rpm (left C, right D).

In summary, flow fields in the VP reveal that sharp changes in intake velocity cause instabilities in the intake jet position. This is clear when comparing the average jets in cases C and D. While the current measurement's time-resolution the jet in case C always remains reasonably stable in average shape, the average jet in case D exhibits sharp angle changes in a flapping motion which complement the severe intake velocity changes shown in Figure 9. The jet velocity also dictates the shape and strength of the tumble as indicated by the early formation of stronger tumble vortices with increasing velocity.

The stronger formation of a tumble vortex in case D is made possible by the sudden discharge of mass during the intake flow resurgence. At  $-60^\circ\text{CA}$ , the engine cycle is in late compression and the



piston and tumble vortices for both cases are in view. As shown with the early tumble induced by the intake jets, the late tumble in case D is much more compact and the overall flow field shows higher velocity magnitudes throughout the cylinder. This confirms that the higher impulse in the late intake phase is helpful in generating a flow structure which can contribute to the formation of a favorable combustion process. Valve-plane PIV measurements are useful in relating the intake flow due to the oscillations in  $P_{in,2}$  to flow phenomena in the early-to-middle cycle, but the last sections of this work will use SP PIV measurements to focus on these effects in the late cycle during compression.

### 3.2.2 In-Cylinder Velocities during Compression

#### 3.2.2.1 Global Tumble

As discussed previously, the standard operating conditions of the Darmstadt engine (Table 1) are a low and high intake pressure load case, each at a low and high engine speed. To compare the behavior of the intake manifold pressure with the intake flow and its effect on the evolution of the flow in compression, PIV in the SP is analyzed. Figure 11 shows the global in-cylinder flow fields in the SP normalized to their respective mean piston speeds for each standard operating condition at  $-90^\circ\text{CA}$ . Streamlines represent the flow direction and the blue-yellow colormap represents the phase-averaged flow magnitude. As expected, the normalized flow fields of case A and C are very similar since they experience little high-frequency disturbance without the presence of strong backflow into the intake pipe during valve overlap. However, global flow fields show that case B is similar to the higher pressure cases, despite the presence of backflow (an observation which will be discussed further in later sections). In contrast, the results for case D are significantly different than the others. The normalized velocity magnitudes in the intake valve side during compression are much greater and the streamlines in the high velocity magnitude region are oriented more vertically than in the other cases. Therefore, the resulting tumble vortex for case D is elongated in the  $y$ -direction, centered further up, and further left. In order to understand the difference between the effects of pressure fluctuations in the intake flow on the late-cycle flow evolution, a further analysis of the velocity fields in compression from case C to D is required.

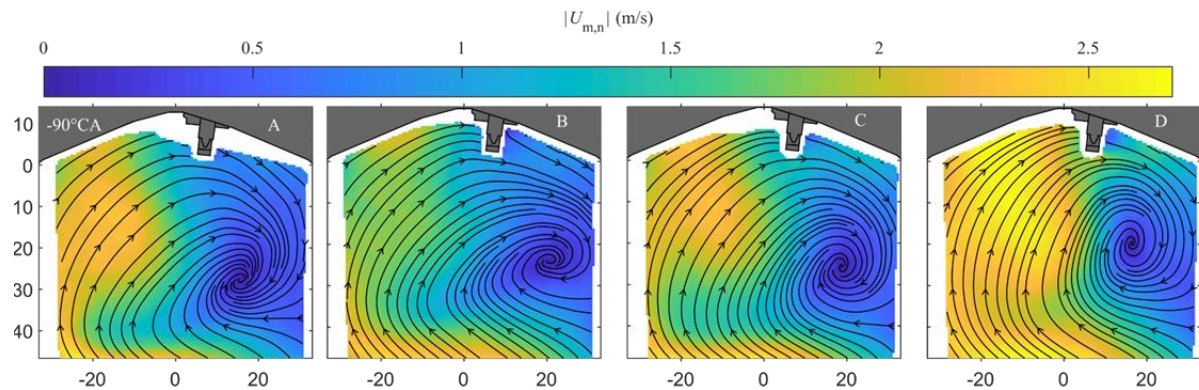


Figure 11. Global in-cylinder flow fields in the SP normalized to their respective piston speeds for each standard operating condition at  $-90^\circ\text{CA}$ .

#### 3.2.2.2 Tumble Evolution and Trajectory

The unsteady intake velocity clearly has an impact on the position and shape of the tumble vortex in compression. To understand the evolution of the tumble and its trajectory throughout early and late compression with different intake pressure loads, the phase-averaged global flow field for select crank angles in the SP is shown in Figure 12. Once again, streamlines represent the flow direction and the colormap represents the velocity magnitude. The difference in intake jet behavior from case C to D heavily influences the speed at which the tumble develops in compression. At  $-130^\circ\text{CA}$  in case D, the flow appears to have developed much faster in the vertical direction due to the higher jet speed,

resulting in smoother, more vertically oriented streamlines and higher overall motion energy. The tumble formation is already well-defined for case D, which affects the resulting trajectory.

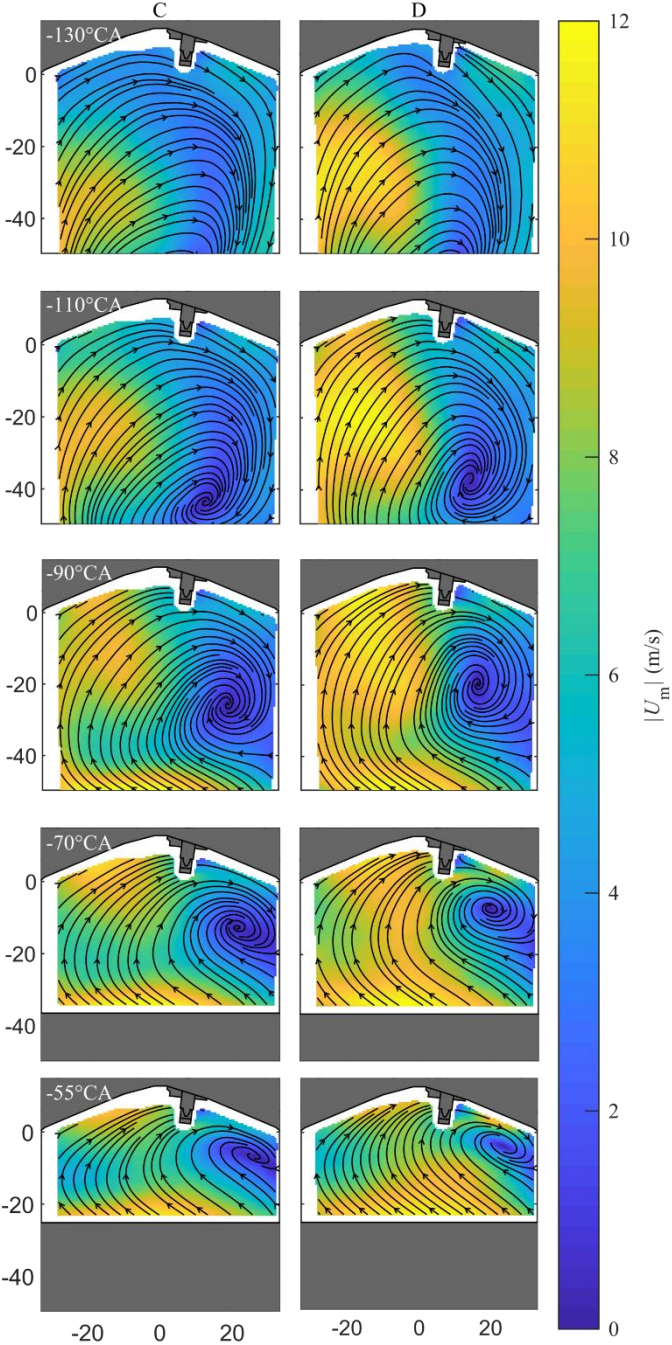


Figure 12. Phase-averaged tumble evolution for 1500 rpm.

At -110°CA, the streamlines indicate once again that the tumble shape is close to fully vertical in the case of low pressure, while the tumble is less circular and oriented diagonally in the high pressure case, as the bulk flow pushes the tumble shape horizontally. For case D, at -110°CA, the flow distribution of high velocities within the cylinder has rotated significantly further than in case C.

Although the piston position and motion has a continual effect on the in-cylinder motion, its effect becomes evident as the piston comes into view at -90°CA. At this crank angle, the piston speed of 6.75 m/s has a visible footprint on both flow fields as the piston approaches late compression (a phenomenon unrelated to laser sheet reflections, which were masked out sufficiently to prevent bias). This is evident as the flow is confined in the volume, while the near wall velocity is combined



with the relative motion of the piston. In the presence of a high magnitude flow in the left of the cylinder the tumble center moves to the right. As in previous crank angles, the tumble shape is an elongated ellipse oriented almost perfectly vertically in the low pressure case. However, since the flow has now reached a more mature state in the high pressure case due to the confinement and effect of the piston speed, the previously prevalent horizontal motion is equalized by the equally prevalent vertical flow, creating a circular shape of the tumble center.

At  $-70^\circ\text{CA}$ , the tumble in the low pressure case has achieved a close horizontal-vertical velocity equalization, which forms the tumble into a circular shape. The change in tumble shape is due in part to the position of the tumble close to the confinement of the cylinder roof, and also due to the high horizontal velocities above, which are beginning to decelerate the tumble's upward motion in combination with the slowing down of the piston motion. In case C, above the tumble, stronger horizontal flows near the cylinder roof are apparent. However, as has been consistent throughout the tumble evolution, the vortex center in case C is below that of case D. Finally, at  $-55^\circ\text{CA}$ , the trend continues as the tumble in case D remains more compact near the cylinder roof.

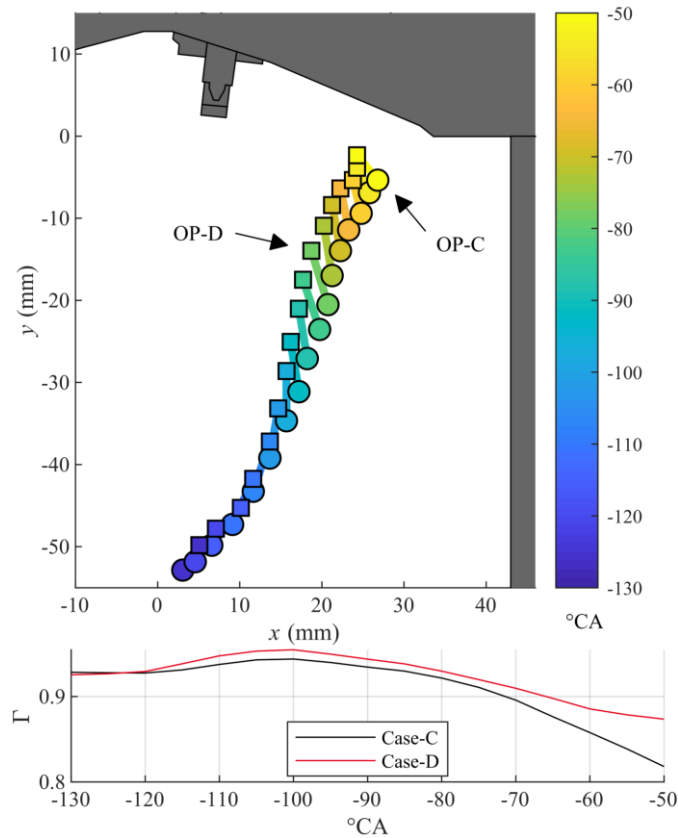


Figure 13. Top: tumble trajectory for cases C and D from  $-130^\circ\text{CA}$  to  $-50^\circ\text{CA}$ . Below: the evolution of the tumble parameter  $\Gamma$ .

A quantification of the evolution of the in-cylinder tumble vortex is shown in Figure 13. The trajectory of the tumble centers, defined by the global maximum of  $\Gamma$  for case C and D, are shown from the first visible instance,  $-130^\circ\text{CA}$ , to the last instance of a clearly defined tumble shape,  $-50^\circ\text{CA}$ .  $\Gamma$ , a dimensionless scalar where the value 1 is reached in the center of a perfect axisymmetric vortex, is defined according to [22] as:

$$\Gamma = \frac{1}{S} \int_S \frac{(PM \times U_M) \cdot z}{\|PM\| \cdot \|U_M\|} dS \quad (4)$$

The most obvious result of the trajectory has already been emphasized: the strong intake jet due to the pressure oscillations in case D cause a faster vertical development of the tumble vortex. This is clear in that the tumble center is always further along the y-axis in case D than C. However, the tumble trajectory also reveals that the tumble center in case D begins further to the right in the positive x-direction than in case C until  $-105^\circ\text{CA}$ , then it consistently remains further to the left due to the relative prevalence of the horizontal flow in case C. Intuitively, this trend agrees with the tumble shape comparison shown in Figure 12 since the shape of case D remains consistently more vertically elongated than in case C due to increased vertical motion.

Furthermore, Figure 13 shows the evolution of the tumble parameter as defined by Equation 4. For case D the tumble parameter  $\Gamma$  is nearly always higher than for case C, implying a more circular shape in the field of view, which is in line with the aforementioned observations. Finally, the tumble in case C weakens faster after  $-75^\circ\text{CA}$ . This is due to the lack of stored energy, which case D has due to the severe gradients in intake velocity.

### 3.3 The Effect of Engine Speed on Intake Pressure Oscillations

As discussed, intake pressure oscillations due to backflow have a significant effect on the intake jet and subsequent in-cylinder flow. However, Figure 10 shows that at a lower engine speed, the bulk in-cylinder flows remain largely similar with different intake pressure loads (case A and B). Therefore, a quantified comparison of in-cylinder flows between different intake pressure loads and engine speeds is required to explain the difference in global flow fields in compression. Figure 14 shows normalized intake velocities  $U_{in,n}$  for cases A, B, C, and D, obtained by SP PIV, and the  $P_{in,2}$  oscillations for cases A and B as well as the valve timing in the bottom panel.

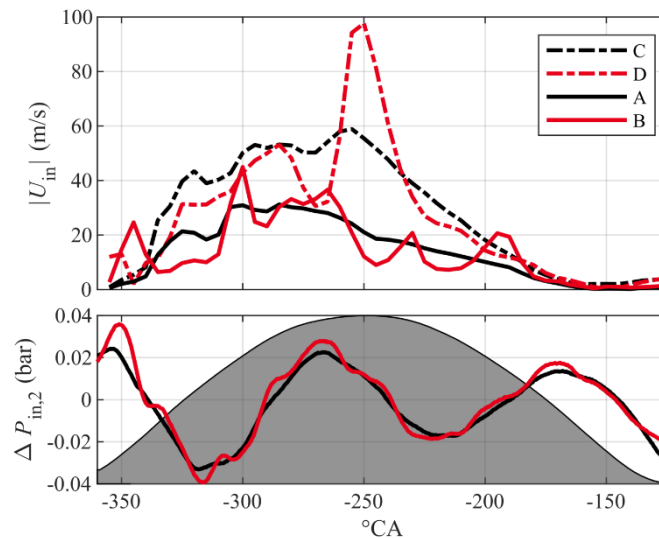


Figure 14. Average intake velocity magnitudes  $U_{in}$  for test case A, B, C, and D obtained by SP PIV (top) and average pressure fluctuations for case A and B and the intake valve timing (shaded gray curve) (bottom).

Lower engine speeds (A and B) imply greater engine time scales and therefore a smaller average momentum of the flow. Conversely the weaker periodic intake flow, which occurs at 6.67 Hz, almost half of the frequency for 1500 rpm, also results in a weaker excitation of the intake system. Comparing the bottom panels of Figure 9 and Figure 14, low- and high- frequency pressure oscillations of reduced amplitude but similar ratio can be observed for the lower engine speeds. Still, the overall intake pressure trace of case B matches better with case A than case D matches with C. Considering the intake velocities, the second effect of engine speed is visible: the time- based pressure wave oscillation (whose frequency is fixed due to the intake geometry) affects the valve movement- and

there-fore crank angle-based intake velocities at different timings. This manifests itself in several ways, with the most obvious being a shift of the intake velocity curve maxima of case A and B to the left and a narrower width than in case C and D. Furthermore, the number of velocity fluctuations due to high-frequency pressure oscillations increases, while the amplitude is on average smaller. As a result, fluctuations of the intake flow's impulse are more evenly distributed over the intake phase for case B than for C. As discussed previously for Figure 9, case C features only one prominent velocity fluctuation late in the intake phase. This observed difference in the intake flow is deemed to be the reason the tumble location, shape, and normalized flow field for B look similar to those in case A and C despite the presence of backflow.

All things considered, the intake flow evolution and thereby the evolution of the tumble and subsequent processes, like spark formation and flame development, are heavily influenced by flow structures formed by the intake port and cylinder head geometry as well as the wave action resulting from standing waves determined by geometry, pressure, and engine speed.

## 4 Conclusions

In this work, the complex interaction between engine intake pressure load, engine speed, and intake port geometry and their effects on intake manifold pressure oscillations, and hence in-cylinder velocity, of an optically accessible research engine is explored. In such an engine configuration, decreasing the intake pressure load induces a high-frequency standing wave mode in the intake manifold due to backflow caused by an unfavorable pressure difference between the intake port and cylinder. Since the parameters in engine operation are complex, simple pipe equations were found to be insufficient in capturing the effect of the backflow on the system. Instead, 1-D simulations capture the resonant excitation due to the backflow and the effect it has on the intake flow. High-speed, high-resolution PIV provides information on the real effects of the pressure oscillations on the evolution of the intake flow at intake and compression. Using a comparison between experimental and simulation data, the following conclusions are drawn:

1. The high-frequency components of the intake wave are attributed to the presence of backflow. Without the presence of backflow (ideal simulation case), the intake manifold oscillates only on a low-frequency scale which is excited by the periodic intake mass transfer. Even in the case of little backflow (0.95 bar intake pressure), high-frequency pressure oscillations have an impact on the intake flow that is not insignificant.
2. To an extent, the resonant modes of the pressure oscillations can be calculated with conventional pipe equations. However, due to the complex phenomena in engine processes, 1-D simulations offer a superior, inexpensive alternative to predict the effects of these phenomena.
3. The presence and degree of high-frequency oscillations are directly linked with the intake pressure load and engine speed, and their effects on in-cylinder velocities differ. Higher engine speeds lead to a stronger backflow and different phase relation to the intake manifold wave propagation.
4. A favorable pressure ratio between the volume before the intake valves and inside the cylinder causes higher intake speeds. This ratio is affected mainly by interplay between the valve motion and the piston speed. However, the effects of the high frequency oscillations due to backflow can be significant in causing local pressure extrema and consequently fluctuations in the intake velocity as the pressures come out of sync.
5. The measured phase-averaged intake jet and resulting flow structure in compression are ultimately affected by the intake pressure oscillations. High-frequency pressure oscillations conducive to sharp intake velocity gradients result in an intake jet with changing flow directions. Additionally, the higher flow magnitudes result in a tumble structure that develops faster and remains stronger

throughout compression. Without the presence of high-speed pressure oscillations, intake velocity gradients are gradual and the intake jet and tumble structure remain steady.

6. Three-dimensional computational fluid dynamics simulations must account for the effects of the whole intake and exhaust systems to accurately capture the pressure and flow associated with realistic engine operation.

Further investigations may focus on the interaction between the flow structures induced by pressure oscillations and subsequent engine combustion processes. The influence of the flow structures on the spark formation, early flame kernel development, and flame-wall interaction needs to be considered to fully understand engine combustion processes.

## References

1. Borée, J. and Miles, P.C., "In-Cylinder Flow," . In: Encyclopedia of Automotive Engineering. (Chichester, John Wiley & Sons, Ltd, 2014), 1-31. ISBN:9781118354179.
2. Geschwindner, C., Kranz, P., Welch, C., Schmidt, M. et al., "Analysis of the Interaction of Spray G and in-Cylinder Flow in Two Optical Engines for Late Gasoline Direct Injection," *Int. J. Engine Res.*, 2019, doi:10.1177/1468087419881535.
3. Stiehl, R., Schorr, J., Krüger, C., Dreizler, A. et al., "In- Cylinder Flow and Fuel Spray Interactions in a Stratified Spray-Guided Gasoline Engine Investigated by High-Speed Laser Imaging Techniques," *Flow Turbul. Combust.* 91(3):431-450, 2013, doi:10.1007/s10494-013-9500-x.
4. Zhang, M., Xu, M., and Hung, D.L.S., "Simultaneous Two- Phase Flow Measurement of Spray Mixing Process by Means of High-Speed Two-Color PIV," *Meas. Sci. Technol.* 25(9):95204, 2014, doi:10.1088/0957-0233/25/9/095204.
5. Dahms, R., Fansler, T.D., Drake, M.C., Kuo, T.-W. et al., "Modeling Ignition Phenomena in Spray-Guided Spark- Ignited Engines," *Proc. Combust. Inst.* 32(2):2743-2750, 2009, doi:10.1016/j.proci.2008.05.052.
6. Peterson, B. and Sick, V., "High-Speed Flow and Fuel Imaging Study of Available Spark Energy in a Spray-Guided Direct-Injection Engine and Implications on Misfires," *Int. J. Engine Res.* 11(5):313-329, 2010, doi:10.1243/14680874JER587.
7. Mounaïm-Rousselle, C., Landry, L., Halter, F., and Foucher, F., "Experimental Characteristics of Turbulent Premixed Flame in a Boosted Spark-Ignition Engine," *Proc. Combust. Inst.* 34(2):2941-2949, 2013, doi:10.1016/j.proci.2012.09.008.
8. Peterson, B., Baum, E., Böhm, B., and Dreizler, A., "Early Flame Propagation in a Spark-Ignition Engine Measured with Quasi 4D-Diagnostics," *Proc. Combust. Inst.* 35(3):3829- 3837, 2015, doi:10.1016/j.proci.2014.05.131.
9. Bode, J., Schorr, J., Krüger, C., Dreizler, A. et al., "Influence of the In-Cylinder Flow on Cycle-to-Cycle Variations in Lean Combustion DISI Engines Measured by High-Speed Scanning-PIV," *Proc. Combust. Inst.* 37(4):4929-4936, 2019, doi:10.1016/j.proci.2018.07.021.
10. Freudenhammer, D., Peterson, B., Ding, C.-P., Boehm, B. et al., "The Influence of Cylinder Head Geometry Variations on the Volumetric Intake Flow Captured by Magnetic Resonance Velocimetry," *SAE Int. J. Engines* 8(4):1826-1836, 2015, doi:10.4271/2015-01-1697.
11. Stiehl, R., Bode, J., Schorr, J., Krüger, C. et al., "Influence of Intake Geometry Variations on In-Cylinder Flow and Flow- Spray Interactions in a Stratified Direct-Injection Spark- Ignition Engine

Captured by Time-Resolved Particle Image Velocimetry,” *Int. J. Engine Res.* 17(9):983-997, 2016, doi:10.1177/1468087416633541.

12. Winterbone, D.E. and Pearson, R.J., “Design Techniques for Engine Manifolds: Wave Action Methods for IC Engines,” Desmond, E.W. and Richard, J.P., (London, Professional Engineering Pub., 1999), ISBN 186058179X.
13. Harrison, M.F. and Stanev, P.T., “A Linear Acoustic Model for Intake Wave Dynamics in IC Engines,” *J. Sound Vib.* 269(1-2):361-387, 2004, doi:10.1016/S0022-460X(03)00196-2.
14. Margary, R., Nino, E., and Vafidis, C., “The Effect of Intake Duct Length on the in-Cylinder Air Motion in a Motored Diesel Engine,” SAE Technical Paper 900057, 1990, <https://doi.org/10.4271/900057>.
15. Justham, T., Jarvis, S., Garner, C.P., Hargrave, G.K. et al., “Single Cylinder Motored SI IC Engine Intake Runner Flow Measurement Using Time Resolved Digital Particle Image Velocimetry,” SAE Technical Paper 2006-01-1043, 2006, <https://doi.org/10.4271/2006-01-1043>.
16. Lee, J. and Farrell, P.V., “Intake Valve Flow Measurements of an IC Engine Using Particle Image Velocimetry,” SAE Technical Paper 930480, 1993, <https://doi.org/10.4271/930480>.
17. Renaud, A., Ding, C.-P., Jakirlic, S., Dreizler, A. et al., “Experimental Characterization of the Velocity Boundary Layer in a Motored IC Engine,” *Int. J. Heat Fluid Fl.*, 71, 366- 377, 2018, <https://doi.org/10.1016/j.ijheatfluidflow.2018.04.014>.
18. Baum, E., Peterson, B., Böhm, B., and Dreizler, A., “On the Validation of LES Applied to Internal Combustion Engine Flows: Part 1: Comprehensive Experimental Database,” *Flow Turbul. Combust.* 92(1-2):269-297, 2014, doi:10.1007/s10494-013-9468-6.
19. Buhl, S., Hain, D., Hartmann, F., and Hasse, C., “A Comparative Study of Intake and Exhaust Port Modeling Strategies for Scale-Resolving Engine Simulations,” *Int. J. Engine Res.*, 19(3), 282-292, 2018, <https://doi.org/10.1177/1468087417707452>.
20. Laperre, J. and Thys, W., “About Standing Waves in an Air Column: Transient Regime and Transfer Function,” *Eur. J. Phys.* 13(5):236-244, 1992, doi:10.1088/0143-0807/13/5/007.
21. Engelman, H.W., “Design of a Tuned Intake Manifold,” ASME Paper No. 73-WA/DGP-2, 1973.
22. Graftieaux, L., Michard, M., and Grosjean, N., “Combining PIV, POD and Vortex Identification Algorithms for the Study of Unsteady Turbulent Swirling Flows,” *Meas. Sci. Technol.* 12(9):1422-1429, 2001, doi:10.1088/0957-0233/12/9/307.

## Contact Information

Benjamin Böhm

Fachgebiet Reaktive Strömungen und Messtechnik (RSM), Technische Universität Darmstadt, Darmstadt, Germany [boehm@rsm.tu-darmstadt.de](mailto:boehm@rsm.tu-darmstadt.de)

## Acknowledgements

The research project (1286) was performed by the Institute of Reactive Flows and Diagnostics (RSM) at the Technische Universität Darmstadt under the direction of Prof. Andreas Dreizler and the Aerothermochemistry and Combustion Systems Laboratory (LAV) at the Eidgenössische Technische Hochschule Zürich under the direction of Prof. Konstantinos Boulouchos. Based on a decision taken by the German Bundestag, it was supported by the Federal Ministry for Economic Affairs and Energy

(BMW) and the AIF (German Federation of Industrial Research Associations eV) within the framework of the industrial collective research (IGF) programme within the framework of the collective research networking (CORNET) programme (IGF/CORNET-No. 206 EN). The project was conducted by an expert group led by Gabriel Dilmac, (Dr. Ing. h.c. F. Porsche AG). The authors gratefully acknowledge funding from the Research Association for Combustion Engines (FVV eV) and the Swiss Federal Office of Energy (grant no. SI/501930-01) and all those involved in the project. In addition, the simulation work of Mr. Mithulan Vasan is gratefully acknowledged.

## A.3 Paper III

### The Influence of In-cylinder Flows and Bulk Gas Density on Early Spray G Injection in an Optical Research Engine

C. Welch, M. Schmidt, C. Geschwindner, S. Wu, M. S. Wooldridge, B. Böhm: The Influence of In-cylinder Flows and Bulk Gas Density on Early Spray G Injection in an Optical Research Engine. *International Journal of Engine Research* 24, 1 (2023) Sage Publishing. <https://doi.org/10.1177/14680874211042320>

#### Paper III Permissions

Paper III is reproduced with permission from Sage Publishing. Permission to include Paper III in this cumulative dissertation: The following page was obtained on July 21, 2023 at 17:57 CET under the URL: <https://uk.sagepub.com/en-gb/eur/journal-author-archiving-policies-and-re-use>.



## Sage's Author Archiving and Re-Use Guidelines

These guidelines should be followed by authors of Contributions published in a Sage subscription journal, including authors whose Contributions were published under a previous version of the author guidelines. For a list of exceptions to these guidelines, please see below.

Three versions of the Contribution are referenced in these guidelines:

- **Original Submission:** the version submitted by the author before peer review
- **Accepted Manuscript:** version updated to include the author's revisions after peer review, prior to any typesetting for the journal. This is often the version accepted by the editor
- **Final Published PDF:** copy-edited and typeset Publisher's PDF, the same version published on the journal's website

## Green Open Access: Sage's Archiving and Sharing Policy

You may share the **Original Submission** or **Accepted Manuscript** at any time after your paper is accepted and in any format. Your sharing of the **Original Submission** or **Accepted Manuscript** may include posting a downloadable copy on any website, saving a copy in any repository or network, sharing a copy through any social media channel, and distributing print or electronic copies. Please note some journals will not consider papers that have been posted as preprints prior to submission and you may check a journal's policy regarding considering previously-posted papers by referring to the journal's submission guidelines.

For information on use of Institutional Repository (IR) copies by authors and IR users, see [Posting to an Institutional Repository - Green Open Access](#).

You may use the **Final Published PDF** (or **Original Submission** or **Accepted Manuscript**, if preferred) in the following ways:

- in relation to your own teaching, provided that any electronic distribution maintains restricted access
- to share on an individual basis with research colleagues, provided that such sharing is not for commercial purposes
- in your dissertation or thesis, including where the dissertation or thesis will be posted in any electronic Institutional Repository or database
- in a book authored or edited by you, at any time after the Contribution's publication in the journal.

*Provided that:*



- Access to the Original Submission and Accepted Manuscript is provided at no charge.
- Any re-use terms for users of websites and repositories (where your **Original Submission** or **Accepted Manuscript** are posted) are restricted to non-commercial and no derivative uses.
- You may not post the **Final Published PDF** on any unrestricted website or repository without permission from Sage.
- You may not republish or translate any version of your Contribution in another journal without prior permission from Sage.
- The journal as the original publication of your Contribution is appropriately credited by including the full citation information each time your Contribution, or excerpts, are further distributed or re-used:
  - After your Contribution has been accepted for publication and until it is assigned a DOI, please include a statement that your Contribution has been accepted for publication in the journal.
  - Once full citation information for your Contribution is available, please include this with your posted Contribution, in a format similar to the following:  
**Author(s), Contribution Title, Journal Title (Journal Volume Number and Issue Number) pp. xx-xx. Copyright © [year] (Copyright Holder). DOI: [DOI number].**

## Journal Exceptions

**Exceptions to this Author Re-Use policy:** The following journals have a different author re-use policy in place. The re-use terms for these journals are stated in the Contributor Agreement used by the Journal.

If you have questions regarding the following titles, contact the permissions team through our [Sage Permissions Portal](#).

- *California Management Review*
- *Acta Radiologica* (from January 2018)
- *Index on Censorship*
- *Pain News*
- *Political Insight*

## Related Information

Authors of Contributions published as Sage Choice or in a Gold Open Access journal should reference [Reusing Open Access and Sage Choice Content](#). For a list of Sage's Gold Open Access journals, please see [Gold Open Access journals](#).

Authors of Contributions published under a Creative Commons license may re-use their work under the terms of the Creative Commons license attached to their Contributions and additionally have all rights to re-use their work stated above.

For information about requesting permission for content published in Sage journals, see [Process for Requesting Permission](#).

For information about author copies, see [Author e-prints policy](#).

If you are submitting a manuscript to a Sage journal and wish to include previously published materials within the manuscript, visit our Author Gateway [Copyright and Permissions FAQs](#).

---

# DECLARATION ON THE CONTRIBUTION TO THE SCIENTIFIC PUBLICATION

## Erklärung zum Eigenanteil der wissenschaftlichen Veröffentlichung

Cooper Welch, M.Sc.

### PAPER

C. Welch, M. Schmidt, C. Geschwindner, S. Wu, M. S. Wooldridge, B. Böhm: The Influence of In-cylinder Flows and Bulk Gas Density on Early Spray G Injection in an Optical Research Engine. *International Journal of Engine Research* 24, 1 (2023). <https://journals.sagepub.com/doi/10.1177/14680874211042320>

### CO-AUTHORS

Marius Schmidt, M.Sc.

Christopher Geschwindner, M.Sc.

Shengqi Wu, Prof. Dr.

Margaret S. Wooldridge, Prof. Dr.

Benjamin Böhm, Dr.-Ing.

### INDIVIDUAL CONTRIBUTIONS

- **Cooper Welch**

- Jointly conducted Experiment I with Christopher Geschwindner and Marius Schmidt, jointly conducted Experiment II with Marius Schmidt, and conducted Experiment IV with support from Lars Illmann (not listed as co-author).
- Jointly conducted processing of data from Experiment I and II with Marius Schmidt.
- Conducted processing of data from Experiment IV.
- Conducted post-processing and analysis of all data.
- Coordinated cooperation with co-authors from different institutions.
- Main and corresponding author of the paper: performed literature research, generated all figures except the optical schematic, wrote the manuscript, and wrote and managed the review process.

- **Marius Schmidt**

- Jointly conducted Experiment I with Cooper Welch and Christopher Geschwindner, jointly conducted Experiment II with Cooper Welch, and jointly conducted Experiment III with Christopher Geschwindner.
- Jointly conducted processing of data from Experiment I and II with Cooper Welch.
- Assisted in processing of data from Experiment III.
- Supported in the analysis and interpretation of the results and the proofreading of the manuscript.

- **Christopher Geschwindner**

- Jointly conducted Experiment I with Cooper Welch and Marius Schmidt and jointly conducted Experiment III with Marius Schmidt.
- Conducted processing of data from Experiment III.
- Generated the optical schematic figure, supported in the analysis and interpretation of the results, and supported in the proofreading of the manuscript.

- **Shengqi Wu and Margaret S. Wooldridge**

Supported in the interpretation and discussion of the results and the proofreading of the manuscript.

- **Benjamin Böhm**

Provided resources for the conduction of the experiments. Supported in the interpretation and discussion of the results and the proofreading of the manuscript.

---

**OVERALL CONTRIBUTION OF COOPER WELCH**

A leading role in the conduction of the experiments, data analysis and interpretation, and main author of the manuscript.

**USE OF PAPER CONTENTS IN OTHER DISSERTATIONS**

This publication is not the subject of another ongoing or completed dissertation.

**SIGNATURES OF ALL AUTHORS**



Cooper Welch



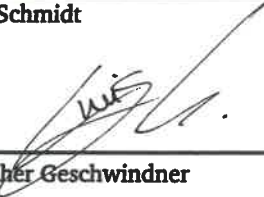
Shengqi Wu



Marius Schmidt



Margaret S. Wooldridge



Christopher Geschwindner



Benjamin Böhm

# The influence of in-cylinder flows and bulk gas density on early Spray G injection in an optical research engine

Cooper Welch<sup>1\*</sup>, Marius Schmidt<sup>1</sup>, Christopher Geschwindner<sup>1</sup>, Shengqi Wu<sup>2</sup>, Margaret S Wooldridge<sup>3</sup>, Benjamin Böhm<sup>1</sup>

<sup>1</sup>Technical University of Darmstadt, Department of Mechanical Engineering, Reactive Flows and Diagnostics, Otto-Berndt-Str. 3, 64287 Darmstadt, Germany

<sup>2</sup>School of Aeronautics and Astronautics, Shanghai Jiao Tong University, Shanghai, China

<sup>3</sup>Departments of Mechanical Engineering and Aerospace Engineering, University of Michigan, Ann Arbor, MI, USA

\*Corresponding author: Cooper Welch, email: [welch@rsm.tu-darmstadt.de](mailto:welch@rsm.tu-darmstadt.de)

## Abstract

A well-characterized multi-hole gasoline injector, the Engine Combustion Network's (ECN) Spray G injector, was investigated in an optically accessible research engine under four motored operating conditions with early injection. The experiments were conducted at intake pressures of 0.4 bar and 0.95 bar, nearly matching the ECN's standard early injection operating conditions, Spray G2 (flash boiling) and Spray G3 (early injection), respectively. This was combined with two engine speeds at 800 rpm and 1500 rpm. Using particle image velocimetry and volumetric Mie scatter imaging, the in-cylinder flows were evaluated and the effects on the spray morphology were characterized. The in-cylinder flow was evaluated to understand the spray-flow interaction, including the turbulent kinetic energy. Little effect on turbulent energy was observed in the region examined near the exit of the fuel injector nozzle shortly after injection. Mie scatter imaging was used to characterize the spray morphology and wall wetting was clearly visible on the spark plug. Cyclic variability of the sprays was found to be insignificant; and major differences in spray morphology are attributed to the in-cylinder velocity and intake pressure at the time of injection. Decreasing the bulk gas density by decreasing the intake pressure had a number of effects on the evolution of the spray including faster evaporation, increased axial liquid penetration, and decreased spray angle. Increasing the in-cylinder flow magnitudes by increasing the engine speed had a similar effect on spray morphology by also increasing the evaporation rate, increasing the axial penetration, and decreasing the spray opening angle. Comparison of the motored spray cases with a no-flow case (when the fuel is sprayed into the engine without the piston present) further illustrated the extent to which the intake flow influenced the spray shape.

## Keywords

Direct injection spark-ignition, Spray G, particle image velocimetry, spray-flow interaction

## 1 Introduction

In order for passenger cars employing combustion engines to remain a viable option in a quickly changing global mobility transformation, next-generation engines must be designed to meet and exceed stringent emissions regulations. One promising technology for increasing efficiency and decreasing emissions is direct injection spark-ignition (DISI) engines, which offer the advantages of precise control of the amount of fuel injected, the timing of injection, and the location of injection, which in the case of stratified combustion, allows for lean mixtures.<sup>1</sup> While stratified charge spark-ignition (SI) engines offer the advantage of a high specific power output in low load operation, they

are plagued by seemingly random misfires and partial burns resulting from sensitivity to minimal changes in the mixture at the time of ignition<sup>2,3</sup> as well as a susceptibility of spray impingement on the piston due to late injection timings, leading to increased particulate emissions.<sup>3,4</sup> For the aforementioned reasons, research, and manufacturing of passenger car engines over the last decades has largely shifted from stratified charge, late injection, to homogeneous (stoichiometric), early injection, DISI technology because of the benefits of precise control of the fuel injection, efficient use in full load and speed ranges, charge cooling associated with the evaporation of the fuel in the cylinder, and the effectiveness of the use of three-way catalyst systems with stoichiometric mixtures, which achieve significant reductions in NO<sub>x</sub>, CO, and HC emissions.<sup>1,5</sup>

A recent movement in DISI technology has placed the emphasis not on the design of the engine geometry to facilitate atomization and proper mixing near the spark plug, as in older wall-guided configurations, but on the design of the injector, which itself should achieve the same goals, ideally without wall wetting.<sup>1</sup> These spray-guided engine configurations therefore require careful design of the injector systems and much research and development has to be done to first understand, then optimize the mechanisms involved in efficient DISI combustion.

Even in early injection systems, the mixture preparation processes are much more complex than in port fuel injection because the spray must rapidly evaporate before impingement on in-cylinder surfaces and must properly mix before ignition. Multi-hole nozzles with wide global spray angles<sup>6</sup> have emerged as a preferred design solution for achieving adequate dispersion and mixing, but the in-cylinder flow motion, usually characterized as a tumble-inducing flow, plays a big role in these processes.<sup>1</sup> However, spray impingement on in-cylinder surfaces remains an important consideration in the design of DISI engines because apart from injector nozzle and cylinder geometry design, recent studies have shown that more factors such as fuel temperature, coolant temperature, injection pressure, injection timing, fuel concentration, and engine load affect fuel film deposition and subsequent particulate emissions due to locally rich combustion.<sup>7-9</sup> Therefore, it is crucial to identify wall wetting on all surfaces so that it may be avoided in future implementations.

As mixing and dispersion processes are largely dominated by the in-cylinder motion, recent investigations with optical research engines have explored the effects of the in-cylinder flows on spray formation in detail by using advanced optical diagnostics. In an early study, Serras-Pereira et al.<sup>10</sup> recognized that the flow significantly affects spray morphology by comparing Mie scatter imaging of multi-hole injection sprays in ambient chamber conditions with part-load engine sprays. Marchi et al.<sup>11</sup> observed a reduction in the angle of a hollow-cone spray due to the flow induced by a first injection and Stiehl et al.<sup>12</sup> observed a similar trend in that with more than one hollow-cone injection, subsequent injections exhibited more cycle-to-cycle variations (CCVs) and an upward flow toward the cylinder head was identified as the main contributor to the spray deformation. In a subsequent study by Stiehl et al.<sup>13</sup> simultaneous particle image velocimetry (PIV) and Mie scatter imaging revealed correlations between the tumble motion and the spray formation of a second hollow-cone spray, while the first spray remained largely undisturbed. The addition of a hollow-cone spray into a motored engine flow was shown by Peterson et al.<sup>14</sup> to increase the turbulent kinetic energy, shear, and vorticity distributions by means of comparing tomographic PIV from experiments with and without spray. In a more recent investigation, Chen et al.<sup>15</sup> used PIV to focus on the effects of a multi-hole injector spray on the ensuing flow field in early and late injection and found that the sprays did not significantly increase CCVs of the air flow, especially by the time of ignition. Finally, Sharma et al.<sup>16</sup> compared the spray droplet size and velocity from a multi-hole injector in a constant volume chamber (CVC) and in a fired engine environment and found that the in-cylinder flows significantly hindered the spray droplet velocities. While the aforementioned investigations have widely advanced the field of DISI engine research, many of the findings are injector specific and none of them examined in detail and quantified the effects of the in-cylinder flow on macroscopic spray morphology for early injection.

In the pursuit of pooling the knowledge and resources of multiple research institutions around the world into the better understanding of the topic of spray-guided DISI combustion, the Engine Combustion Network (ECN) established a standardized multi-hole injector geometry with certain operating guidelines as a common framework for collaborative studies. The ECN's<sup>17</sup> gasoline operating conditions, the so-called *Spray G* conditions have expanded from the high-density late injection standard *Spray G*, to a low-density early injection flash boiling *Spray G2* condition, to an ambient density early injection *Spray G3* condition, and to four other conditions over a wide range of parameters which are supposed to cover most of the possible phenomena involved in multi-hole spray-guided engine combustion. The injector used for this collaborative effort has eight evenly spaced holes, each with an orifice drill angle of 37°. A wide range of research has been conducted to study the injector and the *Spray G* operating conditions (OCs) using advanced imaging techniques in CVC experiments through spray morphology and injector detail characterization<sup>18-21</sup> and multi-parameter inter-plume aerodynamics measurements.<sup>22</sup>

Recent experiments have combined the *Spray G* injector and operating conditions in more realistic configurations by using optical research engines, instead of CVCs, for a more complex injection environment including in-cylinder motion. First, through Mie scatter imaging in the bottom view of an optical research engine, it was shown that engine speed plays a large role in the spray characteristics of early injection *Spray G2* and *G3*, indicating that CVC experiments can miss important phenomena involved in the spray-flow interaction.<sup>23</sup> Then expanding upon these findings, a joint effort between two optical research engine groups equipped with *Spray G* injectors was carried out by studying the in-cylinder flows by means of PIV and their effects on spray morphology in late injection.<sup>24</sup> The results of the late injection investigations have shown that higher engine speeds lead to a more stable spray (angle) since the upward velocity induced by the piston in compression acts against the downward spray plumes and helps limit interactions between individual plumes.<sup>24</sup>

With the availability of experimental data sets from different research institutions, numerical models have been developed to simulate *Spray G*, first in the CVC environment,<sup>25,26</sup> then in the motored engine environment,<sup>27</sup> using open source code based on Reynolds-averaged Navier–Stokes (RANS). While these studies show promising progress in the field of high fidelity spray modeling, more experimental data are required to help identify the complex relationships involved in DISI engine operation and to equip researchers with accurate validation data in these environments.

Previous experimental investigations have shown that the in-cylinder velocity plays a crucial role in the development of sprays, but few investigations have quantified the effects of the flow on the spray morphology. With the goal of increasing the experimental data base and decreasing the knowledge gap of *Spray G* DISI engine operation, this work uses advanced laser diagnostics and imaging techniques to provide a comprehensive study of early injection *Spray G* in increasingly complex research engine experiments by examining the effects of bulk gas density and in-cylinder flows on the spray development. This work is organized as follows: first, the engine test stand as well as diagnostic and post-processing methodologies are introduced. Then, the in-cylinder velocity and its implications on spray atomization are examined. Afterward, the effects of decreasing bulk gas density and increasing in-cylinder velocity on spray shape evolution and inter-plume interaction are investigated. The results and discussion are then completed with a comparison of the morphology of each OC as well as a simplified no-flow engine spray case, which directly exemplifies the strong influence of in-cylinder flows on direct injection sprays. Finally, conclusions about early injection *Spray G* in DISI configurations are discussed and recommendations for future research topics are made.

## 2 Experimental Setup

### 2.1 Engine Test Bench

Measurements were conducted at the Technical University of Darmstadt in a well-documented, well-characterized optical research engine test bench (*Darmstadt engine*).<sup>28–30</sup> The single-cylinder spark-ignition research engine from AVL consists of a Bowditch piston extension, flat quartz glass piston surface, and a quartz glass cylinder liner for optical access. A four-valve spray-guided cylinder head configuration was employed, in which the Spray G injector and spark plug were both nearly vertically mounted and visible through the pent-roof quartz glass access. Table 1 shows the most relevant parameters for the Darmstadt engine configuration and Spray G injector used in this study. The early injection Spray G conditions outlined by the ECN<sup>17</sup> use CVCs for precisely controlled characterization measurements.<sup>19,20</sup> The engine experiments were conducted using the four principle operating conditions (OCs) of the Darmstadt engine using two intake pressures and two engine speeds, as shown in Table 2. Since the fuel temperature in this experiment was tied to the standard coolant temperature of 60°C, flash boiling was not achieved for cases B and D. Nevertheless, the OCs of early injection Spray G with the parameters of Table 1 are closely related to the Spray G2 (*Flash Boiling*) and G3 (*Early Injection*) condition outlined by the ECN.<sup>17</sup> Fuel temperature aside, one more difference between the measurements and the ECN's conditions is in the bulk gas density, as the in-cylinder gas temperature depends on the cylinder head's temperature equilibrium. The in-cylinder temperature was estimated using the intake temperature as well as in-cylinder gas temperature measurements.<sup>31</sup> Using such an estimation, the air density for case A and C at hydraulic start of injection (SOI) was 1.08 kg/m<sup>3</sup>, while that of Spray G3 is 1.12 kg/m<sup>3</sup>, a difference of 4.7 %. Furthermore, the bulk air density for OCs B and D was 0.45 kg/m<sup>3</sup>, while Spray G2 is 0.5 kg/m<sup>3</sup>, a difference of 10.1 %. The densities of the spray conditions within the engine and ECN guidelines are shown in Table 1 for comparison. Additional

information regarding the Darmstadt engine test bench can found in Baum et al.<sup>28</sup> and Freudenhammer et al.<sup>29</sup>

Table 1. Darmstadt engine and ECN Spray G2 and G3 injection parameters.

Parameter	Engine			
Cylinder head configuration	Spray-guided 4V pent-roof			
Spray G injector number	AV67-027			
Injector angle (°)	8			
Bore 3 stroke (mm)	86 × 86			
Compression ratio (2)	8.7			
Parameter	Engine spray G2	ECN spray G2 <sup>17</sup>	Engine spray G3	ECN spray G3 <sup>17</sup>
Facility	Darmstadt	ECN CVC	Darmstadt	ECN CVC
Fuel	Iso-octane	Iso-octane	Iso-octane	Iso-octane
Bulk gas	Air (dry)	0% O <sub>2</sub>	Air (dry)	0% O <sub>2</sub>
Engine speed (rpm)	800/1500	–	800/1500	–
Electronic SOI (°CA)	-270	–	-270	–
Hydraulic SOI (°CA)	-268.56/-267.29	–	-268.56/-267.29	–
Elec. inj. Duration (ms)	0.680 (Mie)/0.660 (PIV)	0.680	0.680 (Mie)/0.660 (PIV)	0.680
Hydr. inj. duration (ms)	0.780 (Mie)/0.760 (PIV)	0.780	0.780 (Mie)/0.760 (PIV)	0.780
Gas pressure at hydr. SOI (bar)	0.4	0.5	0.95	1.0
Gas density at hydr. SOI (kg/m <sup>3</sup> )	0.45	0.5	1.08	1.12
Fuel pressure (bar)	200	200	200	200
Fuel temperature (°C)	60	90	60	90
Fuel mass (mg/cycle)	10 (estimated)	10	10 (estimated)	10

Table 2. Standard operating conditions of the Darmstadt engine.

	Intake pressure	
	0.95 bar	0.4 bar
800 rpm	A	B
1500 rpm	C	D



## 2.2 Optical Arrangement

Four experimental campaigns were conducted in this work to provide a comprehensive study of early injection Spray G in an optical engine environment. The optical setups of PIV and Mie scatter imaging are described in the following sections and a summary of the experimental details is found in Table 3. In addition, a schematic detailing the engine geometry and different optical setups is provided in Figure 1.

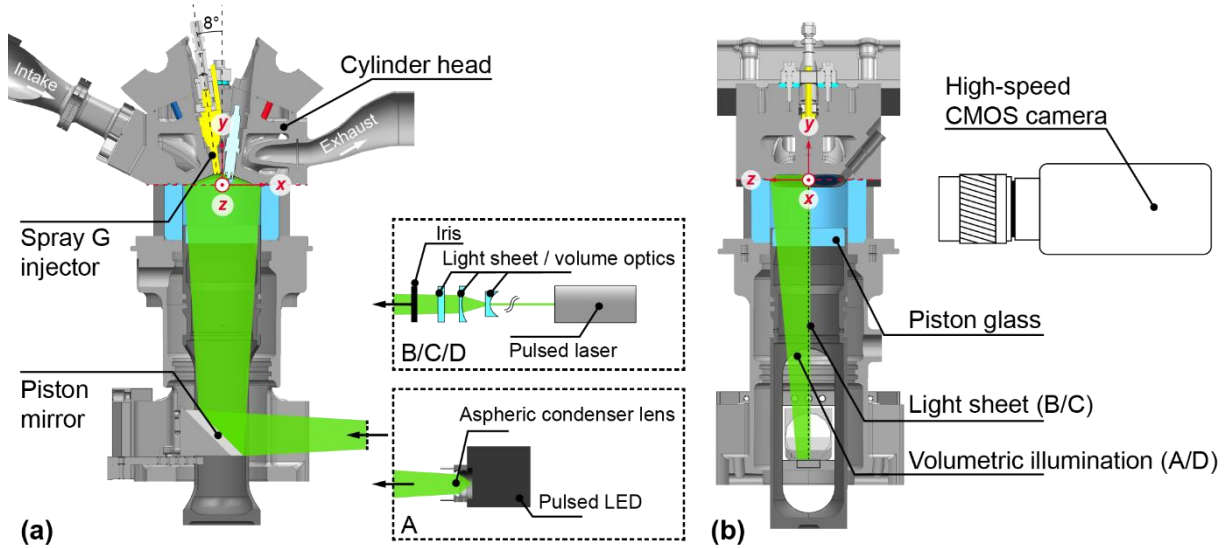


Figure 1. Experimental setups used within this study. (a) Section view of the x–y plane including the optical arrangement of the employed illumination sources. The injector and spark plug are located centrally in the x–y plane as indicated by the section view. (b) Section view of the y–z plane.

Table 3. Summary of experimental setups.

Parameter	Experiment I	Experiment II	Experiment III	Experiment IV
Description	HS PIV - spray	HS PIV - motored	Mie scat. - motored	Mie scat. - NF
Light source	Nd:YAG sheet (532 nm)	Nd:YAG sheet (532 nm)	LED volume (525 nm)	Nd:YVO <sub>4</sub> volume (532 nm)
Optics	–50 mm cyl. + –200 mm cyl. + 1000 mm cyl.	–50 mm cyl. + –200 mm cyl. + 1000 mm cyl.	Aspheric condenser lens 40 mm	–50 mm cyl. + 1000 mm cyl. + 200 mm cyl. + –50 mm cyl.
Camera	Phantom v711	Photron Fastcam SA-X2	Phantom v711	Phantom UHS v2640
Lens	Sigma $f = 105 \text{ mm} + f/11 + 20 \text{ mm}$ extension	Sigma $f = 105 \text{ mm} + f/11 + 20 \text{ mm}$ extension	Nikon $f = 50 \text{ mm} + f/5.6$	Nikon $f = 85 \text{ mm} + f/16 + 35 \text{ mm}$ extension
Rep. rate (Hz)	4800 at 800 rpm + 4500 at 1500 rpm	960 at 800 rpm + 1800 at 1500 rpm	16000	25000
Int. window or pixel size	(2.54 mm) <sup>2</sup> int. window + 635 mm vector spacing	(2.02 mm) <sup>2</sup> int. window + 504 mm vector spacing	13 $\mu\text{m}/\text{pixel}$	65.2 $\mu\text{m}/\text{pixel}$

### 2.2.1 Particle Image Velocimetry

In-cylinder flow was measured using high-speed PIV by illuminating silicon oil droplets ( $\approx 0.5$  mm, DOWSIL 510, Dow Corning) with two laser sheets (532 nm, 1.3 mm thickness at 13.5 % of the maximum intensity) introduced by frequency-doubled Nd:YAG cavities through the optical piston via the Bowditch extension and piston mirror. Flow data used in this work comes from two different experimental campaigns, designated Experiment I and Experiment II, as outlined in Table 3.

For Experiment I, the main focus of this study, a Phantom v711 high-speed CMOS camera equipped with a Sigma lens ( $f = 105$  mm,  $f/11$ , 20 mm extension tube) was used to acquire image pairs from the side of the glass cylinder, maximizing the possible field-of-view of the combustion chamber ( $58 \times 63$  mm<sup>2</sup>). Image pairs were acquired at a crank angle (CA) resolution of 1°CA for an engine speed of 800 rpm (4.8 kHz) and 2°CA for an engine speed of 1500 rpm (4.5 kHz) with varying time separation between laser pulses  $dt$  from 51 ms to as low as 3 ms.

Experiment II is used in this work simply to provide context for the in-cylinder flows without the direct injection of fuel and represents the well-documented PIV approach of Welch et al.<sup>32</sup> For details on Experiment II not found in Table 3 and the processing of image pairs, please refer to Welch et al.<sup>32</sup>

### 2.2.2 Mie Scatter Imaging

Experiment III represents the high-speed imaging of liquid spray using Mie scattering. Even though diffuse back-illumination (DBI) is the ECN's technique of choice for morphological comparisons, the authors of this work have chosen to use bottom illumination Mie scattering instead of DBI because of two reasons: firstly, the cylinder roof obstructs much of the incoming LED light from the diffuser, blocking about half of the spray from being illuminated; and secondly, the disadvantage of increased beam steering and the susceptibility of overestimation of the liquid phase of the spray associated with DBI.<sup>24,33</sup> As shown in Figure 1, light from a pulsed LED equipped with an aspheric condenser lens was introduced to the cylinder volume via the piston mirror assembly and images were acquired from the side of the cylinder. The high-speed CMOS camera used for image acquisition was a Phantom v711 equipped with a Nikon lens ( $f = 50$  mm,  $f/5.6$ ) operating at a frame-rate of 16 kHz.

In addition to the Mie scattering experiments described above, an additional no-flow (NF) experiment, Experiment IV, was conducted to act as a baseline for comparison. In the NF case, the engine's piston was completely replaced by an exit flow duct with a quartz glass bottom plate and the stationary intake valves were set to 9.21 mm, which corresponds with the valve lift at  $-270^\circ\text{CA}$ , ( $270^\circ\text{CA}$  before compression top dead center), allowing for an unobstructed open channel for the spray to travel through. The simplified open-engine geometry is introduced in Hausmann et al.<sup>34</sup> as a flow bench experiment; however, in this current study, no intake flow is introduced into the channel, the Spray G injector replaces a blank dummy injector, and sprays occur after a sufficient amount of time to allow residual fuel from previous sprays to evaporate and exit the channel (a purge of 0.517 kg/h was used to facilitate movement of residual gas). A mirror below the channel still allowed for bottom illumination from a volumetric light source of two Nd:YVO<sub>4</sub> high-speed laser cavities for a combined effective repetition rate of 25 kHz. No-flow Mie scatter images were acquired using a Phantom UHS v2640 high-speed CMOS camera equipped with a Nikon lens ( $f = 85$  mm,  $f/16$ , 35 mm extension tube) from the side of the engine cylinder in the same manner as the motored engine Mie scattering experiments.

## 2.3 Post-processing

### 2.3.1 Vector Calculation

In both Experiment I and II data were pre-processed and vectors were calculated using the commercial software *DaVis 8.4*. A progression of five steps were followed to bring raw image pairs to processed vector fields:

1. *Image pre-processing* A spatial sliding background correction of pixel length 8 was used to reduce noise and reflections. In addition, a particle intensity normalization filter of length was applied to help increase particle contrast.
2. *Image masking* First a geometric mask followed by an algorithmic mask was applied to each image to remove areas of high multiple scattering due to highly reflective objects such as the spark plug, or in the case of Experiment I, the liquid spray. The algorithmic mask consisted of first a local standard deviation filter over 10 pixel, then with the new image, a minimum and maximum threshold of 9 and 350, respectively to remove the remaining stationary and non-illuminated objects from further calculation.
3. *Image correction* Before vector calculations began, the masked images had to be dewarped and scaled using a third order polynomial based on images acquired of a 3D calibration plate (LaVision plate 058-5).
4. *Vector calculation* Vectors were calculated using a cross-correlation PIV algorithm with multiple passes of decreasing window size. The first two passes used interrogation window (IW) sizes of  $64 \times 64$  with 50% overlap. The final two passes decreased their window size to  $32 \times 32$  with 75% overlap and employed the adaptive PIV Gaussian weighting function.
5. *Vector post-processing* Post-processing of vectors was executed without any smoothing. First a peak ratio criterion was applied which deletes any vectors whose first and second correlation peaks in the IW are below 1.3. Next, a universal outlier detection was applied, consisting of normalized median filter sliding in a  $7 \times 7$  vector window. Finally, with the overlap of 75% a remove group criterion of five vectors was used, that is if less than five vectors out of the possible 16 are available, the entire group is removed. This is done to remove more spurious vectors that were missed by the median filter due to, for example, high reflections.

Vector files for each crank angle and cycle were then imported into MATLAB and the phase-average, that is, the average vector field at each crank angle over all cycles, was computed with a minimum of 25 vectors per IW required.

Regarding vector calculation and statistical uncertainties, possible sources of error have been extensively discussed for a similar PIV setup in the Darmstadt engine.<sup>34</sup> For the present work, phase-averaged uncertainties for Experiment I and II were estimated using the built-in correlation statistics approach included in *DaVis*.<sup>35</sup> The uncertainties range between  $\approx 2\%$  and  $4\%$  within the relevant region of interest defined in Figure 3.

### 2.3.2 Spray Boundary Calculation

The detection of spray boundaries of Mie scatter images was conducted with in-house *MATLAB* code and followed the same exact procedure as in Geschwindner et al.<sup>24</sup> and is summarized in four steps:

1. *Image correction* As with raw PIV images, the raw Mie scatter images were first dewarped and transformed into lab coordinates using the same 3D target and a third order polynomial.

2. *Image masking* In a similar manner to PIV image pre-processing objects such as the spark plug and intake valves were masked out to remove reflective engine features.
3. *Background subtraction and noise reduction* The mean of the first three images before injection was used as a background subtraction for all subsequent spray images and a  $3 \times 3$  median filter was applied to reduce noise.
4. *Threshold definition and binarization* Each spray cycle was assigned a single threshold of the normalized intensity of the cycle. To define the threshold, the maximum intensity of the mean background image (which was previously subtracted) was added to the 2D spatial standard deviation of the mean background multiplied by a separation factor of 250. The separation factor of 250 was selected to create sufficient separation between the foreground and background signal and corresponds to the spatial placement of the segmentation edge in the region of the sharp intensity gradient at the spray's boundary. However, strong variations of the separation factor do not cause significant deviations in the calculated geometrical spray parameters.

Due to the slightly in-homogeneous intensities from the two laser cavities used in Experiment IV, a separate threshold was calculated for all images of each cavity, that is, two thresholds were calculated, one for odd- numbered images and one for even-numbered images. This resulted in a significantly different threshold value than the combined set of images. Yet, using two separate sets, the thresholds were very close (within a 10th of a percentage difference) and were therefore averaged to one single value. The resulting average threshold over all cycles for Experiment IV is 11.14 % while for Experiment III the values ranged from 5.33 % to 6.63 % of their maximum normalized intensity of each injection, depending on the OC.

### 2.3.3 Extraction of Spray Parameters

The axial penetration length  $L$  and spray angle  $\alpha$  are geometric parameters calculated based on the binarized spray images using in-house *MATLAB* code. The axial penetration is defined as the maximum distance of the spray boundary from the injector tip along the injector axis. In accordance with the definition of Payri et al.,<sup>19</sup>  $\alpha$  is the angle between the lines determined by a linear least- squares fit of the two outer edges of the spray boundary between 1 % and 50 % of the maximum  $L$ . Figure 2 provides a visual representation of the defined parameters.

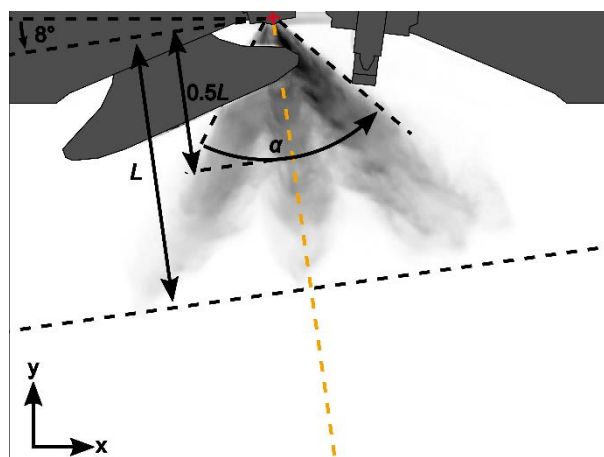


Figure 2. Definitions of geometrical parameters penetration length  $L$  and spray angle  $\alpha$ .

## 3 Results and Discussion

### 3.1 In-Cylinder Velocity

#### 3.1.1 Velocity without Injection

Before investigating the effects of the flow field on the evolution of sprays, it is first important to understand and characterize the in-cylinder flows before SOI. Under the four standard operating conditions (OCs) of the Darmstadt engine, shown in Table 2, phase-averaged flow fields of the velocity magnitude at  $-270^\circ\text{CA}$  normalized by the piston speed in the symmetry plane  $|U_{m,n}|$  are shown in Figure 3. The phase-averaged flow fields represent the average of 222 cycles for OC A and B and 296 cycles for C and D at  $-270^\circ\text{CA}$ , with the blue-yellow colormap indicating the velocity magnitude and the streamlines indicating the flow directions. Since the electronic injection signal for the early injection begins at  $-270^\circ\text{CA}$ , these flow fields reflect the state of the in-cylinder motion just before the spray commences.

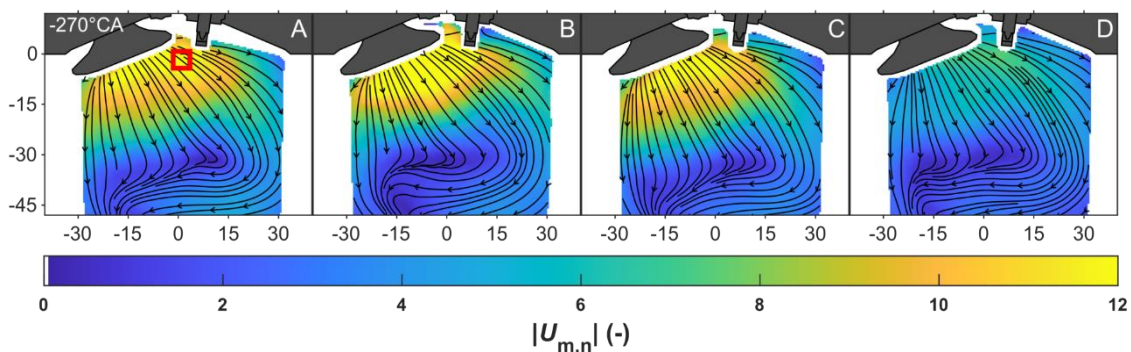


Figure 3. Phase-averaged flow fields of the velocity magnitude at  $-270^\circ\text{CA}$  normalized by the piston speed. The red box in the first panel represents the region of interest for the velocity profile in Figure 4.

In a previous study by Welch et al.,<sup>32</sup> it has been shown that OCs B and D (part-load OCs) exhibit a pressure equalizing backflow from the cylinder to the intake pipe, due to the intake pressure being below atmospheric pressure. This induces pressure oscillations in the intake manifold, which ultimately affect the intake flow. As shown in Figure 3, OC D has much lower normalized velocities than OC B at the time of electronic start of injection (eSOI), despite all OCs having similar flow structures (indicated by the streamlines).

Due to the transient local pressure ratio at the valves in the case of part-load operation, the equalization of the pressure induces strong fluctuations in the flows entering the cylinder. Figure 4 shows the effects of the pressure instabilities on the average absolute intake velocity magnitude in the region of interest below the injector, highlighted by the red box in the flow field of OC A in Figure 3. Figure 4 also highlights the definition of a “theoretical spray event” by showing the timing for eSOI and the end of injection (EOI) for the two engine speeds. The timing for EOI is determined from Experiment II (PIV with spray), by the absence of strong Mie scattering stemming from dense liquid spray clouds and large droplets in the laser sheet, which induce a bias in the vector calculations as well as more deleted vectors (further visualization of the 2D-projected area obtained on a planar slice at EOI is provided by Figure 7; in the case of Figure 4 no fuel is injected). The intake velocity profiles during theoretical injection show that the intake flow of OCs A and B slightly decelerates during a theoretical injection event, yet these flows may still be considered relatively stable. Operating condition C also exhibits a relatively stable intake flow as it first accelerates then steadies out before decelerating to similar speeds as before the theoretical injection event. On the other hand, in the case of OC D, which

has a liquid injection duration spanning from  $-267.3^{\circ}\text{CA}$  to  $-261.4^{\circ}\text{CA}$ , the flow rapidly accelerates to velocities far exceeding those of OCs A and B and therefore, introduces a high amount of turbulence into the cylinder by the end of the injection. While these absolute velocity magnitude comparisons actually reflect the in-cylinder intake flows without injection occurring, it is safe to assume that the flows follow the same trends when a spray is injected; this will be further explored in the next section. It is important to point out again, that these velocities only reflect one region of interest below the injector; yet, the influx of flow in this region is still representative of the bulk intake flow, which has also been demonstrated by flow measurements in the valve plane.<sup>32</sup>

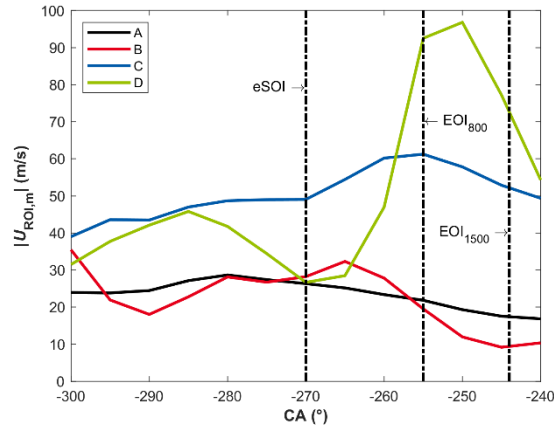


Figure 4. Phase-averaged velocity profiles near the intake valve without injection. The time range shown represents the duration of an injection event. The velocities are obtained from the average of the region of interest shown in the first panel of Figure 3. The vertical dashed lines represent the electronic start of injection and the end of injection for 800 and 1500 rpm.

### 3.1.2 Turbulent Kinetic Energy and Mixing

In the quiescent environment of a constant volume chamber, evaporation of a multi-hole injector spray is achieved through a coupling of the effects of the surrounding gas density, temperature, and the turbulence generated by the spray itself, which is designed to be significant. Yet, the actual application for such injectors includes the complex addition of turbulent flows and moving engine parts, constantly changing the boundary conditions (chamber pressure and temperature) as the piston and valves move. The ECN gasoline injector OCs considered in this work represent a short, early injection at ambient (G3, here case A and C) and part-load (G2 flash boiling, here case B and D) pressures. Global pressure and temperature are constant in the case of early injection, which reduces the complexity of such a problem, minimizing the consequential phenomena to the chosen intake load and the in-cylinder flows. The parametric variations of engine speeds and intake pressures of OCs A through D allow the examination of the effects of these properties on the evolution, evaporation, and mixing of sprays within a dynamic, highly turbulent in-cylinder flow field. The turbulent kinetic energy  $k$ , defined as the mean kinetic energy per unit mass in the fluctuating velocity field,<sup>36</sup> can be used to examine the evolution of turbulence in a flow field through the change of measured root mean square velocity fluctuations. In terms of the two-dimensional  $x - y$  velocity components  $u$  and  $v$  typical of experimental data, two-dimensional  $k$  can be written as:

$$k = \frac{1}{2} \left( \overline{(u')^2} + \overline{(v')^2} \right) \quad (1)$$

or simply:

$$k = \frac{1}{2} (S_x^2 + S_y^2) \quad (2)$$

where the over-line bar and “prime” in equation (1) denote the mean and fluctuations from the mean, respectively, and  $S$  in equation (2) denotes the standard deviation of the planar velocity components. Turbulent kinetic energy over time provides context for the state of the in-cylinder gas motion before an injection event and allows the determination of the amount of turbulence introduced into the system by the spray motion. Figure 5 shows an example  $k$  field within a mask marked by the red outline as well as the phase-averaged velocity indicated by the black arrows of scaled length and direction for OC B at  $-270^\circ\text{CA}$ . For the following analysis of  $k$ , the mean  $k$  within the same mask shown in Figure 5 is used for each OC and at each CAD to provide a global quantification of turbulence in the approximate cross-sectional area where the spray appears. Such a method for quantifying turbulence neglects the spatial distribution of local smaller-scale flow structures since the mask (relative to this engine’s optical access) is nearly global. However, the spatial mean  $k$  of this region of interest (where the liquid spray occurs) does capture the effects of all of the resolved scales of this technique and can be compared over time and over different OCs. As shown in Figure 5, the greatest  $k$  magnitude distribution just before the liquid spray begins is spread in a crescent shape 20–40 mm from the intake valves. This phenomenon can be explained by the increase in velocity fluctuations just beyond the high-velocity intake flow region of the symmetry plane. The spots of higher  $k$  are representative of the high gradient of the ensemble average velocity visible, for example, in the orange flow region for OC B in Figure 3.

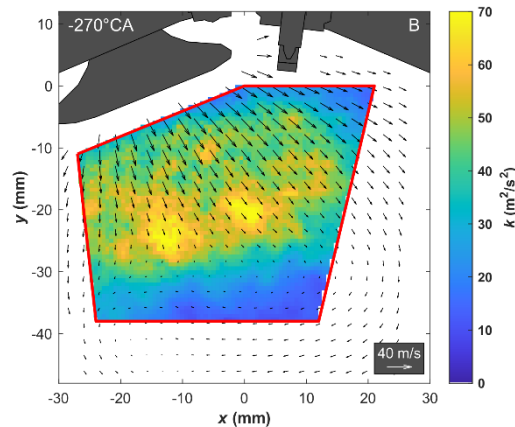


Figure 5. Global turbulent kinetic energy  $k$  at  $-270^\circ\text{CA}$  for OC B (800 rpm, 0.4 bar) within a conservative mask (red line). The blue-yellow colormap represents  $k$  and the black arrows represent the phase-averaged velocity magnitude (arrow length relative to the legend in the bottom right corner) and direction.

The turbulent kinetic energy  $k$  for OCs A through D with spray and without spray (labeled as *motored*) during intake is shown in Figure 6. Once again, for this visualization, EOI is defined as the end of the effect of the liquid spray on the PIV calculations and  $k$  is removed from the plot from SOI until EOI because of the absence of a sufficient number of viable vectors. The overall shapes of the curves reflect the intake velocity profile taken from the red region of interest shown in Figure 3, which indicates a correlation between mean intake velocity magnitude and velocity component fluctuations. When comparing experiments with and without injections, Figure 6 reveals that there is not a significant increase in  $k$  due to the highly turbulent spray. Shortly after the indicated EOI for the higher engine speed cases, the remaining fuel in the region of interest should be sufficiently evaporated so that the droplets do not affect the calculations through excess Mie scattering in the laser sheet. However, in the case of C, it appears that the remaining fuel droplets have an influence on the vector calculations, creating a bias because the large scattered fuel droplets cannot follow the flow as well as the oil seeding droplets. At  $-234^\circ\text{CA}$ ,  $k$  in the spray case of C begins to converge with that of the motored case, indicating a more accurate end of the effect of the spray on the flow field measurement, that is, a better EOI. The amount of turbulence, or better, lack thereof, added to the cylinder by the



spray may stem from a number of factors such as the time of injection, injection duration, engine speed, intake pressure, and injection pressure. However, it seems likely in this case that the lack of increase in  $k$  comes mainly from the field of view of the PIV experiment and the chosen region of interest, which only consists of an area directly below of the injector tip. Much of the added turbulence is likely convected downwards with the motion of the bulk flow and adds to the formation of the tumble vortex, which is largely left out of the chosen region of interest until the middle of the compression stroke because the piston remains near bottom dead center within this time range.

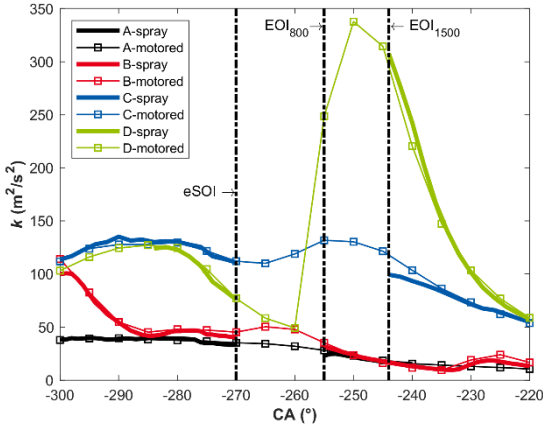


Figure 6. Mean turbulent kinetic energy  $k$  of the masked region shown in Figure 5 for OCs A through D from experiments with spray and without spray (motored) during intake. When vectors are affected by the presence of liquid spray,  $k$  is removed (indicated by black lines labeled EOI).

While it is highly likely that  $k$  increases during the injection of a high-speed disperse phase, as observed in several previous studies,<sup>12,37,38</sup> the strong multiple scattering of the fuel droplets render the flow fields at these times unusable for analysis. Yet, in a similar experiment by Chen et al.<sup>15</sup> it was observed that in the case of early injection, the flow structures and  $k$  did not change at the time of ignition. During late compression when ignition occurs, the turbulence should already have broken down into smaller structures, which may not be well- captured with the spatial resolution and in the single plane of these measurements. This implies that while the flow may have a significant effect on the spray morphology during intake, the spray's effect on the flow is minimal, especially in late compression, when the turbulence is dissipated, a finding which aligns well with the conclusions drawn by Figure 6.



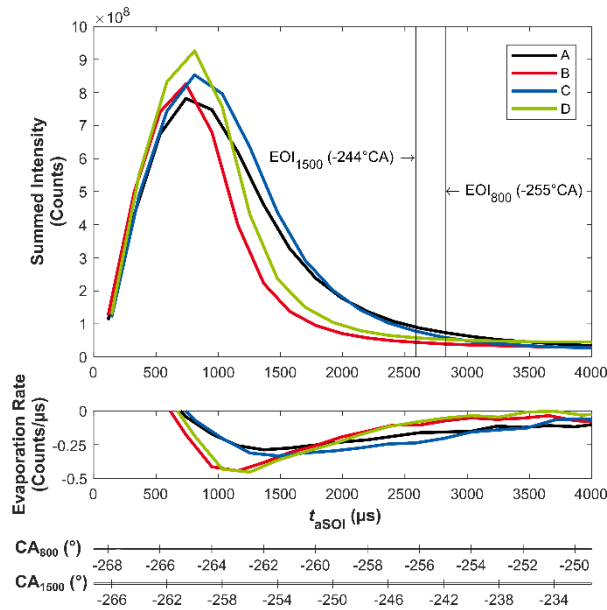


Figure 7. Estimation of the evaporation of the liquid spray after the start of injection. Top panel: sum of the spatial intensity by the CMOS camera. Bottom panel: rate of evaporation assumed to be the rate of change of the summed intensity at each time aSOI. The corresponding crank angles are provided for reference.

In the absence of evidence of an increase in turbulence due to the spray within the given region of interest, the interaction between the spray and in-cylinder velocity must be further analyzed. Perhaps the most important consideration in implementing a direct injection into an engine design is the evaporation and efficient mixing of the spray with the air. Without further optical techniques such as laser-induced fluorescence (LIF), it is difficult to quantify fuel-air mixing. However, using the Mie scattering of liquid fuel from a PIV experiment, it is possible to measure the relative evaporation of liquid fuel and assume that the fuel-air mixing is likely correlated with the rate of evaporation and in-cylinder velocity by summing the intensity of raw images and plotting the total intensity over time. Using such a method, the influence of seeding droplets and in-cylinder reflections on the intensity of the raw image must be eliminated before the sum of counts is performed so that the intensity only due to the presence of liquid fuel is considered. To achieve this strategy, first the average image over all cycles before ( $-270^{\circ}\text{CA}$ ) and after liquid injection is taken, resulting in an image with a uniform distribution of seed appearing blurred throughout the illuminated plane before injection and an average spray image (at each CAD) with the uniform blurred seed surrounding the spray. Then, a mask is applied to reflective objects such as the intake valves, spark plug, and cylinder roof for all images. Finally, the average image before spray is subtracted from the average spray images and the spatial intensity is summed, resulting in a time-series of spatial intensity. The top panel of Figure 7 displays the evolution of the total intensity and the bottom panel shows the assumed rate of evaporation for each OC. Here, assumed rate of evaporation refers to the rate of change of the summed spatial intensity of each image over time and thus reveals a quantity which is assumed to be the evaporation rate. Once again, the real hydraulic injection duration is 780 ms, which can be observed as the peak in summed intensity in the top panel, and EOI is chosen as points where the summed intensity is nearly zero. Two main conclusions may be drawn from this figure: first, the greater ambient gas density found in OCs A and C results in slower fuel evaporation from EOI until approximately  $t_{aSOI} = 1500$  ms, at which point the intensity of B and D is quickly approaching zero counts. The rapid rate of evaporation for OC B and D is due to the lower exertion on the surface of the droplets at lower ambient gas pressures (with constant intake temperature). Second, with increasing in-cylinder velocity, the magnitude of the evaporation rate is generally higher (bottom panel) from  $t_{aSOI} = 1000$  ms to  $t_{aSOI} = 2500$  ms. For this time window, the in-cylinder velocities for C and D reach a maximum as the valve lifts approach their

maximums (at  $-250^{\circ}\text{CA}$ ), while for A and B, the velocities are decreasing. When comparing cases with the same intake pressure, the differences of intake flow at this time period play their biggest roles in affecting the rate of evaporation. Increased rates of evaporation during this critical time window stem from the availability of fresh air for the spray to evaporate into, since fuel is more likely to evaporate when the local mixture is not saturated.

A tertiary conclusion from Figure 7 can be drawn from the relative magnitudes of the summed intensities in that with increasing total intensities, the cross-sectional liquid spray area appears to be larger. A larger spray area can manifest itself in several morphological features, for example, greater axial penetration or cross-sectional spray area. In the next section of this paper, the effects of variations of the in-cylinder pressure and velocity on the liquid spray shape will be examined in more detail.

## 3.2 Spray Morphology

In this section, results from the volumetric Mie scatter imaging approach are used to further evaluate the effect of pressure and in-cylinder velocity on the spray evolution.

### 3.2.1 Plume Interaction: Wall and Inter-Plume

One aspect of spray experiments in engine configurations that is largely negligible in pressure chamber experiments is the effect of wall wetting, that is, spray impingement on solid surfaces such as the piston. In ideal DISI engine designs, the injector and timing would be designed in a way to avoid such plume-wall interactions. Yet, this is a difficult task considering the relative length of spray duration required to achieve a combustible mixture compared with the positions of moving engine parts; in early injection cases the spray of a multi-hole injector might interact with the intake valves, spark plug, the piston surface (depending on engine speed and injection timing), and/or the cylinder walls. Therefore, it is important to acknowledge this phenomenon and understand its effects on spray and subsequent engine performance.

Figure 8 shows the spray evolution of instantaneous raw Mie scatter images for each OC (every 4th image displayed). The liquid spray, represented by illuminated liquid droplets, is displayed from the beginning, middle, and end of a typical spray event. Due to the line-of-sight used in this setup, individual plumes cannot be distinguished and the intake valves obstruct part of the view of the volumetric spray measurement. However, it appears that beginning from early spray at 198.7 ms aSOI that the outer plume on the exhaust side comes into contact with the spark plug for all cases. This phenomenon is even more clearly visible in the case of B and D at 698.7ms aSOI, where white streaks due to wetting appear downstream of the spark plug. While the effects of such wall wetting are difficult to quantify using the given experimental technique, it appears in the cases of B and D that this spray-wall interaction causes a deficiency in axial penetration on the exhaust-side plumes. The wall wetting observed in these images is supplemented by the findings of Pati et al.<sup>27</sup> in which the same engine using OC A with Spray G3 was simulated, and a fuel film was observed not only on the intake valves, but also on cylinder walls and even the piston surface, despite the early injection and short duration of Spray G3.

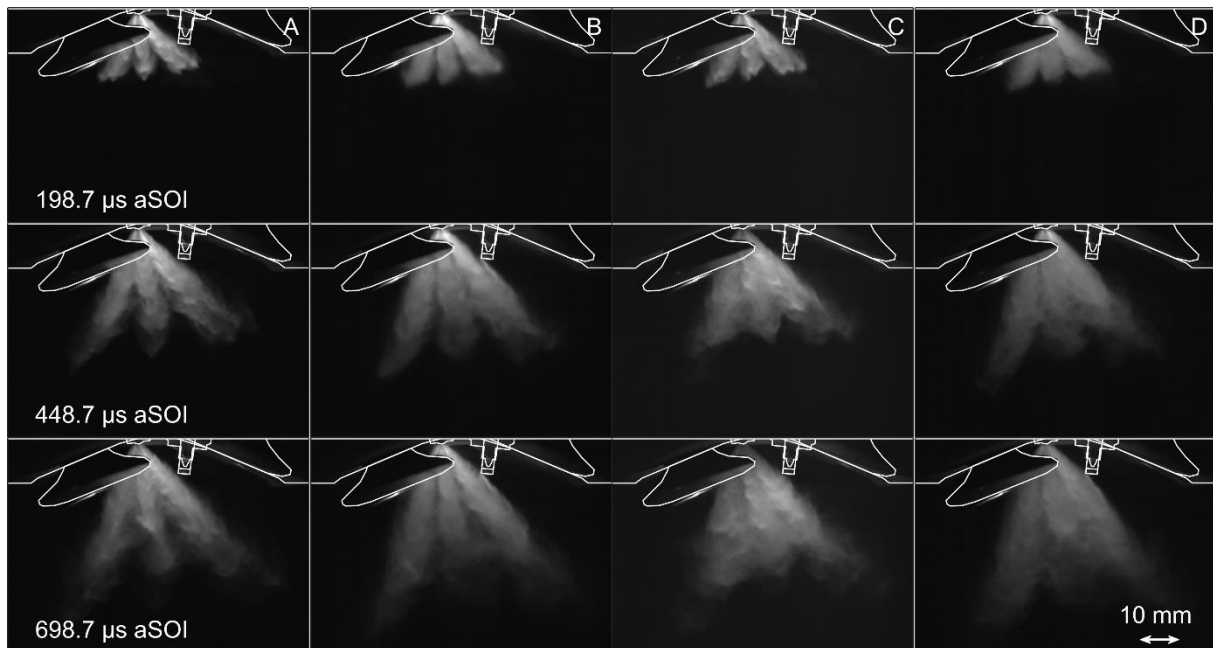


Figure 8. Evolution of instantaneous Mie scatter images for each OC.

As previously stated, the line-of-sight of these volumetric Mie scattering measurements does not allow direct visualization of individual plumes and important quantities for spray characterization, such as the individual plume angle, are still missing. However, a measure of the amount of interaction between plumes can be deduced by examining the Mie scatter images. Figure 9 displays the normalized average spray of 100 cycles at 698.7 ms aSOI. For this normalization, the images were first averaged, then the images were normalized to the highest intensity out of the four cases for a valid comparison between OCs. But examining the average spray images also reveals the extent to which individual plumes can be distinguished. It is clear that OC C has the most plume-to-plume interaction since there are no clear lines separating them. This can also be observed at the same time-step in Figure 8; however, in the instantaneous snapshots, plumes in case D also appear to have merged in a similar manner to C.

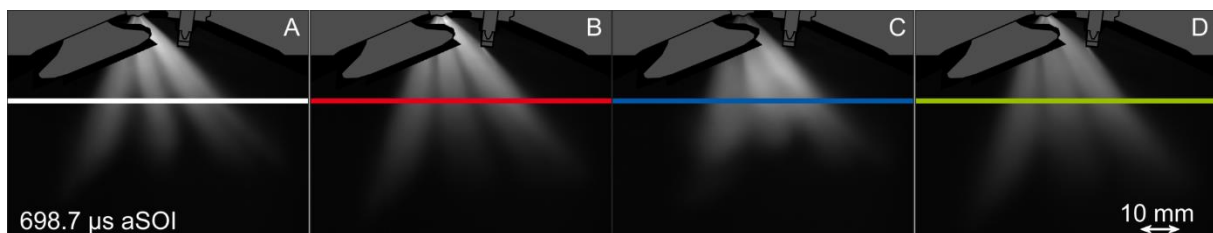


Figure 9. Average normalized Mie scatter image at 698.7 ms aSOI. Color-coded lines represent the line profiles of Figure 10.

To further quantify the inter-plume interaction, Figure 10 plots the normalized intensity profiles indicated by the colored lines in Figure 9. The vertical location of the line profiles was selected to be at approximately 50% of the penetration length, but the trends were found to hold true for other locations. Increasing the engine speed for the case of full-load intake pressures has the most obvious effect on plume-to-plume interaction as displayed in Figure 10 by the lack of distinct peaks of intensity for C. The effects of intake pressure are also evident by the large difference between peaks and troughs of the profile for A compared with B.

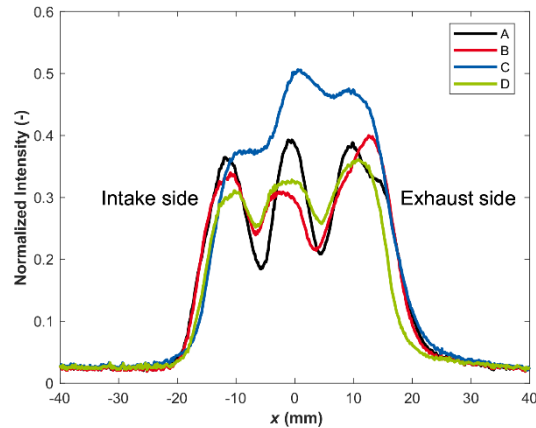


Figure 10. Normalized intensity profile along lines from Figure 9. Plume-to-plume interaction indicated by the distinction of plumes from one another.

In addition to plume-to-plume interaction, Figure 10 can also convey a comparison between the cases for the global spray angle as well as the tendency of the spray to evolve in a certain direction. Since the spray angle calculated from binarized Mie scatter images will be described in more detail in the following section, it will only be pointed out that D appears to have the smallest opening angle, indicated by the comparatively narrow intensity profile. While D has an intensity profile much narrower than the other cases, case C appears to have a skewed profile toward the exhaust side (right side of Figure 10). This is interesting because it indicates that the strong intake flow, which is characterized in Figure 3 as a distinctly downward and rightward (piston- and exhaust valve-directed) flow with high magnitudes (Figure 4) near the spray region, not only affects the evaporation and inter-plume interaction, but it also seems to push the bulk spray shape in the direction of the exhaust valves. If OC A and B are considered nearly symmetric, it appears that C has significant asymmetry in its intensity profile.

Sphicas et al.<sup>22</sup> studied the inter-plume interaction and its effect on the flow recirculation in the spray center in a constant volume chamber. It was hypothesized that the spray angle is stabilized by radial air entrainment. Intense inter-plume interaction stops this radial entrainment and can ultimately lead to a collapse of the spray toward the center. Chen et al.<sup>15</sup> found a weakening of the engine intake flow inside the spray along the injector axis, which can be attributed to a superimposed recirculation induced by the spray. In the current work, the spray orientation and multi-scattering effects restrict the amount of flow information that could be gathered in the spray center. Still, when comparing flow fields at the spray tip along the injector axis, the downward-directed intake flow does not seem to weaken (not shown), which limits such a phenomena to the inaccessible region inside the spray.

In this context, compared to quiescent conditions, the intake flow could have three effects on the spray: first, a stronger intake flow reduces the slip velocity between spray and air, and therefore reduces air entrainment. This possible difference in air entrainment in the engine case weakens the importance of radial air flow stabilizing the spray center and ultimately spray angle. In Figures 9 and 10 this effect is supported by the presence of strong inter-plume interactions in case C and D, but total or extreme collapse never occurs. Second, with increasing intake velocity, the drag reorients the plumes toward the flow direction, which leads to asymmetric spray evolution and smaller spray angles. Third, the intake flow induces quicker evaporation due to higher dispersion and turbulent mixing.

In both cases of higher engine speed, turbulence, and its accompanying phenomena, namely enhanced dispersion of liquid droplets and mixing, as well as the directed intake flow, cause a

noticeable difference in the spray angle and inter-plume interaction when compared with the lower engine speed cases. These effects will be further explored in the following section.

### 3.2.2 Binarized Spray Evolution

Using the binarization technique outlined in the experimental setup and by Geschwindner et al.,<sup>24</sup> the spray morphology is further examined and quantities are derived for further characterization and comparison. A useful visualization for the comparison of spray morphology is a probability map, in which the phase-average of all binarized spray images is plotted to show the statistical likelihood that liquid spray will occur in a position. The evolution of the binarized probability for all cases is displayed in Figure 11. The blue-yellow colormap makes it clear that cycle-to-cycle variations (CCVs) are quite insignificant on the onset of spray by the almost completely yellow spray probability (meaning 100% probability) in each case. Yet, CCVs also appear to remain small throughout the entire spray event, indicating a stable, repeatable injection at each condition. However, as is common throughout this work, the different OCs vary greatly from one another, a fact that highlights the importance of such parametric studies in gaining a more complete understanding of the multi-hole injection in engine operation, since the engine speed and load of an engine is constantly changing in normal operation. Interestingly, case B and D appear to have a very similar liquid spray morphology evolution despite the different levels of turbulence, especially at EOI. Yet, upon the closer inspection of spray morphology quantities, more differences emerge.

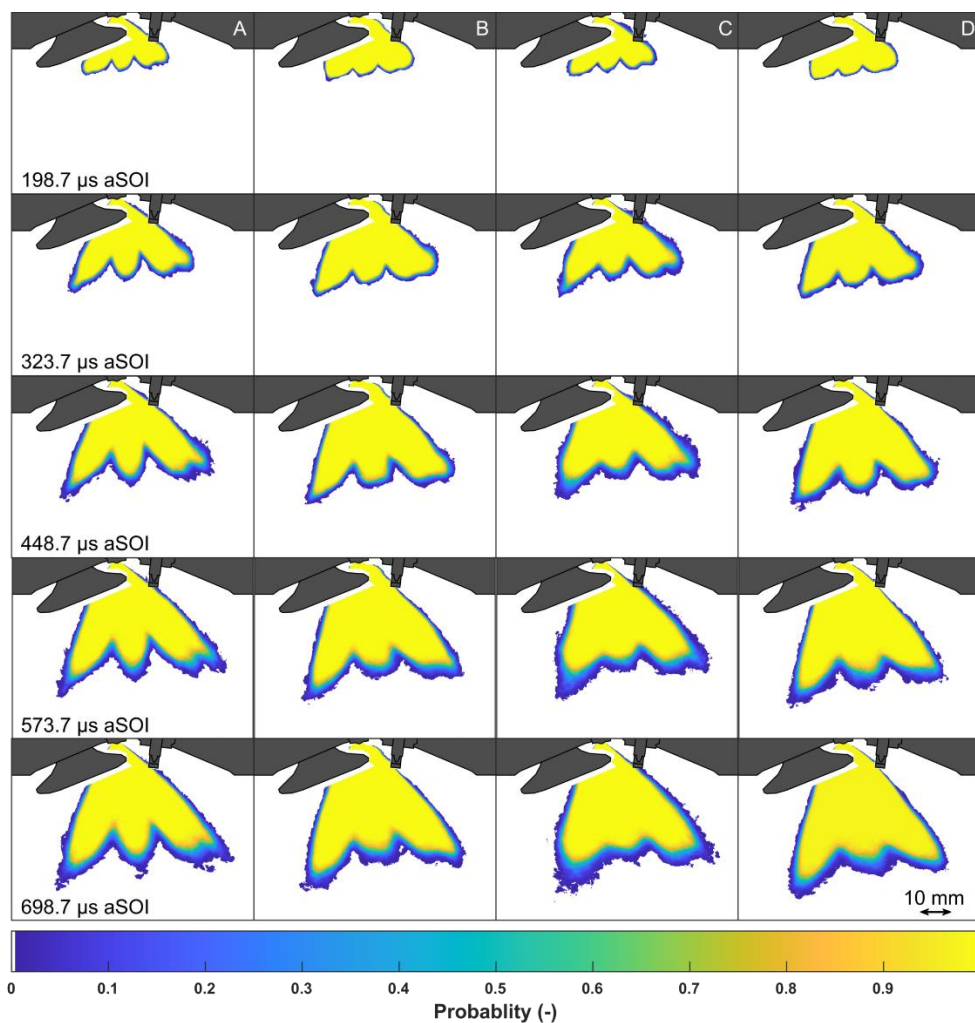


Figure 11. Evolution of binarized spray probability obtained from volumetric Mie scattering (Experiment III).

It is clear that variations in flow properties from the different OCs cause morphological changes in the spray. From Figure 11 it is possible to observe a trend of decreasing liquid spray symmetry with increasing in-cylinder velocity, as OC A appears to have a more symmetric distribution about the spray axis than OC C. By introducing Experiment IV into the comparison, the engine spray without flow, this trend confirmed. Figure 12 displays the average liquid spray and its calculated boundary for the NF case at 680 ms aSOI as well as the outlines of the average liquid spray boundary for the two nearly atmospheric OCs A and C at 698.7 ms aSOI. Although Experiments III and IV employ slightly different illumination techniques and have different camera systems, the principles of volumetric Mie scattering apply to both data sets and make this a valuable comparison. A number of observations can be made through this comparison, the first being that the penetration length of the NF case is far greater than the motored cases. This can be attributed to the lack of turbulent dispersion as well as less evaporation in the absence of intake flow interacting with the spray. In addition, the spray opening angle decreases significantly with the presence of flow and decreases further with higher speeds. Not only does this tendency of increasing spray collapse with increasing intake flow velocity emerge, but also the boundaries on either side of sprays reveal that on the exhaust side, with or without flow, the liquid spray expands on a similar trajectory. A slight variation from this tendency is that the NF case tapers down at the plume tip, which probably occurs because of the limited illumination region. Conversely, on the intake side, increasing flow velocity brings an angle shift toward the exhaust, which is visible by the intake-side and middle plumes, while the NF case seems to exhibit a spray expanding symmetrically along the spray axis. One final observation is that in this line-of-sight view, the average NF spray plumes have less interaction with another and remain more distinct from the injector tip to the plume tips. This agrees well with the previous analysis of Figure 9 and further exhibits the degree to which turbulence affects the plume-to-plume interaction as well as spray collapse.

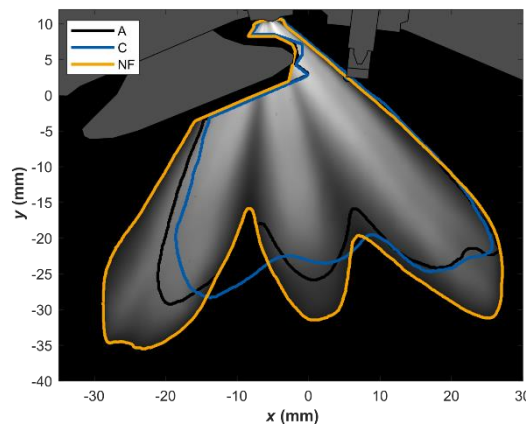


Figure 12. Average spray in a no-flow (NF) configuration in which the piston is removed. The average binarized spray contour is displayed for the near-atmospheric operating conditions.

Further quantification of spray parameters can provide further evidence of the impact of intake flow on spray morphology. Figure 13 shows the average axial penetration  $L$  derived from the binarization of the liquid spray. Table 4 shows the sample standard deviations for  $L$  and the opening spray angle  $\alpha$  (Figure 14) at the middle and end of liquid injection. Despite the appearance of similar morphology for B and D in Figure 11, here it is obvious that with increasing in-cylinder velocity and decreasing bulk gas density, the penetration increases. This is unsurprising, since a higher bulk gas density means a higher amount of drag acting against the spray, while higher velocities work in an opposite way, facilitating penetration and decreasing the spray angle. The effects of flow dynamics on the penetration is even more evident by the addition of the NF case, which is a comparison that isolates the effects of the flow on the spray since the density is nearly atmospheric for cases A, C, and NF. In addition, for cases of lower intake pressure, the liquid penetrations are similar until the later stages of



injection. However, for OC A and C this is not necessarily true as the slope of the penetration length curve for C appears to fluctuate until the later stages of injection; whereas for A, the curve remains smooth. Furthermore, the slope of case B seems to taper off toward the end of the injection event, while the rest have similar slopes at the end. This phenomenon is likely explained by the rate of evaporation of case B shown in Figure 7, in which the evaporation rate during injection is the greatest of all cases.

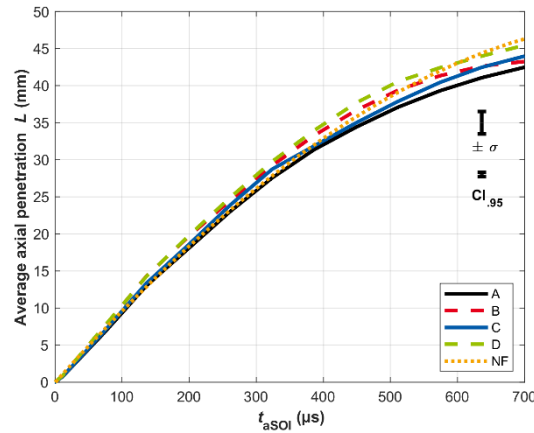


Figure 13. Average axial liquid penetration  $L$ . The interval given by the sample standard deviation  $s$  (cf. Table 4) and the student-t 95 %-confidence interval (CI.95) of the mean are plotted as an example for case A at  $t = 636.2$  ms.

Table 4. Sample standard deviations for  $L$  and  $\alpha$  at the middle ( $t_{mid} \approx 320$  ms aSOI) and end ( $t_{end} \approx 640$  ms aSOI) of liquid injection.

OC	$L_{mid}$ (mm)	$L_{end}$ (mm)	$\alpha_{mid}$ (°)	$\alpha_{end}$ (°)
A	0.59 (2.2%)	1.5 (3.7 %)	1.7 (2.2 %)	1.4 (1.8 %)
B	0.47 (1.6 %)	1.4 (3.3 %)	1.4 (1.9 %)	1.2 (1.7 %)
C	0.73 (2.5 %)	2.0 (4.8 %)	2.5 (3.2 %)	2.0 (2.8 %)
D	0.49 (1.6 %)	1.4 (3.2 %)	1.3 (1.7 %)	1.3 (1.9 %)
NF	0.48 (1.7 %)	1.1 (2.5 %)	2.3 (2.8 %)	0.90 (1.1 %)

The average global spray angle  $\alpha$  is shown in Figure 14 As with penetration length, spray angle has clear relationships with bulk gas density and in-cylinder flows. In the presence of decreasing bulk gas density,  $\alpha$  also decreases. While Spray G2 (flash boiling) is not exactly achieved in this study due to the lower fuel temperature, lower  $\alpha$  with lower intake pressure trends toward the principles of flash boiling, which causes total collapse, since the inner-spray recirculation is blocked by a pronounced plume-to-plume interaction.<sup>22</sup> Yet, with higher in-cylinder speeds, the spray also has a lower spray angle, which follows the trend shown by increasing  $L$  with increasing in-cylinder velocity. Combining these phenomena, a common trend emerges: the bulk spray morphology is heavily shaped by the in-cylinder flow since the downward flow acts in the same direction as the incoming spray, rather than opposing it. The enhancement of the spray penetration due to the downward and rightward-directed intake flow is the opposite trend as is present in the case of late injection, where the bulk gas motion is pointed upward with the compressing piston, and this motion inhibits the downward spray penetration while simultaneously preventing spray collapse.<sup>24</sup> In the case of late injection, however, a

trade-off exists which places the desired increased spray stability at increasing engine speed against the unacceptable increase of wall wetting as the spray comes into contact with the piston surface earlier and therefore, longer. Therefore, for future Spray G investigations, in light of a trend toward decreased spray stability with increasing in-cylinder velocities, there is much to be gained in further examining the early injection cases.

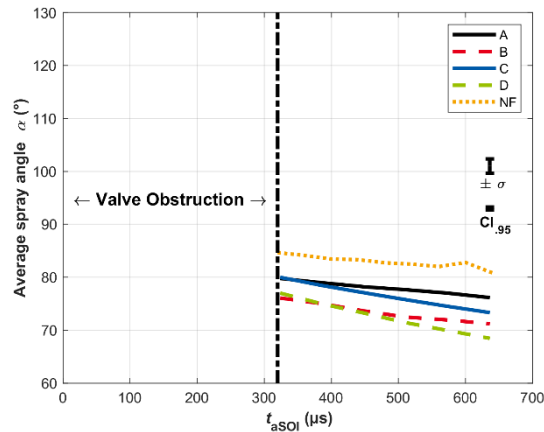


Figure 14. Average global spray angle  $\alpha$ . The interval given by the sample standard deviation  $s$  (cf. Table 4) and the student-t 95 %-confidence interval (CI.95) of the mean are plotted as an example for case A at  $t = 636.2$  ms.

## 4 Conclusions

Through the use of PIV and volumetric Mie scatter imaging, the effects of in-cylinder flow velocity and bulk gas density were investigated for early injection Spray G conditions in an optical research engine. Extending the available research of early injection Spray G from generic test cases in constant volume chambers and bottom-view spray morphology investigations in more realistic engine conditions,<sup>23</sup> this work provides a more complete characterization of the spray morphology and the blueprint for future investigations to help increase efficiency and reduce emissions in DISI engine combustion through the following conclusions:

1. Turbulent kinetic energy  $k$  showed a high correlation between velocity magnitude and fluctuations; yet, the introduction of sprays during early injection did not generate more turbulence in the chosen region of interest long after injection. The lack of apparent added velocity fluctuations within the chosen region of interest (beginning 10 mm downstream of the injector tip) is probably due to the added turbulence being carried downward in the direction of the bulk flow out of the engine's optical access. The result that early injection does not increase  $k$  is supported by the findings of Chen et al.<sup>15</sup> who found that by the time of ignition,  $k$  was unchanged by the addition of an early injection from a multi-hole injector. Finally, the sprays themselves were shown to exhibit little variability, a phenomenon that may prevent greater  $k$  after injection. Regardless of the causes of little to no addition of  $k$ , in future investigations a longer injection duration or multiple injections would expand the data set of  $k$  to a larger range of conditions valuable to modern DISI operating strategies.
2. Wall wetting is clearly visible on the spark plug in this engine configuration and evidence strongly suggests that the spray interacts significantly with the intake valves. It is also plausible that wall wetting occurs on the cylinder walls as well as the piston surface, especially given a longer injection duration. While it is difficult to quantify wall wetting on all surfaces in such a complex engine experiment, future experiments could utilize



well-known methods such as LIF or refractive index matching (RIM) to measure the fuel film on the piston surface<sup>7,39</sup> and investigate the effects of wall wetting with Spray G on engine performance and emissions.

3. With decreasing intake pressure (decreasing bulk gas density) and increasing engine speed (increasing in-cylinder velocity magnitude) a number of phenomena, which are not possible to observe in constant volume chambers, occur. First, evaporation occurs quicker in the low density environment and this is accelerated by increased convection and presumably mixing at increased velocities. Second, plume-to-plume interaction is increased, especially by increased intake velocities compressing the plumes in the direction of the exhaust valves. This leads to a decrease in spray angle  $\alpha$ , especially at lower bulk densities. Third, a greater axial liquid penetration  $L$  occurs due to decreased drag, an effect of density, and a downward guiding motion due to the downward flow momentum.
4. Contrary to the case of late Spray G injection, early injection spray morphology is dominated by the downward (toward piston) and rightward (toward exhaust valves) bulk flow motion, which guides the spray further downward and pushes the spray toward the exhaust with increasing velocity. In the case of late injection Spray G, higher engine speeds act to prevent spray collapse; while in early injection cases the opposite effect occurs. The simplified engine no-flow case exemplified the influence of the intake flow motion on the spray shape in a more engine-relevant geometry by eliminating other factors such as dynamic components or variations in bulk gas density. In the complete absence of surrounding air motion, the spray exhibits an ideal, symmetric shape without much inter-plume interaction or collapse. Therefore, further studies should characterize the degree to which spray stability is affected and what effect this has on combustion performance.

There is still much knowledge to be gained in simpler DISI configurations like the no-flow case of Experiment IV investigating direct injection within a flow bench. Such configurations can be used to bridge the complexity gap between CVC sprays and optical research engine sprays. With the help of advanced diagnostics and numerical simulations in simpler and increasingly realistic DISI configurations alike, future engines still employing combustion will continue to improve in efficiency and emissions.

## Acknowledgements

The authors would like to thank the whole ECN for their support, in particular S. Parrish for modifying the injector, and L. Pickett and G. Bruneaux for fruitful discussions on the topic.

## Declaration of Competing Interests

The author(s) declared no potential conflicts of interest with respect to the research, authorship, and/or publication of this article.

## Funding

The author(s) disclosed receipt of the following financial support for the research, authorship, and/or publication of this article: Deutsche Forschungsgemeinschaft through SFB/ Transregio 150 (project number 237267381-TRR150).

## References

1. Heywood JB. *Internal combustion engine fundamentals*. 2nd ed. New York, NY: McGraw-Hill Education, 2018.
2. Peterson B, Reuss DL and Sick V. High-speed imaging analysis of misfires in a spray-guided direct injection engine. *Proc Combust Inst* 2011; 33(2): 3089–3096.
3. Fansler TD, Reuss DL, Sick V and Dahms RN. Invited review: combustion instability in spray-guided stratified-charge engines: a review. *Int J Engine Res* 2015; 16(3): 260–305.
4. Zhao F, Lai MC and Harrington DL. Automotive spark-ignited direct-injection gasoline engines. *Prog Energy Combust Sci* 1999; 25(5): 437–562.
5. Heywood JB. *Internal combustion engine fundamentals*. New York, NY: McGraw-Hill, 1988.
6. Robert Bosch GmbH. *Bosch automotive handbook*. 7th ed. Gerlingen and Chichester: Robert Bosch GmbH and John Wiley, [distributor] 2007.
7. Ding CP, Vuilleumier D, Kim N, Reuss DL, Sjöberg M and Böhm B. Effect of engine conditions and injection timing on piston-top fuel films for stratified direct-injection spark-ignition operation using e30. *Int J Engine Res* 2020; 21: 302–318.
8. Lee Z, Kim D and Park S. Effects of spray behavior and wall impingement on particulate matter emissions in a direct injection spark ignition engine equipped with a high pressure injection system. *Energy Convers Manag* 2020; 213: 112865.
9. Shahbaz MA, Jungst N, Grzesik R and Kaiser SA. Endoscopic fuel film, chemiluminescence, and soot incandescence imaging in a direct-injection spark-ignition engine. *Proc Combust Inst* 2021; 38: 5869–5877.
10. Serras-Pereira J, Aleiferis P, Richardson D, et al. Spray development, flow interactions and wall impingement in a direct-injection spark-ignition engine. SAE paper 2007-01-2712, 2007.
11. Marchi A, Nouri J, Yan Y and Arcoumanis C. Spray stability of outwards opening pintle injectors for stratified direct injection spark ignition engine operation. *Int J Engine Res* 2010; 11(6): 413–437.
12. Stiehl R, Schorr J, Krüger C, Dreizler A and Böhm B. In-cylinder flow and fuel spray interactions in a stratified spray-guided gasoline engine investigated by high-speed laser imaging techniques. *Flow Turbul Combust* 2013; 91(3): 431–450.
13. Stiehl R, Bode J, Schorr J, Krüger C, Dreizler A and Böhm B. Influence of intake geometry variations on in-cylinder flow and flow–spray interactions in a stratified direct-injection spark-ignition engine captured by time-resolved particle image velocimetry. *Int J Engine Res* 2016; 17(9): 983–997.
14. Peterson B, Baum E, Ding CP, Michaelis D, Dreizler A and Böhm B. Assessment and application of tomographic piv for the spray-induced flow in an ic engine. *Proc Combust Inst* 2017; 36(3): 3467–3475.
15. Chen H, Zhuang H, Reuss DL, et al. Influence of early and late fuel injection on air flow structure and kinetic energy in an optical sidi engine. SAE paper 2018-01-0205, 2018.
16. Sharma N, Bachalo WD and Agarwal AK. Spray droplet size distribution and droplet velocity measurements in a firing optical engine. *Phys Fluids* 2020; 32(2): 023304.

17. Engine Combustion Network. Gasoline spray combustion. <https://ecn.sandia.gov/gasoline-spray-combustion/> (2017, accessed 26 February 2019).
18. Manin J, Jung Y, Skeen SA, et al. Experimental characterization of di gasoline injection processes. SAE paper 2015-01-1894, 2015.
19. Payri R, Salvador FJ, Martí-Aldaravi P and Vaquerizo D. ECN spray g external spray visualization and spray collapse description through penetration and morphology analysis. *Appl Therm Eng* 2017; 112: 304–316.
20. Lacey J, Poursadegh F, Brear MJ, et al. Generalizing the behavior of flash-boiling, plume interaction and spray collapse for multi-hole, direct injection. *Fuel* 2017; 200: 345–356.
21. Montanaro A, Allocca L and Lazzaro M. Iso-octane spray from a gdi multi-hole injector under non- and flash boiling conditions. SAE paper 2017-01-2319, 2017.
22. Sphicas P, Pickett LM, Skeen SA and Frank JH. Inter- plume aerodynamics for gasoline spray collapse. *Int J Engine Res* 2018; 19(10): 1048–1067.
23. Gutierrez L, Mansfield AB, Fatouraie M, et al. Effects of engine speed on spray behaviors of the engine combustion network “spray g” gasoline injector. SAE paper 2018-01- 0305, 2018.
24. Geschwindner C, Kranz P, Welch C, et al. Analysis of the interaction of spray g and in-cylinder flow in two optical engines for late gasoline direct injection. *Int J Engine Res* 2020; 21(1): 169–184.
25. Paredi D, Lucchini T, D’Errico G, et al. Combined experimental and numerical investigation of the ECN spray g under different engine-like conditions. SAE paper 2018-01-0281, 2018.
26. Paredi D, Lucchini T, D’Errico G, Onorati A, Pickett L and Lacey J. Validation of a comprehensive computational fluid dynamics methodology to predict the direct injection process of gasoline sprays using spray g experimental data. *Int J Engine Res* 2020; 21(1): 199–216.
27. Pati A, Paredi D, Lucchini T and Hasse C. CFD modeling of gas-fuel interaction and mixture formation in a gasoline direct-injection engine coupled with the ECN spray g injector. SAE paper 2020-01-0327, 2020.
28. Baum E, Peterson B, Böhm B and Dreizler A. On the validation of les applied to internal combustion engine flows: part 1: comprehensive experimental database. *Flow Turbul Combust* 2014; 92(1-2): 269–297.
29. Freudenhammer D, Baum E, Peterson B, Böhm B, Jung B and Grundmann S. Volumetric intake flow measurements of an ic engine using magnetic resonance velocimetry. *Exp Fluids* 2014; 55(5): 1724.
30. Renaud A, Ding CP, Jakirlic S, Dreizler A and Böhm B. Experimental characterization of the velocity boundary layer in a motored ic engine. *Int J Heat Fluid Flow* 2018; 71: 366–377.
31. Bürkle S, Biondo L, Ding CP, et al. In-cylinder temperature measurements in a motored ic engine using tdlas. *Flow Turbul Combust* 2018; 101(1): 139–159.
32. Welch C, Schmidt M, Keskinen K, et al. The effects of intake pressure on in-cylinder gas velocities in an optically accessible single-cylinder research engine. SAE paper 2020-01-0792, 2020.
33. Hamzah A, Poursadegh F, Lacey J, et al. A comparison of diffuse back-illumination (dbi) and mie-scattering technique for measuring the liquid length of severely flashing spray. In: Proceedings of the 20th Australasian fluid mechanics conference, Perth, Australia, 5–8 Decem- ber 2016. <https://people.eng.unimelb.edu.au/imarusic/proceedings/20/669%20Paper.pdf>

34. Haussmann M, Ries F, Jeppener-Haltenhoff JB, et al. Evaluation of a near-wall-modeled large eddy lattice boltzmann method for the analysis of complex flows relevant to ic engines. *Computation* 2020; 8(2): 43.
35. Wieneke B. Piv uncertainty quantification from correlation statistics. *Meas Sci Technol* 2015; 26(7): 074002.
36. Pope SB. *Turbulent flows*. Cambridge: Cambridge University Press, 2012.
37. Zeng W, Sjöberg M, Reuss DL and Hu Z. The role of spray-enhanced swirl flow for combustion stabilization in a stratified-charge disi engine. *Combust Flame* 2016; 168: 166–185.
38. Aleiferis PG and Behringer MK. Modulation of integral length scales of turbulence in an optical si engine by direct injection of gasoline, iso -octane, ethanol and butanol fuels. *Fuel* 2017; 189: 238–259.
39. Drake MC and Haworth DC. Advanced gasoline engine development using optical diagnostics and numerical modeling. *Proc Combust Inst* 2007; 31(1): 99–124.

## A.4 Paper IV

### Experimental Evaluation of Spark Behavior under Diluted Conditions in an Optically Accessible Engine

C. Welch, L. Illmann, M. Schmidt, A. Dreizler, B. Böhm: Experimental Evaluation of Spark Behavior under Diluted Conditions in an Optically Accessible Engine. *International Journal of Engine Research* (2023) Sage Publishing. <https://journals.sagepub.com/doi/10.1177/14680874231197492>

#### Paper IV Permissions

Paper IV is reproduced with permission from Sage Publishing. Permission to include Paper IV in this cumulative dissertation is granted by Sage Publishing: The following page was obtained on July 21, 2023 at 17:57 CET under the URL: <https://uk.sagepub.com/en-gb/eur/journal-author-archiving-policies-and-re-use>.



## Sage's Author Archiving and Re-Use Guidelines

These guidelines should be followed by authors of Contributions published in a Sage subscription journal, including authors whose Contributions were published under a previous version of the author guidelines. For a list of exceptions to these guidelines, please see below.

Three versions of the Contribution are referenced in these guidelines:

- **Original Submission:** the version submitted by the author before peer review
- **Accepted Manuscript:** version updated to include the author's revisions after peer review, prior to any typesetting for the journal. This is often the version accepted by the editor
- **Final Published PDF:** copy-edited and typeset Publisher's PDF, the same version published on the journal's website

## Green Open Access: Sage's Archiving and Sharing Policy

You may share the **Original Submission** or **Accepted Manuscript** at any time after your paper is accepted and in any format. Your sharing of the **Original Submission** or **Accepted Manuscript** may include posting a downloadable copy on any website, saving a copy in any repository or network, sharing a copy through any social media channel, and distributing print or electronic copies. Please note some journals will not consider papers that have been posted as preprints prior to submission and you may check a journal's policy regarding considering previously-posted papers by referring to the journal's submission guidelines.

For information on use of Institutional Repository (IR) copies by authors and IR users, see [Posting to an Institutional Repository - Green Open Access](#).

You may use the **Final Published PDF** (or **Original Submission** or **Accepted Manuscript**, if preferred) in the following ways:

- in relation to your own teaching, provided that any electronic distribution maintains restricted access
- to share on an individual basis with research colleagues, provided that such sharing is not for commercial purposes
- in your dissertation or thesis, including where the dissertation or thesis will be posted in any electronic Institutional Repository or database
- in a book authored or edited by you, at any time after the Contribution's publication in the journal.

*Provided that:*

- Access to the Original Submission and Accepted Manuscript is provided at no charge.
- Any re-use terms for users of websites and repositories (where your **Original Submission** or **Accepted Manuscript** are posted) are restricted to non-commercial and no derivative uses.
- You may not post the **Final Published PDF** on any unrestricted website or repository without permission from Sage.
- You may not republish or translate any version of your Contribution in another journal without prior permission from Sage.
- The journal as the original publication of your Contribution is appropriately credited by including the full citation information each time your Contribution, or excerpts, are further distributed or re-used:
  - After your Contribution has been accepted for publication and until it is assigned a DOI, please include a statement that your Contribution has been accepted for publication in the journal.
  - Once full citation information for your Contribution is available, please include this with your posted Contribution, in a format similar to the following:  
**Author(s), Contribution Title, Journal Title (Journal Volume Number and Issue Number) pp. xx-xx. Copyright © [year] (Copyright Holder). DOI: [DOI number].**

## Journal Exceptions

**Exceptions to this Author Re-Use policy:** The following journals have a different author re-use policy in place. The re-use terms for these journals are stated in the Contributor Agreement used by the Journal.

If you have questions regarding the following titles, contact the permissions team through our [Sage Permissions Portal](#).

- *California Management Review*
- *Acta Radiologica* (from January 2018)
- *Index on Censorship*
- *Pain News*
- *Political Insight*

## Related Information

Authors of Contributions published as Sage Choice or in a Gold Open Access journal should reference [Reusing Open Access and Sage Choice Content](#). For a list of Sage's Gold Open Access journals, please see [Gold Open Access journals](#).

Authors of Contributions published under a Creative Commons license may re-use their work under the terms of the Creative Commons license attached to their Contributions and additionally have all rights to re-use their work stated above.

For information about requesting permission for content published in Sage journals, see [Process for Requesting Permission](#).

For information about author copies, see [Author e-prints policy](#).

If you are submitting a manuscript to a Sage journal and wish to include previously published materials within the manuscript, visit our Author Gateway [Copyright and Permissions FAQs](#).

---

# DECLARATION ON THE CONTRIBUTION TO THE SCIENTIFIC PUBLICATION

## Erklärung zum Eigenanteil der wissenschaftlichen Veröffentlichung

Cooper Welch, M.Sc.

### PAPER

**C. Welch, L. Illmann, M. Schmidt, A. Dreizler, B. Böhm:** Experimental Evaluation of Spark Behavior under Diluted Conditions in an Optically Accessible Engine. *International Journal of Engine Research* (2023).  
**Submission in Progress.**

### CO-AUTHORS

Lars Illmann, M.Sc.  
Marius Schmidt, M.Sc.

Andreas Dreizler, Prof. Dr.  
Benjamin Böhm, Dr.-Ing.

### INDIVIDUAL CONTRIBUTIONS

- **Cooper Welch**
  - Jointly conducted experiments with Lars Illmann.
  - Conducted processing and analysis of all data.
  - Main and corresponding author of the paper: performed literature research, generated all figures, and wrote the manuscript.
- **Lars Illmann**

Jointly conducted experiments with Cooper Welch. Supported in the interpretation of the results and the proofreading of the manuscript.
- **Marius Schmidt**

Assisted in conduction of experiments through advice from experience. Supported in the interpretation of results and the proofreading of the manuscript.
- **Andreas Dreizler and Benjamin Böhm**

Provided resources for the conduction of the experiments. Supported in the interpretation and discussion of the results and the proofreading of the manuscript.

### OVERALL CONTRIBUTION OF COOPER WELCH

A leading role in the conduction of the experiments, data analysis and interpretation, and main author of the manuscript.

### USE OF PAPER CONTENTS IN OTHER DISSERTATIONS

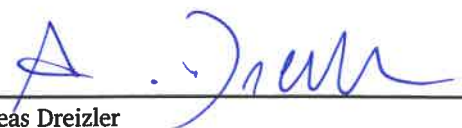
This publication is not the subject of another ongoing or completed dissertation.

### SIGNATURES OF ALL AUTHORS

  
\_\_\_\_\_  
Cooper Welch

  
\_\_\_\_\_  
Marius Schmidt

  
\_\_\_\_\_  
Lars Illmann

  
\_\_\_\_\_  
Andreas Dreizler





---

*BB*

Benjamin Böhm

# Experimental Evaluation of Spark Behavior under Diluted Conditions in an Optically Accessible Engine

Cooper Welch\*, Lars Illmann, Marius Schmidt, Andreas Dreizler, Benjamin Böhm

Technical University of Darmstadt, Department of Mechanical Engineering, Reactive Flows and Diagnostics, Otto-Berndt-Str. 3, 64287 Darmstadt, Germany

\*Corresponding author: Cooper Welch, email: [welch@rsm.tu-darmstadt.de](mailto:welch@rsm.tu-darmstadt.de)

ORCID ID:

Cooper Welch: 0000-0001-9067-9405

Lars Illmann: 0000-0001-6907-0064

Marius Schmidt: 0000-0002-5424-1251

Andreas Dreizler: 0000-0001-5803-7947

Benjamin Böhm: 0000-0003-2654-6266

## Abstract

An optically accessible single-cylinder spark-ignition engine operated under homogeneous, part-load conditions is experimentally investigated using optical and spark diagnostics to evaluate the relationship between the spark, flow, and flame with increasing dilution using several levels of exhaust gas recirculation (EGR). Voltage and current measurements of the secondary spark circuit are compared with simultaneous high-speed spark plasma imaging, particle image velocimetry measurements of the flow field, and burned gas images. Specifically, characteristic restrike cycles and normal cycles are examined under the 0% EGR and 12.9% EGR conditions to reveal a relationship between the magnitude and direction of the velocity near the spark plug and the spark's behavior coupled with that of the subsequent flame propagation. Through the use of conditional statistics and correlation analysis of data sets of all non-restrike and all restrike cycles, the horizontal velocity across the spark gap was identified as a critical quantity in facilitating more stable and faster combustion under diluted mixture conditions.

## Keywords

Cycle-to-cycle variations, exhaust gas recirculation (EGR), spark-ignition engine, optically accessible engine, Spark energy

## 1 Introduction

Due to increasing concerns about the environment, it is widely accepted that the improvement of the efficiency of internal combustion engines (ICEs) is a necessary short-term solution for ground transportation in the race against climate change. Battery electric vehicles are the preferred long-term alternative to ICEs; yet, their widespread implementation is hindered by several factors including high cost, relatively short battery lifetimes, battery safety, and lack of charging infrastructure.<sup>1</sup> Another attractive option for auto manufacturers to achieve net zero CO<sub>2</sub> emissions is the use of hydrogen-fueled ICEs (H<sub>2</sub>-ICEs) due to their relative adaptability to existing industry supply chains. Nevertheless, high NO<sub>x</sub> emissions from high combustion temperatures and safety concerns remain significant challenges to the implementation of H<sub>2</sub>-ICEs.

Operating conventional gasoline, methane-fueled, or H<sub>2</sub>-ICEs lean or under diluted conditions through exhaust gas recirculation (EGR) offers the advantages of reducing fuel consumption and combustion temperatures leading to lower NO<sub>x</sub> emissions.<sup>2</sup> Notwithstanding the benefits, lean combustion and EGR are associated with a decrease in flame speed and an increase in cyclic combustion instability or cycle-to-cycle variations (CCV). Cyclical variations in spark-ignited (SI) engines are caused by several variables; for example, gas mixture formation, spark energy deposition, and in-cylinder velocity. In homogeneous SI ICE configurations, the main stages of combustion are the sparking and flame initiation, initial flame kernel advancement, and the turbulent flame propagation,<sup>3</sup> all of which affect each subsequent stage and ultimately the combustion performance.

Typical automotive engines employ a transistorized coil ignition (TCI) system, where the energy is stored in the inductance of a coil and released over ~2 ms. Once the coil's charge is released, the applied voltage between the two spark plug electrodes, on the order of kilo-volts, results in the acceleration of electrons through the gap and the rapid ionization of the gas molecules. This so-called *breakdown* phase lasts only a brief amount of time (~10 ns). The subsequent phase, referred to as the *arc*, is characterized by the expansion of the plasma due to heat conduction and diffusion, and it lasts on the order of a few milli-seconds. Arc is the critical stage of the spark discharge for this work as it initiates the exothermic reactions leading to a propagating flame. The final phase of the spark discharge is referred to as the *glow* in which the remaining energy is released.<sup>4,5</sup>

Various simplified engine-like pressure chamber and flow chamber experiments have been utilized to study the underlying variables leading to spark phenomena such as restrike (RS) and combustion instability. Understanding the ignition process and early flame kernel propagation of lean or diluted mixtures, large flow velocities near the spark plug, or high pressures has been a motivating factor for researchers due to the increased spark and flame instabilities associated with such conditions. Research by Maly and Vogel represents an early example of chamber measurements of spark ignition in which the ignition and the size, expansion velocity, and radial temperature of the flame front of varying lean methane-air mixtures were measured using interferometry.<sup>5</sup> More recently, chamber measurements with optical access have employed varying pressures,<sup>6,7</sup> varying or very high spark gap velocities,<sup>7-10</sup> varying discharge current,<sup>7,9</sup> or spark gap<sup>11</sup> settings to study the ignition and flame propagation characteristics. Spark channel elongation and RS have been identified as by-products of enhanced spark gap velocity and, depending on the spark gap size or amount of energy deposited, may decrease ignition stability.<sup>7,8,10,12-14</sup>

Optical techniques have also been expanded to engine-like compression and expansion machines to investigate the temperature of the spark discharge and early flame kernel using measured emission spectra<sup>15</sup> or to measure the effect of varying the discharge current and the in-cylinder flow on the ignition and early flame.<sup>16</sup> In addition, advanced ignition strategies, such as using nanosecond-pulsed high-frequency discharges<sup>17</sup> or single- and dual-channel nanosecond-discharge,<sup>18</sup> have been employed to enhance the stability and reliability of the ignition process.

Likewise, similar phenomena to those studied in chamber and engine-like configurations have been investigated in more realistic research engine experiments to examine CCV. Experiments ranging from waveform measurements in a research engine<sup>19</sup> to waveform and flame visualization in a borescope research engine<sup>20</sup> have been used to study the lean limits of engine operation. Furthermore, full-scale optically accessible engine experimental studies have examined the relationship between the ignition process and the cyclic performance. Specifically, Fansler et al.;<sup>12</sup> Smith and Sick;<sup>21</sup> Peterson and Sick;<sup>13</sup> Drake et al.;<sup>22</sup> and Dahms et al.<sup>14</sup> are early examples of researchers using high-speed (HS) imaging of the spark and flame,<sup>12,14,22</sup> laser diagnostics, for example particle image velocimetry (PIV) to measure the local velocity<sup>13,14,22</sup> or laser-induced fluorescence (LIF) to measure the local mixture field near the spark,<sup>13,21</sup> and spark waveform measurements<sup>12-14,21</sup> in optically accessible spray-guided engine configurations to investigate the underlying variables influencing engine performance. The

review paper by Fansler et al. published in 2015 discusses CCV in stratified-charge engine configurations and provides a comprehensive summary of the relevant experimental research and the subsequently developed numerical models for the simulation of ignition up to that time.<sup>23</sup> More recently, however, Bode et al., employed quasi-simultaneous multi-plane PIV and spark luminosity imaging in an optically accessible engine. Statistical analysis techniques, namely correlation fields and conditional averages revealed a strong dependency of the spark position on the flow field and CCV,<sup>24</sup> a finding similar to one made by the aforementioned work of Drake et al.<sup>22</sup> The preceding studies each used advanced diagnostics to measure the behavior of ignition under different engine conditions. It is clear from the previous research that the interplay between the cyclical flow, spark, and flame characteristics has an influence on the deterministic nature of the combustion in SI engines. However, to the authors' knowledge, a comprehensive study, employing high statistics (thousands of cycles in total) of simultaneous high-speed flow, flame and spark plasma imaging, and spark circuit measurements with varying levels of controlled dilution to enhance instability in an ICE, is still missing from the literature. With the addition of highly resolved ignition data, this work aims to build upon previous research by the authors where the in-cylinder flow was correlated with the flame characteristics and cyclic performance under the effects of homogeneous EGR.<sup>25</sup> Through the measurement of simultaneous spark voltage and current data as well as HS spark plasma imaging to the already presented flow and flame data of the engine, a more complete analysis of the combustion dynamics under part-load and diluted conditions is provided. Specifically, this work aims to focus on the phenomenon of spark RS to assess whether it enhances the combustion speed or if the presence of RS inhibits combustion speed due to too fast velocities and blow-off.<sup>10,14</sup> Furthermore, through the simultaneous multi-parameter measurements and the well-controlled boundary conditions, this work provides high-fidelity validation data for numerical simulations and the development of models.

This paper is presented in the following manner: first, the experimental setup describes the engine test stand and operating conditions, the optical diagnostics, and the processing techniques employed. Then, the results are presented by characterizing the operating conditions of the EGR cases; next, singular representative cycles are analyzed for the interaction between the ignition, the flame, and the flow; and finally, conditional statistical and correlation analysis of the full datasets is performed to confirm the phenomena observed in the singular cycles and to draw generalizations about the behavior of the spark and its role in the cyclic combustion performance. At the end of the paper, conclusions are made and suggestions for future work for the improvement of the understanding of CCV in future IC engines are given.

## 2 Experimental Setup

### 2.1 Test Bench and Operating Conditions

The engine test stand of the present study is the well-characterized<sup>26,27</sup> single-cylinder optically accessible research engine of TU Darmstadt; further details of the engine test stand are provided by Baum et al.<sup>26</sup> The engine test bench employs a gas mixture system (GMS) for precise control of the gas concentrations and supplied pressure and is equipped with pressure and temperature sensors along the intake and exhaust manifolds for further boundary condition control. Experiments from this study employed a four-valve, pent-roof spray-guided cylinder head with a compression ratio of 8.7: 1.<sup>28</sup> The engine's optical access is realized with a quartz glass cylinder liner and flat piston window with Bowditch extension and a stationary piston mirror. Within the engine cylinder, a pressure sensor (GU22C from AVL List GmbH) is used to measure the in-cylinder pressure. Figure 1(a) shows a diagram of the test bench from the GMS to the exhaust manifold and Figure 1(b) displays a cross-section diagram of the engine test bench with relevant geometrical features.

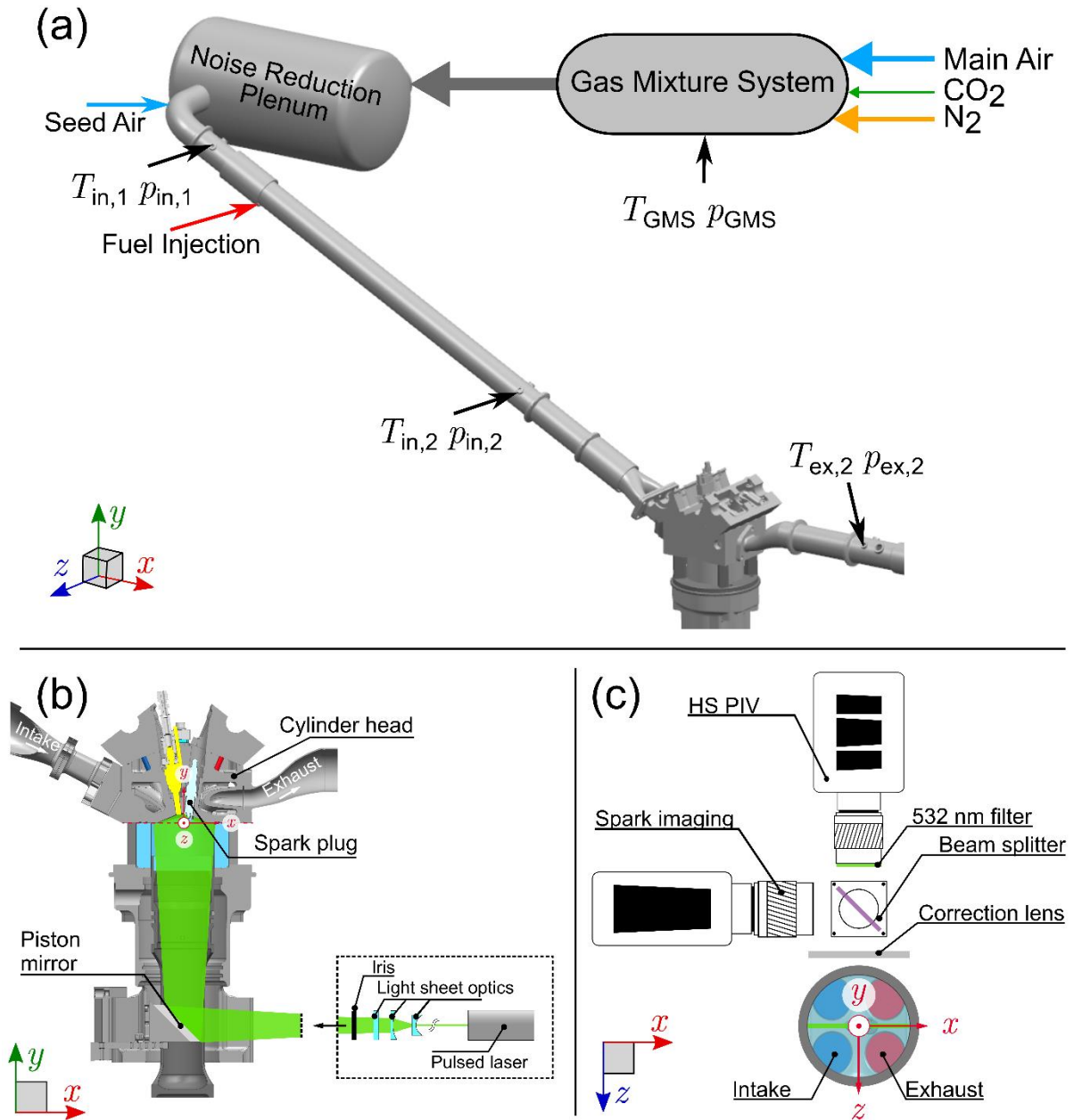


**Figure 1. (a) Diagram of the experimental test bench; (b) cross-sectional side-view diagram of the engine and laser arrangement; and (c) cross-sectional top-view diagram of the engine cylinder and camera arrangement.**

In order to simulate controlled EGR rates, the experiments of this study employed the GMS to introduce and mix dry air (supplied by a compressor with condenser, relative humidity of 1.8% at 4°C) with nitrogen (> 99.95% purity) and carbon dioxide (99.5% purity) gas far upstream of the intake manifold. Furthermore, the gas mixtures were held homogeneous by injecting fuel in the intake port approximately  $22D$  ( $D = 56.3$  mm) upstream of the intake valves and during operation a skip-fire scheme of 6: 1 was employed in which after every fired cycle, 6 unfired cycles followed to flush out residual exhaust gases. Four operating conditions (OCs) of increasing homogeneous external EGR were used to increase the importance of effects leading to CCV, namely the interaction of the flow with the ignition and early flame kernel development due to the decreasing flame speed associated with EGR. In addition, slightly upstream of the port-fuel injection, nebulized silicone oil droplets (DOWSIL 510,

Dow Inc., ~500  $\mu\text{m}$  diameter) were seeded to properly mix with the homogeneous intake gas for the use of planar Mie scatter imaging. The part-load standard OC D of the Darmstadt engine,<sup>25,27,29</sup> which has an engine speed of 1500 rpm and intake pressure of 0.4 bar, was used for the variation of EGR rates from a no-EGR case of 0% EGR to an extremely unstable case of 14.3% EGR. The highest EGR rate of 14.3% was selected to provide a large data set of unstable and misfire cycles as a contrast to the highly stable 0% EGR condition. In order to keep the same combustion phasing, the ignition timing  $t_{\text{ign}}$  was moved earlier for each increasing EGR rate as the flame speed decreases with greater dilution, such that the mean crank angle of a set of cycles' 50% mass fraction burned was 8°CA (crank-angle degrees after compression top dead center). This allows direct comparison of the resulting combustion parameters and flame propagation for each OC. As previously mentioned, pressure sensors and thermocouples are employed from the intake manifold to the cylinder head until the exhaust manifold for the control and measurement of accurate boundary conditions (see Figure 1(a)). Table 1 provides details of relevant engine parameters and the boundary conditions for the OCs of the present study. In this paper, misfires are defined as cycles where the gross indicated mean effective pressure is less than zero.

**Table 1. Summary of engine parameters and boundary conditions. Combined standard uncertainties are indicated by the parentheses.**

Condition	No EGR	Medium EGR	High EGR	Extreme EGR
EGR [%]	0(0)	10.5(0.4)	12.9(0.4)	14.3(0.4)
Cycles [-]	439	966	1288	805
$\dot{m}_{\text{air}}$ [kg/h]	7.33(0.08)	6.63(0.08)	6.48(0.08)	6.40(0.08)
$\dot{m}_{\text{N}_2}$ [kg/h]	0.00(0)	0.651(0.035)	0.810(0.035)	0.901(0.035)
$\dot{m}_{\text{CO}_2}$ [kg/h]	0.00(0)	0.174(0.006)	0.216(0.006)	0.241(0.006)
$\dot{m}_{\text{fuel}}$ [kg/h]	0.489(0.012)	0.434(0.012)	0.428(0.012)	0.418(0.012)
$t_{\text{ign}}$ [°CA]	-24.6	-39.0	-47.0	-51.2
$\lambda_{\text{calc}}$ [-]	1.00(0.02)	1.02(0.02)	1.01(0.02)	1.02(0.02)
Speed [rpm]	1500	1500	1500	1500
$p_{\text{in},2}$ [bar]	0.400(0.001)	0.401(0.001)	0.402(0.001)	0.403(0.001)
$T_{\text{in},2}$ [K]	316.9(0.5)	317.1(0.5)	316.0(0.5)	315.7(0.5)
$T_{\text{ex},2}$ [K]	484.0(0.5)	456.7(0.5)	453.3(0.5)	450.5(0.5)
$p_{\text{max-COV}}^a$ [%]	3.86	7.75	12.8	25.1
Misfires [%]	0	0	0.78	11.2

The voltage and current of the spark coil's secondary circuit were measured using a Tektronix P6015A high voltage probe and a Tektronix TCP303 current probe equipped with a TCPA300 amplifier, respectively. The voltage was measured in parallel to the ignition coil. The signals were recorded using a Tektronix DPO7104 digital phosphor oscilloscope at a sampling rate of 5 MHz.

## 2.2 Optical Diagnostics

Simultaneous HS optical diagnostics were employed for the measurement of the velocity field, the flame propagation, and the spark plasma development at high spatial and temporal resolutions. The

<sup>a</sup>COV: coefficient of variation.

velocity field was obtained via HS PIV in the tumble (symmetry) plane in which a pair of laser sheets (FWHM of approximately 800  $\mu\text{m}$  at the piston's position at  $-90^\circ\text{CA}$  and 200  $\mu\text{m}$  at  $-30^\circ\text{CA}$  since the laser focus was positioned inside the cylinder head) from frequency doubled HS Nd:YVO<sub>4</sub> laser cavities (EdgeWave GmbH) entered the engine cylinder vertically through the piston glass while an HS CMOS camera recorded the Mie scattering of illuminated seeded particles from the side of the cylinder. The PIV camera (Phantom v2640, Vision Research Inc.) was equipped with a 180 mm Sigma lens with the f-number set to 5.6 and a 532 nm bandpass filter was attached to the end of the lens. Image pairs were recorded every second crank-angle degree from  $-180^\circ\text{CA}$  to  $-4^\circ\text{CA}$ , resulting in an acquisition rate of 4.5 kHz and 89 flow fields each cycle. Figure 1(b-c) shows the optical setup in cross-sectional diagrams of the engine test bench.

The burned gas regions for the flame imaging were measured using the second image of each PIV pair. Due to the high contrast between the Mie scattering of the laser-illuminated oil droplets and the dark evaporated areas, the burned gas regions were detected. It is assumed that the borders of the resulting binarized burned gas region images represent the flame location in the symmetry plane and they may either be referred to as flame images or images of the burned gas throughout this work. The binarization of the flame images is detailed in the next section.

Spark plasma imaging was conducted from the same side of the engine as the PIV camera using a beam splitter arrangement so that the back side of the cylinder could be painted black to reduce reflections. The HS CMOS camera used for the plasma imaging (Phantom v711, Vision Research Inc.) was likewise equipped with a 180 mm Sigma lens ( $f/5.6$ ). Images were recorded on a time basis from approximately 200  $\mu\text{s}$  before ignition until  $\sim 1750 \mu\text{s}$  after the start of ignition at a sampling rate of 20 kHz, resulting in 40 images per cycle. The trigger was received from the engine's timing unit and there was a slight offset between the trigger and the time of ignition  $t_{\text{ign}}$  so that the ignition would begin just before the 5<sup>th</sup> image ( $t = 0$ ). The true onset of the spark is uncertain by the duration of one camera exposure (50  $\mu\text{s}$ ). The beam splitter arrangement (see Figure 1(c)) included a T470lpxr-UF3 beam splitter (Chroma Technology Corporation) which reflects UV from the range of 300 nm to 470 nm for the spark images and transmits the range of 470 nm to 700 nm for the PIV images. Between the beam splitter arrangement and the engine cylinder glass, an  $f = +2000$  cylindrical lens was used to correct astigmatism due to the curvature of the cylinder glass.<sup>30</sup>

For PIV, flame, and spark images, each camera on each measurement day recorded images of a 3-dimensional (dual-plane) calibration plate (058 – 5, LaVision GmbH) for perspective correction and conversion of pixels from raw to world coordinates using a 3<sup>rd</sup> order polynomial-based calculation in the commercial software DaVis (LaVision GmbH).

## 2.3 Data Processing

Flow field vector calculations were computed using DaVis 10.1.2 (LaVision GmbH) and can be summarized in the following steps: first, reflective components such as the cylinder roof, spark plug, and intake valves were removed by a geometrical mask. Next, image pairs were corrected using the dewarping procedure described in the previous section. Then, a multi-pass cross-correlation algorithm was employed, which consists of two initial passes with interrogation window size of 64 px  $\times$  64 px and an overlap of 50%, then two final passes with interrogation window size of 32 px  $\times$  32 px and an overlap of 75%. After each vector calculation pass, several vector post-processing schemes were employed to remove spurious vectors. These schemes include: a peak ratio criterion filter, which removed vectors whose first and second correlation peaks were below 1.3. Next, a universal outlier detection filter was applied, which consists of a sliding median filter of size 7 vectors  $\times$  7 vectors. Finally, a removal criterion filter was applied, which removed any interrogation window overlap groups that contained fewer than 5 vectors.

Burned gas (flame) and spark plasma image processing and binarization were conducted using in-house scripts developed in MATLAB (MATLAB version R2021b, MathWorks). The procedure for flame binarization was conducted on a cyclic basis using the second image of each PIV pair from ignition until  $-4^\circ\text{CA}$  and is as follows: first, the images were corrected and scaled using the dewarped grid and calibration file from DaVis. Then, each image was normalized by the maximum intensity of the cycle. In the next step, a sliding entropy filter<sup>31</sup> of  $5\text{ px} \times 5\text{ px}$  was applied and then each image was divided by a background image (before ignition, also underwent the same previous steps), such that any pixels whose intensity was  $> 1$  was set to 0 and the rest were set to 1. Final post-processing steps include an erosion around the edges with a disk shape of radius 4 px, a size criterion which removed binarized areas of smaller than 200 px, a dilation of the same disk shape and size as the erosion to restore the size of flames, and finally all holes within a binarized flame were filled. Using such a technique for the detection and binarization of flame images, fine details around and the flame front itself are not resolved; however, for the purposes of this work, which is concerned with the relative 2-dimensional flame size and location within the measurement plane, the detection of the burned gas regions is more than sufficient.

The algorithm for the processing and binarization of spark plasma images is likewise conducted on a cyclic basis from just before ignition until the last recorded image in a cycle. The processing was conducted using the following strategy: first, as with the other techniques, the images were corrected and a scaling for real world coordinates was defined. Next, a subtraction of the first image without a spark from all images of the cycle was conducted as a background correction and the images were then normalized by the maximum cyclic intensity. Subsequently, a binarization threshold of 3% was applied to set any of the normalized pixels below 3% maximum intensity to 0. All other pixels were then set to a value of 1. As with the flame binarization, a pixel group size criterion (100 px) was applied, all holes were filled, and an erosion and subsequent dilation of a disk with a radius of 2 px was applied. The resulting binarized spark plasma arcs are columns of up to  $\sim 16$  px wide. For the purposes of this work, which is concerned with the location and length of the plasma arcs, the skeletal trace of the binarized spark plasma is used, whereby the MATLAB function *bwske*<sup>32</sup> was applied to yield the centerline of each spark plasma.

Spark voltage and current signals were also processed using MATLAB. After importing the CSV files into MATLAB, the raw voltage and current signals underwent a low-pass filter of 100 kHz and 50 kHz, respectively, to reduce signal noise. Additionally, the signals were offset on the  $x$  and  $y$ -axes of all plots so that breakdown begins at  $t = 0$  ms and the mean voltage and current both return to a value of 0 after the discharge glow.

All plots were generated using MATLAB version R2022b and schematic figures and some post-processing of figures, such as the combination of subfigures, was conducted using Inkscape version 1.2.2.

## 3 Results and Discussion

### 3.1 Characterization of Operating Conditions

The operating conditions have already been well-characterized in a previous work by the same authors in terms of the effects of EGR on the stability of the combustion.<sup>25</sup> In the aforementioned work, the in-cylinder pressure comparison of the various EGR OCs shows that increasing EGR rates decreases the maximum in-cylinder pressure  $p_{\text{max}}$  while also increasing the cyclic instability (shown by the fluctuation of the  $p_{\text{max}}$ , see also Table 1). Another important characterization in the previous study is the comparison of the velocity fields at the time of ignition. In principle, the gas composition does not have an effect on the mean flow fields at  $-90^\circ\text{CA}$  and all earlier CADs. However, since the spark timing for each OC was adjusted for combustion phasing, the flow fields near the spark plug at  $t_{\text{ign}}$  are



distinctive, resulting in significantly different early flame propagation directions for 0% EGR compared with 14.3% EGR.

Since the objective of this work is to study the spark's role in the complex interaction between the in-cylinder flow and the early flame growth under increasing rates of dilution, Figure 2 displays the mean (solid line represented symbolically with the angled brackets) and standard deviation SD (dashed lines) of the measured secondary voltage  $V$  and current  $I$ , and the calculated power  $P$  and input energy  $E$  (gap energy) at each EGR rate. The gap  $P$  and  $E$  are calculated using the following formulas:

$$P(t) = (V - I \times R_{sp}) \times I \quad (1)$$

$$E(t) = \int P dt = \int [(V - I \times R_{sp}) \times I] dt \quad (2)$$

where  $R_{sp}$  is the internal resistance of the spark plug, measured to be 3.4 k $\Omega$  by an ohmmeter. The internal spark resistance is considered in these calculations to ensure the calculated values of  $P$  and  $E$  are the power and energy delivered across the spark gap.<sup>13</sup>

Characteristic of a typical automotive TCI system, the energy stored in the coil is released in under 2 ms. The breakdown phase (signified by the red arrow and "B") occurs at  $t = 0$  ms in Figure 2 and lasts such a brief amount of time that the measurements shown in this work cannot properly resolve this stage of the discharge ( $\sim 10$  ns). Nevertheless, the arc phase (signified by the "A") occurs in Figure 2 from approximately  $t \approx 0.03$  ms to  $t \approx 1.5$  ms. The glow phase is the final phase of the spark discharge and is signified by the "G".

As suggested by Lee et al.,<sup>6</sup> the spark traces under higher pressures at  $t_{ign}$ , especially in the 0% EGR case ( $p \approx 3.9$  bar), do not have an obvious transition from the arc to glow phase, typically indicated by a sudden rise of the voltage across the electrodes. However, in the case of the higher EGR rates where the ignition pressure is between 1.5 bar and 2.5 bar, such a rapid rise in the mean voltage appears in Figure 2 from  $t \approx 0.03$  ms to  $t \approx 0.12$  ms (shaded orange region, sharp gradients are smoothed by the mean), indicating that this time period might be characteristic of the arc phase and the following time period until  $t \approx 1.5$  ms could be classified as the glow phase. Since the 0% EGR case seems to remain in the arc phase after  $t \approx 1.5$  ms, while the other OCs seem to have transitioned to the glow phase, the green shaded region in Figure 2 is labelled "A/G" to signify arc or glow.

Further observations from Figure 2 can be made through observations of the mean and SD spark signal traces of the OCs. First, on average, the 0% EGR case has the greatest voltage over the arc phase and the current decreases the quickest. This is associated with the greatest energy deposit, which reaches its maximum the quickest in comparison to the other OCs. As previously mentioned, the 0% EGR OC has the greatest pressure at ignition, which equates to a higher resistance in the spark gap. Therefore, the secondary circuit must compensate for the higher resistance and thus deposits more energy into the system to achieve a spark. Apart from the 0% EGR case having significantly different characteristic mean signals from the others, the EGR OCs are hardly distinguishable from one another with such a comparison of smoothed line plots.

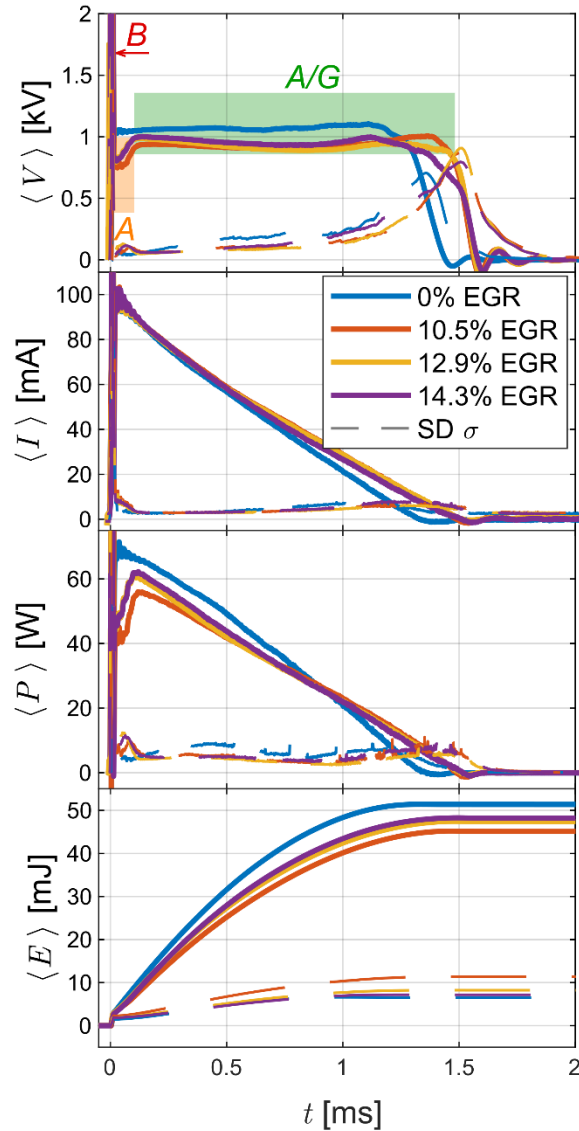


Figure 2. Mean (thick lines) and standard deviation (dash lines) of the measured secondary circuit voltage  $V$  and current  $I$  and computed power  $P$  and input energy  $E$ .

### 3.2 Ignition of Representative Restrike Cycles

A critical aspect determining the spark characteristics is the gas composition of the OCs. As the dilution increases and the flame speed decreases, increased turbulence is required to enhance the flame propagation and increase combustion stability. However, as previously suggested, the differences of the mean in-cylinder flow of the 4 OCs are mainly determined by the flow field at the different ignition timings  $t_{\text{ign}}$ , meaning that on average, the 0% EGR case has the greatest velocity near the spark plug. Hence, variations of the spark discharge and resulting flame growth on a cyclic basis become more prevalent with CCV of the flow field near the spark electrodes at ignition, especially under higher dilution. A by-product of enhanced velocity at spark onset is the strong convection (elongation) of the spark plasma channel and the resulting blow-off followed by RS while charge still lasts. It has been shown in previous research that RS can lead to multiple ignitions inducing a corrugated, non-spherical early flame kernel.<sup>14,22</sup> Such early flame conditions would lead to faster growth given the same conditions with a spherical flame kernel of the same size. However, Sayama et al. contend that RS may not always lead to faster combustion if the flame kernel detaches from the spark RS and blows off downstream, resulting in a wasted energy deposit and cyclic instability.<sup>10</sup> Therefore, since the effects

of RS on flame growth are highly dependent on the flow conditions at ignition, this section aims to further examine the role of RS on the ensuing combustion in the case of increasing dilution of homogeneous mixtures by analyzing individual characteristic RS and non-RS cycles of the stable 0% EGR and highly unstable 12.9% EGR OCs before confirming the observed phenomena through statistical analysis in the next section.

Figure 3 displays a comparison of the secondary circuit voltage and computed input energy for selected representative normal (non-RS) and RS cycles for the 0% EGR and 12.9% EGR OCs. For both OCs, the normal cycles undergo a smooth decrease and then increase of the voltage before a sharp plateau and coil oscillation. In all, the glow discharge phase for the displayed normal cycles lasts until approximately  $t = 1.5$  ms. On the contrary, the RS cycles represent a short, jagged voltage curve with multiple sharp peaks that are greater on average than the smooth curve voltages of the normal cycles. The greater voltage over the shorter period of time results in the rapid deposition of the electrical energy in the case of the RS cycles. Additionally, the RS cycles have slightly higher peak energies which occur approximately 0.5 ms faster than their normal cycle counterparts. The energy deposited by the ignition of a given OC is generally constant from cycle-to-cycle due to the same amount of energy being released as was stored. However, this is not the case in the 12.9% EGR RS cycle shown in Figure 3, where the energy is greater than that of the normal cycle and the mean energy shown in Figure 2. The incongruous release of energy can occur when not all of the coil's energy is released. Yet, as evident by the high SD of the energy traces shown in Figure 2, the CCV of the energy release is quite significant, a result that is likely tied to the cyclic variations of the flow. Furthermore, as in Figure 2, the 0% EGR cycles require more energy input to achieve ignition due to the greater velocities at ignition. These high velocities lead to more resistance as the plasma channel elongates further with higher flows. Finally, the higher velocity cycles at ignition (0% EGR cycles) have a shorter spark duration than the lower velocity cycles (12.9% EGR) due to the faster release of the energy associated with the RS.

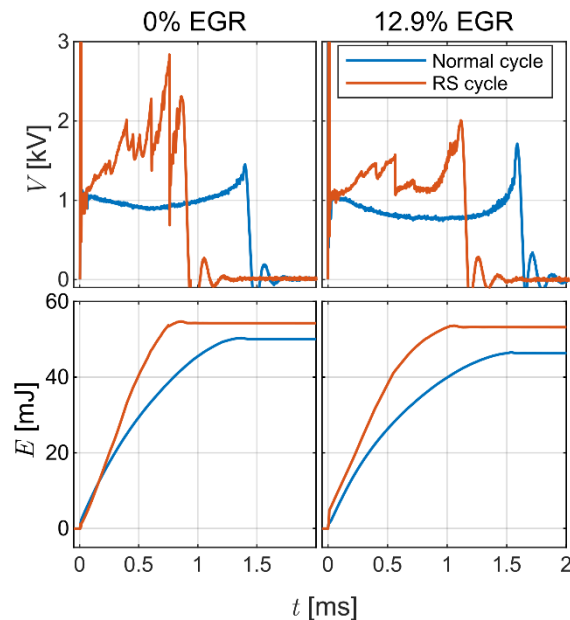


**Figure 3. Secondary circuit voltage and computed input energy for selected normal and restrike cycles for 0% EGR ( $t_{\text{ign}} = -24.6^{\circ}\text{CA}$ ) and 12.9% EGR ( $t_{\text{ign}} = -47.0^{\circ}\text{CA}$ ).**

The voltage traces of the selected RS cycles shown in Figure 3 can be compared with the plasma images in order to associate the sharp voltage drop events with the spatial characteristics of the plasma channel. Figure 4 displays the voltage trace and its corresponding spark plasma evolution for the RS cycle of the 0% EGR case shown in Figure 3. To provide spatial reference of the relative position of the spark plug, a white outline of the approximate position of the spark plug is provided. Relevant spark

events are highlighted by the different colors in Figure 4(a) and appear in the bottom of the corresponding spark images of the same time window. The measured camera intensity in counts is represented by the color map. Before interpretation of the figure, it is important to note that the exact timing of the HS imaging and the voltage signals could not be matched due to the sampling rates being different; however, the HS imaging is still captured within an offset of a maximum of 50  $\mu\text{s}$ . Additionally, it is important to note that the spark plasma imaging cannot always capture a RS in two sequential images due to the relatively long exposure time ( $\sim 50 \mu\text{s}$ ); rather, it is often the case that a RS event appears in one frame as the camera captures the older and newer positions of the plasma in one exposure (for example, at  $t = 100 \mu\text{s}$ , where the dashed lines marked “1” and “2” point to the two plasmas in one exposure).

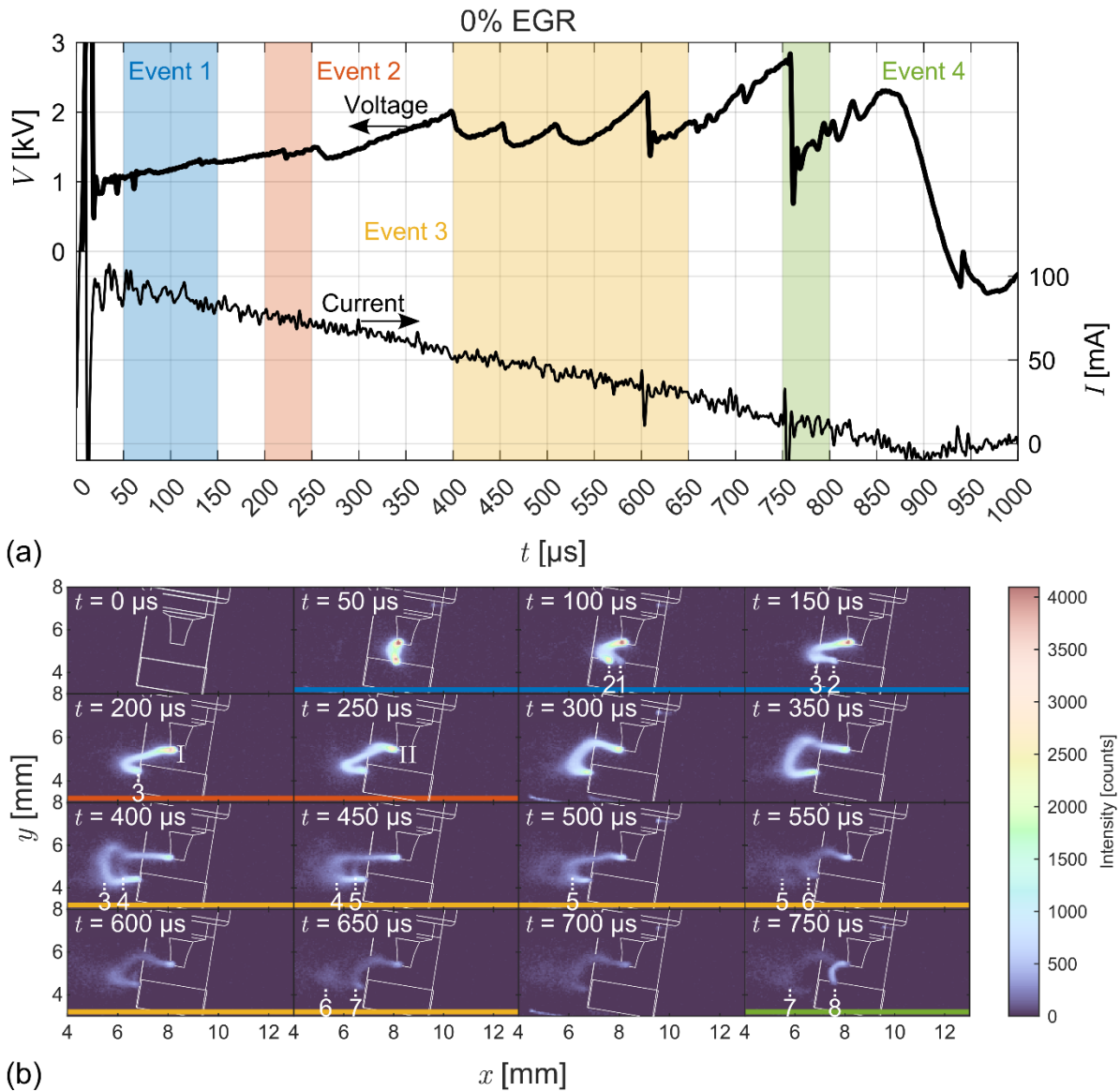


**Figure 4.** Voltage (left axis) and current (right axis) trace (a) and evolution of spark plasma (b) for a selected cycle of the 0% EGR case exhibiting restrike originally shown in Figure 3 ( $t_{\text{ign}} = -24.6^\circ\text{CA}$ ). Roman and Arabic numerals denote changes in the plasma contact point at the center and ground electrode, respectively.

As previously emphasized, the 0% EGR case ignites later in the cycle compared with the diluted OCs with external EGR. With a higher velocity magnitude at  $t_{\text{ign}}$ , the spark duration is shorter, while the voltage is higher. Due to the higher velocities in the vicinity of the spark plug at  $t_{\text{ign}}$ , Figure 3 shows that in the selected cycle for 0% EGR, many more RS events occur than in the 12.9% EGR case. The

first highlighted event in Figure 4 occurs between  $t = 50 \mu\text{s}$  and  $t = 100 \mu\text{s}$ , where a small voltage drop occurs (Figure 4(a),  $t = 61 \mu\text{s}$ ), before rapidly recovering. This is labelled in Figure 4(b) by the positions “1” and “2” at  $t = 100 \mu\text{s}$  where the high intensity plasma attached to the ground electrode shifts to the left by  $\sim 0.5 \text{ mm}$  in the same exposure. At the end of Event 1, the spark channel is further elongated towards the intake valves, which is the direction of the bulk flow at ignition, and between  $t = 100 \mu\text{s}$  and  $t = 150 \mu\text{s}$  another RS occurs, indicated by the two spark plasma positions (jump from “2” to “3”) on the ground electrode in the image labelled  $t = 150 \mu\text{s}$ . After  $t = 200 \mu\text{s}$  where the plasma remains attached to the ground electrode at position “3”, Event 2 begins, in which another plasma shift occurs, this time by leftward movement lightly visible at the center electrode from  $t = 200 \mu\text{s}$  and  $t = 250 \mu\text{s}$ , signified by the shift in position near the Roman numerals “I” and “II” and appearing at  $t = 223 \mu\text{s}$  in Figure 4(a). Roman numerals are chosen to distinguish spark phenomena at the center electrode from spark phenomena at the ground electrode (Arabic numerals). Although there is a visible drop in the voltage trace at this event, it is likely that the plasma does not experience full RS; instead, the plasma can shift positions along the electrodes while maintaining contact. The end of Event 2 marks a  $144 \mu\text{s}$  period of unbroken spark channel elongation coupled with steadily increasing voltage. Physically, as the spark channel elongates, more resistance between the electrodes builds as more ionized gas separates the connection between the electrodes, evident by the increasing voltage in Figure 4(a). Once the resistance becomes too high, the spark channel resets taking a path of least resistance before the process repeats. Event 3 contains several minor RS events which culminate between  $t = 600 \mu\text{s}$  and  $t = 650 \mu\text{s}$  in a larger RS event. The elongation of the older spark channel and newer RS channel within each exposure is signified once again by the white dashed lines. Finally, at  $t = 750 \mu\text{s}$  one last RS occurs, which shows an almost total reset of the spark plasma position (from position “7” to “8”) in the single image exposure and a voltage drop of over 2 kV.

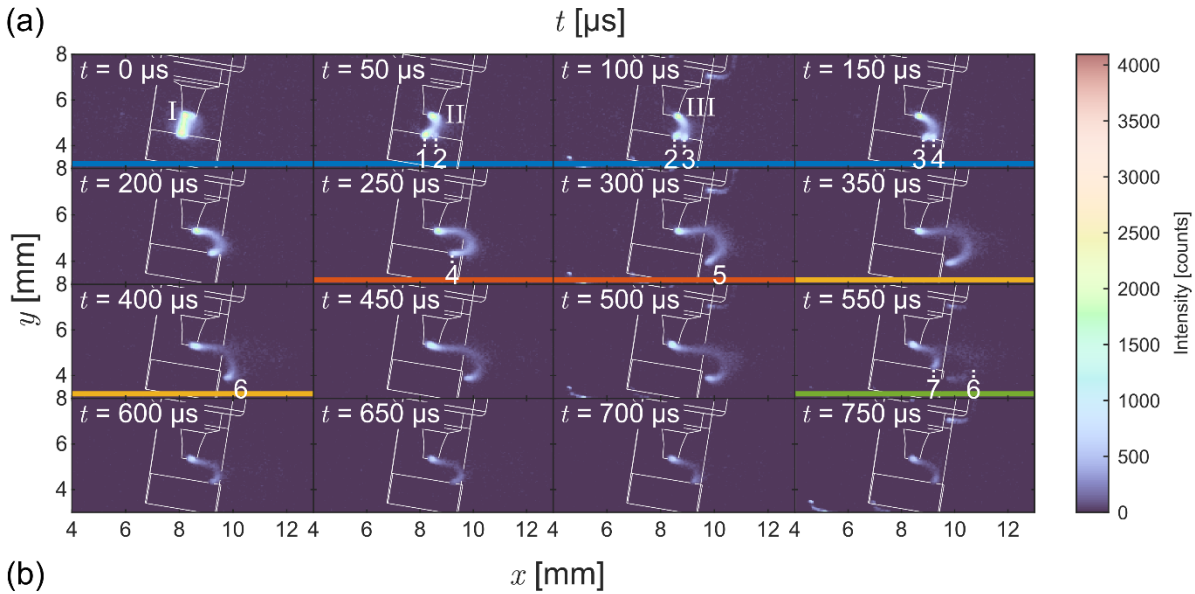
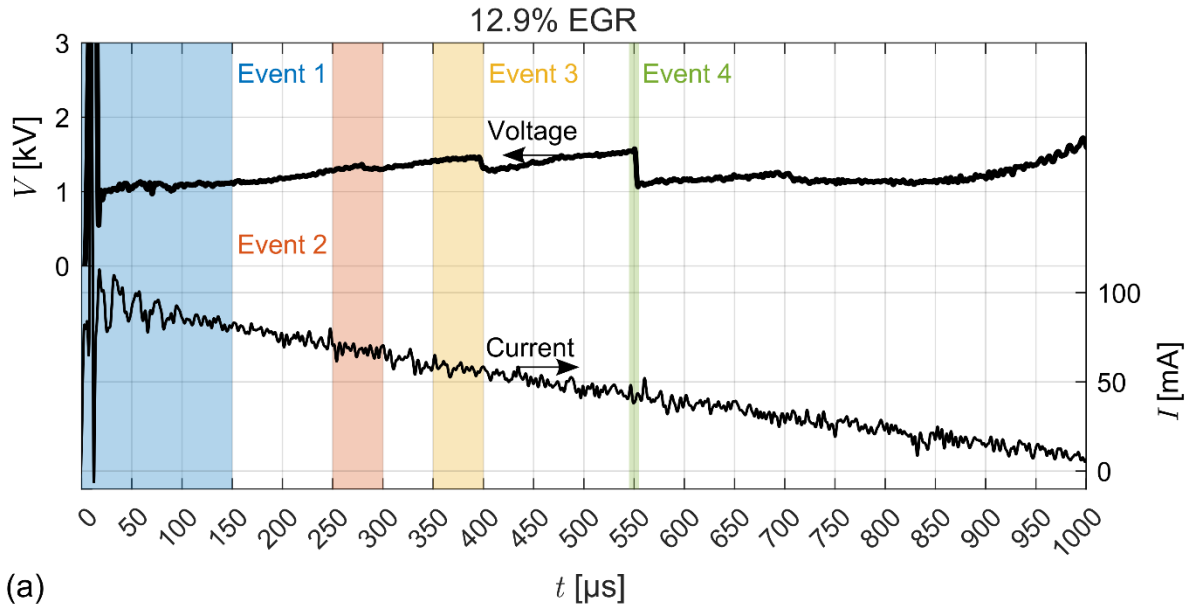


**Figure 5.** Voltage (left axis) and current (right axis) trace (a) and evolution of spark plasma (b) for a selected cycle of the 12.9% EGR case exhibiting restrike originally shown in Figure 3 ( $t_{\text{ign}} = -47.0^\circ\text{CA}$ ). Roman and Arabic numerals denote changes in the plasma contact point at the center and ground electrode, respectively.

While the representative cycle of the 0% EGR case shown in Figure 4 contains many RS events over the whole spark discharge, the selected cycle of the 12.9% EGR case has a longer spark duration (due to the lower velocities) and fewer, less pronounced RS events. Figure 5 displays the voltage trace and corresponding spark image sequence of the characteristic cycle of the 12.9% EGR case first shown in Figure 3. The direction of the plasma elongation indicates that for this particular cycle, the velocity across the spark gap is strongly pointing from the intake to the exhaust side. Based on the elongation lengths and the magnitude of the voltage drops of the highlighted events, it can also be deduced that the velocity across the spark gap is lower than in the case of the 0% EGR cycle (compare Figure 6).

Event 1 and Event 4 highlighted in Figure 5 represent particularly interesting phenomena. From the onset of ignition until  $t = 150 \mu\text{s}$ , Event 1 shows the evolution from a relatively direct initial plasma channel to the rightward elongation associated with a strong horizontal flow across the gap. Yet, of particular significance are the RS events evident in each image from  $t = 50 \mu\text{s}$  and  $t = 150 \mu\text{s}$  by the capturing of two high intensity channels in each exposure. These RS events, which progress the plasma channel's location along both electrodes in the positive  $x$ -direction (plasma shifts attached to

the center electrode are represented by Roman numerals and ground electrode shifts are signified by the white dashed lines and plasma positions “1” through “4”), are coupled with an unstable phase in the voltage signal of Figure 5(b), which displays a series of jagged edges in quick succession. The spark image sequence of Event 1 is significant in that it unmistakably showcases that voltage signals which may have simply been considered noisy due to their close proximity and relatively low voltage drops may in fact hold physical meaning. The rest of the spark discharge is characterized by an elongation towards the exhaust side of the cylinder and smooth rise in voltage until two rather minor RS events or shifts in plasma positions along the electrodes (signified by jumps from positions “4” to “6”) and finally a larger RS signified by Event 4, where the plasma channel’s length is cut approximately in half (jump from position “6” to “7”) and the voltage drops by  $\sim 0.5$  kV.

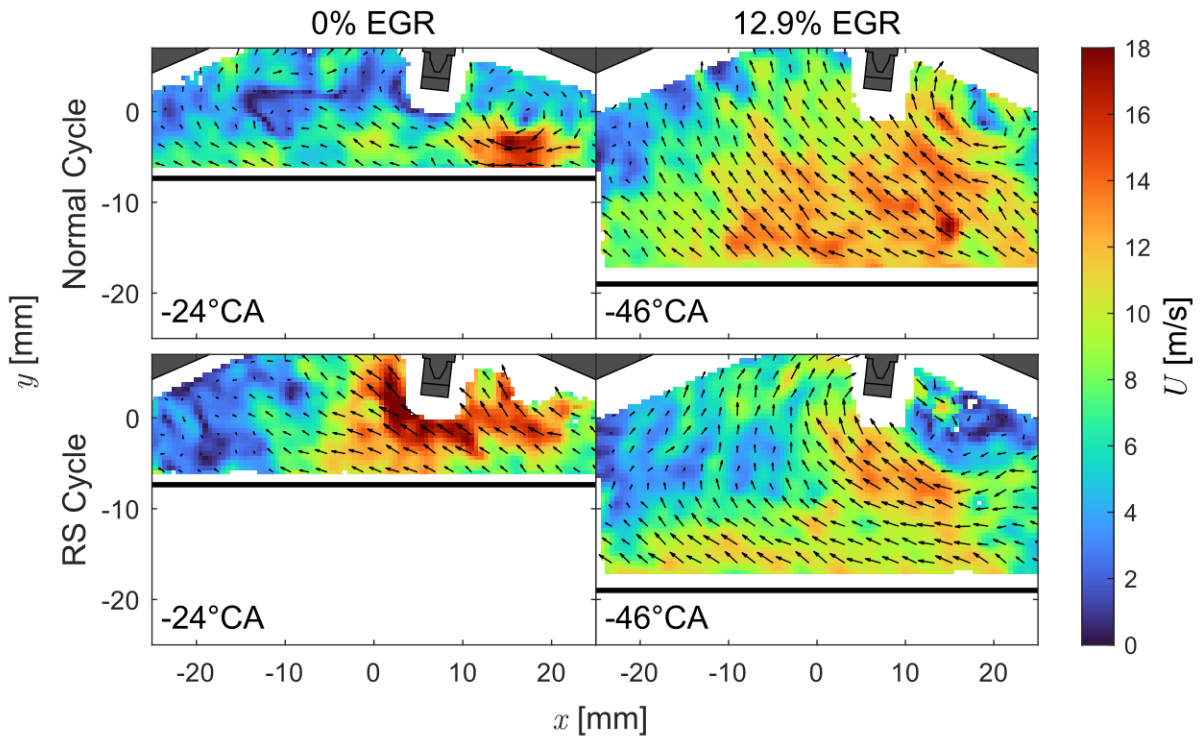


**Figure 6.** Instantaneous velocity fields at ignition timing  $t_{\text{ign}}$  for selected normal and restrike cycles for 0% EGR and 12.9% EGR originally shown in Figure 3.

To assess the degree at which the chosen characteristic cycles’ plasma channel elongation directions and lengths are correlated to their velocity fields across the spark gap at ignition, Figure 6 displays a comparison of the velocity field at  $t_{\text{ign}}$  for the normal (non-RS) and RS cycles chosen and compared in Figure 3. As hypothesized, the RS cycles exhibit considerable differences in their flow fields in the region surrounding the spark plug from their non-RS counterparts. In the case of 0% EGR, the normal cycle has a nearly stagnant velocity field in the vicinity of the spark plug, while the RS cycle has velocities between 12 m/s and 18 m/s in the negative  $x$ -direction. The normal cycle does contain a small region with similarly high velocity magnitudes, but it is near the surface of the piston and is part of a lingering tumble vortex remaining in the field of view. At  $t_{\text{ign}}$  of the 12.9% EGR case,  $22^\circ\text{CA}$  earlier than the ignition of the non-diluted case, the flow fields of both the non-RS and RS cycles have a different global flow structure than the 0% EGR case cycles with a global flow surrounding the tumble vortex center to the right of the spark plug. Although the normal cycle has greater velocity magnitudes coming off the piston surface pointing towards the intake valves, the RS cycle has a larger tumble vortex resulting in horizontal vectors across the spark plug. Furthermore, a comparison of the flow fields of the two RS cycles of different OCs shows that the 0% EGR cycle may have double the velocity magnitude across the spark gap as the 12.9% cycle, which induces the more extreme elongation of



the spark channel and the more frequent RS events (compare Figure 4, Figure 5, and Figure 6). While vectors cannot be calculated within the spark gap through PIV, the surrounding instantaneous flow fields in the vicinity of the gap shown in the RS cycles are clear evidence that the spark elongation direction and length are heavily influenced by the stochastic behavior of the cyclic flow. It is important to note that instantaneous spark gap velocities can also be calculated through correlations using the measured secondary circuit voltage and thermodynamic conditions, such as the one proposed by Wörner and Rottenkolber;<sup>33</sup> however, the development of such correlations require calibration in an optically accessible system such as a wind tunnel or flow bench and the directionality of the flow is not available. In the present study, voltage rise anemometry is not necessary as the simultaneous instantaneous velocities are available surrounding the spark plug as a supplement to the circuit and spark imaging data.

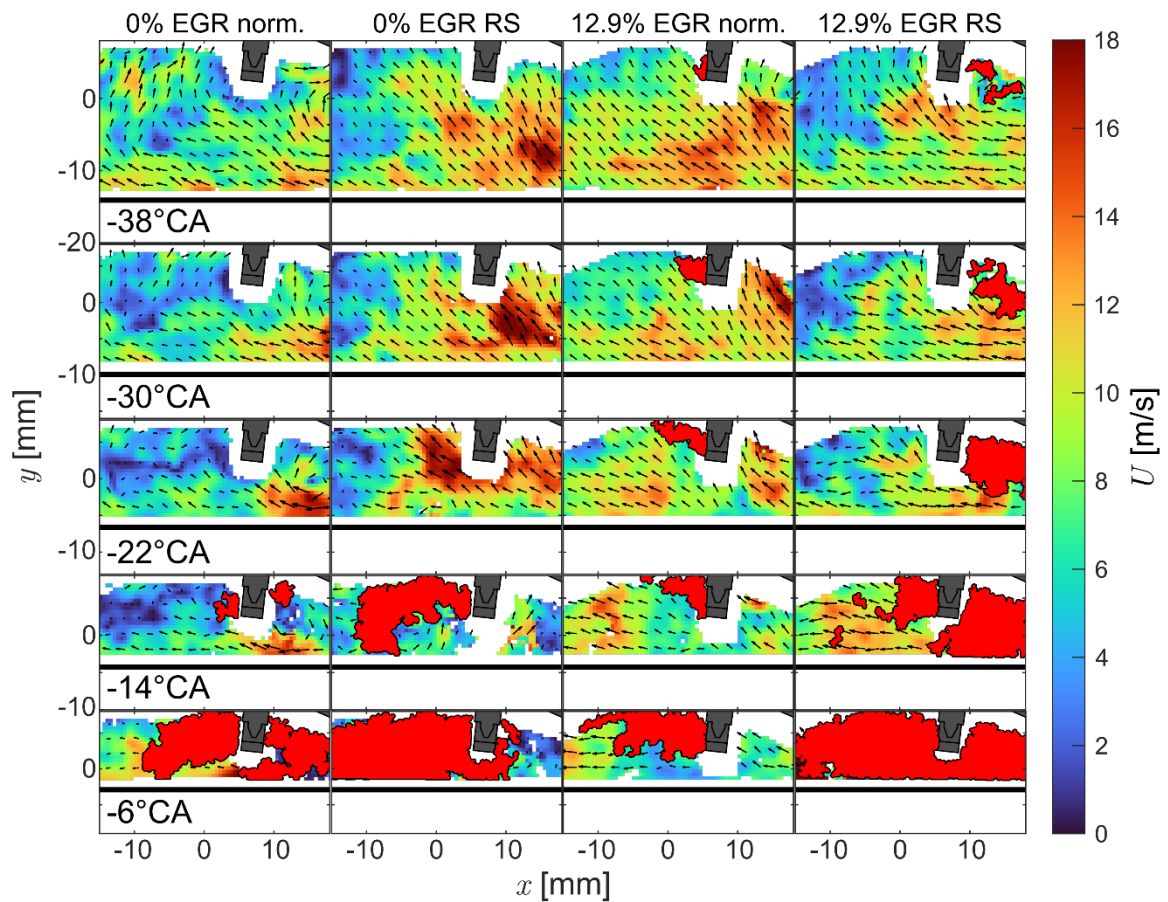


**Figure 7. Instantaneous velocity field and flame evolution for selected normal and restrike cycles for 0% EGR and 12.9% EGR originally shown in Figure 3.**

Similar to the spark channel elongation, the instantaneous flame propagation evolution is heavily influenced by the flow across the spark gap and the surrounding region. Figure 7 displays the evolution of the velocity field and binarized flame in  $8^\circ\text{CA}$  increments for each of the chosen characteristic normal and RS cycles first compared in Figure 3. The instantaneous velocity magnitude  $U$  is represented by the color map and the flow directions are represented by the vector arrows (every 4<sup>th</sup> vector is shown). Shortly after ignition (0% EGR:  $t_{\text{ign}} = -24.6^\circ\text{CA}$ ), the near stagnant flows surrounding the spark plug in the normal cycle of the 0% EGR case are coupled with two nearly identically sized flame areas on opposite sides of the spark plug in the measurement plane.  $8^\circ\text{CA}$  later, the binarized flame area continues to exhibit symmetric growth about the spark plug. In the case of the RS cycle, which has a considerable flow pocket surrounding the spark plug pointing towards the



intake valves, the early flame cross-section is noticeably larger only 2°CA after  $t_{\text{ign}}$  than in the normal cycle and it propagates first towards the left side of the cylinder in the direction of the flow. Although this figure only represents the cross-sectional burned gas regions, previous work with the same OCs used 3D large eddy simulations and showed that the cross-sectional flame surface area is reasonably well-representative of the 3D flame's volume.<sup>34</sup> This can be quantified with the exemplary cycles by comparing the  $p_{\text{max}}$ , a quantity representing the speed of the combustion. The normal cycle with the slower flame growth has a  $p_{\text{max}}$  of 12.94 bar while the RS cycle has 13.52 bar, an increase of 4.5%.

The cycles of the 12.9% EGR OC ( $t_{\text{ign}} = -47.0^\circ\text{CA}$ ) show a different trend. The normal cycle has a large upward velocity in the vicinity of the spark plug similar to the RS cycle of the 0% EGR case. Additionally, analogous to the 0% EGR RS cycle, this velocity in the negative  $x$ -direction forces the flame to propagate first towards the left, but it is more inclined to grow along the cylinder roof. However, the heat losses at the roof combined with the slower flame speed of the diluted mixture cause the flame to grow far slower than its 0% EGR RS cycle's counterpart. On the other hand, the RS cycle which is characterized by a horizontal flow across the spark gap in the positive  $x$ -direction and a rightward spark plasma channel elongation, has an early flame that first grows within the tumble center. Although the flame cross-section in the RS cycle also appears to initially grow slowly, since it is allowed to propagate away from the colder cylinder roof, its size quickly surpasses that of the normal cycle's flame. As with the 0% EGR cycles, the RS cycle of the 12.9% EGR case has a higher  $p_{\text{max}}$  of 11.99 bar compared with 11.83 bar of the non-RS cycle, a 1.4% increase. While  $p_{\text{max}}$  differences of 4.5% and 1.4% are not large, these cycles represent only singular events and by chance they happen to coincide with the flame-flow models of leftward and rightward propagating flames described in a previous work by the authors, where the high EGR case showed that rightward flows across the spark plug correlated with rightward early flames and consequently higher  $p_{\text{max}}$ .<sup>25</sup> However, RS is a phenomenon that is independent of the flow direction. Therefore, the next section is concerned with analyzing the RS cycles on a statistical basis to remove selection bias or chance as sources for the discussed tendencies.

### 3.3 Statistics of Restrike Cycles

The separation of the OCs into a set of all non-RS cycles and all RS cycles proved to be a challenge due to the requirement of a thresholding technique which always contains a cut-off. As a consequence, categorization was performed manually, whereby cycles with large voltage drops, such as the RS cycles of Figure 3, were placed in the RS category. Although the manual selection criterion is subjective, the categorization of the vast majority of the cycles was obvious, leaving only some potential borderline cycles that may have been incorrectly categorized as a source of error. With such large datasets, the error of manual selection can potentially be revealed in the conditional statistics by reducing the prominence of trends. The size of each dataset and the percentage of RS cycles is displayed in Table 2. Since the 0% EGR OC has a greater velocity on average at its  $t_{\text{ign}}$  (shown in Welch et al.<sup>25</sup>), it also contains the most RS cycles by far. Due to higher velocities at ignition timing, decreasing EGR rates lead to a higher percentage of RS cycles. This is not the case for the 14.3% EGR case, however, since this condition is highly unstable and the ignition timing is so early that the flow frequently causes misfire.

**Table 2.** Size of the categorized datasets representing the non-RS and RS cycles.

Category	0% EGR	10.5% EGR	12.9% EGR	14.3% EGR
Non-RS [-]	229	867	1187	707
RS [-]	210	99	101	98
RS [%]	47.8	10.3	7.84	12.2

The mean (solid lines) and SD (shaded area) of the secondary circuit voltage of each dataset for each OC is displayed in Figure 8. As occurred in the selected single cycles, the mean RS cycles generally have a shorter spark duration and a greater discharge voltage. Additionally, the SD envelope for the RS cycles is generally far larger than the non-RS cycles due to the voltage drops characteristic of RS. Although not shown here, the shorter spark duration and greater voltage translates to the quicker deposition of energy, as shown in the single cycles in Figure 3. As RS is associated with greater elongation of the spark channel due to the local velocity, the quicker deposition of the coil energy in the presence of higher velocities translates to the swift spread of the energy and the flame kernel grows faster.

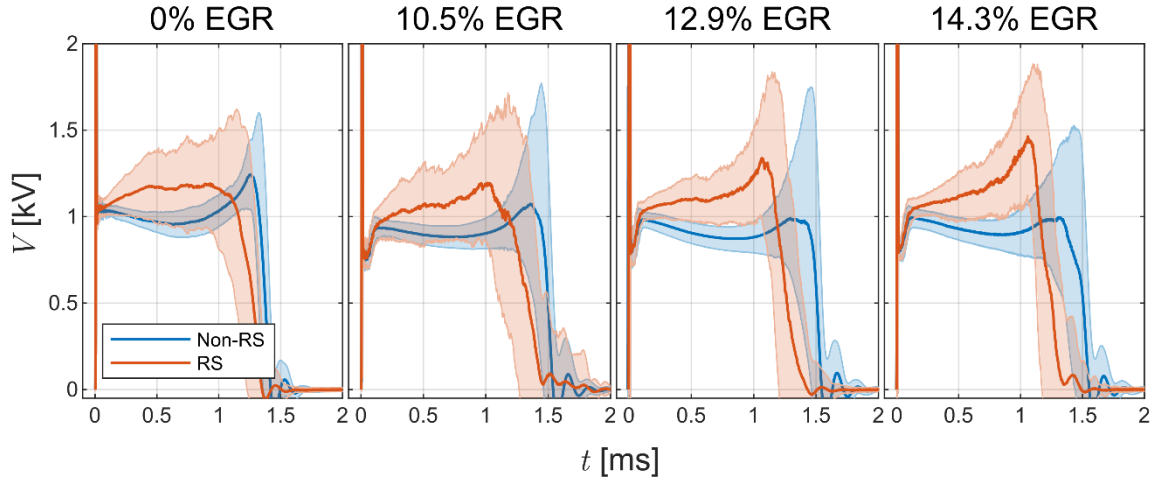


**Figure 8. Conditioned mean and standard deviation (shaded area) of all non-restrike and restrike cycles for each EGR level.**

Figure 9 shows a comparison of the mean flow fields of all non-RS and RS cycles at each EGR level at their respective ignition timing. The mean velocity magnitude  $\langle U \rangle$  is represented by the color map and the mean flow directions are represented by the streamline arrows. Despite differentiating characteristic voltage curves for 0% EGR (compare Figure 8), the conditional mean velocity field of the non-RS set is indistinguishable from that of the RS set. Nevertheless, as the EGR levels increase, the effect on the conditional statistics increases: the conditional mean velocities across the spark gap for RS cycles point horizontally in the positive  $x$ -direction with increasing prominence at higher EGR levels. Although the selected characteristic cycles of the 0% EGR case suggest that RS occurs under the conditions of a strong leftward flow at  $t_{\text{ign}}$ , the conditioned mean flow fields point to stochastic behavior, which smooths out over the mean of hundreds of cycles. To examine this further, the evolution of the probability density function (PDF), or the mean of the binarized skeletal spark plasma positions is displayed in Figure 10. In Figure 10, the position of the spark plug is represented by long exposure images without spark (with inverted grayscale colormap) and the approximate positions of the spark plug are marked by the black lines. Additionally, the non-RS and RS cycle sets are indicated by the labels and by a blue and orange outline, respectively. While the conditioned mean flow fields of the two 0% EGR sets are nearly identical, the conditioned spark PDFs reveal a greater tendency for leftward-elongated plasma channels to have a more extreme curvature for RS cycles. Moreover, there are more RS cycles with extreme rightward elongation than non-RS cycles, while most of the non-RS cycles have a tendency to elongate towards the left. This may induce a balance in the mean flow field by cancelling out extreme velocities in either direction. On the other hand, the conditioned spark PDFs of the EGR conditions agree with the conditioned flow fields in that increasing EGR leads to increasing rightward velocity across the spark gap and a corresponding decreasing tendency of straight spark plasma channels for RS cycles. Non-RS cycles, in contrast, have a milder distribution of the plasma channels, while with increasing EGR (earlier  $t_{\text{ign}}$ ) they also tend to elongate towards the right.

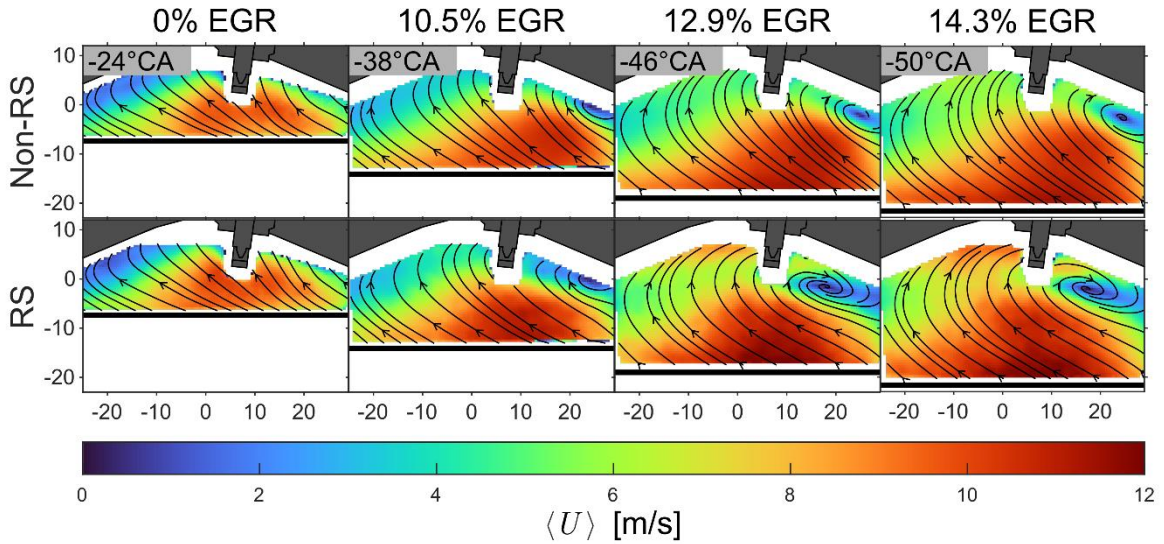


Figure 9. Conditioned mean velocity field of all non-restrike and restrike cycles for each EGR level.

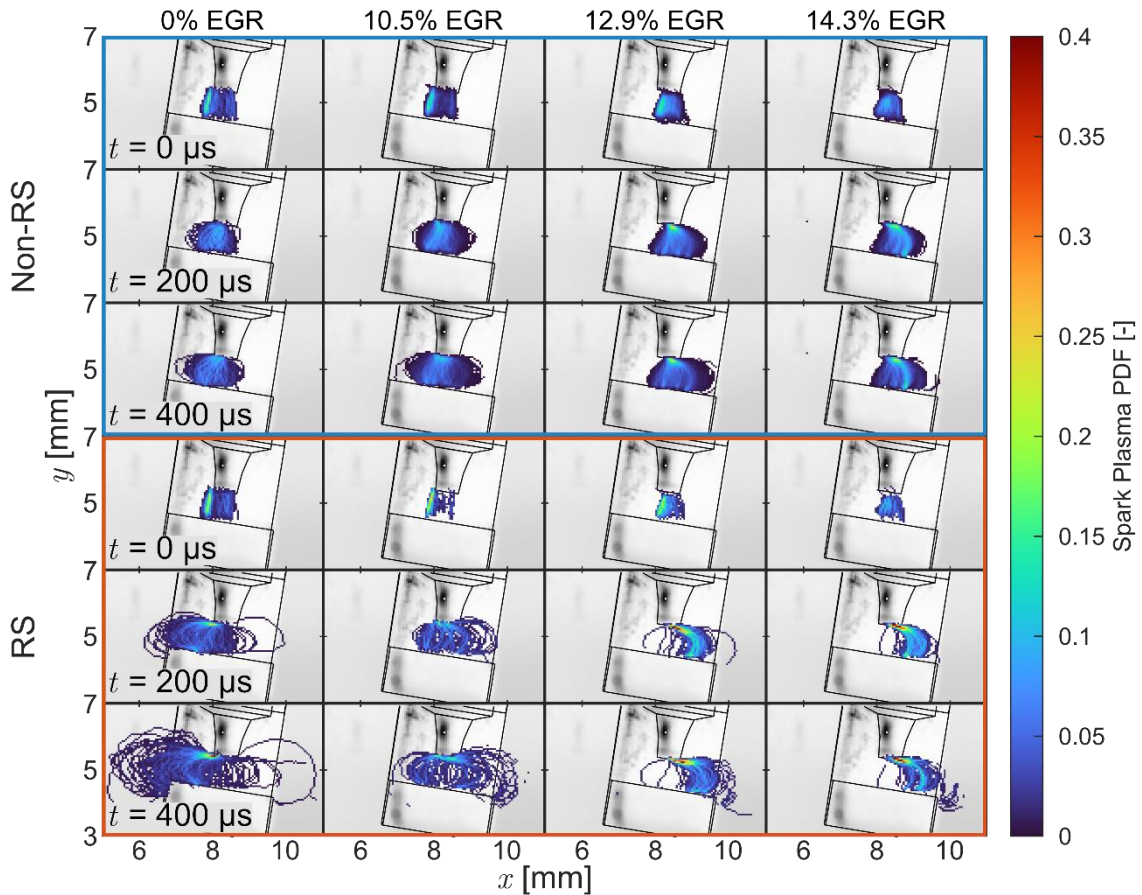
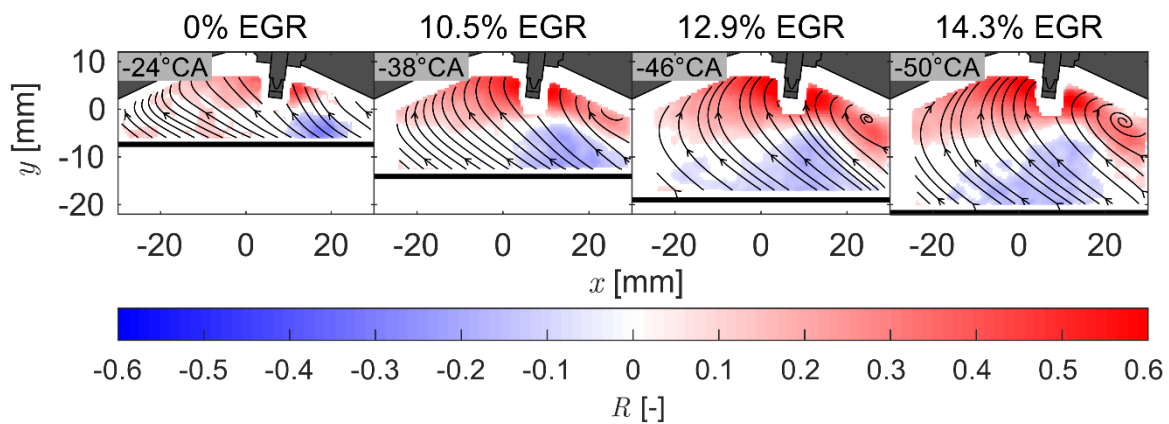


Figure 10. Evolution of the conditioned probability density function of the skeletal spark location for cycles without and with restrike.

A complimentary method to assess the velocity field's interaction with the spark plasma position is to visualize the correlation field of the  $x$ -component of velocity  $u$  and the  $x$ -coordinate of the furthest point horizontally along the binarized plasma channel. To achieve this, the  $x$ -coordinate of the binarized skeletal plasma channel furthest from the electrode center ( $x_{\text{elong}}$ ) was obtained for each cycle at  $t = 400 \mu\text{s}$  after spark onset and the Pearson correlation coefficient  $R$  was calculated

between this quantity  $x_{\text{elong}}$  and the  $u$  at each vector position over all cycles. Using such a method, a scatterplot between  $x_{\text{elong}}$  and  $u$  for each vector position could be visualized similar to the ones shown in Figure 11 of Welch et al.<sup>25</sup> A significance filter was applied to the resulting correlation fields, whereby correlation positions whose  $p$ -value<sup>b</sup> was greater than 0.05 were set to zero. The resulting correlation fields of the velocities at each OC's ignition timing are displayed in Figure 11 with the mean flow directions overlain as streamlines to indicate the general motion. An interesting aspect of correlation field analysis is the directionality associated with the sign of  $R$ , that is, positive  $R$  indicates a positive linear regression, meaning stronger velocities in one direction are correlated with spark elongation in the same direction. The opposite directionality is true for negative values of  $R$ . Although Figure 9 may suggest a lack of relationship between RS and velocity of the 0% EGR case due to the same conditional flow fields, Figure 11 may refute this notion assuming that spark elongation is related to RS. The significant correlations up to approximately  $R = 0.5$  to the right of the spark plug in the 0% EGR case reveal a statistically significant relationship between the flow and the spark behavior where such relationships are unclear from the conditional statistics. Therefore, using the holistic approach of analyzing first the flow fields and spark PDFs individually for context and then the correlation field as a summary of the flow interactions with the spark plasma is crucial in the comprehension of such complex processes.



**Figure 11. Correlation field of the  $x$ -component of velocity  $u$  and the  $x$ -coordinate of the furthest point of the spark channel elongation  $x_{\text{elong}}$ .**

<sup>b</sup> $p$ -value is defined as the probability of observing the outcome without any relationship between the variables.<sup>35</sup>

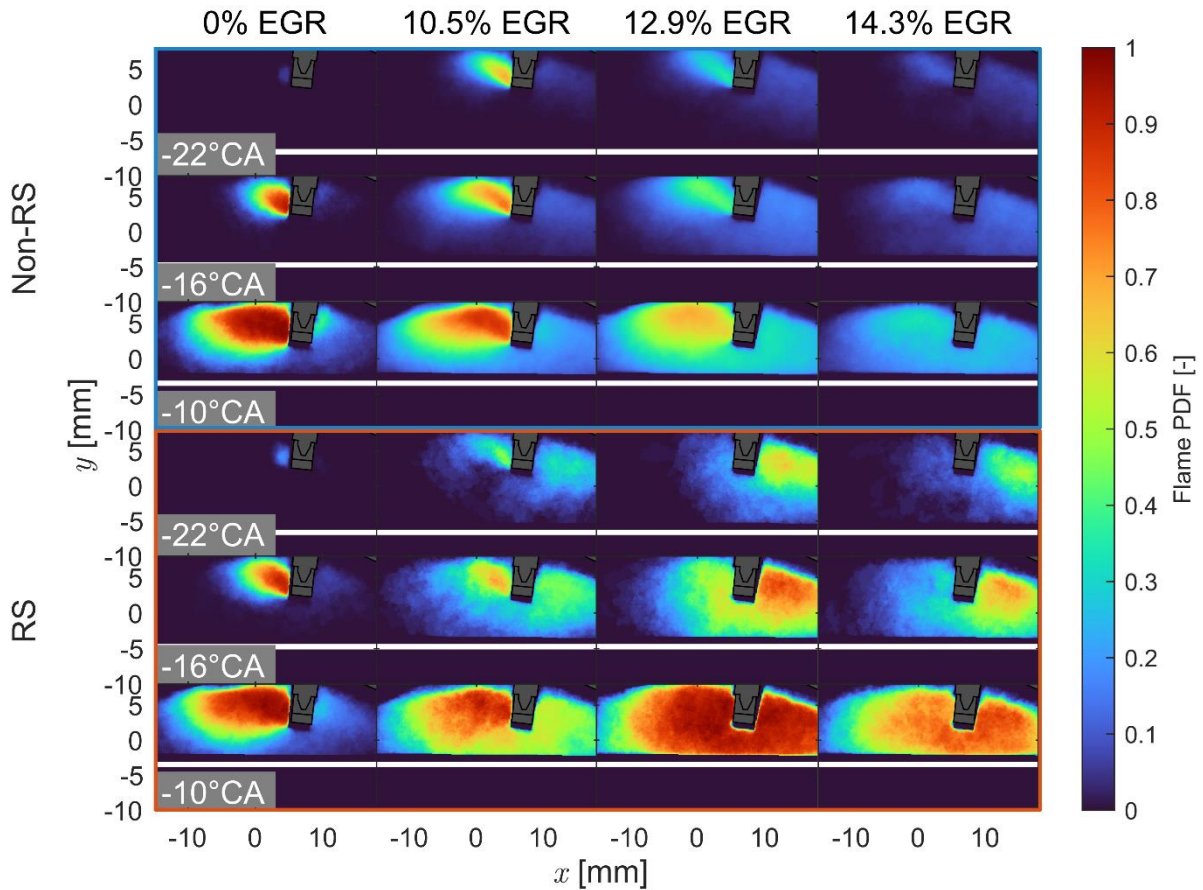


**Figure 12.** Evolution of the conditioned probability density function of the burned gas for cycles without and with restrike.

The conditioned PDFs of the binarized burned gas regions are displayed in Figure 12 with the piston position appearing in white. As is the case with the conditioned mean flow fields of 0% EGR, the flame PDFs of this case's non-RS and RS cycles appear similar. However, upon closer inspection, the RS cycles have slightly greater flame areas towards the left and more flames appearing to the right of the spark plug than those of the non-RS set. This agrees with the spark PDFs which showed further elongation for RS cycles towards the left and more extreme cycles with elongation towards the right. Although the majority of flames in both the RS and non-RS cycles for the 10.5% EGR OC propagate first towards the left, the RS cycles have many more flames growing around the spark in both directions as extremes to one direction or as larger flames by  $-10^{\circ}\text{CA}$ . In the case of 12.9% EGR and 14.3% EGR the majority of RS flames propagate first towards the right where the low velocity region of the tumble center remains (see Figure 9).



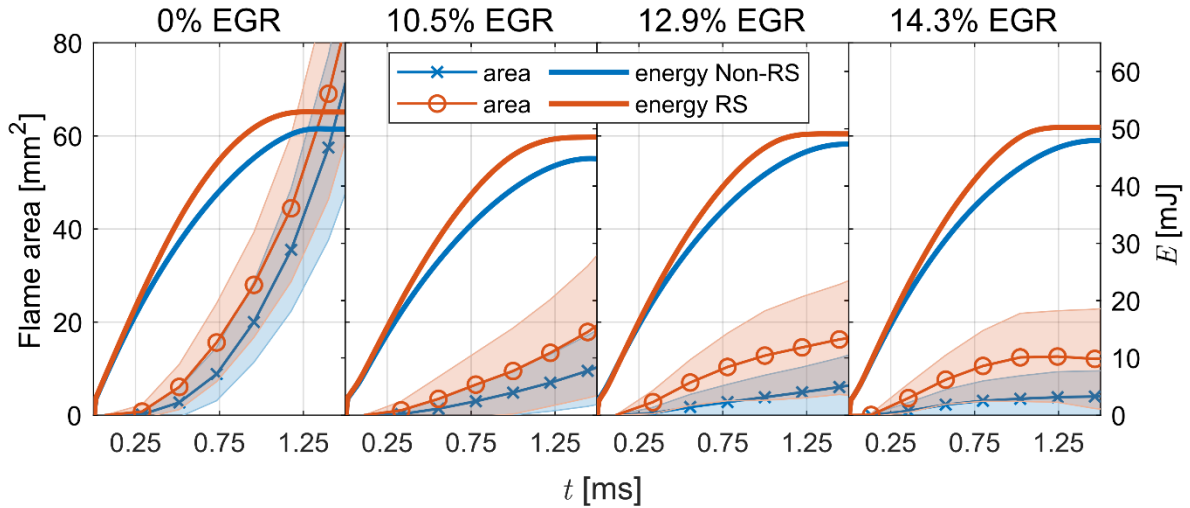


**Figure 13.** Conditional mean (solid lines with markers) and standard deviation (shaded area) of the cross-sectional area of the flame and the mean deposited spark energy (solid thick lines) after onset of spark for non-RS and RS cycles.

The mean and SD of the conditional flame areas for the non-RS and RS sets are shown in Figure 13 by the solid lines with markers and the shaded areas, respectively. Additionally, the conditional mean deposited spark energy is displayed for each OC. Due to the reflective spark plug and the Mie scattering strategy for flame detection, the initial flame kernel is not resolved. However, shortly after ignition, Figure 13 shows that RS cycles have larger flame areas indicating faster flame growth than non-RS cycles. In addition, the mean energy curves show a faster energy deposition for the RS cycles. In Figure 13, the time scales of the energy deposition and early flame growth may also be directly compared because the acquisition rates are sufficiently high and the processes occur at a similar rate. While the peaks of the mean energy traces occur within 1.5 ms of spark onset, flame growth continues for between  $\approx 2$  and 6 times longer (based on the different ignition timings until TDC). Nevertheless, within the time frame of the rapid deposition of spark energy, the early flame areas of RS cycles are still distinguishable from non-RS cycles, suggesting a relationship between the higher energies and faster flame growth with RS. This relationship can likely be attributed to two phenomena: first, the plasma elongation associated with the higher velocities across the spark plug gap of RS cycles leads to a larger ignition area along the plasma channel (as previously discussed, larger elongation is related to higher voltages and energies); and second, each RS causes an energy deposit in a volume with fresh unburned gas as the flame from the elongated spark flows downstream of the spark plug. Therefore, these phenomena likely result in an attached corrugated aspherical flame as each RS event adds to the flame volume and shape irregularity, while the high-velocity flow field forces the flame away from the spark plug gap, similar to the mechanism described by Drake et al.<sup>22</sup> and Dahms et al.<sup>14</sup>

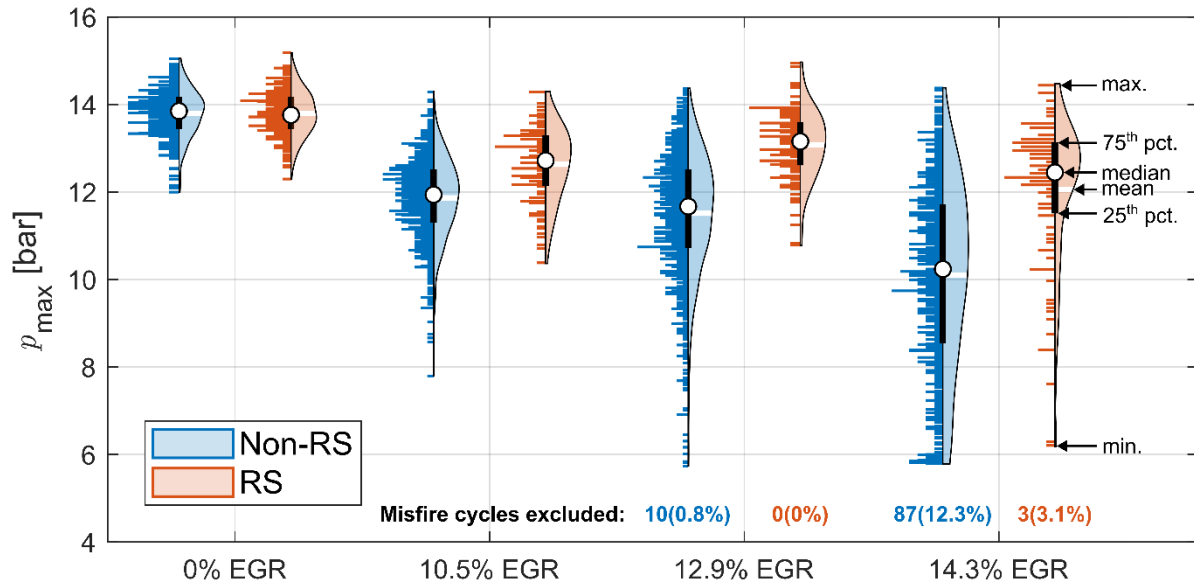


**Figure 14. Violin plot comparison of the maximum in-cylinder pressure for non-restrike cycles and restrike cycles with misfire cycles excluded.**

Overall, RS cycles have larger flame areas than non-RS cycles. Therefore, the final quantity of interest is the cyclical maximum in-cylinder pressure  $p_{\max}$ , a measure of CCV. Figure 14 displays violin plots of the  $p_{\max}$  of conditioned statistics for the non-RS and RS cycles at each EGR level. The violin plots were adapted using the MATLAB scripts of Bechtold<sup>36</sup> and show box plots of the conditioned samples (white circles: median, black rectangles: interquartile range, and black whiskers: maximum and minimum values) as well as the distribution of the samples as histograms and kernel density estimates (KDEs) and the mean of the sample (white horizontal lines, see right side of Figure 14 for summary of key components). The widths of the histograms and KDEs are normalized to the maximum of each sample and have the same maximum width for display on the same figure. The histograms represent each cycle of each sample, while the KDEs represent fitted distributions. In addition, misfires are excluded from the samples and the number of cycles and percentage of misfires in each sample is shown at the bottom of Figure 14. As in the conditional mean velocities in Figure 9 and the flame PDFs in Figure 12, the non-RS and RS sets of the  $p_{\max}$  for the 0% EGR condition do not differentiate significantly from one another. That means in this OC there is no significant correlation between RS and fast combustion. However, if the velocities would have greater cyclical variations (in magnitude and direction of velocity and in frequency of occurrence), the effect of the velocity would overcome the high flame speed associated with the undiluted mixture of the reactants and greater disparity would emerge. To the contrary, the EGR conditions each have larger flame areas and consequently higher  $p_{\max}$  when RS occurs. While the representative cycles of Section 3.2 only displayed increases of less than 5% of the  $p_{\max}$  of RS cycles over non-RS cycles, the statistics show increases of 6.5%, 13.0%, and 25.5% of the median  $p_{\max}$  for the 10.5% EGR, 12.9% EGR, and 14.3% EGR cases, respectively. Additionally, RS is related to lower cyclical variability due to generally smaller interquartile ranges and fewer extreme or misfire cycles. Consequently, with the given engine geometry and homogeneous conditions under higher dilution mixtures, greater horizontal velocities across the spark plug are desirable in order to achieve faster, more stable combustion.

## 4 Conclusions

In this work, the interaction between the in-cylinder velocity at ignition, the spark behavior, and the resulting flame propagation of a homogeneously mixed internal combustion engine with varying levels of EGR was investigated through simultaneous multi-parameter measurement techniques. Through

the use of EGR, the flame speed was decreased to induce a higher degree of cyclical variations as the effects of the in-cylinder velocity on the spark and combustion accordingly become more pronounced. Under such conditions, spark restrike (RS) was identified as a potential by-product of the higher CCV of the flow field and the hypothesis that RS is associated with faster combustion was confirmed. The strategy employed in this work of first examining single characteristic RS cycles to analyze the sparking and subsequent combustion behavior was then enhanced by using statistical approaches to substantiate the analysis. The main findings and conclusions from this work are summarized by the following:

- The velocity near the spark plug at the time of ignition determines not only the rate at which energy is deposited, but also the direction of the plasma elongation, the number of RS events, and the size and propagation of the early flame kernel.
- Although the conditioned statistics of RS and non-RS cycles of the 0% EGR case show the least absolute difference in terms of combustion speed, the individual cycle and the correlation analyses exhibited a significant role of the flow on the spark behavior.
- Under higher EGR conditions, RS tends to usually occur when there is a strong velocity in the positive  $x$ -direction across the spark gap, following the mechanism of fast combustion cycles presented by the authors in a previous study,<sup>25</sup> where propagation of the early flame kernel into a lingering tumble vortex to the right of the spark plug allows the flame to grow away from the relatively cold surfaces of the spark plug and the cylinder head, inducing faster combustion. Conversely, when the flow near the spark plug points mainly upward or to the left, the initial flame loses heat to the walls, slowing its growth.
- Given the operating conditions of higher dilution of the engine test stand investigated, RS enhanced combustion speed and stability significantly, rather than hindering it through blow-off.<sup>10</sup> This may indicate that flame growth in the relatively stagnant tumble region is not the only mechanism driving faster combustion, but rather higher and faster energy deposition over more volume in the cylinder associated with RS may also play a role.

As all phenomena in this work are related to the velocity field, stable and fast combustion under such high EGR conditions in this engine geometry can be facilitated through manipulation of the intake port geometry to achieve stronger horizontal flows across the spark gap. Such modifications would be necessary to achieve stable engine operation under higher EGR rates; however, more research on the wear and fouling of the spark plug under such proposed conditions is required due to the potential increase in energy flux associated with RS and the lower combustion temperatures of mixtures with high EGR. An additional future study could employ the same EGR conditions and ignition timings but with controlled laser ignition to rule out the CCV of energy deposition as a variable for the mechanism of faster combustion under higher EGR rates. Such an ignition strategy would also allow the measurement of the initial flame kernel immediately after ignition due to the absence of the reflective spark plug. Finally, a critical aspect of future work is the transferability of the mechanisms described in this study: first, to other conditions such as homogeneous lean mixtures or different fuels; then, to other engine configurations and geometries.

## Availability of Data Materials

Data are available upon request to Benjamin Böhm at boehm@rsm.tu-darmstadt.de.

## Author Contributions

All authors contributed to the study conception and design. A.D. and B.B. acquired funding. Experimental preparation and data collection were performed by C.W. and L.I. Data analysis, generation of figures, and the preparation of the first draft of the manuscript were performed by C.W. All authors commented on previous versions of the manuscript. The final discussion and analysis of results were performed by C.W and M.S. All authors read and approved the final manuscript.



## Funding

Support by Deutsche Forschungsgemeinschaft through FOR 2687 “Cyclic variations in highly optimized spark-ignition engines: experiment and simulation of a multi-scale causal chain”–project number 423224402 - is kindly acknowledged.

## COMPLIANCE WITH ETHICAL STANDARDS

### Conflict of Interest

The authors declare that they have no conflict of interest.

## REFERENCES

1. Deng J, Bae C, Denlinger A, et al. Electric Vehicles Batteries: Requirements and Challenges. *Joule* 2020; 4: 511–515.
2. Fontana G and Galloni E. Experimental analysis of a spark-ignition engine using exhaust gas recycle at WOT operation. *Applied Energy* 2010; 87: 2187–2193.
3. Ozdor N, Dulger M and Sher E. Cyclic Variability in Spark Ignition Engines A Literature Survey. *SAE Technical Paper 940987* 1994.
4. Heywood JB. *Internal combustion engine fundamentals*. Second edition. New York: McGraw-Hill Education, 2018.
5. Maly R and Vogel M. Initiation and propagation of flame fronts in lean CH<sub>4</sub>-air mixtures by the three modes of the ignition spark. *Symposium (International) on Combustion* 1979; 17: 821–831.
6. Lee MJ, Hall M, Ezekoye OA, et al. Voltage, and Energy Deposition Characteristics of Spark Ignition Systems. In: *SAE Technical Paper Series*, APR. 11, 2005: SAE International 400 Commonwealth Drive, Warrendale, PA, United States.
7. Shiraishi T, Teraji A and Moriyoshi Y. The Effects of Ignition Environment and Discharge Waveform Characteristics on Spark Channel Formation and Relationship between the Discharge Parameters and the EGR Combustion Limit. *SAE Int. J. Engines* 2016; 9: 171–178.
8. Yu X, Yang Z, Yu S, et al. Discharge Characteristics of Current Boosted Spark Events Under Flow Conditions. In: *Proceedings of the ASME Internal Combustion Engine Division Fall Technical Conference 2017: Presented at ASME 2017 Internal Combustion Engine Fall Technical Conference, October 15-18, 2017, Seattle, Washington, USA*, Seattle, Washington, USA, 10/15/2017 - 10/18/2017. New York, N.Y.: American Society of Mechanical Engineers.
9. Yang Z, Yu X, Yu S, et al. Impacts of Spark Discharge Current and Duration on Flame Development of Lean Mixtures Under Flow Conditions. In: *Proceedings of the ASME Internal Combustion Engine Fall Technical Conference -2018-: Presented at ASME 2018 Internal Combustion Engine Fall Technical Conference, November 4-7, 2018, San Diego, California, USA / sponsored by the Internal Combustion Engine Division, ASME*, San Diego, California, USA, 11/4/2018 - 11/7/2018. New York, N.Y.: American Society of Mechanical Engineers.
10. Sayama S, Kinoshita M, Mandokoro Y, et al. Spark ignition and early flame development of lean mixtures under high-velocity flow conditions: An experimental study. *International Journal of Engine Research* 2019; 20: 236–246.
11. Huang S, Li T, Ma P, et al. Quantitative evaluation of the breakdown process of spark discharge for spark-ignition engines. *J. Phys. D: Appl. Phys.* 2020; 53: 45501.
12. Fansler TD, Drake MC, Düwel I, et al. Fuel-spray and spark plug interactions in a spray-guided direct-injection gasoline engine. In: *Proceedings of the Seventh International Symposium on Internal combustion diagnostics*, Baden Baden, 18-19 May 2006, pp. 81–97. Mainz-Kastel: AVL Deutschland.
13. Peterson B and Sick V. High-Speed Flow and Fuel Imaging Study of Available Spark Energy in a Spray-Guided Direct-Injection Engine and Implications on Misfires. *International Journal of Engine Research* 2010; 11: 313–329.

14. Dahms RN, Drake MC, Fansler TD, et al. Understanding ignition processes in spray-guided gasoline engines using high-speed imaging and the extended spark-ignition model SparkCIMM. Part A: Spark channel processes and the turbulent flame front propagation. *Combustion and Flame* 2011; 158: 2229–2244.
15. Kawahara N, Hashimoto S and Tomita E. Spark discharge ignition process in a spark-ignition engine using a time series of spectra measurements. *Proceedings of the Combustion Institute* 2017; 36: 3451–3458.
16. Windarto C and Lim O. Spark discharge energy effect on in-cylinder characteristics performance of rapid compression and expansion machine with spark ignition direct injection strategy. *Fuel* 2023; 337: 127165.
17. Opacich KC, Ombrello TM, Heyne JS, et al. Analyzing the ignition differences between conventional spark discharges and nanosecond-pulsed high-frequency discharges. *Proceedings of the Combustion Institute* 2021; 38: 6615–6622.
18. van Mai T, Shy S and Chen Y-R. Single- and dual-channel nanosecond repetitively pulsed discharges at small and large spark gaps for turbulent premixed spherical flame initiation. *Proceedings of the Combustion Institute* 2022.
19. Jung D, Sasaki K, Sugata K, et al. Combined Effects of Spark Discharge Pattern and Tumble Level on Cycle-to-Cycle Variations of Combustion at Lean Limits of SI Engine Operation. In: *SAE Technical Paper Series*, APR. 04, 2017: SAE International400 Commonwealth Drive, Warrendale, PA, United States.
20. Tsuboi S, Miyokawa S, Matsuda M, et al. Influence of spark discharge characteristics on ignition and combustion process and the lean operation limit in a spark ignition engine. *Applied Energy* 2019; 250: 617–632.
21. Smith JD and Sick V. A Multi-Variable High-Speed Imaging Study of Ignition Instabilities in a Spray-Guided Direct-Injected Spark-Ignition Engine. In: *SAE Technical Paper Series*, APR. 03, 2006: SAE International400 Commonwealth Drive, Warrendale, PA, United States.
22. Drake MC, Fansler TD and Peterson KH. Stratified Ignition Processes in Spray-Guided SIDI Engines. In: *Proceedings of the Ninth International Symposium on Internal Combustion Diagnostics*, Baden Baden, 8-9 June, 2010, pp. 87–98. Mainz-Kastel: AVL Deutschland.
23. Fansler TD, Reuss DL, Sick V, et al. Invited Review: Combustion instability in spray-guided stratified-charge engines: A review. *International Journal of Engine Research* 2015; 16: 260–305.
24. Bode J, Schorr J, Krüger C, et al. Influence of the in-cylinder flow on cycle-to-cycle variations in lean combustion DISI engines measured by high-speed scanning-PIV. *Proceedings of the Combustion Institute* 2019; 37: 4929–4936.
25. Welch C, Schmidt M, Illmann L, et al. The Influence of Flow on Cycle-to-Cycle Variations in a Spark-Ignition Engine: A Parametric Investigation of Increasing Exhaust Gas Recirculation Levels. *Flow Turbulence Combust* 2023; 110: 185–208.
26. Baum E, Peterson B, Böhm B, et al. On The Validation of LES Applied to Internal Combustion Engine Flows: Part 1: Comprehensive Experimental Database. *Flow Turbulence Combust* 2014; 92: 269–297.
27. Schmidt M, Ding C-P, Peterson B, et al. Near-Wall Flame and Flow Measurements in an Optically Accessible SI Engine. *Flow Turbulence Combust* 2021; 106: 597–611.
28. Freudenhammer D, Peterson B, Ding C-P, et al. The Influence of Cylinder Head Geometry Variations on the Volumetric Intake Flow Captured by Magnetic Resonance Velocimetry. *SAE International Journal of Engines* 2015; 8: 1826–1836, <http://dx.doi.org/10.4271/2015-01-1697> (2015).
29. Welch C, Schmidt M, Keskinen K, et al. The Effects of Intake Pressure on In-Cylinder Gas Velocities in an Optically Accessible Single-Cylinder Research Engine. *SAE Technical Paper* 2020-01-0792 2020.
30. Renaud A, Ding C-P, Jakirlic S, et al. Experimental characterization of the velocity boundary layer in a motored IC engine. *International Journal of Heat and Fluid Flow* 2018; 71: 366–377.

31. The MathWorks, Inc. *MATLAB Function Reference: entropyfilt*. 2021b. Natick, MA, 2021.
32. The MathWorks, Inc. *Image Processing Toolbox Reference: bwskel*. 2022b. Natick, MA, 2022.
33. Wörner M and Rottenkolber G. Voltage rise anemometry in turbulent flows applied to internal combustion engines. *Exp Fluids* 2021; 62.
34. Chu H, Welch C, Elmestikawy H, et al. A Combined Numerical and Experimental Investigation of Cycle-to-Cycle Variations in an Optically Accessible Spark-Ignition Engine. *Flow Turbulence Combust* 2023; 110: 3–29.
35. The MathWorks, Inc. *MATLAB Function Reference: corrcoef*. 2021b. Natick, MA, 2021.
36. Bastian Bechtold. *Violin plots for Matlab*: Github Project, 2016.



## A.5 Paper V

### The Influence of Flow on Cycle-to-Cycle Variations in a Spark-Ignition Engine: A Parametric Investigation of Increasing Exhaust Gas Recirculation Levels

C. Welch, M. Schmidt, L. Illmann, A. Dreizler, B. Böhm: The Influence of Flow on Cycle-to-Cycle Variations in a Spark-Ignition Engine: A Parametric Investigation of Increasing Exhaust Gas Recirculation Levels. *Flow, Turbulence and Combustion* 110: 185-208 (2023) Springer Nature. <https://doi.org/10.1007/s10494-022-00347-5>

#### Paper V Permissions

Paper V is reproduced with permission from Springer Nature. Permission to include Paper V in this cumulative dissertation is also granted by the authors who hold the copyright under a Creative Commons Attribution 4.0 International License. To view a copy of this license, visit <https://creativecommons.org/licenses/by/4.0/>.

---

# DECLARATION ON THE CONTRIBUTION TO THE SCIENTIFIC PUBLICATION

## Erklärung zum Eigenanteil der wissenschaftlichen Veröffentlichung

Cooper Welch, M.Sc.

### PAPER

C. Welch, M. Schmidt, L. Illmann, A. Dreizler, B. Böhm: The Influence of Flow on Cycle-to-Cycle Variations in a Spark-Ignition Engine: A Parametric Investigation of Increasing Exhaust Gas Recirculation Levels. *Flow, Turbulence and Combustion* 110: 185–208 (2023). <https://doi.org/10.1007/s10494-022-00347-5>

### CO-AUTHORS

Marius Schmidt, M.Sc.  
Lars Illmann, M.Sc.

Andreas Dreizler, Prof. Dr.  
Benjamin Böhm, Dr.-Ing.

### INDIVIDUAL CONTRIBUTIONS

- **Cooper Welch**
  - Jointly conducted experiments with Lars Illmann.
  - Conducted processing and analysis of all data.
  - Main and corresponding author of the paper: performed literature research, generated all figures, and wrote the manuscript.
- **Marius Schmidt**

Assisted in conduction of experiments through advice from experience. Supported in the analysis and interpretation of the results and the proofreading of the manuscript. Jointly managed the rebuttal submission with Lars Illmann.
- **Lars Illmann**

Jointly conducted experiments with Cooper Welch. Supported in the interpretation of results and the proofreading of the manuscript. Jointly managed the rebuttal submission with Marius Schmidt.
- **Andreas Dreizler and Benjamin Böhm**

Provided resources for the conduction of the experiments. Supported in the interpretation and discussion of the results and the proofreading of the manuscript.

### OVERALL CONTRIBUTION OF COOPER WELCH

A leading role in the conduction of the experiments, data analysis and interpretation, and main author of the manuscript.

### USE OF PAPER CONTENTS IN OTHER DISSERTATIONS


This publication is not the subject of another ongoing or completed dissertation.

### SIGNATURES OF ALL AUTHORS

  
\_\_\_\_\_  
Cooper Welch

  
\_\_\_\_\_  
Lars Illmann

  
\_\_\_\_\_  
Marius Schmidt

  
\_\_\_\_\_  
Andreas Dreizler


---

Benjamin Böhm

# The Influence of Flow on Cycle-to-cycle Variations in a Spark-ignition Engine: A Parametric Investigation of Increasing Exhaust Gas Recirculation Levels

Cooper Welch\*, Marius Schmidt, Lars Illmann, Andreas Dreizler, Benjamin Böhm

Technical University of Darmstadt, Department of Mechanical Engineering, Reactive Flows and Diagnostics, Otto-Berndt-Str. 3, 64287 Darmstadt, Germany

\*Corresponding author: Cooper Welch, email: [welch@rsm.tu-darmstadt.de](mailto:welch@rsm.tu-darmstadt.de)

ORCID ID:

Cooper Welch: 0000-0001-9067-9405

Marius Schmidt: 0000-0002-5424-1251

Lars Illmann: 0000-0001-6907-0064

Andreas Dreizler: 0000-0001-5803-7947

Benjamin Böhm: 0000-0003-2654-6266

## ABSTRACT

Cyclic variability is investigated in an optically accessible single-cylinder spark-ignition research engine by introducing artificial exhaust gas in controlled amounts to the homogenous air-fuel mixture before ignition. A skip-fire scheme ensures the absence of internal exhaust gas recirculation (EGR) and allows the engine to be fired continuously for acquisition of large statistics. Four operating conditions ranging from a stable 0% EGR case up to a highly unstable extreme EGR case are analyzed to examine the increasing effects of homogeneous EGR on the cycle performance. To that end, high-speed measurements of the velocity field via particle image velocimetry and flame imaging in the tumble plane allow the determination of phenomena leading to various flame positions and sizes as well as faster and slower combustion cycles. Through extensive conditional statistical and multivariate correlation techniques, flames are found to be heavily influenced by large-scale velocity motion, especially with the presence of greater EGR which leads to lower flame speeds. The greater sensitivity of slower flames to variations in the velocity field manifests itself in an exponential increase in cyclic variability of the maximum in-cylinder pressure and causes misfire cycles where the flame is blown off or quenched at the cylinder roof. In the most extreme cycles at the highest EGR level, the state of the large-scale velocity structures at the time of ignition determines whether the flame propagates towards the center of the cylinder (and is blown off or quenched) or if the flame sustains growth by propagating within the lingering tumble vortex.

## KEYWORDS

Cycle-to-cycle variations, exhaust gas recirculation, early flame kernel, IC engine, multivariate statistics

## STATEMENTS AND DECLARATIONS

Open Access funding was provided by Projekt DEAL. Support by Deutsche Forschungsgemeinschaft through FOR 2687 “Cyclic variations in highly optimized spark-ignition engines: experiment and simulation of a multi-scale causal chain”—project number 423224402 - is kindly acknowledged. The authors have no competing interests nor conflicts of interest to declare.



# 1 INTRODUCTION

The need for a transition to cleaner energy systems has never been clearer as average global temperatures have steadily increased over the last 4 decades leading to dangerous changes in the earth's climate [1]. In 2020, the transport sector alone accounted for 20% of greenhouse gas emissions as CO<sub>2</sub> [2], with nearly half of that attributed to light duty vehicles [3]. Although the market for electric vehicles is growing rapidly, the industry and global infrastructure to support the industry is still in its infancy. Therefore, highly efficient internal combustion (IC) engines cannot be completely ruled out for passenger vehicles in the near future.

Researchers focusing on cleaner technologies, such as the retrofitting of current engines with viable e-fuels or the development of engines using hydrogen fuel, are faced with significant challenges related to reliability, safety, availability of fuels, and more importantly for the environment, toxic gas emissions. Exhaust gas recirculation (EGR) in spark-ignition (SI) IC engines offers the advantage of reducing fuel consumption via the reduction of throttling loss at part-load conditions as well as reduced flame temperatures leading to a reduction of thermal NO<sub>x</sub> [4]. However, the benefits of decreasing fuel consumption and NO<sub>x</sub> emissions are counterbalanced by an increase in cycle-to-cycle variations (CCV) eventually leading to an exponential growth in cyclic instability.

Understanding the causes of CCV in SI engines has long been the focus of researchers in the pursuit of further optimizing modern engines [5]. With the dawn of significant improvements in advanced imaging, laser, and computing technologies over the last decade, engine CCV has been studied with detailed spatial and temporal scales. Recent experimental studies have related the in-cylinder velocity to fired engine CCV [6–14] using high-speed particle image velocimetry (PIV) combined with other techniques such as in-cylinder pressure measurements as well as flame and spark imaging. In particular, Buschbeck et al. and Zeng et al. studied homogenous mixtures with varying equivalence ratios to examine the influence of the flame speed on cyclic performance; it was shown that large-scale flow structures can have a significant effect on the flame development and subsequent combustion speed, a finding which is amplified when the flame speed is slower [6, 10]. The availability of larger sets of highly resolved engine data has also allowed for the use of advanced statistical techniques to study CCV. The investigation of conditional statistics [15, 16], multivariate statistics [9, 17], flow-feature correlations [8, 11, 12], and machine learning techniques [13, 14, 18, 19] have shed new light on the causal chain of engine CCV.

This paper aims to combine the strategies of conditional statistics with multivariate analysis using a large data set obtained from parametric high-speed PIV and flame imaging experiments with increasing levels of homogeneously-mixed external EGR to further delineate the causal chain for fired CCV in SI engines. First, the experimental setup and boundary conditions are described. Next, the effects of EGR on the engine performance, average flow field, and early flame kernel development are examined to establish a characterization of the parametric operating points. Then, several flame features are defined and evaluated using a multivariate correlation approach and a relative feature importance analysis. With the highest correlated flame feature identified, the investigation is narrowed down to a correlation field and conditional statistical analysis to identify the cause for such correlations between the flame and large-scale flows. Finally, a similar correlation field and conditional statistical analysis technique is used to examine the causal chain for misfires and cycles of very fast combustion in the highest EGR case.

## 2 EXPERIMENTAL SETUP

### 2.1 Engine Test Bench and Boundary Conditions

The single-cylinder optically accessible research engine test stand at the Technical University of Darmstadt (*Technische Universität Darmstadt*) was employed in this investigation. The engine's optical

access is granted through a quartz glass flat piston (with a Bowditch piston extension) and quartz glass cylinder liner with a pent roof. In this work, a well-documented spray-guided cylinder head with a compression ratio of 8.7:1 was used [20–22]. The engine test stand has been designed to consistently operate with precisely controlled conditions to investigate phenomena in SI IC engines [23], namely in this study, the effect of external homogeneous EGR on combustion and CCV. To that end, a gas mixture system (GMS) was used to mix dry air (1.8% relative humidity) with the desired amount of pure nitrogen and carbon-dioxide gas upstream of a storage plenum before the gas mixture entered a noise reduction plenum and finally the intake manifold. Figure 1(a) shows a simplified schematic of the GMS, the noise reduction plenum, the intake manifold, and the engine cylinder. Temperature and pressure probes are located throughout the test stand and are displayed in relevant locations in Figure 1(a). Air seeded with silicone oil droplets (see sec. 2.2 Optical Diagnostics) was introduced just after the noise reduction plenum to be used for the PIV and flame imaging. In addition, isoctane fuel was injected far upstream of the cylinder to allow sufficient evaporation and homogeneous mixing with the gas mixture.

Four operating conditions (OCs) of increasing EGR were employed to compare the effects of EGR in a completely homogeneous environment during engine operation. The four OCs are based on the standard D-fired OC of the Darmstadt engine [24], which has a part-load intake pressure of 0.4 bar and a speed of 1500 rpm. The conditions in this work consist of a highly stable OC of 0% EGR, a stable OC of 10.5% EGR, an unstable OC of 12.9% EGR, and a highly unstable OC of 14.3% EGR. Here, stability is defined by the coefficient of variance (COV) of the maximum in-cylinder pressure  $P_{cyl,max}$ . The latter 2 OCs have higher COVs which also includes the misfire cycles, here defined as cycles whose gross indicated mean effective pressure (IMEP<sub>g</sub>) were negative. Table 1 summarizes the differences in the boundary conditions for each OC. A skip-fire scheme was used in which for every combustion cycle the 6 following cycles were not ignited to allow residual exhaust gases to fully leave the system before the next ignition. Since this skip-firing scheme eliminated internal EGR due to valve overlap and other possible causes, the EGR OCs' boundary conditions significantly changed from the standard D-fired OC. To achieve stable combustion with increasing EGR levels, less fuel had to be injected to achieve an equivalence ratio of 1 and the ignition timing had to be moved earlier, whereby the ignition timing  $t_{spark}$  shown in Table 1 was optimized such that the crank angle at 50% mass fraction burned was 8°CA (degrees crank angle relative to compression TDC), further reducing influencing factors for CCV.

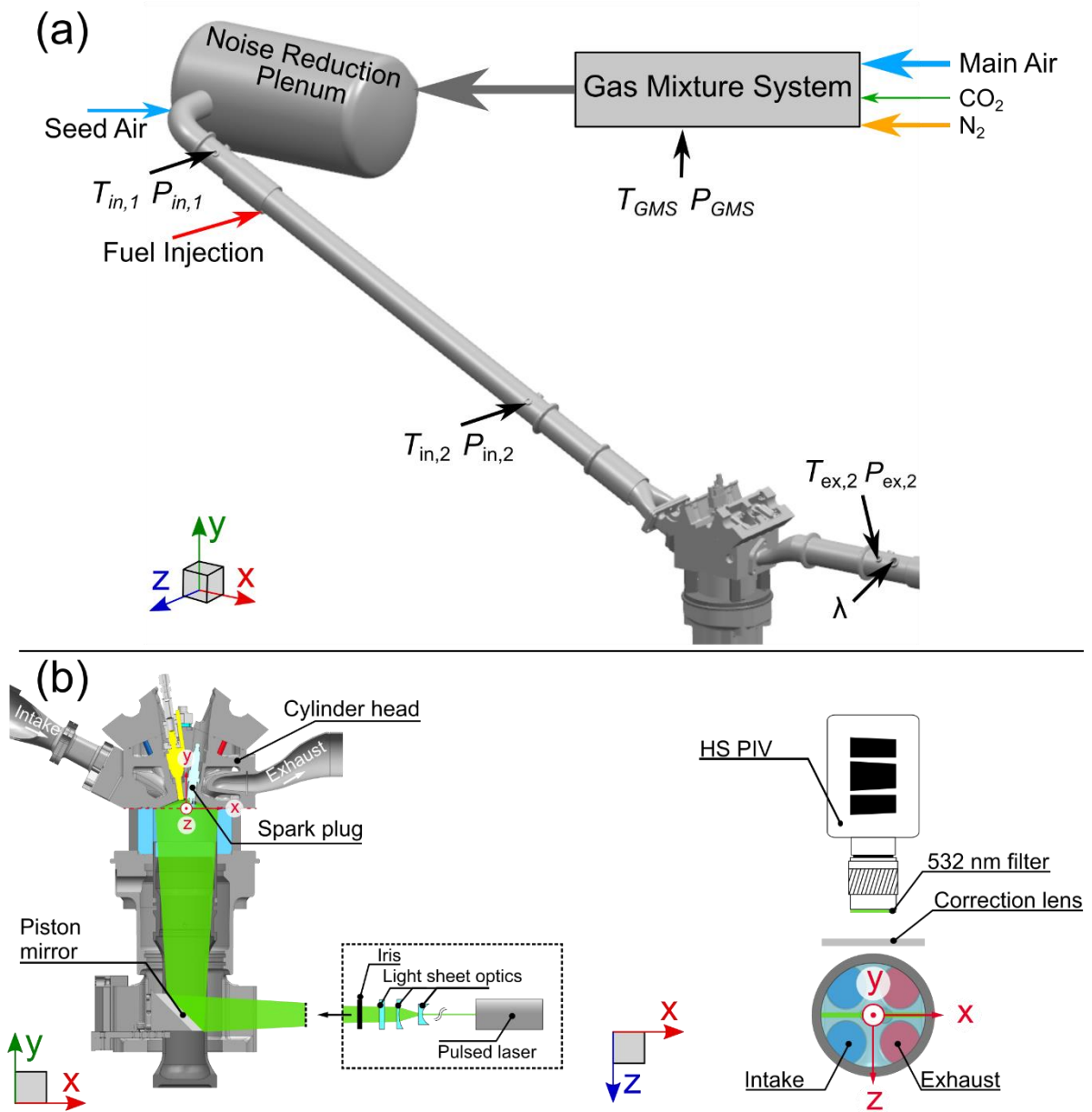


Figure 1 (a) Engine test bench and boundary condition probe locations. (b) Optical setup for PIV and flame imaging.

**Table 1. Experimental boundary conditions. Combined standard uncertainties are indicated in parentheses.**

Condition	No EGR	Medium EGR	High EGR	Extreme EGR
EGR [%]	0(0)	10.5(0.4)	12.9(0.4)	14.3(0.4)
$\dot{m}_{\text{air}}$ [kg/h]	7.33(0.08)	6.63(0.08)	6.48(0.08)	6.40(0.08)
$\dot{m}_{\text{N}_2}$ [kg/h]	0.00(0)	0.651(0.035)	0.810(0.035)	0.901(0.035)
$\dot{m}_{\text{CO}_2}$ [kg/h]	0.00(0)	0.174(0.006)	0.216(0.006)	0.241(0.006)
$\dot{m}_{\text{fuel}}$ [kg/h]	0.489(0.012)	0.434(0.012)	0.428(0.012)	0.418(0.012)
$t_{\text{spark}}$ [°CA]	-24.6	-39.0	-47.0	-51.2
$\lambda_{\text{calc}}$ [-]	1.00(0.02)	1.02(0.02)	1.01(0.02)	1.02(0.02)
Speed [rpm]	1500	1500	1500	1500
$P_{\text{in},2}$ [bar]	0.400(0.001)	0.401(0.001)	0.402(0.001)	0.403(0.001)
Cycles [-]	483	966	1288	805
$T_{\text{in},1}$ [K]	305.0(0.5)	305.1(0.5)	303.9(0.5)	303.5(0.5)
$T_{\text{in},2}$ [K]	316.9(0.5)	317.1(0.5)	316.0(0.5)	315.7(0.5)
$T_{\text{ex},2}$ [K]	484.0(0.5)	456.7(0.5)	453.3(0.5)	450.5(0.5)
$P_{\text{cyl,max-COV}}$ [%]	3.82	7.75	12.8	25.1
Misfires [%]	0	0	0.78	11.2

## 2.2 Optical Diagnostics

Both optical techniques in this study involve the planar illumination of seeded oil droplets. Particle image velocimetry in the symmetry (tumble) plane was used to measure the in-cylinder velocity from  $-180^\circ\text{CA}$  to  $-4^\circ\text{CA}$  (minus signifies before compression TDC) in increments of  $2^\circ\text{CA}$ . Figure 1(b) shows a schematic of the optical setup combined with the cross-sectional view of the engine in the symmetry plane as well as a top view of the imaging system. To acquire high-speed PIV in the engine, silicone oil droplets ( $\approx 0.5 \mu\text{m}$ , DOWSIL 510, Dow Corning) were nebulized in air by a Palas AGF 10.1 seeder and introduced into the intake pipe immediately after the noise reduction plenum (see Figure 1). The oil particles were then illuminated by two Nd:YVO<sub>4</sub> laser sheets (FWHM  $\approx 800 \mu\text{m}$ ,  $200 \mu\text{m}$  at  $-90^\circ\text{CA}$  and  $-30^\circ\text{CA}$ , respectively) with optimized time separation  $dt$  between laser pulses ( $dt$  ranged from 18 to 32  $\mu\text{s}$ ). The planar Mie scattering of droplets was captured using a Phantom v2640 high-speed CMOS camera equipped with a 180 mm Sigma lens ( $f/5.6$ ), a 532 nm bandpass filter, and a correction lens ( $f = +2000$ , to counteract astigmatism due to the curvature of the cylinder glass), as displayed in Figure 1(b). Finally, for each measurement day, a series of target images was captured, whereby a 058-5 dual-plane calibration target (LaVision) was placed inside the engine and imaged to provide scaling and dewarping to the raw images in processing.

As previously mentioned, image pairs were captured from  $-180^\circ\text{CA}$  to  $-4^\circ\text{CA}$  at every second CAD, resulting in a measurement speed of 4.5 kHz. For the flame imaging, the second frame of each image pair was used to extract the burnt gas areas where the oil droplets were evaporated by the flame and the Mie scattering signal is absent. Although this is a measurement of the burnt gas region and not a direct measurement of the flame, it serves as an indicator of the flame location. Therefore, extracted burnt gas regions will be referred to as the flame for the remainder of this work.

## 2.3 Data Processing

Particle image velocimetry vectors were calculated using the commercial software DaVis 10.1.2 (LaVision). First, images were masked to remove reflective objects, such as the spark plug and cylinder roof. The image pairs were run through a multi-pass cross-correlation vector calculation program consisting of perspective correction (using a 3<sup>rd</sup> order polynomial based on calibration target images), 2 initial passes of interrogation window size  $64 \times 64$  with 50% overlap, then 2 final passes of size  $32 \times 32$  with 75% overlap. After each pass, vector post-processing, namely a peak ratio criterion of 1.3 was used to remove vectors whose first and second correlation peaks were below 1.3, a universal outlier detection consisting of a sliding median filter of size 7 vector  $\times$  7 vector was used, and finally a removal criterion of size 5 was used, meaning if less than 5 vectors are available out of a window overlap group, the entire group is removed.

Flame images were binarized using an in-house code developed in MATLAB (version R2021b). To achieve flame binarization from PIV images, the second image of each pair beginning from the start of ignition until  $-4^\circ\text{CA}$  was selected. Then a mask was used to remove reflective surfaces as with PIV processing. The mask for the flame imaging was more conservative than with PIV because near the cylinder walls reflections decrease the signal-to-noise ratio, making it more difficult to discriminate between flame and particle signals. Next, flame images were separated by cycle and the binarization algorithm was used on each cycle. The binarization algorithm first normalizes all images in a cycle by dividing each pixel's intensity by the maximum cyclic intensity. Then a sliding entropy filter of size  $5 \text{ px} \times 5 \text{ px}$  is applied, which outputs the entropy value of the surrounding pixel's neighborhood [25]. The next step divides the filtered images of a cycle by the first filtered image without a flame. Since flame images are divided by images without flames, pixels below a threshold criterion of  $< 1$  signify burnt gas or a flame. Then remaining pixels are set to a value of 1, before undergoing an erosion, which removes pixels along the edges of remaining structures using a disk shape with a radius of 4 pixels. Then an area criterion of 200 pixels is applied, which removes flames smaller than 200 pixels in size. Finally, dilation of the same size as the erosion is applied to restore the flames to their original sizes and all holes within a flame are filled. Although the flame front and detailed wrinkling cannot be accurately captured with such an evaporation method (also due to the erosion and dilation processing steps), the bulk of the burnt gas region and flame curvature is well-captured and will be assumed to represent the cross-sectional flame for this work.

Further processing and generation of plots and figures was conducted using MATLAB (version R2021b) and some post-processing, for example, combining plots, was done using Inkscape (version 1.1.2).

## 3 RESULTS

### 3.1 Effect of EGR on Performance and Flow

#### 3.1.1 In-cylinder Pressure and Temperature

A characterization of the four OCs with varying levels of external EGR is required before further analysis of the flame and flow can be done. Figure 2(a) displays the mean and standard deviation (std) of the measured in-cylinder pressure  $P_{\text{cyl}}$  vs. crank-angle-degree (CAD). The mean pressure is represented by the solid lines and the std by the shaded areas. The pressure traces reveal that the maximum pressure  $P_{\text{cyl,max}}$  for each condition is relatively well phase-locked. This is due to the spark timing optimization, which was conducted to ensure that 50% mass fraction burned occurred at  $8^\circ\text{CA}$  for each OC as the combustion slows down significantly with the introduction of EGR. While this leads to varying thermodynamic and flow conditions near the spark plug at the time of ignition for each OC, a basis for comparison must be established when defining OCs. One effect of employing different spark timing can be observed by comparing the exhaust temperature  $T_{\text{ex},2}$  (Table 1), which shows that earlier spark

timing and increasing EGR leads to lower exhaust temperatures; this is a decrease of 6% from no EGR to 10.5% EGR. If the spark timing were left constant, then the higher EGR cases would not properly burn and it would be impossible to analyze the relationships between the early flame and the flow field. Finally, it should be noted that for the 14.3% EGR OC, it was impossible to fully optimize the spark timing because the number of misfires increased exponentially when the spark timing was moved any earlier. A further observation that can be made from Figure 2(a) is a trend of decreasing maximum pressure  $P_{cyl,max}$  and an increase in variation as EGR increases. This is in line with the decreasing  $T_{ex,2}$  with increasing EGR.

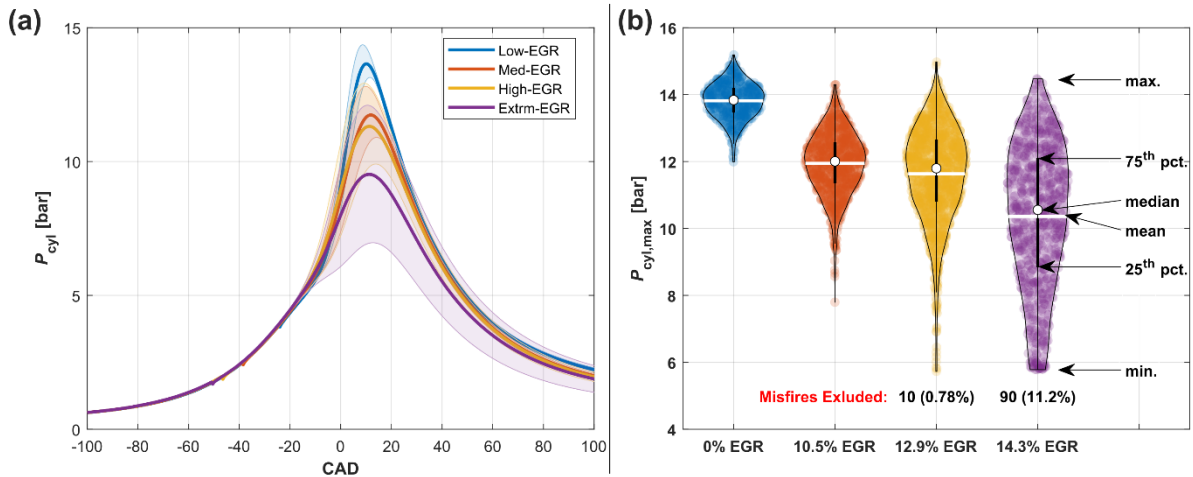


Figure 2. (a) Mean and standard deviation (shaded area) of  $P_{cyl}$  for each EGR rate (misfires included). (b) Violin plot of  $P_{cyl,max}$  for each EGR rate.

To further compare the OCs to one another, especially in relation to their variability, a so-called violin plot of the  $P_{cyl,max}$  is displayed in Figure 2(b) and was rendered using code from [26]. The violin plots shown combine conventional box plots (white circle: median, black rectangle: inter-quartile range, and black whiskers: maximum and minimum values), with the kernel density estimation (KDE) of the distribution of the  $P_{cyl,max}$ , represented by the shape and outline of the colored *violins* (scaled to the same maximum width and mirrored along the center line, respectively), and the scattered data (color-shaded circles), which represent the corresponding  $P_{cyl,max}$  values where they occur along the y-axis, randomly distributed along the x-axis within the bounds of the *violins*. In addition, the mean  $P_{cyl,max}$  is represented by the white lines, and coincides very well with the median. Such a plot shows a more complete representation of the in-cylinder pressure variation than the pressure trace because it provides context for the high stds shown in Figure 2(a). All OCs exhibit mono-modal, almost normally distributed KDEs. The inter-quartile range and spread of the KDE increases steadily from the no-EGR to the 14.3% OC, while the median and mean decreases. The distributions of maximum in-cylinder pressures are negatively skewed, which is evident in the longer tail of low pressures, even though misfire cycles are excluded. Notably, the upper bound of pressures is higher for the 12.9% and 14.3% than for the 10.5% OC. This is likely an effect of the earlier ignition timing, which allows cycles with optimal conditions for flame growth, such as ideal flow structures and early flame positions, to reach higher cylinder pressures as the volume decreases during late compression. This scenario occurred less frequently in the cases of low CCV because the optimized ignition timing (using the mean of hundreds of cycles) was more representative of all the cycles.

### 3.1.2 Mean Velocity

The prominence of extreme cycles for the higher EGR OCs and the large quantity of cycles acquired allows for conditional statistical analysis to be conducted to aid in the understanding of cyclic variations within each OC. However, first the velocity field before ignition should be characterized to discern the

effects of EGR on the flow field. Since solely the intake gas composition is changed between different OCs and the engine is operated in a skip-fire mode with 6 motored cycles prior to each analyzed fired cycle, no significant effect of the gas composition on the average flow field is expected. Figure 3 shows the mean velocity field for each OC during the compression stroke at  $-90^\circ\text{CA}$  and at their respective ignition timing. The multi-colored colormap is chosen to help convey the lack of contrast between velocity magnitudes of each case at  $-90^\circ\text{CA}$ . In addition, the streamlines represent the flow direction and show that the velocities remain the same. These flow fields show that on average, the amount of EGR and the resulting slightly different engine temperatures do not have a significant effect on the in-cylinder velocity. Although the flow field during compression is unaffected by the gas composition, the mean velocity at the time of ignition does vary as the piston position and speed is different at the distinct ignition timings of each OC (lower panel of Figure 3).

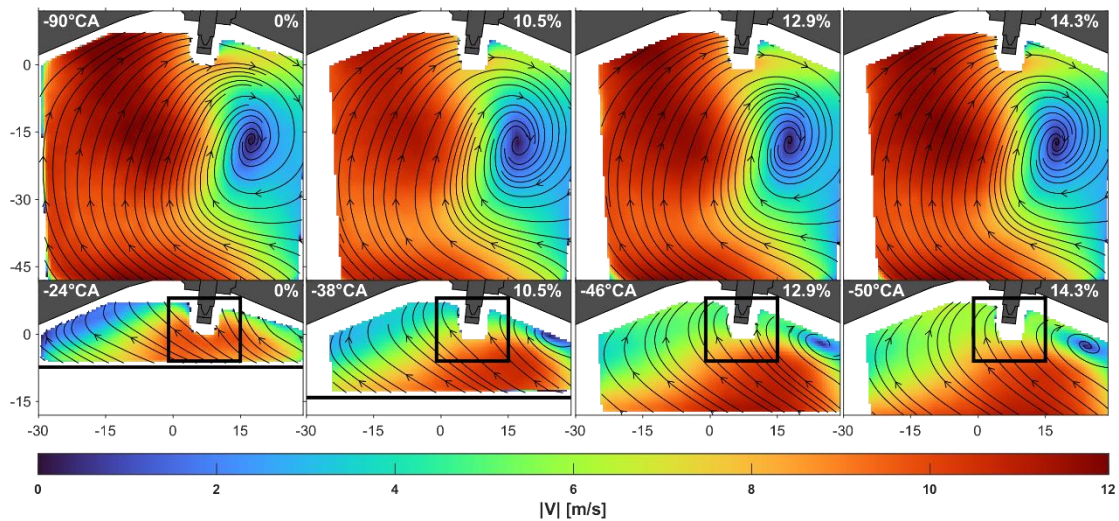


**Figure 3. Mean velocity fields for each EGR case during the compression stroke ( $-90^\circ\text{CA}$ ) and at the respective time of ignition (lower panel). The velocity magnitude is represented by the same color map and streamlines indicate the flow direction. The black square in the lower panels represents the region used to compute the mean velocity shown in Figure 6.**

### 3.2 Effect of EGR on the Flame

Although the different EGR levels have no significant effect on the mean in-cylinder velocity, the combustion is greatly affected by the in-cylinder conditions at ignition, as evidenced by the decreasing flame speed, in-cylinder pressure, and temperature and by the increasing variance of the pressure with increasing EGR levels. To examine the differences in combustion, the first approach is to investigate the early flame at each EGR level. Figure 4 shows the spatial probability, or probability density function (PDF), of flames at early combustion for each OC. The PDF is calculated using the entire sample of each case; therefore, a value of 1 means all cycles contain a flame at that pixel position. Although the different ignition times cause the flames to be in different stages of combustion at the same CAD for different OCs, towards the end of compression the kernel sizes become more similar. With the increase in CCV and misfire at higher EGR rates comes a decrease in the flame PDF. In addition, the presence of EGR increases the likelihood of a flame to propagate to the right of and below the spark plug; whereas for the 0% EGR case, most of the flames propagate towards the center of the cylinder until very late in the compression when the flames begin to grow around the spark plug. This exemplifies two phenomena: first, the direction of the flame propagation coincides with the mean flow direction at the time of ignition shown in the lower panels of Figure 3. The preferential, often unidirectional propagation away from the spark plug may also be augmented by heat losses at the spark plug. Second, the faster flame speed of the no EGR case leads to a smaller influence of flow variations near the spark plug at the time of ignition and early flame growth, resulting in fewer variations of the flame position.



On the contrary, with increasing EGR and decreasing flame speed, the flame's position is more heavily affected by convection as the flame is influenced by the clockwise tumble motion displayed in Figure 3. Furthermore, since there are more flames located below the spark plug with increasing EGR, there is likely a link to the extreme cycles associated with the more CCV-driven higher EGR cases which have some cycles with much faster combustion, as indicated by the violin plot in Figure 2(b). Finally, the 14.3% EGR case at  $-10^{\circ}\text{CA}$  highlights this case's instability since the flames are relatively evenly spread out, but not above 50% probability.

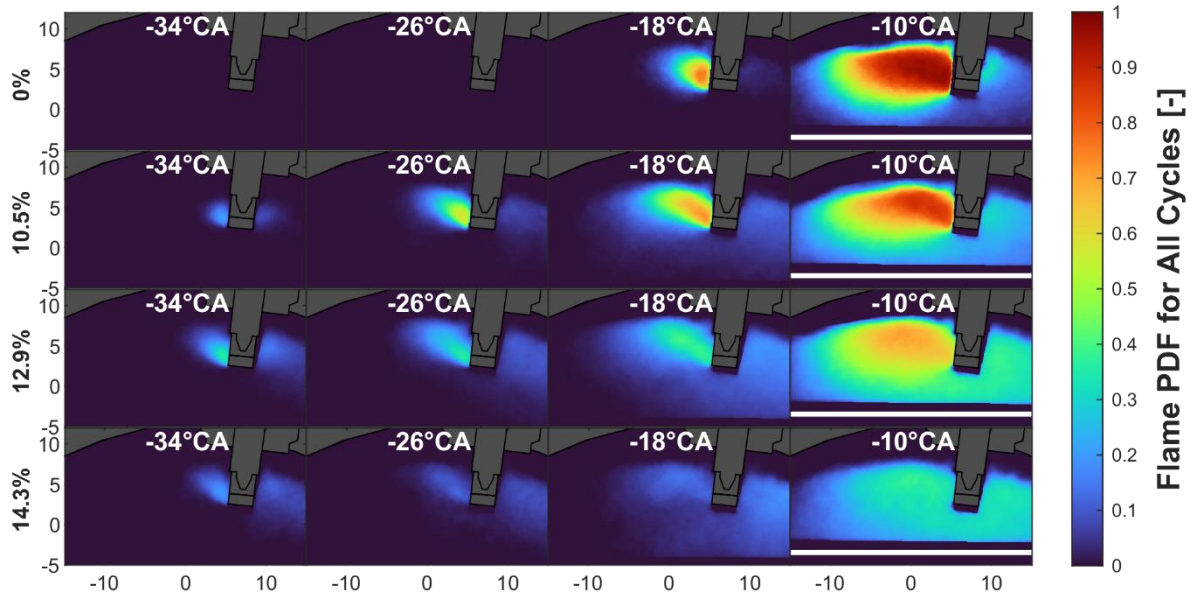


Figure 4. Spatial flame probability (PDF) over all cycles for each level of EGR.

To distinguish the flames between fast and slow combustion cycles, Figure 5 displays the PDF of low-speed cycles (LC), high-speed cycles (HC), and all cycles at  $-18^{\circ}\text{CA}$ . In this case, LC and HC are defined as the 10% of cycles with the lowest and highest  $P_{\text{cyl,max}}$ , respectively.  $-18^{\circ}\text{CA}$  was selected to allow comparison of the early flames of each OC as they appear to have reached relatively similar development at this time. It is unsurprising that for 0% EGR both LC and HC have similar flame PDFs at  $-18^{\circ}\text{CA}$  since this is a very stable OC. This remains the case for 10.5% EGR with some HC cycles exhibiting flames surrounding the spark plug, a configuration which allows flame growth in all directions. For the 12.9% case, there are 10 cycles with misfire out of the sample of 1288 cycles, so the low flame density in the LC sample reveals very slow combustion for the remaining 119 cycles and a tendency for the flame to propagate towards the center of the cylinder. On the HC side, 30% of the flames nearly cover the entire field of view (FOV) shown at  $-18^{\circ}\text{CA}$  and over 50% appear to the immediate left and right of the spark plug, showing the stark contrast between LC and HC flames. Furthermore, more flames appear to the right of the spark plug than to the left, which is linked to the greater influence of the flow on the flame propagation and a higher tendency of the flow near the spark plug to move towards the right at ignition (compare Figure 3) when compared with cases of lower EGR. Finally, for the 14.3% EGR case, there are 90 misfire cycles which explains the absence of flames on the LC side, while for HC, there is an even distribution of flames all around the spark plug, with a few more appearing to the right.



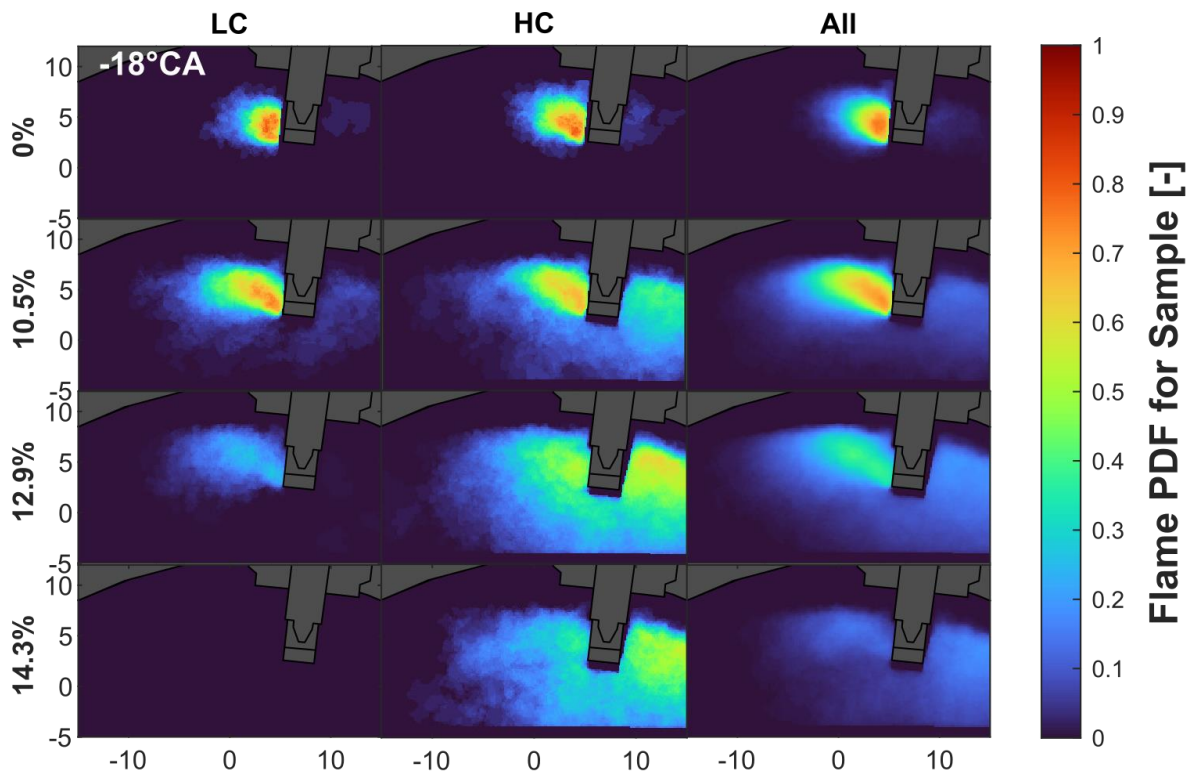


Figure 5. Spatial flame probability over selected samples at  $-18^\circ\text{CA}$ . HC and LC represent the probability over the 10% highest and lowest pressure cycles, respectively.

Figure 6 displays the mean flame centroid position for HC and LC cycles over all crank angles (indicated by the color bars) from ignition until  $-4^\circ\text{CA}$ . The left column represents LC and HC selected using the median  $P_{\text{cyl,max}}$  as the criterion, meaning half of the cycles are LC and the other half are HC, while the right column uses the 10% lowest and highest  $P_{\text{cyl,max}}$  cycles as its criterion for separation. The LC centroid trajectories are represented by the cool colormap, while the HC are represented by the warm colormap. In addition, blue (LC) and red (HC) vectors stemming from the first centroid at ignition represent the mean velocity in the black squares shown in Figure 3 at the time of ignition. The arrow directions indicate the actual mean velocity directions in the square region and the arrow lengths represent the magnitude of the velocity (also displayed in the top left corner of each panel). When comparing trajectories of increasing EGR (with the exception of the 14.3% case), the difference between LC and HC increases, and this is also amplified when examining the extreme LC and HC trajectories on the right. This is unsurprising since the CCV increases greatly with more EGR. In addition, HC trajectories tend to be located further from the cylinder roof than for LC because they represent more even propagation throughout the FOV. Another important phenomenon to note is that with increasing EGR the centroids shift from beginning from the left of the spark plug to the right. While it was possible to observe a trend of some flames beginning to grow to the right of the spark plug in Figure 4 and Figure 5, it seemed that this higher population of flames to the right of the spark plug was simply due to more even and faster propagation of the flame. However, Figure 6 shows that this trend is skewed towards the right of the spark plug, meaning many flames either begin to the right, or first appear to the right of the spark plug as they sporadically come in and out of the symmetry plane, then they propagate to the left of and surrounding the spark plug within this plane. This trend in the trajectory beginning correlates with a shift in the average velocity around the spark plug, as the arrows rotate clockwise with increasing EGR and as a consequence thereof, with earlier ignition timing. In addition, the LC centroid trajectories support the PDFs in Figure 5 in that slower combustion cycle flames tend to be convected to the left and upward. The parametric increase in EGR in this study shows how convection begins to play a bigger role in the flame's development since other complex

phenomena such as inhomogeneities in the mixture and gas composition are removed due to the experimental boundary conditions. Although the vectors in Figure 6 do not appear to differ too greatly from LC to HC cycles, likely due to the large sampling region dulling local flow phenomena, some differences emerge: while a strong mean flow towards the left of the spark plug seems to aid combustion in the 0% OC, the change in general flow direction for the higher EGR OCs alternates this relation and a weaker flow, which is less likely to convect the flame towards quenching-relevant geometry, like the spark plug stem and cylinder head, and more likely to convect the flame with the tumble, is beneficial for faster combustion. In the highest EGR case, which has the greatest amount of instability, the velocity magnitude near the spark plug for LC is 37% (65% for the extreme cycles on the right) greater than for HC and is directed more toward the left. Interestingly, the general tumble trajectory does not change much for the median LC and HC cases despite these velocity differences, while the extreme case on the right leads to misfire in all LC cycles. Since there appears to be a correlation between the flame, the flow, and the in-cylinder pressure, these aspects are further explored in the next section to elucidate the mechanisms leading to IC engine CCV.

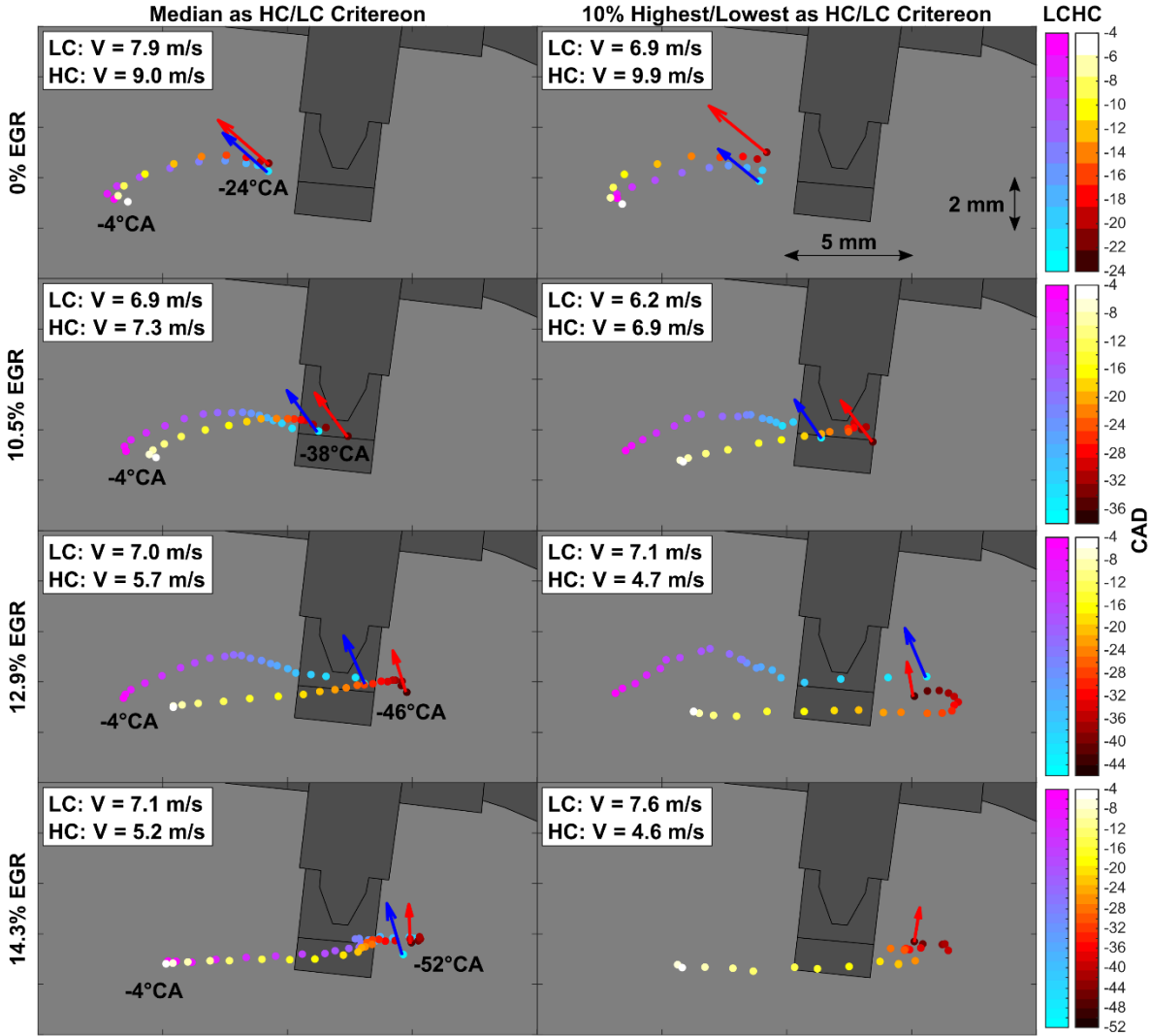


Figure 6. Calculated mean centroid of the flame over time for each EGR rate using the median (left) and 10% extreme cycles (right) as the HC/LC criterion. LC and HC cycles are represented by the blue-pink (cool) and black-red-white (warm) color bars, respectively.

### 3.3 Flame Correlations

#### 3.3.1 Definition of Flame Features

Rather than employing machine learning (ML) methods requiring hundreds [14] or several thousand [13] cycles to predict CCV, this work proposes the use of the correlation between several flame features and the flow field to select specific OCs and features to closer analyze the relationships between the flame, flow, and CCV. Building from the feature importance analysis allowed by the decision tree-based ML models used in the same engine for flames of a full-load OC [14], this work uses the 10 features with the highest calculated importance to examine their relevance in the homogenous EGR OCs. Table 2 lists the flame features used in this work with the previously used names given by [14] and new descriptive names. As in the previous work using only flame images for analysis [14], each feature represents one calculated quantity for each flame image, for example, centroidX is the x-coordinate of the centroid for the flame of one cycle at one CAD and can be correlated to other quantities of the same cycle such as  $P_{cyl,max}$ . Position-related features are denoted with the gray shaded background and size-related features have a white background.

**Table 2. List of flame features for analysis. The gray shaded section denotes position-related features and the white zone denotes size-related features.**

Feature	[14] Feature	Description
centroidX	$f_1$	Centroid x (horizontal direction)
centroidY	$f_2$	Centroid y (vertical direction)
leftmostX	$f_9$	x-coordinate of leftmost point
leftmostY	$f_{10}$	y-coordinate of leftmost point
bottomX	$f_{13}$	x-coordinate of bottommost point
bottomY	$f_{14}$	y-coordinate of bottommost point
area	$f_{20}$	Total cross-sectional area
contourXstd	$f_{30}$	x-coordinate of contour points std
distanceMean	$f_{31}$	Distance of contour points to centroid (mean)
distanceStd	$f_{32}$	Distance of contour points to centroid (std)

#### 3.3.2 Correlation Between Flame and Combustion Speed

The correlations between the flame features and  $P_{cyl,max}$  over CAD (for each flame image) is the first set of quantities to examine in the delineation of the causal chain of the CCV caused by EGR. The Pearson correlation coefficient R is calculated using the linear regression of the scattered data at each CAD, that is, one flame feature value and one  $P_{cyl,max}$  for every cycle at each CAD. The correlation of all 10 features to  $P_{cyl,max}$  is displayed in Figure 7. The position-related (gray zone) and size-related (white zone) features each have self-similar trends to one another. The x-position-related features show increasing correlation of up to 0.6 shortly after ignition as the flame first appears in the FOV and begins to grow near the spark plug. This is due to the either left or right early flame development, which turns out to be a decisive factor in higher EGR cases. Then correlation values decrease, as the initial flame kernel expands. In the case of leftmostX the correlation switches sign and increases again. Towards TDC, cycles that exhibit a delayed flame development into the left half of the cylinder result in low  $P_{cyl,max}$ . On the other hand, the y-position-related features have a relatively steady or an increase in correlation to  $P_{cyl,max}$ . For the higher EGR-cases these features tend to correlate with the cross-sectional area and are simultaneously bound by the upward moving piston.

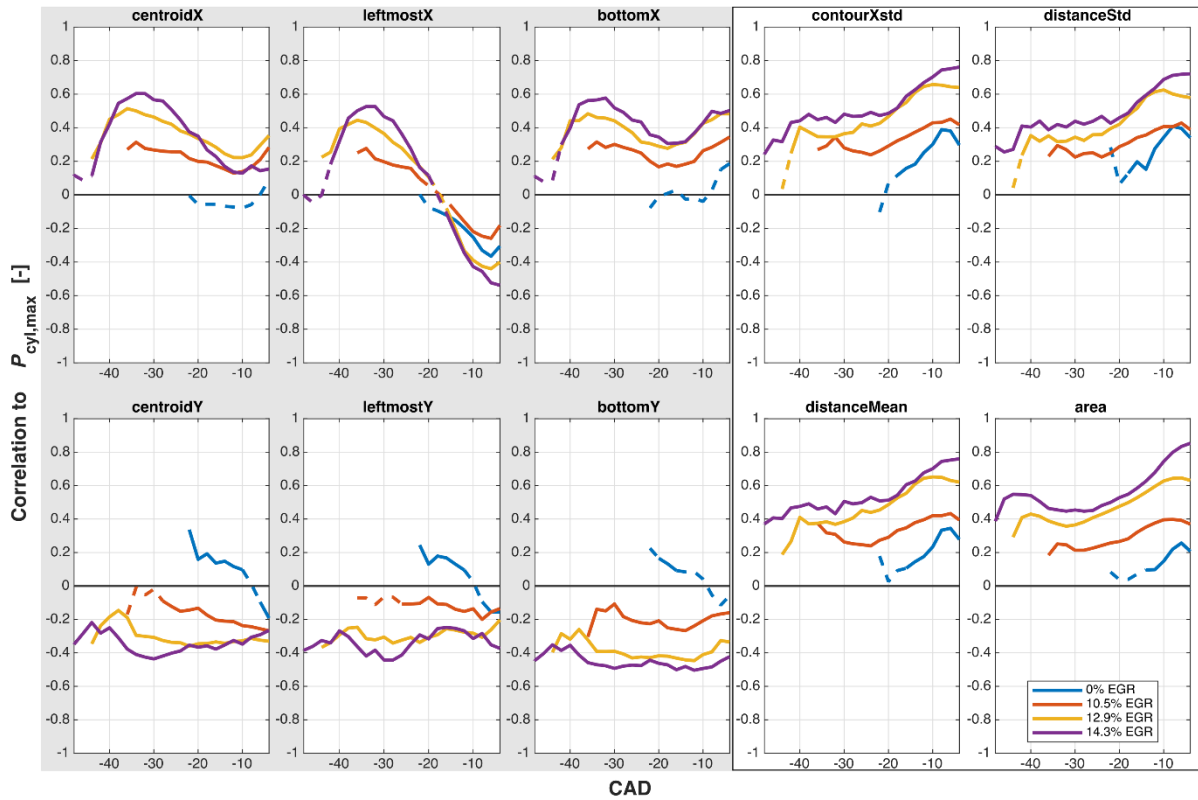


**Figure 7. Correlation between  $P_{cyl,max}$  and flame feature for each EGR rate. The gray shaded section denotes position-related features and the white zone denotes size-related features. Each correlation starts shortly after ignition. Correlations which are not significant (significance level of 0.05) are shown as dashed lines.**

As EGR levels are increased, correlations generally increase which indicates a link between the pressure COV and the flame development. Initially, x-position features have positive correlation which means that a flame whose center position is further to the right is likely to have faster combustion. Maximum correlation values of up to 0.6 are observed already at  $-30^{\circ}\text{CA}$ , roughly 40-50 CADs before maximum cylinder pressures are reached, which emphasizes the importance of early combustion on the subsequent flame growth. Conversely, y-position features generally have negative correlations to the pressure, indicating an inverse relationship, that is, a flame whose y-position is located closer to the piston (more negative y-position) is likely to exhibit faster combustion. The size-related features, especially the cross-sectional flame area, exhibit constant increasing correlations, which shows that the cross-sectional flame area represents the flame volume well.

### 3.3.3 Flame-Flow Correlations

To correlate flame features with the flow, each PIV vector at a certain position and CAD can be correlated with a flame feature over all cycles. The resulting correlations can then be displayed in the position of the corresponding vector on a 2D plot with a colormap representing the R values to allow a spatial analysis of the feature and flow field's correlation. The method of spatial correlations with flow fields has already been utilized in optical research engines to examine the relationship between cyclic features such as the IMEP [8], the spark position [11], and the flame position [12] with the velocity.

In this work, the spatial flame-flow correlations are first compared with one another and with the features from the different EGR levels on one coherent chart before specific OCs and features are selected for closer examination. For the flame features, one CAD, namely  $-30^{\circ}\text{CA}$  was selected based on the high correlations between the x-position features and the maximum in-cylinder pressure displayed in Figure 7. At  $-30^{\circ}\text{CA}$  the 0% EGR OC is not included since the ignition occurs later; however,

the correlations of the no EGR OC at later CADs are lower than those with higher EGR since the flow has less of an effect on the flame development in this case, and are thus less relevant. A reduction of complexity must first be done because the resulting number of correlation fields is 2670 (3 OCs  $\times$  10 features  $\times$  89 PIV CADs). Figure 8 displays the comparison of spatio-temporal average correlations between the flame feature and the x- and y-component of velocity by taking the mean absolute value of R over all flow fields and CADs. To ensure a high probability that the correlation R is significant (and a low probability of observing the null hypothesis), each correlation undergoes a significance filter in which the p-values must be less than 0.05, where low p-values mean a more significant correlation in R [27]. The resulting quantity is the correlation coefficient normalized to all possible vector positions over each CAD in time. As the quantities are normalized, they offer a direct comparison of the correlation between the velocity and flame features at each EGR level. Therefore, Figure 8 presents a non-ML-based feature importance in terms of their relationship to the flow. The correlations agree generally well with Figure 7 in that increasing EGR and CCV leads to increasing correlation. However, at the highest EGR level, the x-position features of the flame correlate less with the flow than at 12.9% EGR which is probably due to the significant amount of out of FOV and plane motion of the flames present in the 14.3% EGR OC. While the correlations in Figure 7 relate the flame to the in-cylinder pressure, and thereby CCV, Figure 8 relates the flame features at  $-30^{\circ}\text{CA}$  to the flow, at which point the flame may be underdeveloped (due to the many partial misfires), out of the plane (due to the greater influence of convection on the flame), or highly developed and out of the FOV, washing out the correlations. The correlations also agree well with Figure 7 in that features related to the position of the flame have higher correlations than those related to the size, which is because most of the flames at  $-30^{\circ}\text{CA}$  are very small in the FOV. Therefore, the direction of the initial flame propagation plays a large role in the determination of the cyclic performance. In addition to higher EGR having higher correlations,  $V_y$  component correlations are also generally greater than  $V_x$  correlations, indicating that upward motion induced by the compression has a more significant role in the placement and shape of the flame or it is more descriptive of the final tumble position. It is especially interesting to consider the flame feature with the greatest correlations: centroidX. The y-component of the velocity correlates higher than the x-component even for the x-coordinate of the flame's centroid, meaning that the centroid's horizontal position is more sensitive to variations in the upward flow.

Since the highest correlations between the flame (at  $-30^{\circ}\text{CA}$ ) and the flow occur for the 12.9% EGR OC, further analysis of this EGR condition can be done to better understand the link between the velocity field and the flame development. Figure 9 displays the average spatial correlation between flow fields from the late intake phase until late compression and flame features at  $-30^{\circ}\text{CA}$ . It is not only remarkable that significant correlations exist between the flame and the velocity fields as early as the intake phase, but also that peaks in average correlation correspond to physical events such as the closing of the intake valves, the appearance of the tumble center within the given FOV, and the piston deceleration. Furthermore, such a visualization provides context for quantities in Figure 8 that are averaged over all CADs. Each flame feature has a phase-locked correlation to the physical events dictating the in-cylinder velocity. However, while Figure 8 and Figure 9 provide a broad generalized overview of the relationships between flame features and velocity fields, they cannot provide spatial information about these relationships; yet they offer a hint to which specific correlation fields may be of note.

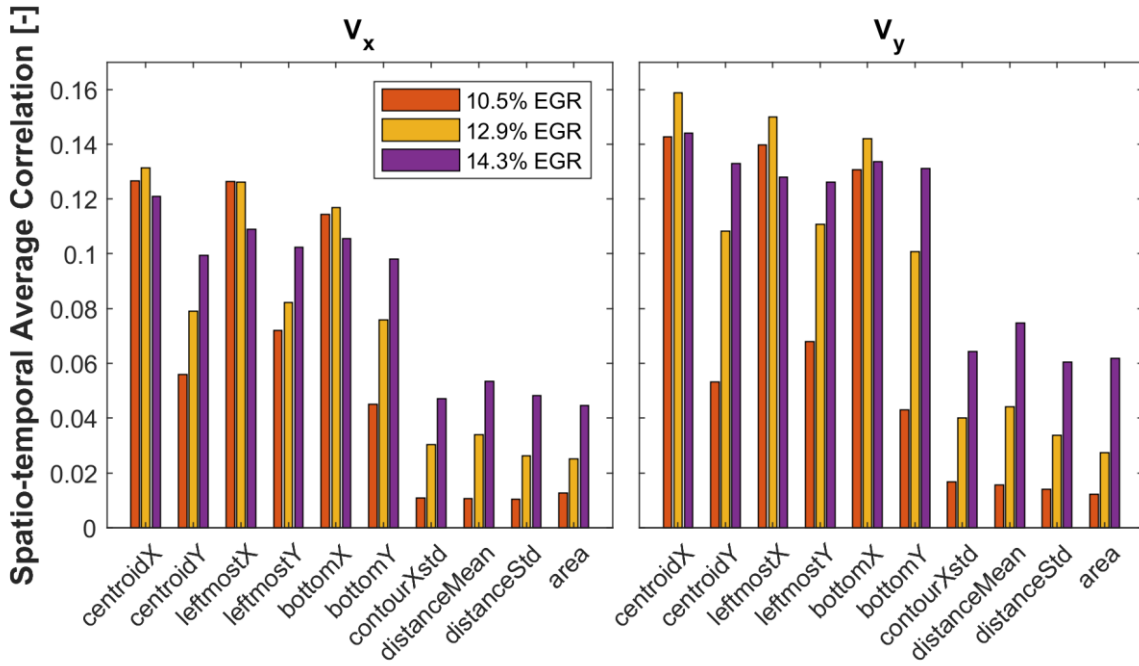


Figure 8. Sum of correlation over the field and over CADs normalized to the total sum at all available vector positions. Flame features are calculated at  $-30^{\circ}\text{CA}$ .

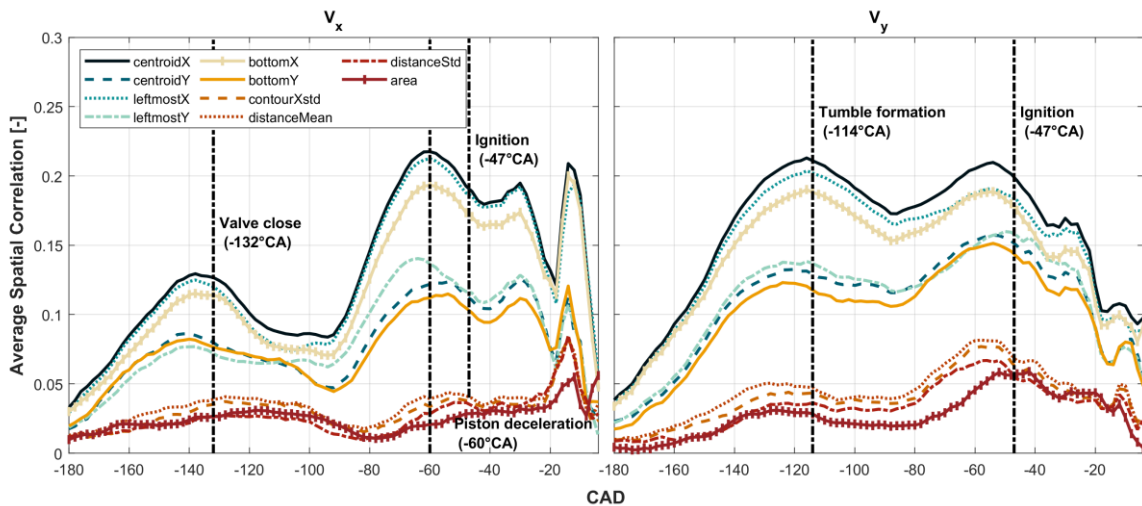


Figure 9. Sum of correlation over the field at each CAD normalized to the total sum at all available vector positions. Flame features are calculated at  $-30^{\circ}\text{CA}$ .

Building from the analysis of Figure 8 and Figure 9, the flame feature with the greatest correlations to the flow fields, centroidX, can be further examined at the CADs with physical events highlighted by the vertical dot-dash lines in Figure 9. Figure 10 shows the correlation fields of the horizontal and vertical velocity components with centroidX at the highlighted relevant CADs. The blue-white-red colormap represents the quantity of the correlations with dark blue and red corresponding to a high negative and positive correlation, respectively. The vector field displayed represents the mean velocity magnitude and direction over all cycles at each interrogation window (showing every 6<sup>th</sup> vector). As the correlations represent linear regression relationships between scattered data, a schematic of arrow directions is displayed to help explain the physical meaning of a positive correlation in terms of the velocity component and the horizontal location of the centroid. Moreover, two point locations labeled Point 1 and 2 are indicated by a blue and red pixel and large arrows to describe the point locations for the scatter plots shown in Figure 11. In addition to the aforementioned significance



filter which removes locations with a low probability of having a significant correlation, the symmetric colormap also removes additional locations of very low correlation by the white color.

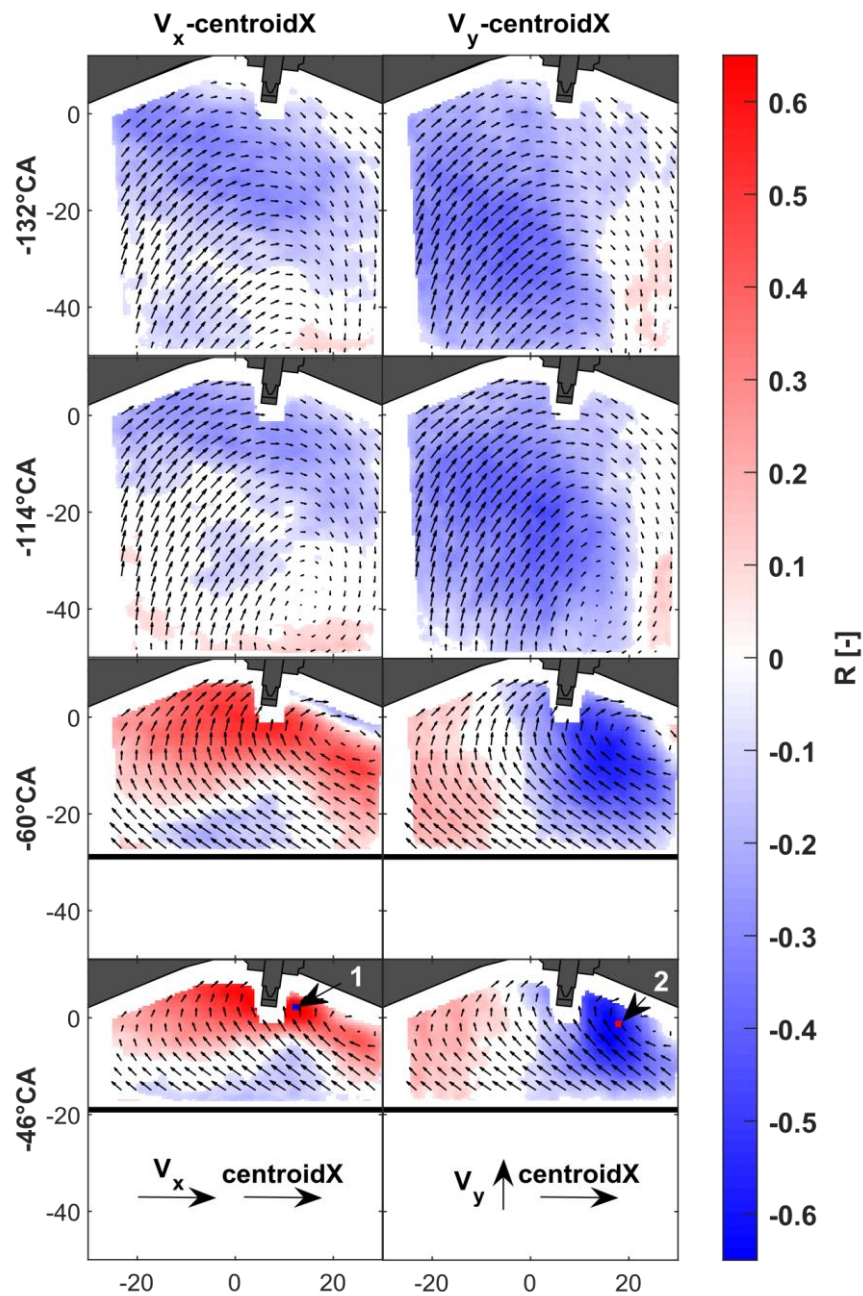


Figure 10. Correlation field for  $V_x$  (left) and  $V_y$  (right) and centroidX (calculated at  $-30^\circ\text{CA}$ ) at selected CADs.

At  $-132^\circ\text{CA}$ , when the intake valves close, the  $V_x$  side of Figure 10 shows widespread significant negative correlations averaging  $R \approx -0.30$ , especially in the region to the left and below the spark plug. Since all of the vectors in this negative  $R$  region point towards the right, it indicates a tendency for positive  $x$ -direction velocities this early in the engine cycle to correlate with a more leftward flame centroid. The negative correlations for the  $V_y$  field are on average greater ( $R \approx -0.35$ ) with a larger presence on the intake side between  $y = -20$  and  $-40$  mm. Since most of these negative correlations occur where the mean velocity is pointed in the positive  $y$ -direction, this indicates that greater upward (or less downward) velocities in these regions at the time of the intake valve closing correlate to more leftward flames at  $-30^\circ\text{CA}$ . As the tumble center begins to come into view at  $-114^\circ\text{CA}$ , the  $V_x$  correlations seem to not change much apart from the decrease in the area of negative  $R$  values and

the emergence of very low positively correlated locations below the tumble center. On the  $V_y$  side a similar trend to  $-132^\circ\text{CA}$  is observed, but the region of negative correlation has grown and velocities in the region tend to be more vertically oriented.

In late compression at  $-60^\circ\text{CA}$ , the correlations near the cylinder roof and especially near the spark plug increase and become strongly positive for the  $V_x$  side. This change of signs is confirmed by negative correlations between  $V_x$  at  $-132^\circ\text{CA}$  and  $-60^\circ\text{CA}$  close to the cylinder head. An analysis of conditioned flow fields (not shown) reveals that cycles featuring an initially stronger upwards directed flow of the tumble lead to lower velocities near the cylinder head and a slightly shifted tumble center during late compression. At this stage in the cycle, the flow's tumble center is still visible in the FOV as the piston compresses it towards the exhaust valves. To the left of the spark plug, positive  $V_x$ -centroidX correlations averaging  $R \approx 0.50$  and a positive  $V_x$  indicate that higher velocities into the spark plug correlate to the flame growing to the right at  $-30^\circ\text{CA}$ . On the  $V_y$  side, the greatest correlations ( $R \approx -0.55$ ) occur near the tumble center to the right and below the spark plug. At the locations of peak negative correlations, the velocity remains in the positive y-direction indicating that greater velocities there lead to the flame growing to the left at  $-30^\circ\text{CA}$ . The trends continue for both velocity components at the time of ignition ( $-46^\circ\text{CA}$ ), but the peak correlations reach up to an average of positive and negative 0.65 near the spark plug. To aid in the interpretation, Figure 11 displays scatter plots of the  $V_x$  and  $V_y$  data with the centroidX at the two points indicated in Figure 10. While the average vector arrows in Figure 10 point in one direction, the scatter plots indicate that there is a wide range of positive and negative velocities for both components which follow a linear trend (indicated by the solid red regression line). The region around centroidX = 5mm shows fewer data due to the spark plug geometry at this position and since the flames at  $-30^\circ\text{CA}$  are typically either to the left or right of the spark plug.

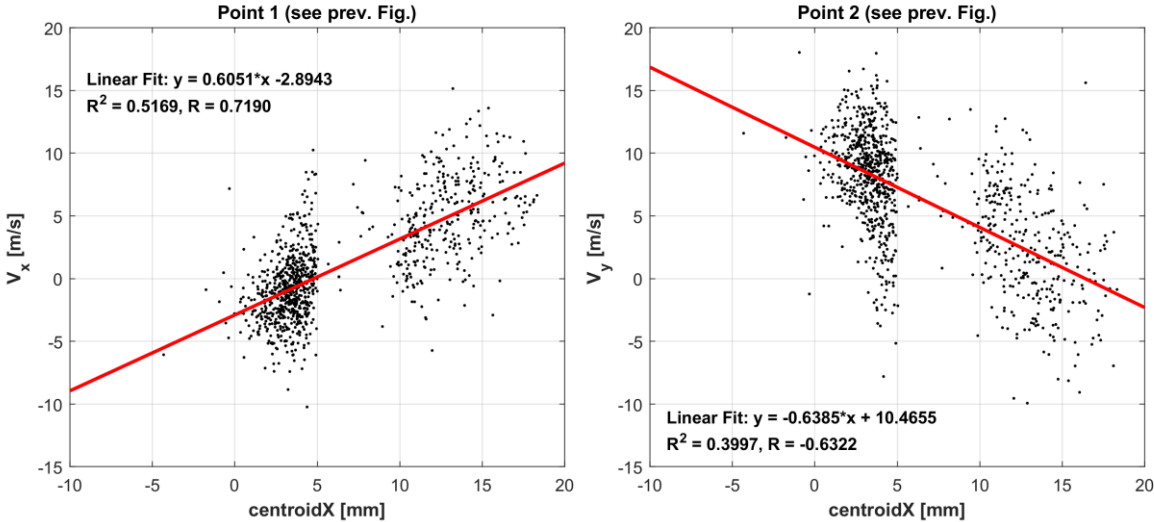


Figure 11. Scatter plot of selected points of the correlation field at  $-46^\circ\text{CA}$  in Figure 10.

Despite the arrow schematic in Figure 10 and the scatter plots of data near the spark plug in Figure 11, it can still be quite difficult to interpret the meaning of the correlation fields at the time of ignition. Therefore, it is helpful to investigate conditional statistics using the cycles of extreme centroidX as the criterion for separation to directly examine the role of convection on the flame propagation. Figure 12(a) shows the mean velocity fields of the 50 lowest (left with blue box) and highest (right with red box) centroidX cycles. There is a substantial difference in average flow direction and magnitude for the two samples. In the high centroidX cases, the tumble center is shifted into the FOV next to the spark plug and a region of strong horizontal flow from the intake to the exhaust side is visible, which directly affects the spark plug gap region. Subsequently, the flames with highest



centroidX are convected to the right side, in stark contrast to the lower centroidX cycles, which appear to the left. The location of the tumble center in the case of the low centroidX sample is nearly out of the FOV and there is a large vertical flow structure that reaches from the piston surface to the spark plug. This high vertical velocity region below and to the right of the spark plug is similar in location to the high negative  $V_y$ -centroidX correlation region in Figure 10. This confirms that very high upward-directed velocities to the right of the spark plug inhibit the flame's growth in that region, leading to a preferred development and convection towards the center of the cylinder. The comparison between the velocity magnitude fields shown on the bottom of Figure 12(a) further shows the importance of higher magnitude velocities reaching from the piston surface to the right of the spark plug in inhibiting the flame growth there.

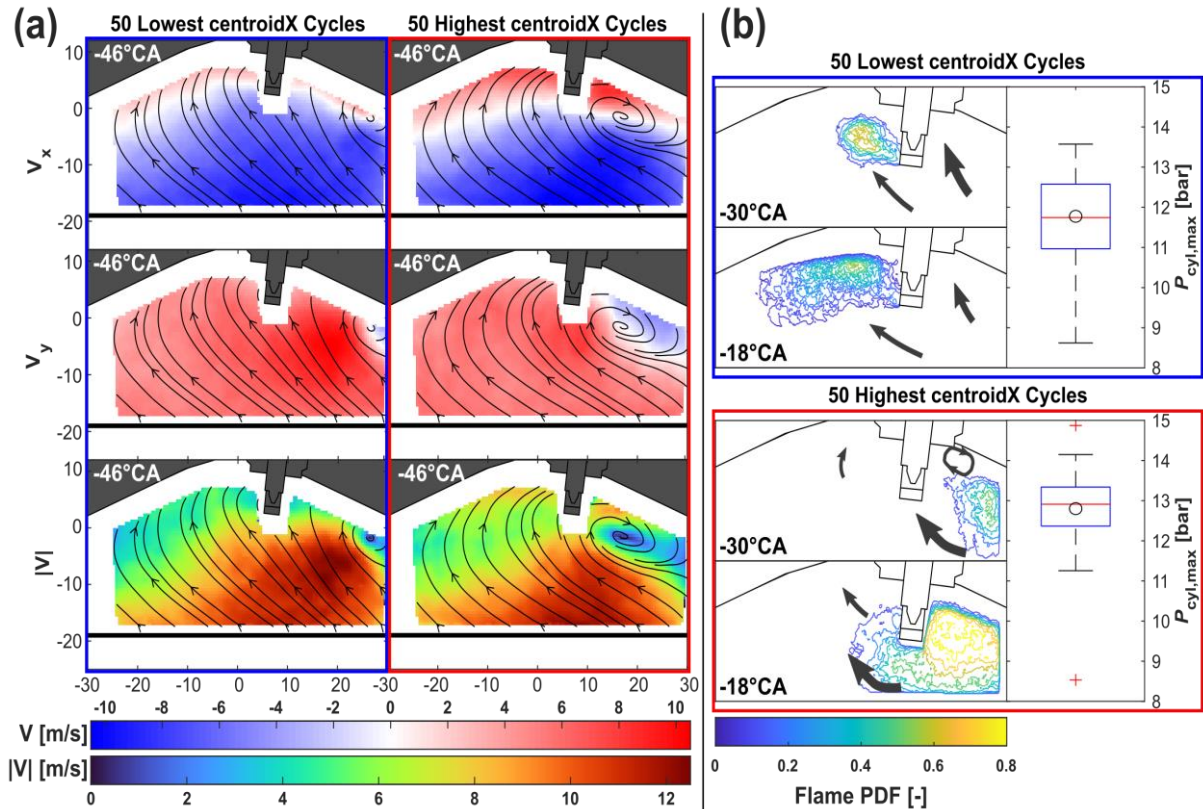


Figure 12. (a) Conditional statistics of the velocity components for 12.9% EGR at -46°CA, (b) flame propagation PDF with flow model, and box plots of  $P_{cyl,max}$  for the 50 lowest and highest centroidX cycles.

In Figure 12(b), the conditional PDFs of the flame at -30°CA and -18°CA are shown to summarize a flame-flow model taken from the mean velocities where vectors are available at the corresponding CADs (not shown). Beginning with the lowest centroidX cycles (blue box), the large upward flow directed from the piston towards the bottom right tip and to the right of the spark plug forces the early flame to begin its propagation away from the flow structure. At -18°CA, the flame within the symmetry plane is partially attached to the spark plug and convected towards the intake valves (much of it out of the FOV) by the remaining upward- and leftward-directed flow from the piston motion. In the case of the highest centroidX cycles, the combination of the presence of the large tumble vortex center to the right of the spark plug (with a strong leftward flow below the tumble) and the rightward-directed velocity starting at the left side of the spark plug cause the flame to propagate to the right (also out of the plane and FOV). At -30°CA, the tumble center remains in the FOV to the right of the spark plug and the flames appear to follow the clockwise convection, moving to the left below the tumble center. At -18°CA, the flame occupies nearly the entire region to the right of the spark plug as the leftward flow stemming from the compression of the tumble continues to convect it towards the center. While it is clear that some of the flame is cut off by the given FOV, the cross-

sectional flame area from the high centroidX sample is significantly larger, which helps explain why the  $P_{\text{cyl,max}}$  box plots on the right side of Figure 12(b) are different, especially in terms of mean (oval) and median (red line) maximum in-cylinder pressure. Since centroidX was calculated at  $-30^{\circ}\text{CA}$ , a time when it correlates relatively high with  $P_{\text{cyl,max}}$  (compare Figure 7), the conditioned cycles of extreme left and right centroidX are not only linked to the stark differences in the flow field, but also to slower and faster combustion, as evidenced by a mean and median  $P_{\text{cyl,max}}$  difference of over 1 bar between samples. Therefore, Figure 12 exhibits a tendency for the early flame's direction of propagation to predict whether the flame will grow quickly or slowly and this is directly correlated with the state of the velocity at the time of ignition. If the flow field is characterized by a strong upward flow onto the right side of the spark plug, the flame is likely to first propagate to the left, where it is convected further upward towards the intake valves, causing it to lose heat at the walls. The consequence is a slower growth of the flame as it must develop against a strong flow that directs its propagation along the walls, leading to lower  $P_{\text{cyl,max}}$ . However, when the clockwise tumble center lingers close to the spark plug, a rightward-directed flow influences the flame to propagate first to the right, where it can grow in a region of lower velocity, then it is propelled by the vortex and then free to quickly grow with a strong leftward velocity towards the rest of the unburnt cylinder gas, leading to higher  $P_{\text{cyl,max}}$ .

### 3.3.4 Correlation of Large-scale Flow Structures to CCV

Earlier research has used planar PIV and flame imaging to show that large-scale flow structures play an important role in determining cyclic combustion speed [6, 10]. In the present work, a link between flame features and the combustion speed (compare Figure 7) and a link between the flame features and flow field has been shown. Figure 12 shows a correlation between the flow field, the flame's x-position, and the in-cylinder pressure. However, to further strengthen the contention of the present work that there is a significant correlation between the flame position, size, and large-scale velocity structures to the combustion speed, conditional analysis of the most unstable case (14.3% EGR) with 90 misfire cycles is selected due to the amplification of the effects causing CCV. Although the same trends for the correlations between flow and  $P_{\text{cyl,max}}$  occur in the 12.9% EGR case, albeit with slightly lower correlations, the 14.3% case offers the unique opportunity to examine the differences between a large number of misfire cycles and fast combustion cycles. For the most acute comparison, conditional statistics between the 90 misfire cycles and the 90 greatest  $P_{\text{cyl,max}}$  cycles are compared in Figure 13. In Figure 13(a) the conditional mean velocity field for the misfire (left, blue box) and the fast combustion (right, red box) cycles is shown for the intake, compression, and the time of ignition. During intake at  $-180^{\circ}\text{CA}$  and compression at  $-90^{\circ}\text{CA}$ , the differences between the velocities are subtle, with the main characteristic difference being greater velocity magnitudes and a more compact tumble center in the case of the misfire set. However, at the time of ignition, greater disparity is apparent. As was observed with cycles with low centroidX (compare Figure 12), misfire cycles have a greater bulk velocity structure extending from the piston surface to the spark plug than their counterpart's flow field. Furthermore, the fast combustion flow fields also have a stronger horizontal flow across the spark plug from the intake to the exhaust side. However, it is interesting to note that both sets exhibit a mean tumble vortex center of similar size and position, despite the aforementioned contrasts. This indicates that the presence of the tumble center to the right of the spark plug is far from the lone influencing attribute causing faster flame growth. Rather, the flame's growth is determined by the direction and magnitude of the flow surrounding the spark plug, as discussed with Figure 12. In this case, the flow around the tumble center varies strongly between the two samples leading to distinct velocity structures around the spark plug at ignition.

Since there are distinct characteristics that emerge in the contrasting conditional flow fields near the spark plug, they also appear in the correlation fields (over all cycles, not conditionally separated) displayed in Figure 13(b). Although correlations are generally lower than those appearing for centroidX at ignition (for the flame at  $-30^{\circ}\text{CA}$  for 12.9% EGR), they have the same structures. The

correlation fields displayed lead to the conclusion that cycles of faster combustion correlate with stronger rightward velocities and weaker upward velocities near the spark plug.

To summarize a conceptual model for the extreme cycles, Figure 13(c) displays the PDFs of the early flame as well as a flow diagram which takes into account the flow at  $-50^\circ\text{CA}$  and the corresponding velocity fields at the times of the flame PDFs (not shown). For the misfire cycles (left, blue box), it may be surprising to observe the presence of early flame kernels despite the negative  $\text{IMEP}_g$  criterion. Nevertheless, the significant bulk flow stemming from the piston's approach to TDC forces the flame to develop towards the left, before blowing off or quenching at the cylinder roof out of the measurement plane. Conversely, the fast combustion cycles sustain flame growth towards the right side due to the horizontal flow across the spark gap and the lack of high velocities forcing the flame against the roof due to the location of the tumble center. In contrast to the flames conditioned to high centroidX shown in Figure 12(b), the fast combustion flames for 14.3% EGR exhibit less clockwise convection along the tumble vortex center because the velocities surrounding the vortex center are more moderate. However, similar to the case of centroidX for 12.9% EGR, after an initial rightward propagation, the flame grows quickly in the low velocity vortex center before being convected by the leftward flow above the piston towards the rest of the unburnt gas in the cylinder.

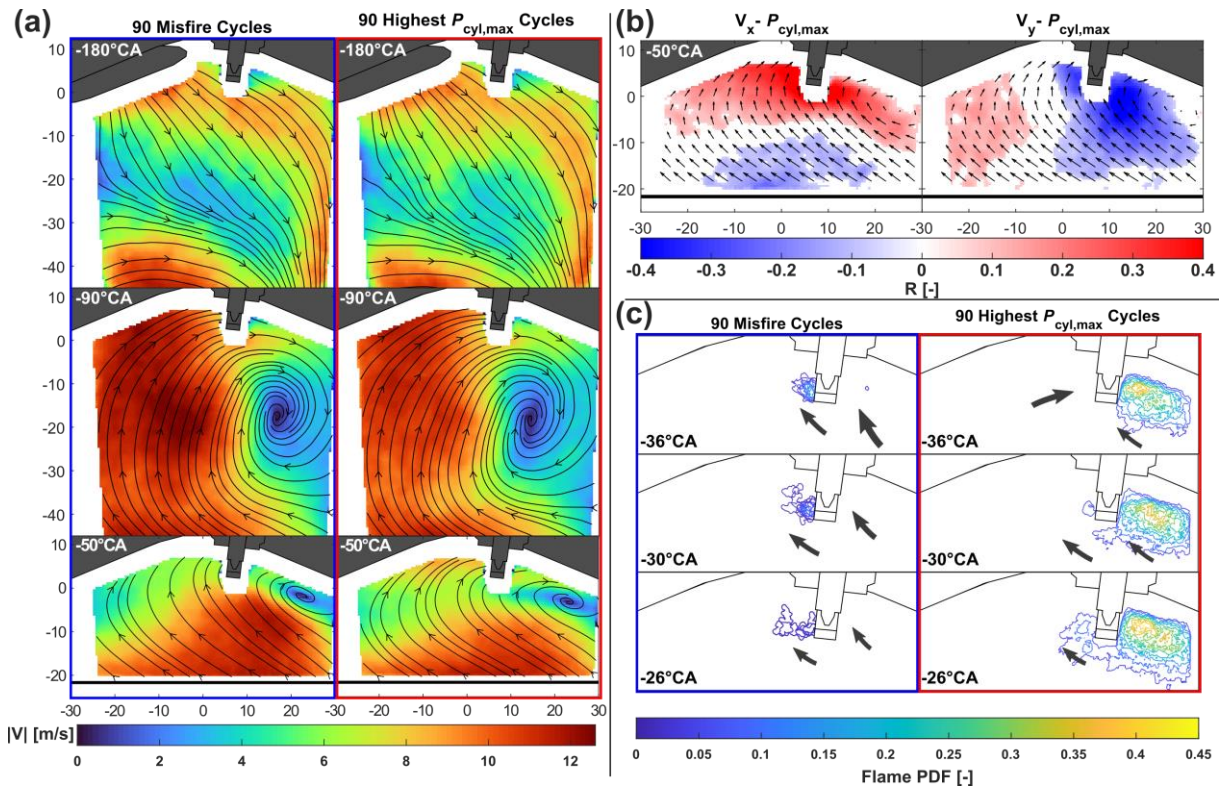


**Figure 13. (a) Conditional average velocity fields for 14.3% EGR with the 90 misfire cycles (left) and the 90 cycles with the highest  $P_{\text{cyl,max}}$  (right). (b) The correlation between the horizontal (left) and vertical (right) velocity components with  $P_{\text{cyl,max}}$ . (c) Propagation of the conditional flame PDF and flow model.**

The analysis accompanied with Figure 12 and Figure 13 shows that the velocity in the vicinity of the spark plug at the time of ignition is critical in determining the cyclic combustion speed. However, when comparing the differences in velocity of HC and LC shown in Figure 6, analyzing the velocity at the spark plug alone is not enough to predict fast and slow cycles since depending on the OC, higher velocity directed towards the intake valves leads to either slow or fast combustion. Because the flame development, and consequently the combustion speed, correlates with the velocity significantly as early as the intake phase, the entire flow history can provide context for an accurate prediction of the cyclic performance. In a previous study with the same engine under full-load conditions, ML techniques

used the flow history from intake until ignition and flame features to predict cycles with high and low  $P_{cyl,max}$  [13]. Although the engine was operated under different conditions such as the intake pressure, ignition timing, and internal EGR levels, the horizontal velocity near the spark plug was found to be important in the prediction of CCV similar to the present study. In addition, the conditional velocity fields displayed that a stronger horizontal flow across the spark plug yields higher in-cylinder pressure. The agreement of results with entirely different OCs is a promising finding that aspects of the analysis of this work can translate to different engine configurations.

## 4 CONCLUSIONS

Various levels of homogeneously mixed exhaust gas recirculation were introduced in a port fuel injection SI engine experiment operating in a skip-fire scheme to ensure proper reactant homogeneity at ignition. The incremental increase in externally-controlled EGR levels led to an exponential increase in cyclic variance. By employing simultaneous high-speed PIV and planar Mie scattering techniques for thousands of cycles, the causes of CCV were investigated by examining the conditional statistics and multivariate correlations of the flame development and the velocity fields in the symmetry plane of the engine.

Although the mean flow field in compression was unaffected by the varying EGR levels, combustion was slowed down with increasing EGR, allowing for an increase in the flame's sensitivity to variations in the in-cylinder velocity. Since there were no differences in gas homogeneity nor the thermodynamic conditions at and after ignition for a given OC, the measured CCV was truly due to observable variations in the bulk velocity field. In the stable case of 0% EGR, flames were always directed towards the center of the cylinder due to the bulk motion induced by the piston at the time of the ignition, causing a tendency for the flame kernel to grow evenly from the center to the cylinder walls. However, to achieve combustion with increasing EGR levels, the spark timing had to be moved earlier to counteract the slowed flame speeds. Consequentially, in higher EGR cases, the flames could be convected by the presence of a lingering tumble vortex center near the spark plug, encouraging flame propagation from right to left following the clockwise vortex. Conversely, when the tumble center shifts further right or there is a stronger upward velocity from the piston surface onto the spark plug tip, the flame is directed towards the center of the cylinder from right to left. In the most sensitive condition with 14.3% EGR, significant correlations between the maximum in-cylinder pressure and the velocity components show that large-scale velocity structures play a crucial role in determining combustion speed. Similar to the conditions affecting the direction of the flame propagation in the 12.9% case, the presence of a higher magnitude upward velocity directed towards the bottom of the spark plug can cause the flame to not only propagate to the left, but also towards the intake valves where they either blow off, or quickly quench at the wall, leading to misfire. Moreover, the lack of this bulk flow directly below the spark plug and an increased velocity from the left to right across the spark plug gap encourages faster combustion.

In future work, analysis of the spark through high-speed imaging of the plasma and spark energy measurements in combination with the flame and flow analysis techniques of this work can help complete the knowledge of the causal chain of cyclic variations with increasing EGR. Furthermore, the extension of the measurement and analysis techniques employed in this work to internally-induced EGR with species concentration measurements will be invaluable in the design of near-future highly optimized IC engines.

### Author Contributions

All authors contributed to the study conception and design. A.D. and B.B. acquired funding. Experimental preparation and data collection were performed by C.W., L.I., and M.S. Data analysis, generation of figures, and the preparation of the first draft of the manuscript were performed by C.W.

All authors commented on previous versions of the manuscript. The final discussion and analysis of results were performed by C.W. and M.S. All authors read and approved the final manuscript.

## Funding

Open Access funding was provided by Projekt DEAL. Support by Deutsche Forschungsgemeinschaft through FOR 2687 “Cyclic variations in highly optimized spark-ignition engines: experiment and simulation of a multi-scale causal chain”—project number 423224402 - is kindly acknowledged.

## COMPLIANCE WITH ETHICAL STANDARDS

### Conflict of Interest

The authors declare that they have no conflict of interest.

### Open Access

This article is licensed under a Creative Commons Attribution 4.0 International License, which permits use, sharing, adaptation, distribution and reproduction in any medium or format, as long as you give appropriate credit to the original author(s) and the source, provide a link to the Creative Commons license, and indicate if changes were made. The images or other third-party material in this article are included in the article’s Creative Commons license, unless indicated otherwise in a credit line to the material. If material is not included in the article’s Creative Commons license and your intended use is not permitted by statutory regulation or exceeds the permitted use, you will need to obtain permission directly from the copyright holder. To view a copy of this license, visit <http://creativecommons.org/licenses/by/4.0/>.

## REFERENCES

1. NOAA National Centers for Environmental Information: State of the Climate: Global Climate Report for Annual 2021. <https://www.ncdc.noaa.gov/sotc/global/202113> (2022). Accessed 9 March 2022
2. Crippa, M., Guizzardi, D., Solazzo, E., Muntean, M., Schaaf, E., Monforti-Ferrario, F., Banja, M., Olivier, J., Grassi, G., Rossi, S., Vignati, E.: GHG emissions of all world: 2021 report. Publications Office of the European Union (2021)
3. IEA: Tracking Transport 2021. <https://www.iea.org/reports/tracking-transport-2021> (2021). Accessed 9 March 2022
4. Fontana, G., Galloni, E.: Experimental analysis of a spark-ignition engine using exhaust gas recycle at WOT operation. *Appl. Energy* (2010). <https://doi.org/10.1016/j.apenergy.2009.11.022>
5. Ozdor, N., Dulger, M., Sher, E.: Cyclic Variability in Spark Ignition Engines A Literature Survey. In: SAE Technical Paper Series. International Congress & Exposition, FEB. 28, 1994. SAE International 400 Commonwealth Drive, Warrendale, PA, United States (1994). <https://doi.org/10.4271/940987>
6. Buschbeck, M., Bittner, N., Halfmann, T., Arndt, S.: Dependence of combustion dynamics in a gasoline engine upon the in-cylinder flow field, determined by high-speed PIV. *Exp. Fluids* (2012). <https://doi.org/10.1007/s00348-012-1384-3>
7. Zeng, W., Sjöberg, M., Reuss, D.L.: Combined effects of flow/spray interactions and EGR on combustion variability for a stratified DISI engine. *Proc. Combust. Inst.* (2015). <https://doi.org/10.1016/j.proci.2014.06.106>
8. Bode, J., Schorr, J., Krüger, C., Dreizler, A., Böhm, B.: Influence of three-dimensional in-cylinder flows on cycle-to-cycle variations in a fired stratified DISI engine measured by time-resolved dual-plane PIV. *Proc. Combust. Inst.* (2017). <https://doi.org/10.1016/j.proci.2016.07.106>



9. Schiffmann, P., Reuss, D.L., Sick, V.: Empirical investigation of spark-ignited flame-initiation cycle-to-cycle variability in a homogeneous charge reciprocating engine. *Int. J. Engine Res.* (2017). <https://doi.org/10.1177/1468087417720558>
10. Zeng, W., Keum, S., Kuo, T.-W., Sick, V.: Role of large scale flow features on cycle-to-cycle variations of spark-ignited flame-initiation and its transition to turbulent combustion. *Proc. Combust. Inst.* (2019). <https://doi.org/10.1016/j.proci.2018.07.081>
11. Bode, J., Schorr, J., Krüger, C., Dreizler, A., Böhm, B.: Influence of the in-cylinder flow on cycle-to-cycle variations in lean combustion DISI engines measured by high-speed scanning-PIV. *Proc. Combust. Inst.* (2019). <https://doi.org/10.1016/j.proci.2018.07.021>
12. Fach, C., Rödel, N., Schorr, J., Krüger, C., Dreizler, A., Böhm, B.: Investigation of in-cylinder soot formation in a DISI engine during transient operation by simultaneous endoscopic PIV and flame imaging. *Int. J. Engine Res.* (2022). <https://doi.org/10.1177/14680874221079764>
13. Dreher, D., Schmidt, M., Welch, C., Ourza, S., Zündorf, S., Maucher, J., Peters, S., Dreizler, A., Böhm, B., Hanuschkin, A.: Deep feature learning of in-cylinder flow fields to analyze cycle-to-cycle variations in an SI engine. *Int. J. Engine Res.* (2021). <https://doi.org/10.1177/1468087420974148>
14. Hanuschkin, A., Zündorf, S., Schmidt, M., Welch, C., Schorr, J., Peters, S., Dreizler, A., Böhm, B.: Investigation of cycle-to-cycle variations in a spark-ignition engine based on a machine learning analysis of the early flame kernel. *Proc. Combust. Inst.* (2020). <https://doi.org/10.1016/j.proci.2020.05.030>
15. Krüger, C., Schorr, J., Nicollet, F., Bode, J., Dreizler, A., Böhm, B.: Cause-and-effect chain from flow and spray to heat release during lean gasoline combustion operation using conditional statistics. *Int. J. Engine Res.* (2017). <https://doi.org/10.1177/1468087416686721>
16. Stiehl, R., Bode, J., Schorr, J., Krüger, C., Dreizler, A., Böhm, B.: Influence of intake geometry variations on in-cylinder flow and flow–spray interactions in a stratified direct-injection spark-ignition engine captured by time-resolved particle image velocimetry. *Int. J. Engine Res.* (2016). <https://doi.org/10.1177/1468087416633541>
17. Truffin, K., Angelberger, C., Richard, S., Pera, C.: Using large-eddy simulation and multivariate analysis to understand the sources of combustion cyclic variability in a spark-ignition engine. *Combust. Flame* (2015). <https://doi.org/10.1016/j.combustflame.2015.07.003>
18. Kodavasal, J., Abdul Moiz, A., Ameen, M., Som, S.: Using Machine Learning to Analyze Factors Determining Cycle-to-Cycle Variation in a Spark-Ignited Gasoline Engine. *J. Energy Resour. Technol.* (2018). <https://doi.org/10.1115/1.4040062>
19. Di Mauro, A., Chen, H., Sick, V.: Neural network prediction of cycle-to-cycle power variability in a spark-ignited internal combustion engine. *Proc. Combust. Inst.* (2019). <https://doi.org/10.1016/j.proci.2018.08.058>
20. Freudenhammer, D., Peterson, B., Ding, C.-P., Boehm, B., Grundmann, S.: The Influence of Cylinder Head Geometry Variations on the Volumetric Intake Flow Captured by Magnetic Resonance Velocimetry. *SAE Int. J. Engines* (2015). <https://doi.org/10.4271/2015-01-1697>
21. Geschwindner, C., Kranz, P., Welch, C., Schmidt, M., Böhm, B., Kaiser, S.A., La Morena, J. de: Analysis of the interaction of Spray G and in-cylinder flow in two optical engines for late gasoline direct injection. *Int. J. Engine Re.* (2020). <https://doi.org/10.1177/1468087419881535>
22. Welch, C., Schmidt, M., Keskinen, K., Giannakopoulos, G., Boulouchos, K., Dreizler, A., Boehm, B.: The Effects of Intake Pressure on In-Cylinder Gas Velocities in an Optically Accessible Single-Cylinder Research Engine. *SAE Technical Paper 2020-01-0792* (2020). <https://doi.org/10.4271/2020-01-0792>
23. Baum, E., Peterson, B., Böhm, B., Dreizler, A.: On The Validation of LES Applied to Internal Combustion Engine Flows: Part 1: Comprehensive Experimental Database. *Flow Turbul. Combust.* (2014). <https://doi.org/10.1007/s10494-013-9468-6>

24. Schmidt, M., Ding, C.-P., Peterson, B., Dreizler, A., Böhm, B.: Near-Wall Flame and Flow Measurements in an Optically Accessible SI Engine. *Flow Turbul. Combust* (2020). <https://doi.org/10.1007/s10494-020-00147-9>
25. The MathWorks, Inc.: MATLAB Function Reference. *entropyfilt*, 2021st edn., Natick, MA (2021)
26. Bechtold, B.: Violin plots for Matlab. Github Project (2016)
27. The MathWorks, Inc.: MATLAB Function Reference. *corrcoef*, 2021st edn., Natick, MA (2021)